Volume 10, Issues 1-4 2009

INTERNATIONAL JOURNAL OF ENERGY FOR A CLEAN ENVIRONMENT

EDITOR-IN-CHIEF
PROF. JOHN R. LLOYD
University of Texas Pan American
Rapid Response Manufacturing Center
Edinburg, Texas 78539-2999, USA

GUEST EDITOR
DR. YAROSLAV CHUDNOVSKY
Gas Technology Institute
1700 South Mount Prospect Road
Des Plaines, IL 60018

FORMERLY KNOWN AS
CLEAN AIR: INTERNATIONAL JOURNAL
ON ENERGY FOR A CLEAN ENVIRONMENT
FOUNDING EDITOR
PROF. MARIA DA GRAÇA CARVALHO
Lisbon, Portugal

begell house, inc.
publishers

The *International Journal of Energy for a Clean Environment* (ISSN 2150-3621) is published quarterly by Begell House, Inc., 50 Cross Highway, Redding, Connecticut 06896. US subscription rate for 2011 is **$493**. Add $10.00 per issue for foreign airmail shipping and handling fees for all orders shipped outside the United States or Canada. All subscriptions are payable in advance. Subscriptions are entered on an annual basis, i.e., January to December. For immediate service and charge card sales, call (203) 938-1300 Monday through Friday 9 AM-PM EST. Fax orders to (203) 938-1304. Send written orders to Subscriptions Department, Begell House, Inc., 50 Cross Highway, Redding, Connecticut 06896.

Printed July 20, 2011

INTERNATIONAL JOURNAL OF ENERGY FOR A CLEAN ENVIRONMENT

INTERNATIONAL JOURNAL OF ENERGY FOR A CLEAN ENVIRONMENT

The principle aim of the International Journal of Energy for a Clean Environment (IJECE) is to describe, compare, and evaluate innovative technologies that will maximize the efficiency of energy production and utilization while minimizing the production of undesirable emissions into our atmosphere, our earth, and our water supply. Fundamental and applied contributions to the IJECE are encouraged, and papers from industry and end users are welcomed. IJECE deals with interconnected themes covering the reduction of local and global environment degrading emissions while increasing the production of high quality energy. We desire to discuss the integration of supply and demand of energy for all end user sectors.

The main objectives of IJECE are:

- Promote innovative and new integrated energy solutions for a green environment
- Contribute to a sustainable energy economy
- Provide a framework for change in global energy systems
- Promote dissemination of knowledge related to new energy technologies appropriate to developing countries

The IJECE constitutes a forum for discussion of emerging issues in energy such as:

- Production, storage, and utilization of hydrogen as an energy producing fuel
- Alternative and renewable energy sources and their potential for impacting the global supply of resources
- Micro and nano technologies for power production, utilization, and conservation
- Clean combustion advancements
- Sustainable energy concepts for developing countries
- Rational use of energy in manufacturing, architecture, and agriculture

Discussions on conservation strategies and how they drive public policy and codes and standards development for the improvement of our global society are sought.

INTERNATIONAL JOURNAL OF ENERGY FOR A CLEAN ENVIRONMENT

VOLUME 10 / ISSUES 1–4 2009

International Journal of Energy for a Clean Environment, 10(1–4), 1–13 (2009)

HYDROGEN GENERATION SYSTEM WITH CRACKING AMMONIA

Takashi Saika,[*] Tetsuo Nohara, Yuji Aoki, Hiroshi Mitsui, Yosuke Saito, & Masato Iwami

Kogakuin University, Tokyo, Japan

[*]Address all correspondence to Takashi Saika E-mail: saika@cc.kogakuni.ac.jp

Global warming is now a serious environmental and societal issue. Accordingly, fuel cells are being developed as new energy systems. In this study we propose the use of ammonia as a liquid hydrogen carrier. Because ammonia does not contain carbon, CO_2 and CH_4 are not generated through ammonia cracking; instead, H_2 and N_2 are generated at a high temperature. Therefore ammonia has the potential to serve as a liquid fuel. In a hydrogen generation system employing ammonia cracking, the reactor temperature and ammonia separation are regulated by a thermal controller. First, liquid ammonia is evaporated in a vaporizer. Then ammonia is cracked by a catalyst in the reactor to generate H_2 and N_2, and some residual ammonia remains. In a heat exchanger, the waste heat of the cracked gas is recovered. At present, however, the system cannot crack ammonia gas completely. If energy efficiency and safety can be improved, this system utilizing ammonia as fuel will be a promising clean energy system for fuel cells in household and automotive applications.

KEY WORDS: *ammonia, hydrogen carrier, fuel cell, clean energy, zero emission*

1. INTRODUCTION

Global warming is now a serious environmental and societal issue. Around the world, the 12 years from 1995 to 2006 were the warmest on record due to the greenhouse effect of CO_2. Therefore, action on the reduction of greenhouse gas emissions is now urgently needed, especially on the part of advanced nations. Japan has set a target to reduce greenhouse gas emissions during 2008–2012 by 6% from the base-year level [1]. Although various measures have been implemented to achieve target reductions in countries worldwide, CO_2 continues to increase from year to year. The combustion of fossil fuels accounts for almost 80% of anthropogenic CO_2 emissions; to reduce CO_2 emission, the current state of energy issues in society must be reviewed. Furthermore, the scarcity of fossil fuels is problematic. Hence as alternatives to fossil fuels, new energy sources are needed that will have a limited impact upon the global environment.

One such alternative fuel is hydrogen, which can be combined with oxygen to generate electric power. Because hydrogen is not a liquid at ordinary temperatures and pressures, however, the energy density of hydrogen is low. Consequently, hydrogen is of limited utility as a transportation fuel, for instance, in automotive applications. Another problem is hydrogen embrittlement, whereby a material (typically a metal) becomes brittle upon exposure to hydrogen. Embrittlement occurs because extremely small hydrogen molecules can easily diffuse through gaps in the materials.

In this study we propose the use of ammonia as a new hydrogen carrier. The worldwide production of ammonia, a fundamentally important chemical commodity, is about 160 million tons per year [2]. Ammonia can easily be cracked to generate H_2 and N_2 at high temperature, and no CO_2 or CH_4 is generated because ammonia does not contain carbon [3, 4]. In recent years new ammonia production processes with lower energy requirements and limited environmental impact have been developed that require no fossil fuels. If these new production processes can be put into practical use, ammonia will be a promising transportation fuel and hydrogen storage material.

2. AMMONIA

2.1 Chemical Characteristics of Ammonia

Ammonia (NH_3) is an essential chemical in nature and plays a vital role in many biological processes, including those in humans. Ammonia, NH_3, is lighter than air at ordinary temperatures and pressures, and is colorless with a pungent odor. The lower calorific value of ammonia is 18.8 MJ/kg, similar to that of methanol and ethanol. Therefore, ammonia is a potential alternative fuel for internal combustion engines and fuel cells. Furthermore, the density of ammonia is 0.7016 kg/m^3 under ambient conditions and 603 kg/m^3 at 1 MPa, and thus the energy density of ammonia is higher than that of hydrogen.

2.2 Physical Chemical Properties

Ammonia is easily recognized because of its characteristic irritating odor. Sufficient caution in handling ammonia gas is necessary because of its toxicity. Ammonia can be liquefied by compression at 846 kPa and 20^{o}C.

Table 1 lists the chemical properties of ammonia. Ammonia gas is flammable, but ignition in air is difficult without a catalyst and its flammability limits are narrow. Nevertheless, ammonia mixed with air has a possibility of explosion [5]. Ammonia is highly soluble in water because an ammonia molecule is combined with a water molecule to form a hydrate NH_3H_2O [6]. The ammonium hydrate is easily separated into ammonia and water by heating.

The toxicity of ammonia is a disadvantageous point. The risks to the environment and to human health must be carefully considered in order to use ammonia

TABLE 1: Chemical properties of ammonia

Property	Value	Conditions
Molecular weight	17.03	
Hydrogen content	17.8 wt %	
Melting point	–77.7°C	1 atm
Boiling point	–33°C	1 atm
Specific gravity (liquid)	0.682	–33.35°C
Specific gravity (gas)	0.596	1 atm, 0°C
Steam density	0.59	1 atm, 25°C
Specific volume (liquid)	7.59×10^{-2} m^3/kg	20°C
Specific volume (gas)	3.18×10^{-4} m^3/kg	20°C
Liquefaction pressure	846 kPa	
Latent heat of vaporization	1186.9 kJ/kg	20°C
Energy density	18.49 kJ/kg	
Solubility for water	0.9 g/mL	0°C

as fuel. Also, exposure for 1 h to ammonia levels above 13 ppm has been reported to lower the output of polymer electrolyte fuel cells [7].

Ammonia is used as a refrigerant because it has a latent heat of evaporation that is 4.4 times higher than that of petrol. Moreover, ammonia corrodes copper, zinc, and alloys containing them. However, iron, aluminum, and steel are not corroded by ammonia. Because ammonia may affect rubber and plastic, those materials are avoided in the handling of ammonia.

2.3 Characteristics

Table 2 shows the comparison of the characteristics of fuels. Ammonia can be seen to have many advantageous features as a hydrogen carrier [8]:

- High hydrogen content
- Ease of storage
- Ease of hydrogen extraction
- Carbon-free hydrogen carrier
- Absence of carbon monoxide in the hydrogen feed stream of the fuel cell
- Great wealth of experience in handling ammonia, mainly as a fertilizer
- The production, storage, and transport of ammonia are well-understood procedures
- Hydrogen production from ammonia is less expensive than cryogenic liquid hydrogen.

TABLE 2: Comparison of properties of liquid fuels

Property	Ammonia	Liquid hydrogen	Methanol	Petrol
Hydrogen content (wt%)	17.8	100	12.6	15
Boiling point (^{o}C)	–33.3	–253	64.4	–
Density of liquid (kg/L)	0.68	0.0709	0.795	0.728
Energy density (MJ/L)	13.3	8.4	15.9	31.6
Vapour pressure at 20^{o}C (kPa)	885.4	–	11.77	–
Lower calorific value (MJ/kg)	18.8	120.0	20.0	44.6
Flammability limits (vol%)	15–28	4.7–75	6.7–36	–
Laminar burning velocity (m/s)	0.015	3.51	0.71	0.58
Self-ignition temperature (^{o}C)	651	571	470	230
Minimum ignition energy (mJ)	8.0	0.018	0.14	0.28

3. HYDROGEN GENERATION SYSTEM EMPLOYING AMMONIA CRACKING

3.1 Overview of Proposed System

Here we propose a hydrogen generation system, as shown in Fig. 1, which utilizes ammonia cracking. Ammonia is supplied to the system in the form of liquid at 846 kPa. The liquid ammonia is evaporated in a vaporizer, heated to a fixed temperature in a heat exchanger, and sent to a cracking reactor. The gaseous ammonia is cracked by an appropriate catalyst in the reactor to give H_2 and N_2, and a small amount of residual ammonia remains. The cracked gas retains heat at a temperature high enough to heat the ammonia in the heat exchanger.

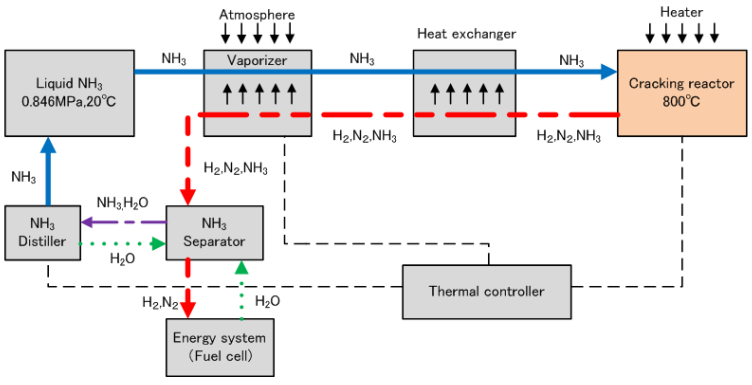

FIG. 1: Outline of hydrogen generation system using ammonia cracking

To remove the residual ammonia, the cracked gas is supplied to an ammonia separator which utilizes ammonia's high solubility in water. Being only slightly soluble in water, H_2 and N_2 are supplied to the fuel cell. The water containing the residual ammonia is sent to the heater and the distiller by the pump, and the mixture is separated into ammonia gas and water. The ammonia gas is pressurized and liquefied with the compressor and returned to the cylinder or the line. If the water is returned to the separator by a pump, the system will be a zero emission system.

3.2 Equilibrium Calculation for Ammonia Cracking

Figure 2 shows result of the equilibrium calculation for ammonia cracking. As the temperature increases, the ammonia concentration decreases and the concentrations of H_2 and N_2 increase. The influence of pressure is small at catalyst temperatures of 500°C or more. The ammonia concentration is 0.5–15% at low catalyst temperatures between 25 and 500°C. In other words, the cracking efficiency will be high at high temperature and low pressure [9, 10].

4. AMMONIA CRACKING EXPERIMENTS

4.1 Experimental Apparatus

Figure 3 shows the experimental apparatus. The ammonia cracking experiment was based upon the results of the equilibrium calculation presented in Sec. 3.2; the optimal conditions for ammonia cracking were determined in the experiment by analyzing hydrogen, nitrogen, and residual ammonia concentrations. The aim of this experiment was to investigate the effects of catalyst material, catalyst form, and

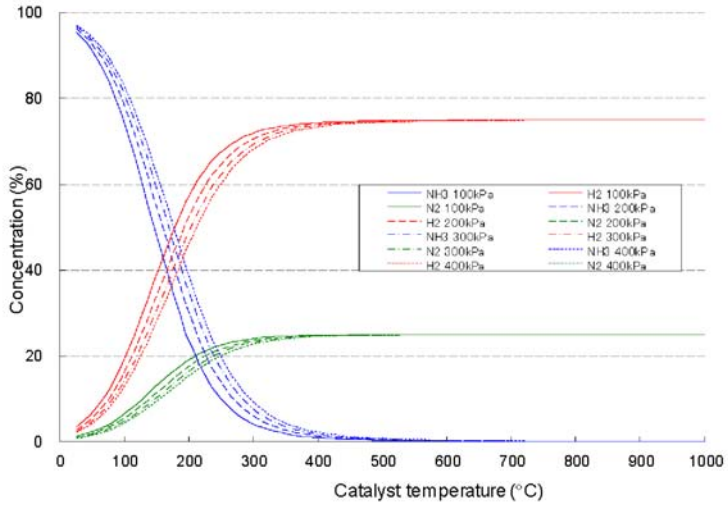

FIG. 2: Result of the equilibrium calculation for cracking of ammonia

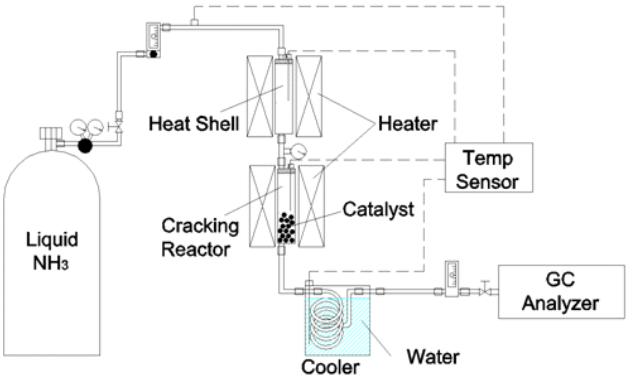

FIG. 3: Experimental setup

temperature in the system. The concentrations of components in the cracked gas were measured by gas chromatography (Shimadzu GC-14B).

In this study we focused on the catalyst for ammonia cracking. When ruthenium (Ru) at 500°C and rhodium (Rh) at 600°C were used, a cracking efficiency of 1.0 was obtained as shown in Fig. 4 [11]. Therefore Ru/Al_2O_3 in pellet form and honeycomb form (Fig. 5) and Ni/Al_2O_3 in pellet form instead of rhodium were used in this study.

4.2 Experimental Conditions

The ammonia cracking efficiencies of the Ni/Al_2O_3 and Ru/Al_2O_3 catalysts were compared through the following experimental procedure [12, 13]. The experimental conditions are listed in Table 3.

1. The cracking reactor and the heat shell are heated to the preset temperature.

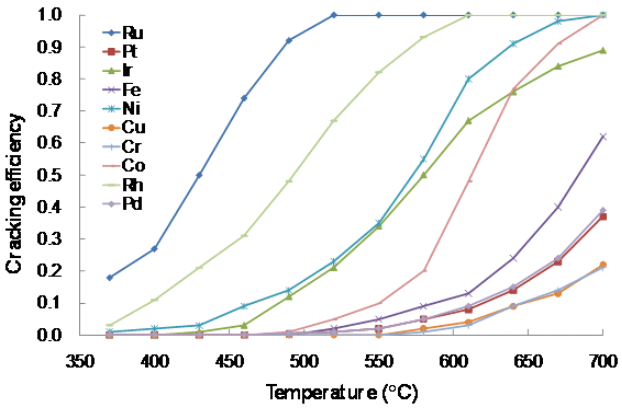

FIG. 4: Ammonia cracking efficiency versus temperature for various catalysts

FIG. 5: Honeycomb form of Ru/Al_2O_3 catalyst

2. Evaporated ammonia is supplied via a regulator at 100 kPa from a liquid ammonia cylinder.
3. The flow rate of ammonia is adjusted with a float-type flow meter.
4. Ammonia is sent to the cracking reactor filled with 300 mL of the catalyst.
5. The cracked gas is cooled to about 20°C with a cooler to enable analysis. The cracked gas is sent to the analyzer at a set exit flow rate. The cracked gas is analyzed by gas chromatography.

4.3 Results of Ammonia Cracking Experiment

4.3.1 *Cracking Efficiency of Catalysts*

Figures 6 and 7 show the comparison results for the cracking efficiency of the catalysts. The vertical axis shows the residual ammonia concentration, and the horizontal axis shows the cracking temperature. The measurements were started after the temperature of ammonia gas reached 25°C. Each experiment was performed in triplicate; mean values are reported.

The cracking efficiency of Ru/Al_2O_3 was higher than that of Ni/Al_2O_3 between 500 and 600°C at flow rates of both 2 and 4 L/min. At 2 L/min the residual ammonia concentration for Ru/Al_2O_3 was found to be 24% at 500°C and 13% at 600°C, which are both lower than in the case of Ni/Al_2O_3.

TABLE 3: Ammonia cracking conditions in the experiment

Property	Conditions
Cracking temperature	500–800°C
Ammonia gas pressure	100 kPa
Ammonia gas flow rate	2, 4 L/min
Catalyst	Ru/Al_2O_3 or Ni/Al_2O_3
Catalyst quantity	300 mL

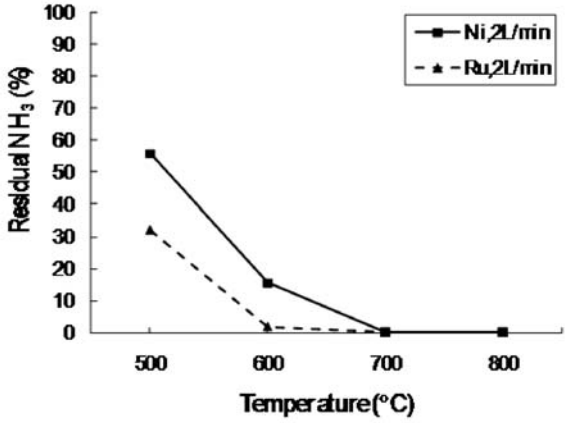

FIG. 6: Comparison of cracking efficiency of catalyst at 2 L/min

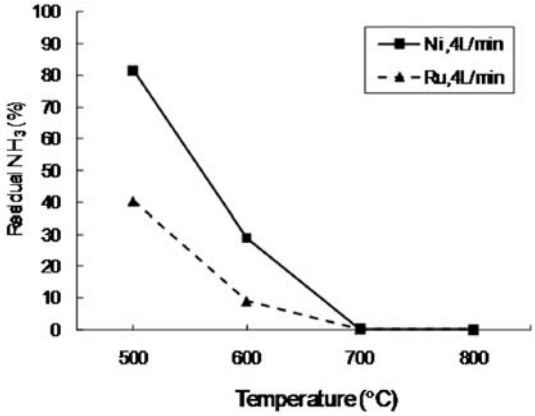

FIG. 7: Comparison of cracking efficiency of catalyst at 4 L/min

At a flow rate of 4 L/min the residual ammonia concentration for Ru/Al_2O_3 was found to be 42% at 500°C, 20% at 600°C, and 500 ppm at 700°C, which are all lower than the corresponding values for Ni/Al_2O_3. A difference in crack efficiency between the two catalysts was not found at 700–800°C. When the flow rate was increased, the residual ammonia concentration increased both for Ru/Al_2O_3 and Ni/Al_2O_3.

In addition, we measured the residual ammonia concentration. The measurements were started after the temperature of the ammonia gas reached 25°C. The residual ammonia gas exceeded 1000 ppm at temperatures between 500 and 700°C and a flow rate of 4 L/min. Because the residual ammonia for both the catalysts re-

mained at about 120 ppm at 800°C, a difference in cracking efficiency was not found. The cracking efficiency of both the catalysts was the same at 800°C and 2 L/min.

4.3.2 *Cracking Efficiency of Different Catalyst Forms*

Figure 8 shows the results of the comparison between the cracking efficiencies of the different catalyst forms. The cracking efficiency of the honeycomb catalyst was higher than that of the pellet catalyst at all temperatures. The residual ammonia concentration of the honeycomb catalyst was about one-fourth that of the pellet catalyst at 500°C and decreases to one-tenth that of the pellet catalyst at 600°C. Because the residual ammonia concentration of the honeycomb catalyst is below 1400 ppm at 700°C and because the cracking temperature of the honeycomb catalyst is about 100°C less than that of the pellet form, a system with a honeycomb catalyst will be able to reduce energy consumption.

5. APPLICATION OF THE SYSTEM

5.1 Household System

The above-mentioned system can be applied to various types of energy systems. Figure 9 shows an outline of a household system with a 1.2 kW fuel cell. The electrically heated catalyst (EHC) is initially heated with a portion of the household electricity. When the temperature of the EHC rises to the setup temperature, ammonia begins to be supplied and the system starts to generate power. Then a portion of the generated electricity is supplied to the thermal controller. The generated electric power is passed through an inverter and is directly used or stored in batteries. With a 10 L ammonia cylinder, the system can operate for about 11

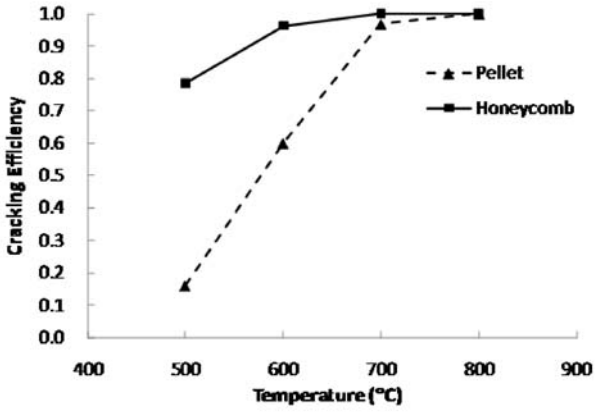

FIG. 8: Ammonia cracking efficiency in two catalyst forms (Ru/Al_2O_3, SV =

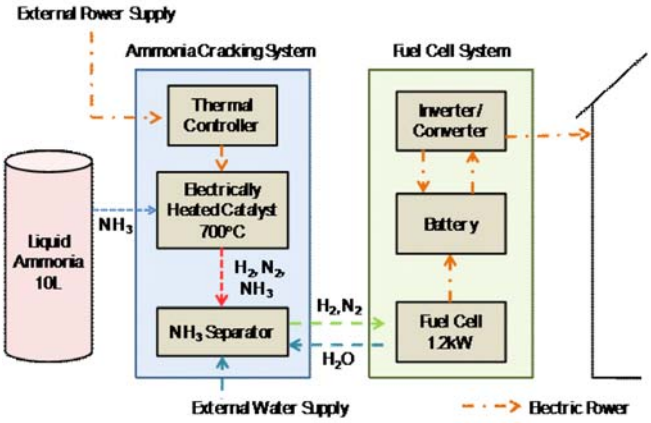

FIG. 9: Schematic diagram of the household system

FIG. 10: Developed household system

h. There must be at least 2 L of water in the ammonia separator. Figure 10 shows a household system developed in our laboratory.

5.2 Onboard System

The system can be also be implemented as an onboard system for vehicles. Figure 11 shows an onboard system with a 10 L ammonia cylinder. The electric heater heats the cracking reactor to the setup temperature by using the domestic power supply and then by using batteries during driving. A fuel cell is operated with the hydrogen obtained from ammonia in order to charge the batteries and to

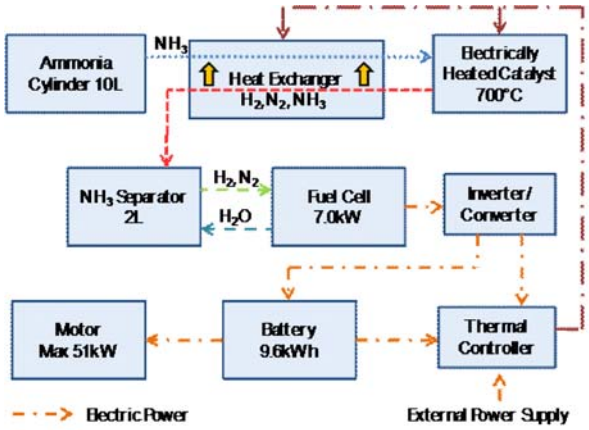

FIG. 11: Schematic diagram of the onboard system

TABLE 4: Specifications of the FCHEV

Length/width/height	3400/1480/2000 mm
Weight	About 930 kg
Motor output	14.4 kW at rated output
Fuel-cell output	7.0 kW at rated output
Secondary cell	Lead-acid batteries
Cruising distance	About 100 km
Maximum speed	120 km/h
Fuel capacity	10 L

supply the thermal controller with power. The water generated in the fuel cell is sent to the ammonia separator so as not to increase the ammonia concentration there.

Table 4 shows the specifications of a fuel-cell hybrid electric vehicle (FCHEV) [14]. In our laboratory we constructed an electric vehicle in 2008. At present the vehicle has a cruising distance of about 47 km and employs eight lead-acid batteries. If the onboard system with a 10 L ammonia cylinder can be used, the operating time will be about 2 h and the cruising distance will be about 100 km.

6. CONCLUSIONS

In this paper we proposed using ammonia as a liquid hydrogen carrier in an ammonia cracking system. The following results were obtained.

1. The hydrogen generation system employing ammonia cracking comprises an ammonia cylinder, a heat exchanger, a cracking reactor, an ammonia separator, an ammonia distiller, a pump, a compressor, batteries, and an inverter.
2. The cracking efficiency of Ru/Al_2O_3 is higher than that of Ni/Al_2O_3 between 500 and 600^{o}C at flow rates of 2 and 4 L/min. However, the cracking efficiency of each catalyst is the same at high temperatures.
3. Because the cracking efficiency of the honeycomb-form catalyst was higher than that of the pellet form at all temperatures, the cracking temperature of the honeycomb form was about 100^{o}C less than that of the pellet form. As a result, the system can consume less energy.
4. We have designed a household system. The operating time is about 11 h when the system is equipped with a 10 L ammonia cylinder. At least 2 L of water are need in the ammonia separator.
5. We have also designed an onboard system. At present the vehicle contains eight lead-acid batteries and has a cruising distance of about 47 km. If an onboard system with a 10 L ammonia cylinder is used, the operating time will be about 2 h and the cruising distance will be about 100 km.

REFERENCES

1. Industrial Property Cooperation Center (IPCC), The Fourth Evaluation Report (2007), http://www.ipcc.ch/ipccreports/ar4-wg1.htm.
2. Japan Fertilizer & Ammonia Producers Association, *Research of the change of the supply and demand structure of the ammonia industry and the direction of technical compatible* (in Japanese), p. 3, 1992.
3. Zamfirescu, C. and Dincer, I., Using ammonia as a sustainable fuel, *J. Power Sources*, 185: 459–465, 2008.
4. Zamfirescu, C. and Dincer, I., Ammonia as a green fuel and hydrogen source for vehicular applications, *Fuel Process. Technol*., 90:729–737, 2009.
5. Japan Society of Refrigerating and Air Conditioning Engineers, *Ammonia Refrigerating Engineering* (in Japanese), p. 9, 2002.
6. Committee on Medical and Biologic Effects of Environmental Pollutants, *Ammonia*, National Research Council, p. 9, 1989.
7. Uribe, F.A., et al., Effect of ammonia as potential fuel impurity on proton exchange membrane fuel-cell performance, *J. Electrochem. Soc*., 149(3):293–296, 2002.
8. Gay, S.E. and Ehsani, M., Ammonia hydrogen carrier for fuel-cell-based transportation, SAE Technical Paper 2003–01–2251, 2003.
9. Nakamura, M., et al., Development of Hydrogen Generation System Fueled with Ammonia (in Japanese), *FC EXPO 2006, 2nd Int'l. Hydrogen & Fuel Cell EXPO*, p. 12, 2006.
10. Ishimatsu, S., et al., Ammonia fueled fuel cell vehicle: The new concept of a hydrogen supply system, *SAE 2004 Trans*., *J. Fuels Lubricants*, 1085–1091, 2005.
11. Ganley, J.C., *Ammonia Fuel Cell Systems*, Seminar, Ammonia as Transportation Fuel- II, Argonne National Laboratory, 2005, http://www.energy.iastate.edu/Renewable/ammonia/ammonia/ammoniaMtg05.htm.

12. Saika, T., et al., Study of hydrogen supply system with ammonia fuel, *JSME Int. J*., Series B, 49(1):78–83, 2006.
13. Saito, Y., et al., Hydrogen generation system with ammonia cracking for a fuel-cell electric vehicle, SAE Technical Paper, 2009–01–1901, 2009.
14. Otoguro, M., et al., Design of a fuel-cell electric vehicle with a hydrogen generation system fueled with ammonia, SAE Technical Paper, 2007–01–3494, 2007.

International Journal of Energy for a Clean Environment 10(1–4), 15–36 (2009)

COMPUTATIONAL EVALUATION OF WALL RINGS IN WET FLUE-GAS DESULFURIZATION PLANTS

C. Montañés,[1] A. Gómez-Samper,[1] N. Fueyo,[1] J. C. Ballesteros,[2] & P. Gómez-Yagüe[2]*

[1]*Fluid Mechanics Group (University of Zaragoza) and LITEC (CSIC), María de Luna 3, 50018 Zaragoza, Spain*

[2]*ENDESA Generación SA, Ribera del Loira 60, 28043 Madrid, Spain*

[*]Address all correspondence to Norberto Feuyo e-mail: Norberto.Fueyo@unizar.es

A wet flue-gas desulfurization plant was simulated using a finite-volume commercial computational fluid dynamics (CFD) code with some extensions. An Eulerian model was used to model the gas phase, while the slurry was simulated using a Lagrangian approach. A mathematical model was formulated and implemented to simulate the SO_2 absorption by the slurry droplets, taking into account the influence of the Reynolds and Schmidt numbers and the temperature. The influence of the mist eliminators was accounted for by introducing a pressure loss which is dependent on the magnitude of the axial velocity. The results from the model are in good agreement with the measurements provided by the plant operators (velocity contours at the absorber entrance and contours of sulfur dioxide at the absorber outlet). The effect on the overall absorption of installing peripheral wall rings was evaluated, resulting in an efficiency improvement of about four percentage points, but penalizing the global pressure loss by about 8%, depending on the operating conditions. A wide-ranging parametric study was carried out, varying physical parameters, such as operating conditions; numerical parameters, such as the mesh size and the wall–droplet interaction; and geometrical designs, such as the wall ring size.

KEY WORDS: *desulfurization, wall rings, CFD, absorption, multiphase*

1. INTRODUCTION

Sulfur dioxide (SO_2) is formed during the combustion of fossil fuels (mainly coal and oil) through the oxidation of their sulfur contents. Once in the atmosphere, SO_2 is the precursor of acid rain and may be deleterious for human health.

Fossil fuel power plants and the metallurgical industry are the main sources of SO_2 emissions. The rapid expansion of these sectors has contributed to an important increase in SO_2 emissions and, consequently, of the environmental and human-

NOMENCLATURE

A_D	projected area of the droplet, m^2	k_{g,SO_2}	gas-side mass-transfer coefficient for SO_2, $kmol/m^2 \cdot s \cdot Pa$
A_d	area of the droplet, m^2	k_{l,SO_2}	liquid-side mass-transfer coefficient for SO_2, m/s
C_A	concentration of species A in the liquid, Pa	m_d	droplet mass, kg
C_D	drag coefficient	$\dot{m}_{H_2O}$	mass transfer of H2O due to evaporation, kg/s
C_{SO_2}	molar concentration of SO_2 in the liquid bulk, $kmol/m^3$	$\dot{m}_{SO_2}$	mass transfer of SO_2 due to absorption, kg/s
c_{Pd}	specific heat of slurry, J/kg·K	$\dot{n}_{H_2O}$	molar flux of H_2O, kmol/s
$D_{A,\text{eff}}$	effective (molecular plus turbulent) diffusivity of species A in flue-gas phase, m^2/s	$\dot{n}_{SO_2}$	molar flux of SO_2, kmol/s
$D_{SO_2,g}$	diffusivity of SO_2 in the gas phase, m^2/s	ΔP	pressure loss in mist eliminators, Pa
$D_{SO_2,l}$	diffusivity of SO_2 in the liquid, m^2/s	P_A	partial pressure of species A in the gas phase, Pa
d_d	droplet diameter, m	Pe	Peclet number
E_{SO_2}	enhancement factor for SO_2	$P_{H_2O,b}$	partial pressure of H_2O in the gas phase, Pa
g_i	ith component of the gravity vector, m/s^2	$P_{H_2O,d}$	partial pressure of H_2O on the droplet surface, Pa
H_A	Henry's constant for species A, $kmol/(m^3 \cdot Pa)$	P_{SO_2}	partial pressure of SO_2 in the gas phase, Pa
H_{L,H_2O}	specific latent heat of evaporation of water, J/kg	R	universal ideal-gas constant [8314 $Pa \cdot m^3/(kmol \cdot K)$]
H^{ref}	Henry's constant at the reference temperature, $kmol/m^3 \cdot Pa$	Re	Reynolds number based on droplet diameter and slip velocity
ΔH_{sol}	solubility enthalpy, $kmol/(m^3 \cdot Pa)$	Sc	Schmidt number
h_g	specific enthalpy of gas phase, J/kg	Sh	Sherwood number
K_{H_2O}	global mass-transfer coefficient for water evaporation, $kmol/m^2 \cdot s \cdot Pa$	S_A	source term in the gas-phase conservation-equation of species A, $kg/m^3 \cdot s$
K_{SO_2}	global mass-transfer coefficient for SO_2 absorption, $kmol/m^2 \cdot s \cdot Pa$	S_{energy}	source term in the gas-phase energy conservation equation, $J/m^3 \cdot s$
k	convective heat-transfer coefficient, $W/m^2 \cdot K$		

S_{mass}	source term in the gas-phase mass conservation equation, kg/m^3·s	**Greek symbols**	
$S_{momentum}$	source term in the gas-phase momentum conservation equation, kg/m^2·s^2	λ_{eff}	effective (molecular plus turbulent) thermal conductivity, W/m·K
T^{ref}	reference temperature (298 K)	μ_{eff}	effective (molecular plus turbulent) dynamic viscosity, kg/m·s
T, T_g, T_d	temperature, gas-phase temperature, droplet temperature, K	ρ_d	slurry density, kg/m^3
		ρ_g	gas-phase density, kg/m^3
		Subscripts	
t	time, s	A	species A
$u_{d,i}$	ith component of one-droplet velocity vector, m/s	b	bulk
		d	droplet
V	absolute velocity, m/s	g	gas phase, gas side
$v_{g,i}$	ith component of gas-phase velocity vector, m/s	H_2O	relative to H_2O
		i	ith component of the vector
$y_{g,A}$	mass fraction of species A in the gas phase		liquid side
		SO_2	relative to SO_2

health problems associated with them. In the early 1970s Japan and the United States imposed strict regulations for these sectors, especially for coal power plants, to reduce their SO_2 emissions. Subsequently, in the mid 1980s European countries issued regulations for SO_2 (and other pollutants) that led to Directive 88/609/EC. Since then, more restrictive regulations in European Comission (EC) have been approved — specifically Directive 2001/80/EC, which imposes limitations on large combustion plant pollutant emissions into the air.

To cope with these restrictions, the first option considered by fossil fuel utilities was switching to low-sulfur fuels. However, this was not always possible due to fuel costs or technical reasons (e.g., the facilities were designed for one specific fuel). The impossibility of changing fuels led to the development of a variety of systems to control SO_2 emissions. These can be categorized as wet flue-gas desulfurization (FGD), dry or semi-dry FGD, and sorbent injection. Of these systems, wet FGD has been the most frequently installed process, since it offers higher desulfurization efficiency and moderate operation and maintenance costs compared to those from the other processes. On the negative side, it has larger investment costs and its operation is more complex. Currently, 85% of the worldwide FGD capacity (180,000 MW) are wet systems (Stultz and Kitto, 1992). Furthermore, a variety of wet systems exists, such as spray scrubbers, packed towers, jet bubbling reactors, and double-loop towers (Kiil et al., 1998). Among these systems, the most commonly used is the spray scrubber (Stultz and Kitto, 1992).

The relative immaturity of FGD technology (compared to others) and the stricter desulfurization requirements from new legislation have motivated intense research in this field, and mathematical modeling has become a relevant tool to investigate the processes involved in FGD systems. Thus, a variety of mathematical models for wet FGD are described in the literature, notably those by Kill et al. (1998), Gómez et al. (2007), Brogren and Karlsson (1997), Eden (1998), Gerbec et al. (1995), Lancia et al. (1997), Marocco and Inzoli (2009), Zhong et al. (2008), Dou et al. (2008), and Warych and Szymanowski (2001). These models carry out a detailed description of the chemical phenomena involved in the FGD process: SO_2 absorption and oxidation, limestone dissolution, and gypsum precipitation.

As desulfurization requirements have increased in recent years, existing facilities have been compelled to improve their desulfurization efficiency. This has motivated the study of different options leading to such an improvement, involving as few modifications to the facilities as possible. These options include the increase of the liquid-to-gas ratio (e.g., with the installation of additional spray levels and additional pumping capacity in the scrubber vessel), the use of more reactive limestone, the production of smaller droplet sizes (by changing the slurry nozzles), the addition of organic acids (Frandsen et al., 2001), or the improvement of the gas-flow distribution in the absorber (with the installation of sieve trays or wall rings). The mathematical models reported above focused on the chemical performance of the process (which is indeed important), but except for those by Gómez et al. (2007) and Marocco and Inzoli (2009), the models were developed assuming simplified gas and slurry flow patterns.

The importance of the gas-flow distribution has been observed in experiments reported by Nygaard et al. (2004), Marocco and Inzoli (2009), and the DOE (2001). In general, in spray towers the flue gas enters the scrubber from the side, and this causes a nonuniform gas-flow distribution in the cross section of the tower. Most wet FGD systems have been installed in existing power plants and therefore have had to be adapted to the available space in the plant layout. In some cases this has forced the installation of an intricate flue-gas pipe system to the inlet of the spray tower, which contributes to the nonuniformity of the pattern of the gas flow in the inlet to the absorber. The nonuniformity reduces SO_2 removal. Since residence time is decreased, gas-slurry contact is worsened and the presence of preferential flow routes for the gas in the absorber (referred to as "sneakage") is favored. Another aspect related to the gas-flow distribution is the so-called wall effect. The placement of nozzles can result in a smaller slurry flow close to the wall, causing a smaller resistance for the flue gas to flow through this zone and leading to lower residence times and desulfurization rates. This behavior of the flow has been observed experimentally by Nygaard et al. (2004), among others. Peripheral wall rings have been used to avoid this effect, with improvements of 2–5% in SO_2 removal, as reported in Marsulex (2005), Alstom (2003), and Frank (2006). Moreover, specific studies about the improvement of desulfurization efficiency with these kinds of devices have been carried out, e.g., by Hofelsauer et al. (2008).

The aim of this work is to evaluate the effect of the hypothetical installation of wall rings in the spray tower of an existing wet FGD plant. Although wall rings are reported as efficiency-increasing devices, the singularities of each spray tower (for example, the distribution of spray nozzles or the inlet of flue gas) can deteriorate the positive effect of the wall rings. An *a priori* assessment can aid the decision-making process by quantifying cost/benefit ratios. To this end, a computational fluid dynamics (CFD) model of the phenomena taking place in the spray tower has been developed in the present work. In this model, the multiphase character of the flow is represented using an Eulerian–Lagrangian approach, and a simplified SO_2-removal mechanism has been included. While not as comprehensive as the full desulfurization model reported in Gómez et al. (2007), the present approach is detailed enough for the assessment of several process-design options. This model has been validated with experimental measurements and is subsequently used to analyze the influence of the wall rings in the overall performance of the wet scrubber, and their effects in parameters such as SO_2 removal, gas flow pattern, and pressure drop. In the next section we describe the FGD plant that is the target of this study. Then the geometrical and mathematical models employed are detailed, and finally the results are presented, followed by the relevant conclusions.

2. THE PLANT

The desulfurization system simulated in this work is a wet FGD with a spray tower. It is installed in a 350 MW group at a coal-fired power plant, where the coal burned has moderate sulfur content (0.85% as received). The spray tower has a diameter of 14.5 m, a height of 20 m from the slurry tank level, and is designed to treat up to 1.2 million Nm^3/h of flue gas.

Figure 1 shows a schematic of this installation. It is a standard spray tower with four levels of slurry injectors. Due to the lack of space to install the FGD system, the layout of flue-gas ducts must be intricate. Upstream from the inlet, the pipe rotates 180^o, goes down, and turns 90^o to the left. Once the gas enters the tower it is sprayed with slurry and the SO_2 is absorbed. Flue gas moves upward and, after the last level of nozzles, it passes through two consecutive mist eliminators, where the small droplets carried by the gas impinge and are returned back to the absorber. There is enough residence time for some of the reactions in the wet FGD to be completed.

The wet FGD process consists basically of the following global reaction:

$$SO_{2(g)} + CaCO_{3(s)} + 1/2O_2 + 2H_2O \rightarrow CaSO_4{\cdot}2H_2O_{(s)} + CO_{2(g)}. \quad (1)$$

This reaction takes place in the following steps:

1. Absorption of SO_2

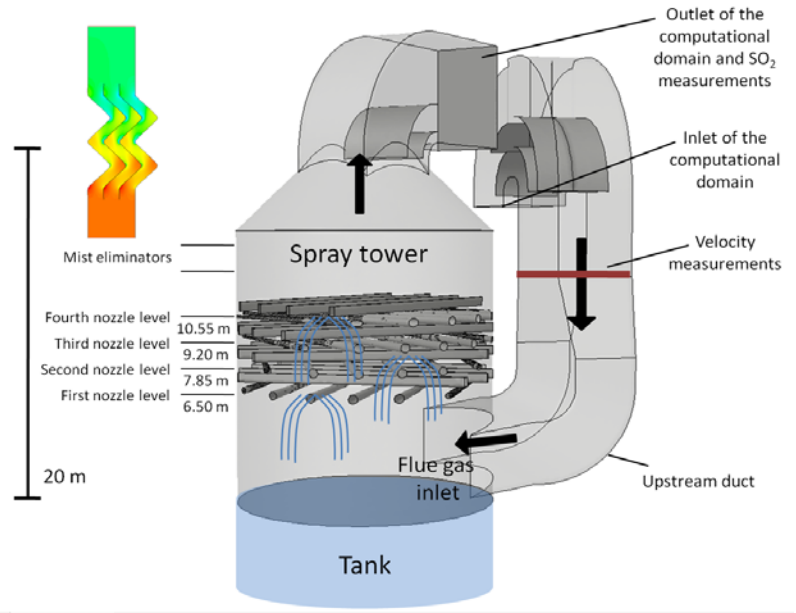

FIG. 1: Scheme of the spray tower simulated in this work

$$SO_{2(g)} + H_2O \leftrightarrow HSO_3^- + H^+, \tag{2}$$

$$HSO_3^- \leftrightarrow H^+ + SO_3^{-2} \tag{3}$$

2. Oxidation

$$HSO_3^- + 1/2O_2 \leftrightarrow H^+ + SO_4^{-2} \tag{4}$$

3. Limestone dissolution

$$CaCO_{3(s)} + 2H^+ \leftrightarrow Ca^{+2} + CO_{2(g)} + H_2O \tag{5}$$

4. Gypsum precipitation

$$Ca^{+2} + SO_4^{-2} + 2H_2O \leftrightarrow CaSO_4 \times 2H_2O_{(s)} \tag{6}$$

Absorption of SO_2 occurs in the spray tower, while oxidation, limestone dissolution, and gypsum precipitation take place mainly in the tank and therefore are not considered in this work.

3. THE MODEL

3.1 Geometry and Mesh

The geometry of the spray tower has been modeled in great detail (Fig. 1), including a large stretch of the upstream ducts for an accurate modeling of the flow at the absorber entrance. Every slurry injection in the spray tower (464 injections,

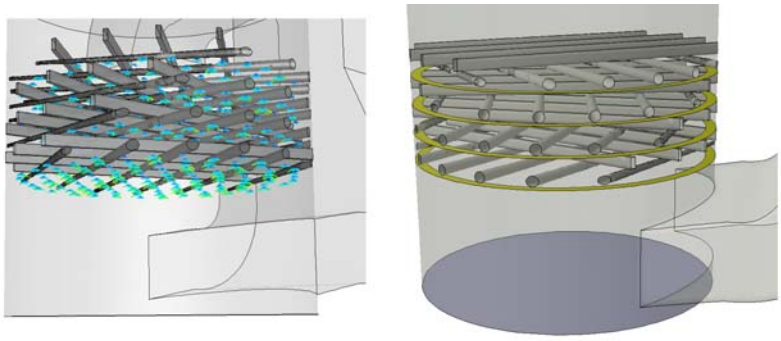

FIG. 2: Detail of slurry injections, pipes, and supporting beams present in the spray tower (left). Detail of analyzed wall rings (yellow) in the spray tower (right)

116 per level) has been included, as have the feeding pipes located in the spray tower and the supporting structure. Figure 2 (left) shows the slurry injections, the pipes, and the supporting beams present in the spray tower in detail. The complex geometry of the mist eliminators and their reduced size (compared with the overall dimensions of the spray tower) would force the use of an unaffordable mesh for a detailed representation of these devices. For this reason, they are not included in the simulated geometry; nevertheless, the pressure drop they generate in the gas phase is modeled as described in the next section. Figure 2 (right) illustrates the geometry and the position of the (hypothetical) peripheral wall rings in the spray tower. The wall rings have a width of 480 mm, and they are placed below each spray level.

The mesh used for the simulations has 1.5 million tetrahedral cells, mainly concentrated in the region where the SO_2 absorption takes place (from the tank-free surface to the fourth spray level), as shown in Fig. 3 (left). Moreover, near the

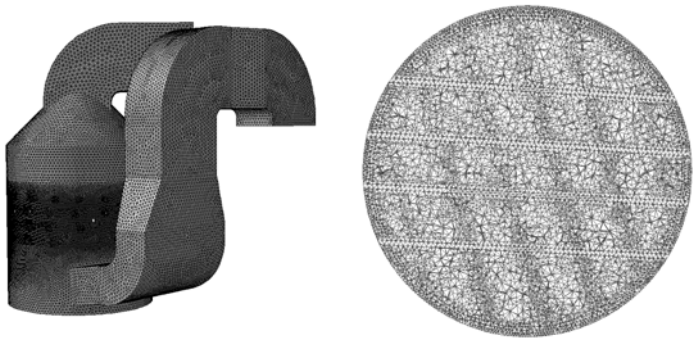

FIG. 3: Computational mesh. General view of the domain (left) and horizontal section at 9 m above the tank free-surface (right)

supporting beams, slurry pipes, and wall rings, the mesh has been refined in order to properly capture the detailed geometry, as shown in the transversal section of the mesh in Fig. 3 (right). Further details on the mesh are supplied in Sec. 3.7.

3.2 Gas Phase

The considered flow is multiphase — the flue gas is regarded as a continuous phase, while slurry droplets are treated as a disperse phase. An Eulerian–Lagrangian approach has been used, as the volume fraction of the disperse phase is small enough for this approach to be applicable, and important disperse-phase phenomena such as droplet-wall interaction can be accounted for more accurately in the Lagrangian framework.

Thus, for the gas phase, the Reynolds-averaged Navier–Stokes equations for mass, momentum, energy, and chemical species have been solved:

$$\frac{\partial \rho_g}{\partial t} + \nabla(\rho_g \vec{v}_g) = S_{mass}\,, \tag{7}$$

$$\frac{\partial}{\partial t}(\rho_g v_{g,i}) + \nabla(\rho_g v_{g,i} \vec{v}_g) - \nabla(\mu_{eff} \nabla v_{g,i}) = -\nabla P + S_{momentum}\,, \tag{8}$$

$$\frac{\partial}{\partial t}(\rho_g h_g) + \nabla(\rho_g h_g \vec{v}_g) - \nabla(\lambda_{eff} \nabla h_g) = S_{energy}\,, \tag{9}$$

$$\frac{\partial}{\partial t}(\rho_g y_{g,A}) + \nabla(\rho_g y_{g,A} \vec{v}_g) - \nabla(\rho_g D_{A,eff} \nabla y_{g,A}) = S_A\,. \tag{10}$$

S_{mass}, S_{momentum}, S_{energy}, and S_A represent the interchange of mass, momentum, energy, and chemical species between the gas phase and the disperse phase (Crowe et al., 1998). These are calculated cell by cell using a balance on the corresponding property in the droplets as they enter and leave the cell. Further, S_{momentum} includes the momentum-sink term in the cells where the mist eliminators are located (Fig. 1). The calculation of this source has been done through 2D simulations of the exact geometry of the upper and lower mist eliminators, in which the pressure drop was calculated as a function of the gas inlet velocity. From the results of these simulations, Eq. (11) was built to model the pressure drop in each mist eliminator, and this pressure drop is imposed in the zones where mist eliminators are located:

$$\Delta P = a\mathrm{V}^2\,. \tag{11}$$

Here, V is the absolute value of the velocity, a = 1.36 for the lower mist eliminator, and a = 3.29 for the upper mist eliminator. The equation is valid for SI units.

Turbulence has been modeled with the realizable k–ε model for single-phase flows (Launder and Spalding, 1972; Shih et al., 1995). The disperse phase affects the turbulent energy and dissipation rate in the continuous phase, but since the volume fraction of the disperse phase is very small, this effect has been neglected.

3.3 Limestone Slurry

The disperse phase has been represented using a Lagrangian approach in which individual equations are solved for every particle. These equations are the mass, force, and energy balances for the particles:

$$\frac{dm_d}{dt} = \dot{m}_{H_2O} + \dot{m}_{SO_2}\,, \tag{12}$$

$$m_d \frac{du_{d,i}}{dt} = \frac{1}{2}\,\rho_d C_D \left| u_{d,i} - v_{g,i} \right| (u_{d,i} - v_{g,i})\, A_D + m_d g_i\,, \tag{13}$$

$$m_d c_{Pd} \frac{dT_d}{dt} = k\,(T_g - T_d)\,\pi d_d^2 + \dot{m}_{H_2O} H_{L,H_2O}\,. \tag{14}$$

In the above equations, $\dot{m}_{H_2O}$ is the mass transfer of water due to evaporation from the slurry droplets moving to the gas phase; $\dot{m}_{SO_2}$ is the mass transfer of SO_2 due to the absorption of SO_2 by the slurry droplets moving from gas phase; C_D is the drag coefficient, calculated with the Morsi and Alexander correlation (Morsi and Alexander, 1972); and k is the convective heat-transfer coefficient, evaluated with the Ranz–Marshall correlation (Ranz and Marshal, 1952). Mass transfer due to evaporation is calculated with the following equation:

$$\dot{n}_{H_2O} = K_{H_2O}\,(P_{H_2O,d} = P_{H_2O,b})\, A_d\,. \tag{15}$$

In Eq. (15), $\dot{n}_{H_2O}$ is the molar flux of water; $P_{H_2O,b}$ is the partial pressure of water in the bulk of the gas phase, which is known from the solution of the transport equation for the chemical species in the gas phase; $P_{H_2O,d}$ is the partial pressure of water at the droplet surface, which is assumed to be equal to the saturated vapor pressure at the droplet temperature; K_{H_2O} is the gas side mass-transfer coefficient calculated with the modified Ranz–Marshall correlation (Rowe et al., 1965); and A_d is the droplet surface. The calculation of the source term $\dot{m}_{SO_2}$ is detailed in the next section.

The turbulent dispersion of particles has been taken into account through the use of a stochastic tracking model that includes the effect of instantaneous turbulent velocity fluctuations on the calculation of the particle trajectory.

3.4 Source Term for SO_2 Absorption

In order to represent the desulfurization process, we used a simplified model that dispenses with the detailed mechanisms outlined in the plant description above, and represented by Reactions (1–6). Thus, the following model has been coded into a set of subroutines which update the concentration of SO_2 in the discrete phase as the droplets move through the domain and introduce the corresponding source term in the SO_2 mass fraction equation solved in the gas phase.

This term is a function of the droplet SO_2 concentration, the gas-droplet relative velocity, the liquid–gas interface temperature, and the gas temperature, which influences the mass-transfer coefficients and Henry's constant.

The source term in Eq. (10) accounts for the SO_2 absorbed by the slurry droplets. Making use of the two-film theory (Levenspiel, 1998), the molar flux can be expressed as follows:

$$\dot{n}_{SO_2} = K_{SO_2} \left(P_{SO_2} - H_{SO_2}^{-1} C_{SO_2}\right) A_d \,, \tag{16}$$

where K_{SO_2} is the global mass-transfer coefficient for species SO_2, given by the following equations and having the same units as the mass-transfer coefficient in the gas-side, k_{g,SO_2}:

$$K_{SO_2} = \left(\frac{1}{k_{g,SO_2}} + \frac{H_{SO_2}^{-1}}{E_{SO_2} k_{l,SO_2}} \right)^{-1} . \tag{17}$$

We have calculated the concentration of SO_2 in the liquid phase C_{SO_2}, assuming that only 5% of the absorbed SO_2 remains in the droplet as $SO_{2(aq)}$. This assumption is made because in the limit of chemical equilibrium in the slurry droplet and for pH values between 4 and 6, HSO_3^- is the dominant species (Kill et al., 1998; Keskinen et al., 2002). Similar assumptions are commonly used in the modeling of FGD processes (Zhong et al, 2008; Dou et al., 2008; Scala et al., 2004), sometimes even considering that all the absorbed SO_2 is in the form of HSO_3^- and that, therefore, C_{SO_2} is negligible. Finally, E_{SO_2} has been chosen so that the global desulfurization obtained in the simulation of the reference case agrees with the experimental global desulfurization in such operating conditions. The resulting value of 50 lies within the range reported by Kiil et al. (1998).

3.5 Henry's Law

Henry's law relates the concentration of a species A in the liquid bulk with its partial pressure in the gas in conditions of equilibrium. Mathematically, it is expressed by the equation

$$C_A = H_A P_A \,. \tag{18}$$

Henry's constant is dependent on temperature according to the following expression obtained from Sander (1999):

$$H = H^{ref} \exp\left[\frac{-\Delta H_{sol}}{R} \left(\frac{1}{T} - \frac{1}{T^{ref}} \right) \right]. \tag{19}$$

Using data for SO_2 (Lide and Frederikse, 1995), H^{ref} = 1.4 kmol/(m^3·atm) and $\Delta H_{sol}/R$ = 2900 K.

3.6 Correlations for the Calculation of the SO_2 Mass-Transfer Constant

In order to obtain a value for the constant k_{g,SO_2} in Eq. (17), the Froessling correlation (Froessling, 1939) has been used:

$$\mathrm{Sh} = 2 + 0.552\ \mathrm{Re}^{0.5}\mathrm{Sc}^{0.33}, \tag{20}$$

TABLE 1: Physical and chemical constants and adjustable parameters used in the simulations

Parameter	Units	Value
$D_{SO_2,g}$	m^2/s	1.5×10^{-5}
$D_{SO_2,l}$	m^2/s	2.8×10^{-9}
H^{ref}	$kmol/(m^3 \cdot atm)$	1.4
DH_{sol}/R	K	2900
E_{SO_2}	–	50

where Sh is the Sherwood number, Re is the Reynolds number, and Sc is the Schmidt number.

To calculate the mass-transfer constant on the liquid side, k_{l,SO_2}, the Brian–Hales correlation (Brian and Hales, 1969) has been used:

$$\mathrm{Sh} = (4 + 1.21\ \mathrm{Pe}^{0.67})^{0.5}, \tag{21}$$

where Sh is the Sherwood number and Pe is the Peclet number.

Using the Fuller–Schettler and Giddings relation, $D_{SO_2,g} = 1.5 \times 10^{-5}$ m^2/s, according to Perry and Green (1984), and using the Einstein relation, $D_{SO_2,l} = 2.8 \times 10^{-9}$ m^2/s, both were calculated at 47°C and have been considered to be constant within the temperature range studied.

A summary of all the physical and chemical parameters used in the simulations is presented in Table 1.

3.7 Numerical Details

As stated in Sec. 3.1, the simulations have been carried out on a 1.5 million cells mesh; however, in order to check the mesh independence, further refinement studies have been conducted, with 3 and 8 million cell meshes. The results show that the same general flow patterns and trends are obtained, while the differences in the pressure drop and desulfurization efficiency do not exceed 2%.

For the pressure-velocity coupling, the SIMPLE algorithm has been used together with second-order discretization schemes. The strategy used to obtain converged results is as follows: first, we obtain the solution for the cold turbulent gas-phase flow; then the slurry-phase is solved, as is its interaction with the gas phase in both momentum and energy; finally, the SO_2 mass fraction is solved as a post-process, as the SO_2 mass exchange is negligible compared to water evaporation and does not significantly perturb the flow. Under-relaxation coefficients have been varied as needed to control the residuals, especially in the first iterations after the initialization and the major changes in the procedure (such as moving from single-phase to two-phase flow), thus using lower values in these situations. Finally, the mass and energy imbalances were checked to ensure convergence.

4. RESULTS AND ANALYSIS

4.1 Operating Conditions

Table 2 shows the operating conditions for the spray tower used in the calculations. Modifications to these values have been made as described in the parametric analysis.

4.2 Current Configuration

We next present the results for the current operation of the FGD tower with no wall rings. Figure 4 shows the velocity profile of the flue gas at the entrance to the absorber; the nonuniformity of the flow is indicative of the importance of including the upstream inlet ducts in the simulation. Figure 5 (left) shows a contour of the vertical component of the velocity in a cross section of the absorber, where it is apparent that the flue gas ascends preferentially by the peripheral zone. This effect, also observed in Fig. 6 (left), is caused by the larger concentration of droplets in the center of the absorber (see Fig. 7, left), which yields a higher resistance to the gas flow.

These high local velocities in the periphery result in smaller residence times for the flue gas (represented in Fig. 8, left) travelling along this region, which causes (together with the lower concentration of slurry droplets) a reduction of the SO_2 absorbed, as shown in Fig. 9 (left).

Due to the larger interphase concentration gradients, higher SO_2 absorption rates are obtained at the absorber entrance, as shown in Fig. 7 (right). Thus, 5 meters above the tank where the inlet duct ends, over 50% of the SO_2 has already been

TABLE 2: Operating conditions for the spray tower

Flue gas	**Units**	
Flow rate	N/m^3h	1,200,000
Temperature	^oC	110
SO_2 concentration	% mass fraction	0.368%
H_2O concentration	% mass fraction	2.91%
Slurry		
Mass flow rate	kg/s by nozzle	16.81
Density	kg/m^3	1124
Temperature	^oC	47
pH	–	5.5
Droplet diameter	mm	2.0
Spray angle	^{o}	120
Particles per nozzle	–	80

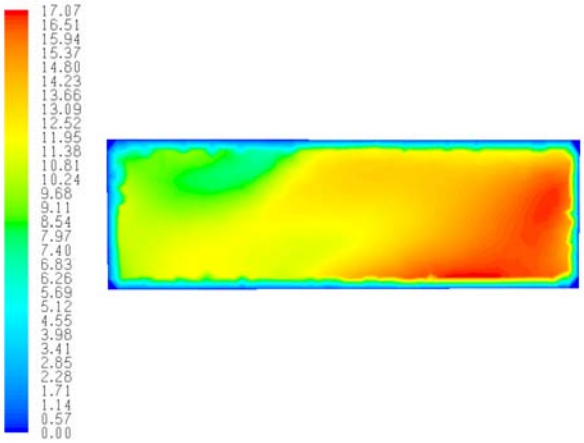

FIG. 4: Velocity profile at the entrance of the absorber

absorbed, and the desulfurization rate decreases with the height along the absorber, as shown in Fig. 10.

As observed in Fig. 9 (left), although lower desulfurization rates are generally achieved in the peripheral area, this is especially true in the zone just above the inlet duct, since the residence time is much smaller there. Figure 11 (left) illustrates this behavior, and Fig. 12 shows how it persists at different heights. Finally, Fig. 13 shows the temperature contours in the absorber, being the decrease observed in the flue-gas temperature due to the water evaporation and the heat transfer with the slurry injected.

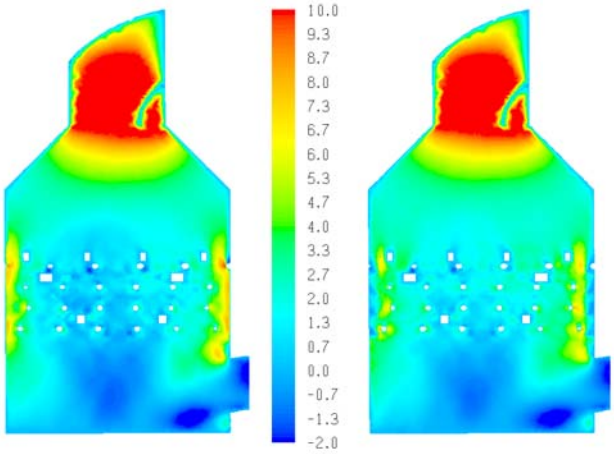

FIG. 5: Vertical-velocity component (m/s) in the absorber for the present situation (left) and with wall rings (right)

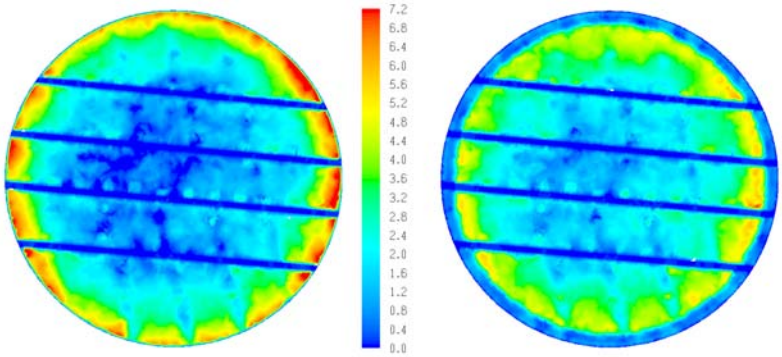

FIG. 6: Vertical-velocity component (m/s) on a horizontal section 9 m above the tank free surface for the present situation (left) and with wall rings (right)

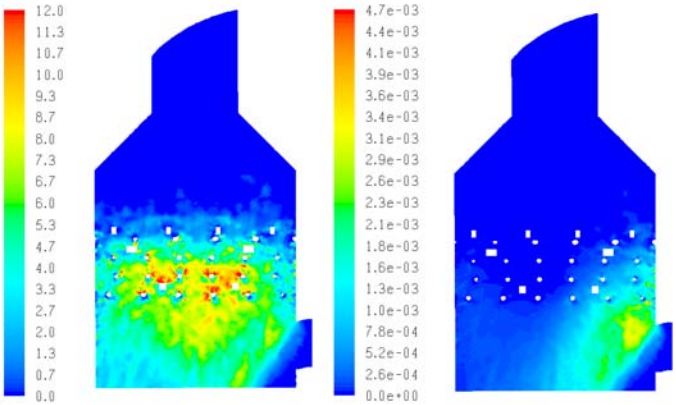

FIG. 7: Concentration (kg/m^3) of slurry droplets (left) and desulfurization rate (kg/m^3·s) (right). Present situation

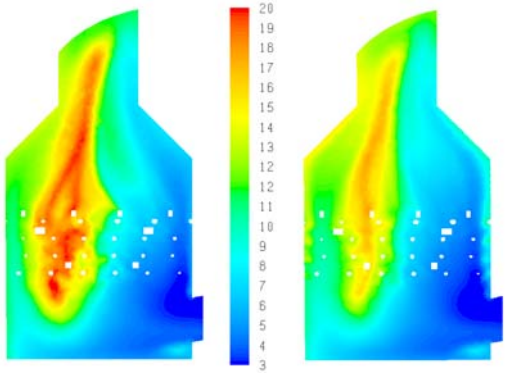

FIG. 8: Residence time (s) in the absorber for the present situation (left) and with wall rings (right)

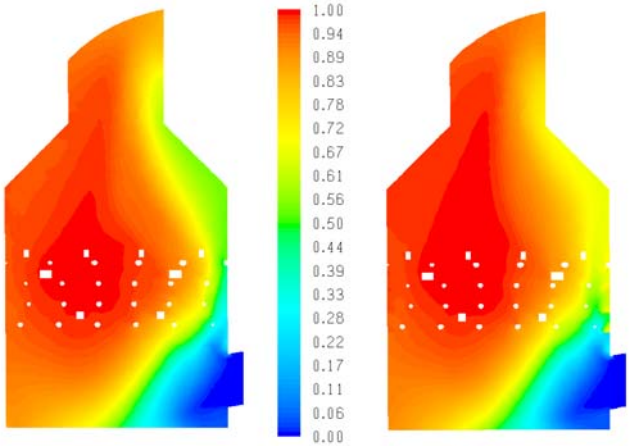

FIG. 9: Contours of desulfurization efficiency in the absorber for the present situation (left) and with wall rings (right)

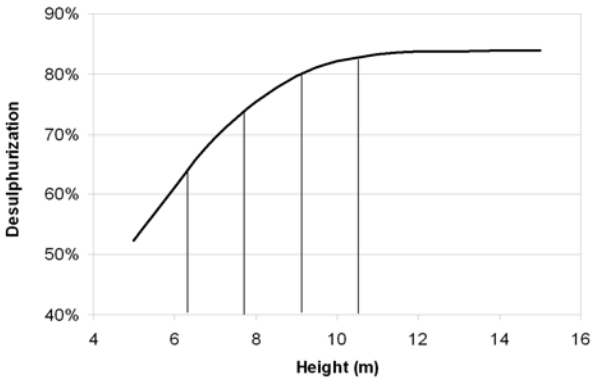

FIG. 10: Variation of the mean desulfurization efficiency with the absorber height. Vertical lines indicate the slurry injection levels

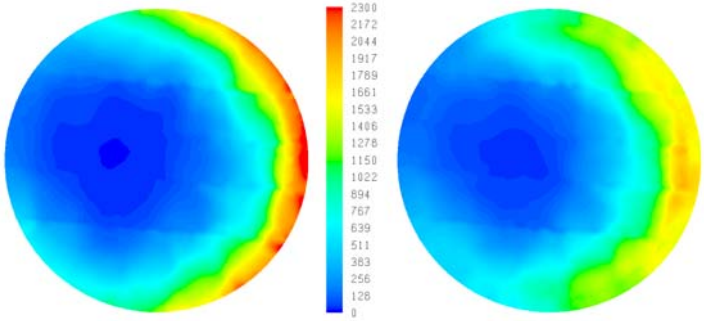

FIG. 11: Contours of SO_2 concentration (mg/Nm^3) at a horizontal section 9 m above the tank for the present situation (left) and with wall rings (right)

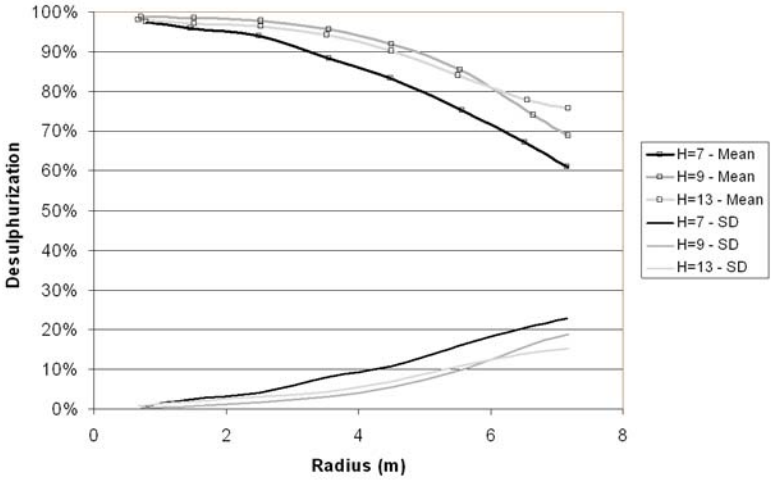

FIG. 12: Mean and standard deviation of the desulfurization efficiency vs the radius at 7, 9, and 13 m above the tank

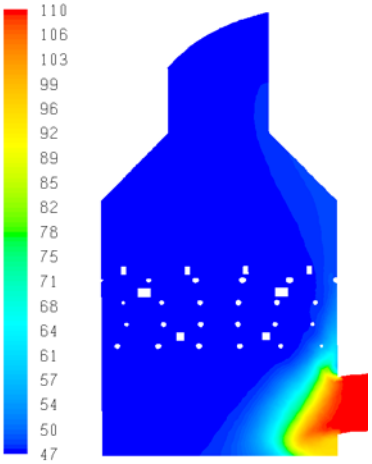

FIG. 13: Temperature contours (^{O}C). Present situation

4.3 Comparison with Plant Measurements

Since we have access to the measurements taken during the normal operation of the plant, we have been able to compare them with the results from the simulation of the tower operating under the same conditions.

Velocity data at the entrance are compared with the simulation results in Fig. 14. We observe that the general pattern is predicted, particularly the high-speed region caused by the presence of the upstream guide vanes.

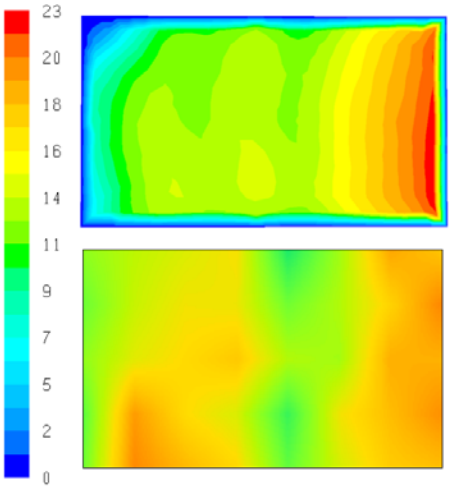

FIG. 14: Velocity (m/s) in the inlet duct. Simulation (above) and measurements (below)

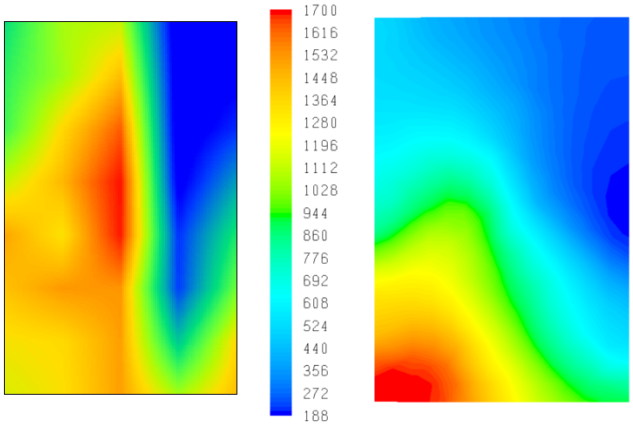

FIG. 15: SO_2 concentration (mg/Nm^3) in the outlet duct. Measurements (left) and simulation (right)

The measured data for SO_2 concentration at the outlet duct in are compared with the simulated results in Fig. 15. The model correctly reproduces high-concentration and low-concentration zones that are consequences of the distribution of residence times in the absorber.

4.4 Configuration with Wall Rings

The aim of the wall rings is to hinder the preferential path of the flue gas along the absorber perimeter, as shown in Figs. 5 (right) and 6 (right), homogenizing the

vertical velocity in the rest of the absorber. As a consequence, the residence time (see Fig. 8, right) is slightly reduced at the center of the absorber while it is substantially increased near the walls, yielding a higher desulfurization rate in those areas where the residence times were previously very low, such as the zone above the inlet duct, as shown in Figs. 9 (right) and 11 (right).

For the wall rings used in this reference case (480 mm wide), the improvement in the desulfurization efficiency is estimated to be about 4%, but this is at the expense of incrementing the pressure loss by about 8%, which for the reference case means around 50 Pa, amounting to an additional power of approximately 20 kW. Overall pressure losses are calculated as averages over the inlet and outlet cross sections indicated in Fig. 1.

4.5 Parametric Analysis

The influence of several parameters on the performance of the FGD systems has been analyzed. Some of these tests were carried out with the aim of assessing the uncertainty in the results due to numerical aspects such as the mesh size or the interactions of the discrete phase with the walls.

Regarding wall–droplet interaction, the reference case assumes that the droplets reaching the walls stick to it and therefore lose their SO_2 absorption capacity. As a more realistic approach is not trivial to formulate or implement, two additional simulations (with and without wall rings) were run, supposing an elastic rebound of the droplets at the walls. The results of this model change are shown in Table 3. While the trends are the same as for the respective cases with no rebound, the numerical results are significantly different. Based on plant data for de-

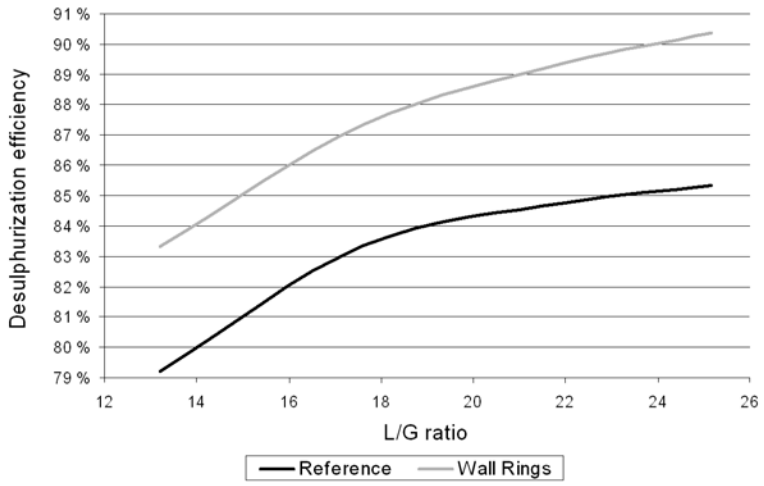

FIG. 16: Influence of the liquid–gas ratio on the desulfurization efficiency with and without wall rings

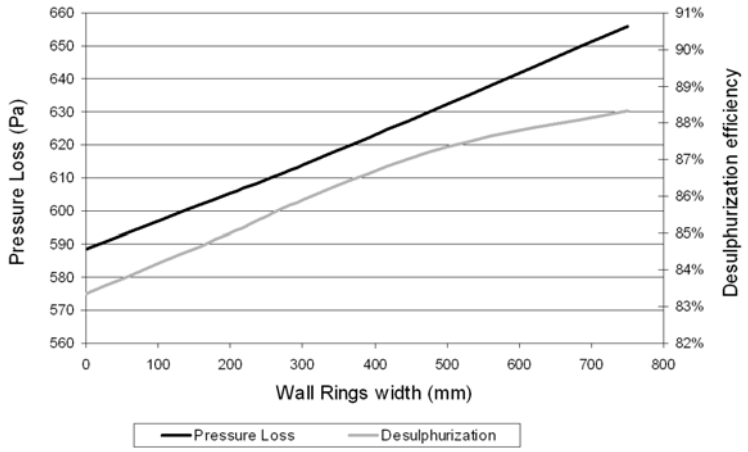

FIG. 17: Influence of the wall ring size on the pressure loss and on the desulfurization efficiency

sulfurization efficiency and pressure loss with no wall rings (particularly the latter), we have adopted the no-rebound approach as, arguably, the one closer to reality.

When attending to operating conditions, Fig. 16 shows that the positive effect of the presence of wall rings holds across the range of liquid–gas ratios. An interesting upshot can be seen at high liquid–gas ratios, at which the presence of wall rings avoids, to some extent, the leveling-off of the efficiency curve for ratios larger than 18.

Finally, it is interesting to assess the influence of the wall rings' size on the desulfurization efficiency, as well as the increase in the pressure loss with the ring width. As shown in Fig. 17, while the increase in the pressure loss is linear, the increase in the desulfurization efficiency shows a change of trend (falling below near-linearity) for rings wider than approximately 500 mm. This is due to the adverse effect on the desulfurization efficiency of the reduced residence times for large ring sizes.

TABLE 3: Influence of the droplet–wall interaction

No droplet rebound	**Desulfurzation Efficiency**	**Overall ΔP**
Reference case	83%	588 Pa
Reference case with wall rings	87%	633 Pa
Droplet rebound		
Reference case	95%	730 Pa
Reference case with wall rings	97%	781 Pa

5. CONCLUSIONS

An existing FGD plant for a coal power station has been modeled and simulated, reproducing the main phenomena found in the absorber, such as a lower concentration of slurry near the walls which causes the velocities to be larger, resulting in lower desulfurization rates.

In order to remedy this shortcoming, the influence of a hypothetical plant modification involving the installation of wall rings has been studied, with the conclusion that they have one positive effect of increasing the global desulfurization efficiency by about 4%, although at the same time increasing the pressure drop in the absorber by about 8%.

Moreover, the results of the simulations have been compared with the available measurements provided by the plant operators, finding a reasonable agreement between them, both for velocities in the inlet duct and for the SO_2 profile at the outlet.

A wide parametric study has been carried out to assess some of the uncertainties present in the study due to numerical issues, such as the mesh or the interaction of the slurry droplets with the walls, and also to research the plant performance in a wider operational envelope. In every case, the wall rings appear to have the same effect on both the desulfurization efficiency and the pressure drop.

Additionally, the influence of the wall ring size has been accounted for, finding that their effect does not vary qualitatively but increases for larger sizes. It is therefore required to find a balance between a better desulfurization efficiency and a higher pressure loss.

Some further improvements of the mathematical model of the FGD process presented here are the inclusion of a detailed aqueous chemistry in the slurry droplets (Gómez et al., 2007) and a more realistic treatment of the wall–droplet interaction.

ACKNOWLEDGMENT

The support and technical direction from the R&D Department (Subdirección General de I+D) of Endesa Generación is gratefully acknowledged.

REFERENCES

Alstom Company, *Flue Gas Desulfurization Technologies*, 2003, Retrieved Nov. 11, 2008, http://www.netl.doe.gov/publications/proceedings/03/NO_xSO2/06-Klitzke%20Sidwell%20Jensen%20presentation%20Part%20123.pdf.

Brian, P. L. T. and Hales, H. B., Effects of transpiration and changing diameter on heat and mass transfer to spheres, *AIChE J.*, vol. 15, no. 3, pp. 419–425, 1969.

Brogren, C. and Karlsson, H. T., Modeling the absorption of SO_2 in a spray scrubber using the penetration theory, *Chem. Eng. Sci.*, vol. 52, no. 18, pp. 3085–3099, 1997.

Crowe, C. T., Sommerfeld, M., and Tsuji, Y., *Multiphase Flow with Droplets and Particles*, CRC Press, Boca Raton, FL, 1998.

DOE, Milliken Clean Coal Demonstration Project: A DOE Assessment, Technical report, U.S. Department of Energy, 2001.

Dou, B., Byun, Y., and Hwang, J., Flue gas desulfurization with an electrostatic spraying absorber, *Energy Fuels*, vol. 22, no. 2, pp. 1041–1051, 2008.

Eden, D., *Simulation von Rauchgassprühwäschern*, PhD Thesis, Gerhard Mercator Universität, GH Duisburg, 1998.

Frandsen, J. B. W., Kiil, S., and Johnsson, J. E., Optimisation of a wet FGD pilot plant using fine limestone and organic acids, *Chem. Eng. Sci.*, vol. 56, no. 10, pp. 3275–3287, 2001.

Frank, M. J., *Meeting Emission Regulations by Innovative Technologies in Flue Gas Cleaning*, Expperts 2006, Krakow, Poland, 2006.

Froessling, N., Ueber die verdunstung fallender tropfen, *Gerlands Beiträge zur Geophysik*, vol. 52, pp. 170–216, 1939.

Gerbec, M., Stergarsek, A., and Kocjancic, R., Simulation model of wet flue gas desulphurisation plant, *Comput. Chem. Eng.*, vol. 19, Suppl. 1, pp. 283–286, 1995.

Gómez, A., Fueyo, N., and Tomás, A., Detailed model of a flue-gas desulfurisation plant, *Comput. Chem. Eng.*, vol. 31, no. 11, pp. 1419–1431, 2007.

Hofelsauer, J., Notter, W., Marocco, L., Agalioti, M., and Leoussis, P., Improvement of SO_2 removal with application of wall rings and advanced CFD modeling — The case of FGD unit megalopolis, *VGB Power Technol.*, vol. 3, pp. 85–89, 2008.

Keskinen, K. I., Alopaeus, V., Koskinen, J., Kinnunen, T., Pitkänen, H., Majander, J., and Wärnström, U., CFD simulation of the oxidation tank reactor of a wet flue gas desulfurization process, *Proc. of the AIChE 2002 Annual Meeting*, Indianapolis, IN, 3–8 November, 2002.

Kiil, S., Michelsen, M. L., and Dam-Johansen, K., Experimental investigation and modeling of a wet flue gas desulfurization pilot plant, *Ind. Eng. Chem. Res.*, vol. 37, no. 8, pp. 2792–2806, 1998.

Lancia, A., Musmarra, D., and Pepe, F., Modeling of SO_2 absorption into limestone suspensions, *Ind. Eng. Chem. Res.*, vol. 36, pp. 197–203, 1997.

Launder, B. E. and Spalding, D. B., *Lectures in Mathematical Models for Turbulence*, Academic Press, London, 1972.

Levenspiel, O., *Chemical Reaction Engineering*, John Wiley & Sons, New York, 1998.

Lide, D. R. and Frederikse, H. P. R., Eds., *CRC Handbook of Chemistry and Physics*, CRC Press, Boca Raton, FL, 1995.

Marocco, L. and Inzoli, F., Multiphase Euler-Lagrange CFD simulations applied to wet flue gas desulphurization technology, *Int. J. Multiphase Flow*, vol. 35, no. 2, pp. 185–194, 2009.

Marsulex Company, *Wet, Semi-Dry & Ammonia FGD Technologies*, 2nd US-China NOx and SO_2 Control Workshop 2005, Retrieved Oct 15, 2008 from http://www.netl.doe.gov/publications/proceedings/05/NOx_SO2/SO2%20Presentations/Tech_Marsulex.pdf.

Morsi, S. A. and Alexander, A. J., An investigation of particle trajectories in two-phase flow systems, *J. Fluid Mech.*, vol. 55, no. 2, pp. 193–208, 1972.

Nygaard, H. G., Kiil, S., Johnsson, J. E., Jensen, J., Hansen, J., and Fogh, F., Full-scale measurements of SO_2 gas phase concentrations and slurry compositions in a wet flue gas desulphurization spray absorber, *Fuel*, vol. 83, no. 9, pp. 1151–1164, 2004.

Perry, R. and Green, D. W., Eds., *Perry's Chemical Engineers' Handbook.*, 6th ed., McGraw-Hill International Editions, 1984.

Ranz, W. E. and Marshal, Jr., W. R., Evaporation from drops — I and II, *Chem. Eng. Prog.*, vol. 48, nos. 3–4, pp. 141–146, 173–180, 1952.

Rowe, P. N., Claxton, K. T., and Lewis, J. B., Heat and mass transfer from a single sphere in an extensive flowing fluid, *Chem. Eng. Res. Des.*, vol. 43A, pp. 14–31, 1965.

Sander, R., *Compilation of Henry's Law Constants for Inorganic and Organic Species of Potential Importance in Environmental Chemistry*, 1999, Retrieved Feb. 4, 2008 from http://www.mpch-mainz.mpg.de/~sander/res/henry.html.

Scala, F., D'Ascenzo, M., and Lancia, A., Modeling flue gas desulfurization by spray-dry absorption, *Sep. Purif. Technol.*, vol. 34, nos. 1–3, pp. 143–153, 2004.

Shih, T. H., Liou, W. W., Shabbir, A., Yang, Z., and Zhu, J., A new k–ε eddy-viscosity model for high Reynolds number turbulent flows — Model development and validation, *Comput. Fluids*, vol. 24, no. 3, pp. 227–238, 1995.

Stultz, S. C. and Kitto, J. B., Eds., *Steam, Its Generations and Use*, Babcock & Wilcox Company, 1992.

Warych, J. and Szymanowski, M., Model of the wet limestone flue gas desulfurization process for cost optimization, *Ind. Eng. Chem. Res.*, vol. 40, no. 12, pp. 2597–2605, 2001.

Zhong, Y., Gao, X., Huo, W., Luo, Z., Ni, M., and Cen, K., A model for performance optimization of wet flue gas desulfurisation systems of power plants, *Fuel Process Technol.*, vol. 89, no. 11, pp. 1025–1032, 2008.

International Journal of Energy for a Clean Environment 10(1–4), 37–56 (2009)

GRAND CANONICAL MONTE CARLO SIMULATION OF HYDROGEN ADSORPTION IN DIFFERENT CARBON NANOSTRUCTURES

Tengfei Luo[1,*] *& John R. Lloyd*[2]

[1]*Department of Mechanical Engineering, Massachusetts Institute of Technology, 77 Massachusetts Avenue, Cambridge, Massachusetts 02139, USA*

[2]*Department of Mechanical and Astronautical Engineering, Naval Postgraduate School, 700 Dyer Road, Monterey, California 93943, USA*

*Address all correspondence to Tengfei Luo, E-mail: tf_luo@mit.edu.

Grand canonical Monte Carlo (GCMC) simulations are performed to study hydrogen physisorption in different nanocarbon porous materials made up of different substructures including carbon nanotubes (CNTs), graphene sheets, and C60. Hydrogen weight percentage (wt%) at different temperatures with pressure ranging from 1 to 20 MPa are predicted. Fugacity and quantum effects on hydrogen adsorption are investigated. Different structural dimensions, including the sizes of the substructures and spacing between the substructures, are used to study the geometrical effects on hydrogen storage capacity in carbon materials. The calculated results of the present study agree well with other available computational data. It is found that CNT arrays, graphite nanofibers (GNFs), and C60 intercalated graphite (CIG) can reach a hydrogen storage weight percent as high as only 3% at room temperature and 20 MPa when equilibrium substructural spacing values are used. The quantum effect is significant in low-temperature hydrogen adsorption simulation, and the particular scheme to include the quantum effect predicts the magnitude of weight percent to vary as much as 3.5%.

KEY WORDS: *grand canonical Monte Carlo, hydrogen, carbon nanotube, graphite nanofibers, C60 intercalated graphite*

1. INTRODUCTION

Hydrogen has been identified as an environmentally sustainable energy carrier because it is clean and renewable. It is a promising alternative fuel to the fossil fuels. However, its implementation in transportation is largely limited by the available storage technology. The U.S. Department of Energy (DOE) set a target of 6.5

2150-3621/09/$35.00

wt% of hydrogen storage for commercial applications to be attained by the year 2010. Among various possible storage techniques, physisorption using nanoporous carbon structures has drawn much attention. There are many studies on hydrogen adsorption using single-walled carbon nanotubes (CNTs), both experimentally (Chen et al., 1999; Liu et al., 1999; Dillon et al., 1997; Ye et al., 1999; Cao et al., 2001) and theoretically (Darkrim and Levesque, 1998; Lee and Lee, 2000; Levesque et al., 2002; Sabir et al., 2007; Wang and Johnson, 1999a, 1999c; Cheng et al., 2008; Zheng et al., 2004; Cheng et al., 2007; Rzepka et al., 1998). Other carbon-based nanostructures such as graphite nanofibers (GNFs) (Chambers et al., 1998; Patchkovskii et al., 2005; Wang and Johnson, 1999b), C60 intercalated graphite (CIG) (Kuc et al., 2007), pillared graphene (Dimitrakakis et al., 2008), and carbon nanoscrolls (Braga et al., 2007; Mpourmpakis et al., 2007) have also been studied mainly by theoretical calculations and simulations. CNT arrays have been regarded as a promising material for hydrogen storage since high weight percent results were reported experimentally. Dillon et al. (1997) found a hydrogen weight percent of 5–10% at ambient pressure near room temperature, and Chen et al. (1999) reported 14–20 wt% in Li- or P-doped CNTs at room temperature. However, some of the experimental results are controversial (Yang, 2000; Wicke et al., 2000), and researchers have not been able to reproduce the results due the difficulty of precisely controlling the experimental conditions. On the other hand, many molecular modeling studies have predicted a much lower weight percent (around 1%) of hydrogen storage in various CNT arrays (Levesque et al., 2002; Wang and Johnson, 1999a; Cheng et al., 2008, 2007; Wang and Johnson, 1999c; Rzepka et al., 1998) at room temperatures. Other pure carbon materials, such as CIG and GNF, also cannot reach the 6.5 wt% target at room temperature, according to various simulation and theoretical predictions (Kuc et al., 2007; Dimitrakakis et al., 2008; Braga et al., 2007; Mpourmpakis et al., 2007).

In theoretical studies of hydrogen storage in carbon structures, molecular dynamics (MD) (Braga et al., 2007; Maruyama and Kimura, 2000; Knippenberg et al., 2008), grand canonical Monte Carlo (GCMC) simulation (Darkrim and Levesque, 1998; Levesque et al., 2002; Wang and Johnson, 1999a, 1999b, 1999c; Cheng et al., 2007, 2008; Zheng et al., 2004; Dimitrakakis et al., 2008; Mpourmpakis et al., 2007; Rzepka et al., 1998), and first-principles calculation (Lee and Lee, 2000; Sabir et al., 2007; Kuc et al., 2007; Dimitrakakis et al., 2008; Mpourmpakis et al., 2007; Meregalli and Parrinello, 2001) are the methods often used. MD is a good method to investigate the hydrogen diffusion processes. However, MD simulations usually need to simulate a large number of hydrogen molecules to model the reservoir environment, and they cannot simulate diffusion processes which may take several minutes to even hours in physical time. GCMC is a suitable approach to simulate the equilibrium state of hydrogen physisorption when the carbon structures are attached to a hydrogen reservoir with well-defined pressure and temperature. First-principles calculation is capable of studying possible chemisorption, but it is not suitable for large-scale simulation.

Although there have been many studies on hydrogen storage in carbon structures, a comprehensive investigation of the factors that influence the hydrogen physisorption weight percent in these materials is still of interest, and such studies will be valuable for further research. In this work, GCMC simulations are performed on hydrogen adsorption in CNT arrays, GNFs, and CIG. Fugacity effects and quantum effects are studied. Temperature, pressure, and structural dimension effects are also investigated.

2. THEORY AND MODEL

2.1 Monte Carlo Method

For a gas adsorption process, the adsorbent structure is attached to a gas reservoir and the gas will diffuse into the adsorbent. At the equilibrium state, the temperature and chemical potential of the adsorbed gas are equal to those of the gas in the reservoir. In a GCMC simulation, the temperature, chemical potential of the reservoir, and the adsorbent structures are input as known parameters, and the equilibrium number of adsorbed gas molecules can be calculated. For hydrogen adsorption in carbon structures, the adsorbed hydrogen gas is in equilibrium with the hydrogen in the reservoir when the temperature and the chemical potential of the hydrogen inside the carbon structures are equal to those of the reservoir. Further details of GCMC method are well documented in Frenkel and Smit (2002).

In a GCMC simulation, instead of setting the chemical potential, it is more intuitive to set the reservoir pressure, which is related to the chemical potential by Eq. (1), using the ideal gas assumption,

$$\mu = \frac{1}{\beta} \ln (\Lambda^3 \beta P) \tag{1}$$

where μ is the chemical potential, $-(1/\beta) = k_B T$, Λ is the thermal deBroglie wavelength, and P is the reservoir pressure.

2.2 Potential Model

In this work, the interaction between hydrogen molecules and the interaction between hydrogen molecules and carbon atoms are modeled by the Lennard-Jones (LJ) potential:

$$U_{LJ}(r) = 4\varepsilon \left[\left(\frac{\sigma}{r} \right)^{12} - \left(\frac{\sigma}{r} \right)^{6} \right] \tag{2}$$

The diatomic hydrogen molecule is treated as an entity. The potential parameters are $\varepsilon_{H_2-H_2} = 0.00316$ eV and $\sigma_{H_2-H_2} = 2.958$ Å for interactions between hydrogen molecules, and $\varepsilon_{H_2-\tilde{N}} = 0.0028$ eV and $\sigma_{H_2-C} = 3.179$ Å for interactions between

hydrogen molecules and carbon atoms. Such a model has been widely used in GCMC simulations of hydrogen adsorption in carbon structures (Darkrim and Levesque, 1998; Levesque et al., 2002; Zheng et al., 2004; Cheng et al., 2007; Dimitrakakis et al., 2008). Besides the aforementioned potential functions, Darkrim and Levesque (1998) and Levesque et al. (2002) also included a quadrupole–quadrupole interaction which was treated by the Coulombic interactions of effective charges. We tested the model which included the quadrupole–quadrupole interaction by simulating hydrogen adsorption in an empty box. The differences of the results from such a model and the model without quadrupole–quadrupole interaction are within 2%. Moreover, since the carbon structures in this study are not charged, there is no Coulombic interaction between hydrogen molecules and carbon atoms. As a result, we ignored the quadrupole–quadrupole interaction in our simulation. The tail correction is applied to our calculation to compensate the cutoff influence.

In our simulations, 1.5×10^7 operations are performed in order to reach equilibrium and other 2.0×10^7 operations are performed for production. Three types of operations (molecule displacement, creation, and deletion) with equal probabilities are performed randomly in the GCMC simulation. Periodic boundary conditions (PBCs) are applied for all three spatial directions in all cases. Different simulation supercells are used for different carbon structures, and these are specified separately in each subsection of Sec. 3.

3. SIMULATION AND RESULT

3.1 Fugacity and Quantum Effect

At very low densities, a gas system can be regarded as a system of noninteracting point particles, which is called an ideal gas. However, when the pressure increases or the temperature lowers, gas molecules get closer and start interacting with each other. Under these conditions, the ideal gas model fails. As a result, the fugacity, which works as the "corrected pressure" for real gases, should be used to describe the reservoir gas, and thus Eq. (1) becomes Eq. (3), which includes the fugacity correction:

$$\mu = \frac{1}{\beta} \ln (\Lambda^3 \beta \phi P) \tag{3}$$

where $\phi \equiv f/P$ is the fugacity coefficient, f is fugacity of nonideal gas, and P is the ideal gas pressure. At temperatures above 0^oC and pressures lower than 300 MPa, the fugacity coefficient can be calculated by the following empirical equation (Shaw and Wones, 1964):

$$\ln \phi = c_1 P - c_2 P^2 + c_3[\exp(-P/300) - 1]$$

$$c_1 = \exp(-3.8402 T^{1/8} + 0.5410)$$

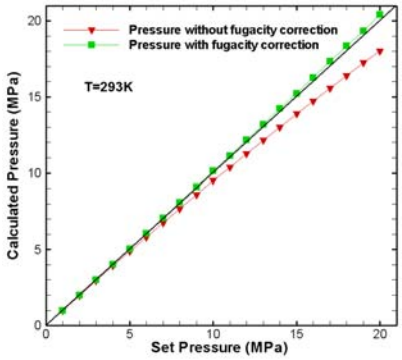

FIG. 1: Effect of fugacity on pressure at 293 K [the black solid line refers to $x = y(x)$]

$$c_2 = \exp(-0.1263T^{1/2} - 15.980)$$
$$c_3 = 300\exp(-0.11901T - 5.941) \tag{4}$$

To test the effect of the fugacity on describing the reservoir hydrogen, hydrogen adsorption in an empty box is simulated. The equilibrium pressure of the box is calculated and plotted versus the set pressure of the reservoir (see Fig. 1). With the fugacity coefficient applied, the calculated equilibrium pressure of the empty box follows the set pressure of the reservoir much closer. This means that the reservoir gas behaves more like interacting LJ gas when the fugacity effect is considered.

However, there are no empirical fugacity coefficient functions available for hydrogen at temperatures lower than 0°C. The fugacity coefficients as functions of the set pressures for lower temperatures are described later in this section.

Because the hydrogen molecular mass is so small, the quantum effect should be considered since it could contribute a lot to the atomic interactions, especially at low temperatures. In this work we employed the method described in Levesque et al. (2002) to use a Feynman–Hibbs effective potential to estimate the quantum effects to the order of $\hbar$, as found in Eq. (5):

$$U_{LJ}^{F-N}(r) = U_{LJ}(r) + \frac{\theta(T)\sigma^2}{24}\left(\frac{d^2U_{LJ}(r)}{dr^2} + \frac{2dU_{LJ}(r)}{r\quad dr}\right) \tag{5}$$

where the dimensionless coefficient $\theta(T)$ is defined as

$$\theta(T) = \frac{\hbar^2}{m_r\sigma^2 k_B T} \tag{6}$$

Here σ refers to the length scale parameter in the LJ potential, $\hbar$ is the reduced Plank constant, and m_r is the reduced mass of the LJ pairs ($m_r = 1.6744 \times 10^{-27}$ for H_2 – H_2 pairs, and $m_r = 2.8675 \times 10^{-27}$ for C – H_2 pairs). For the H_2 – H_2 pair, $\theta(T) = 5.4986/T$, and for the C – H_2 pair, $\theta(T) = 2.7781/T$. To test the quan-

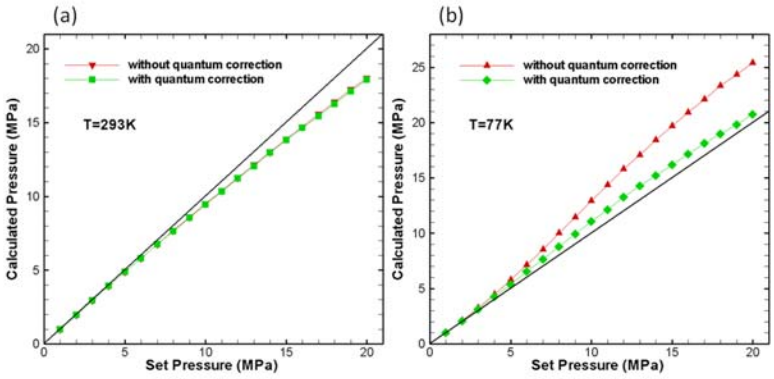

FIG. 2: Quantum effect on pressure at 293 and 77 K [the black solid line refers to $x = y(x)$]

tum effect, we performed GCMC to simulate the hydrogen adsorption in an empty box and plotted the calculated pressure against the set pressure (Fig. 2) at 293 and 77 K. It is seen that the quantum effect at 293 K is very small, but it becomes very significant at 77 K.

To consider the fugacity at 77 K, we calculated the fugacity coefficient according to the data in Fig. 2(b) by taking the ratio of the set pressure to the calculated pressure. The fugacity coefficient is fitted as a function of the set pressure using a 5th-order polynomial as shown in Eq. (7) (Fig. 3). The same process was performed to obtain the fugacity coefficient function at 100 and 200 K. The coefficients are listed in Table 1.

$$\phi = \sum_{i=0}^{5} c_i P^i \tag{7}$$

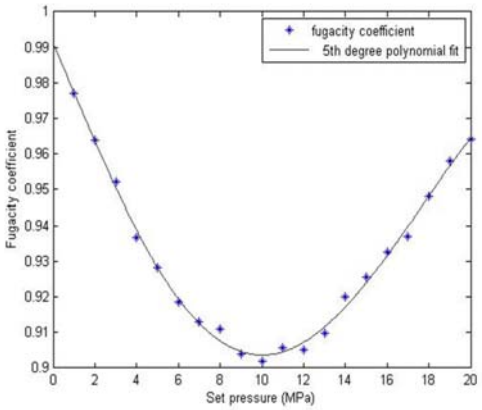

FIG. 3: Fugacity coefficient as a function of set pressure

TABLE 1: Parameters for Eq. (7)

	c_0	c_1	c_2	c_3	c_4	c_5
77 K	0.99117	-1.366×10^{-2}	-2.4193×10^{-4}	1.1282 × 10–4	-4.4165×10^{-6}	4.6108×10^{-8}
100 K	1.0041	-5.9255×10^{-3}	1.1524×10^{-3}	–7.055 × 10–5	2.6498×10^{-6}	-4.0809×10^{-8}
200 K	1.0071	3.8695×10^{-5}	1.5969×10^{-3}	–1.6331 × 10–4	7.8198×10^{-6}	-1.4172×10^{-7}

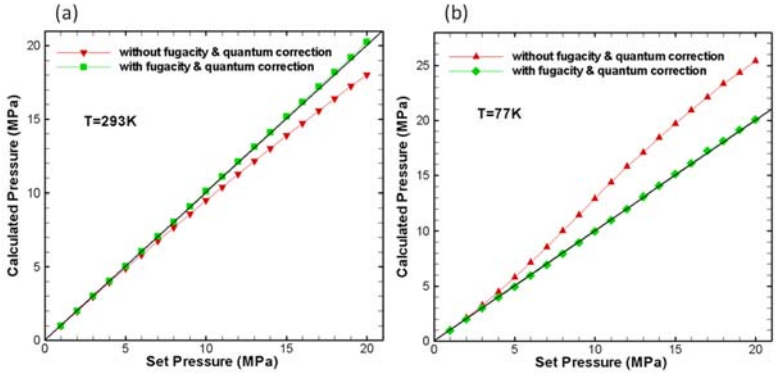

FIG. 4: Calculated pressure vs set pressure after combined fugacity and quantum corrections [the black solid line refers to $y(x) = x$]

Using the model with both fugacity and quantum corrections, we calculated hydrogen adsorption in an empty box again and the pressures are plotted in Fig. 4. After the fugacity correction, the calculated pressure is much closer to the set pressure at 77 K. As a result, after the fugacity and quantum corrections, the hydrogen gas in the reservoir modeled in the GCMC is very close to the real gas described by the LJ potential.

To investigate the combined influence of fugacity and quantum corrections on the hydrogen adsorption in carbon structures, we performed simulations on adsorption in a closely packed (10,10) CNT array at 77 and 293 K with and without the corrections. The cross section of the simulated carbon structure supercell is shown in Fig. 5(c). The 2 × 2 supercell is expanded from the unit cell shown in Fig. 5(a) in x and y directions. The supercell has a length of 19.7 Å in z direction.

The calculated adsorption weight percent isotherms are presented in Fig. 6. It can be seen that at T = 293 K the influence of corrections is very weak at pressures lower than 15 MPa, but it becomes slightly greater as the pressure raises to 20 MPa. At T = 77 K, the effect of the corrections is significant over the whole pressure range. Wang et al. (1999) had similar findings on the great influence from the quantum effect on the hydrogen adsorption in the interstice of CNT arrays, and Patchkovskii et al. (2005) also showed the importance of the correct treatment of quantum effect on theoretical prediction of hydrogen adsorption.

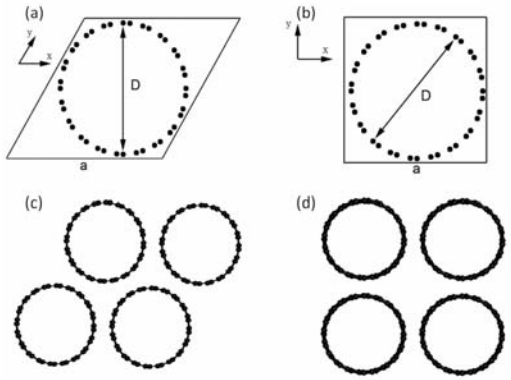

FIG. 5: Cross sections of (a) a triangular unit cell, (b) a square unit cell, (c) a 2 × 2 triangular supercell, and (d) a 2 × 2 square supercell

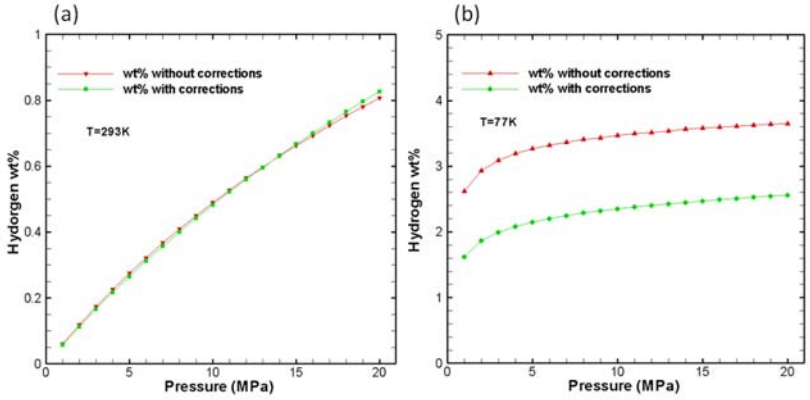

FIG. 6: Combined fugacity and quantum effects on hydrogen adsorption in a closely packed (10,10) CNT array

3.2 Finite Size Effect

In this section, the finite size effects on the hydrogen adsorption in CNT arrays are studied. We performed adsorption simulations at 77 K in a closely packed (10,10) CNT array with different cell lengths and different cross-section areas. To change the cross-section area, the unit cell in Fig. 5(a) is expanded in x and y directions to form 2 × 2 and 3 × 3 supercells. The calculated isotherms are plotted in Fig. 7. It is found that the calculated adsorption isotherms almost overlap on one another in the 2 × 2 (L = 19.7 Å), 2 × 2 (L = 29.5 Å), and 3 × 3 (L = 19.7 Å) cases. Based on the fact that the 2 × 2 supercell with a length of L = 19.7 Å is large enough to ignore the finite size effects, this supercell is used in all simulations on CNT arrays.

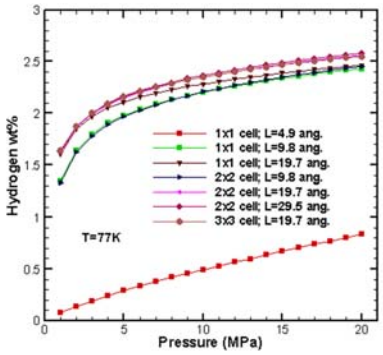

FIG. 7: Finite size effect on hydrogen adsorption weight percent in closely packed (10,10) CNT arrays

3.3 Carbon Nanotubes

3.3.1 *Temperature Effect*

To investigate the temperature effect on the hydrogen adsorption, simulations are performed on the closely packed (10,10) CNT array at 100 and 200 K. The results are presented in Fig. 8, together with the results at 77 and 293 K. From the figure, it is clear that the hydrogen weight percent decreases as temperature increases. The weight percent decreases faster with temperature at lower temperatures (from 77 to 100 K) but slower at higher temperatures (from 200 to 293 K) (e.g., a 23 K temperature increase from 77 to 100 K leads to 0.3 wt% drop at 20 MPa, but a 93 K temperature increase from 200 K to 293 K results in a 0.5 wt% decrease). At low temperatures (from 77 to 100 K) the amount of weight percent decrease due to temperature drop becomes smaller when the pressure increases, while at higher temperatures (from 200 to 293 K) the weight percent decrease due to temperature decrease becomes larger when the pressure is increased.

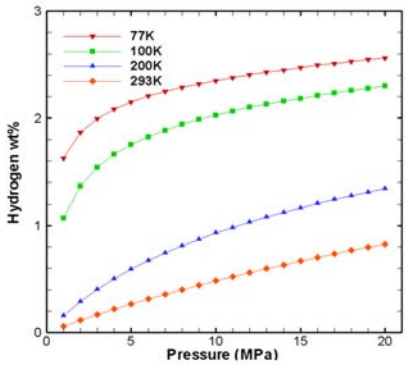

FIG. 8: Temperature effect on hydrogen adsorption weight percent in a closely packed (10,10) CNT array

3.3.2 *Diameter Effect*

To study the CNT diameter effect on the hydrogen adsorption, triangularly packed CNT arrays with different diameters are simulated. All the arrays use the equilibrium lattice constants from Girifalco et al. (2000). The van der Waals (vdW) gap, which is defined as the difference between lattice constant and the CNT diameter, is almost constant (3.1–3.2 Å) among all the arrays with different CNT diameters. CNTs of (6,6), (10,10), (15,15), (20,20), (26,26), (32,32), and (38,38) are studied. The relation between the diameter and the chiral indices is

$$D = \frac{\sqrt{3}}{\pi} a_{c-c}(m^2 + mn + n^2)^{1/2} \tag{8}$$

where D is the diameter, a_{c-c} is the carbon bond length of graphene (1.42 Å), and m,n are chiral indices. Some calculated diameters are tabulated in Table 2.

The calculated hydrogen weight percent at 77 and 293 K at different pressures is shown in Fig. 9. It can be seen that the weight percent increases with diameter increase. This is because the larger CNTs provide more space inside the tubes for hydrogen molecules. According to our calculation [Fig. 9(a)], for closely packed CNT arrays to reach the DOE target of hydrogen 6.5 wt%, the (40,40) CNTs (D = 54.24 Å), a pressure of 20 MPa, coupled with a low temperature of 77 K is necessary. At 293 K it is unlikely that the closely packed CNT arrays will attain the DOE target.

Our data for the closely packed (10,10) CNT array (D = 13.56) are very close to results for the adsorption weight percent from Levesque et al. (2002) on a D = 13.3 Å, a = 16.7 Å CNT array at T = 293 K. Their data are presented at Fig. 9(b) as red crosses. Note that there are three differences between our model and the model used in Levesque et al. (2002): (1) no fugacity was considered in Levesque et al. (2002); (2) the quadrupole–quadrupole interaction was considered in Levesque et al. (2002); and (3) the quantum effect of the interaction between

TABLE 2: Diameters corresponding to CNTs with different chiral indices

Chral indices (*m*,*n*)	**Diameter *D* Å**
6,6	8.14
9,9	12.20
10,10	13.56
18,18	24.41
20,20	27.12
32,32	43.39
38,38	51.53
40,40	54.24

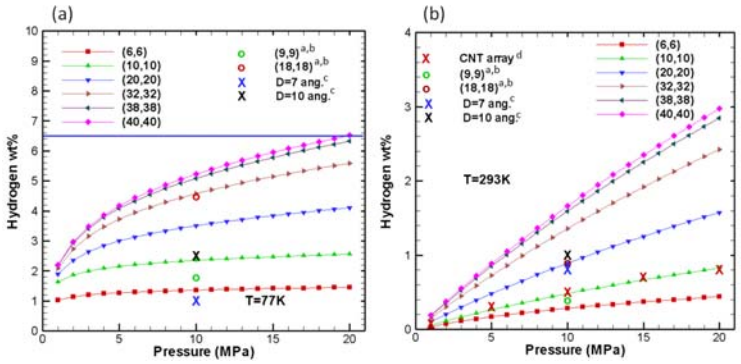

FIG. 9: Diameter effects on hydrogen weight percent at 77 and 293 K in closely packed CNT arrays [The horizontal blue line in (a) refers to the DOE target of 6.5%]. [Refs.: (a) Wang and Johnson, 1999a; (b) Wang and Johnson, 1999c; (c) Rzepka et al., 1998; (d) Levesque et al., 2002.]

hydrogen molecules and carbon atoms is not considered in Levesque et al. (2002). Our predictions for the (6,6) CNT array with D = 8.14 Å are close to the datum from Rzepka et al. (1998) at 77 K for a D = 7 system [blue cross in Fig. 9(a)], but their datum on a D = 10 Å CNT array [black cross in Fig. 9(a)] is slightly larger than our data on the (10,10) CNT array which has D = 13.56 Å. The difference observed could be the result of the quantum effect which was ignored in Rzepka et al. (1998). The weight percent at 293 K is also significantly overestimated compared to other calculations and our data. [NOTE: The original data from Levesque et al. (2002) and Wang and Johnson (1999b, 1999c) are not expressed in weight percent. The weight percent data of these references are from Meregalli et al. (2001).]

For the GCMC calculations using a different potential model (Silvera-Goldman and Crowell-Brown potential) (Wang and Johnson, 1999a, 1999c), the results [shown as green and red circles in Fig. 9(b)] are very close to our data at T = 293K. At 77 K their weight percent of a (9,9) CNT array [green circle in Fig. 9(a)] is not very far from our data on a (10,10) CNT array. However, their data on a (18,18) array [red circle in Fig. 9(a)] is about 26% larger than our (20,20) weight percent. It seems that our potential model predicts weight percent data that are similar to those predicted by the model in Wang and Johnson (1999a, 1999c) at low hydrogen concentration, but there are large differences between the data predicted by these two models when higher hydrogen concentration is involved.

3.3.3 *CNT Spacing Effect*

In this section hydrogen adsorptions in (10,10) CNT arrays with different vdW gaps are simulated. The difference in vdW gaps are reflected by the difference in lattice constants. Both the triangular unit cell [Fig. 5(a)] and the square unit cell

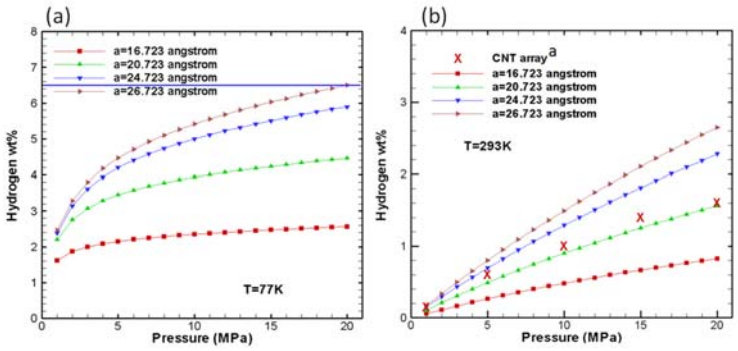

FIG. 10: Spacing effect on weight percent for triangularly packed (10,10) CNT arrays at 77 and 293 K. (The horizontal blue line refers to the DOE target of 6.5%.) [Ref.: (a) Wang and Johnson, 1999a.]

[Fig. 5(b)] are used. The adsorption isotherms for triangular CNT arrays at 77 and 293 K are presented in Fig. 10. It can be seen that the weight percent increases obviously with the vdW gap increase. The amount of weight percent increase due to the vdW gap increase becomes larger at higher pressure. From our calculation, at a temperature of 77 K the (10,10) CNT triangular array with a lattice constant of 26.723 Å can reach the DOE 6.5 wt% target at a pressure of 20 MPa. Changing the vdW gap will not make the (10,10) array a promising hydrogen storage media at room temperature, even though the weight percent increased almost linearly with the increased vdW gap.

The squarely packed (10,10) CNT arrays are also simulated with the same vdW gaps as those used in the triangular arrays and the results are shown in Fig. 11. The squarely packed arrays can adsorb more hydrogen than the triangular arrays for the same vdW gaps. This is because the square arrays are more loosely packed so that the interstitial spaces formed by the CNT walls are larger, and thus more

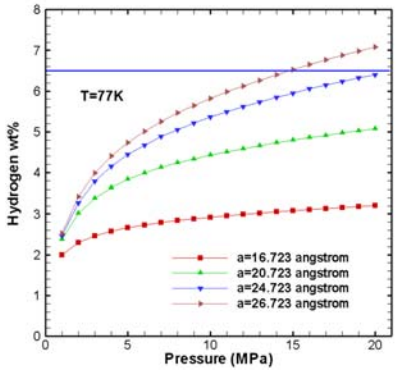

FIG. 11: Spacing effect on weight percent for squarely packed (10,10) CNT arrays at 77 K. (The horizontal blue line refers to the DOE target of 6.5%.)

hydrogen molecules are adsorbed in these spaces. For the square arrays, a lattice constant of 24.723 Å is almost enough to reach the 6.5 wt% target at 77 K and 20 MPa.

Our data for the (10,10) CNT triangular array (D = 13.56) with a = 20.723 Å are close to the results from Levesque et al. (2002) on a D = 13.3 Å, a = 19.3 Å CNT array [red crosses in Fig. 10(b)], but our data are slightly lower. As stated in Sec. 3.3.2, the only differences between our model and the model used in Levesque et al. (2002) are the consideration of fugacity, quadrupole–quadrupole interactions, and the C – H_2 quantum effect. The former two factors are demonstrated to be insignificant according to the discussions in Secs. 2.2 and 3.1. It is also found in Sec. 3.1 that the quantum effect brings down the hydrogen weight percent. As a result, the treatment of the C – H_2 quantum effect explains why our data is lower than the data of Levesque et al. (2002).

3.4 Graphite Nanofibers (GNFs)

In addition to CNT arrays, graphite nanofibers (GNFs) are also regarded as an alternative medium for hydrogen storage (Chambers et al., 1998; Patchkovskii et al., 2005; Wang and Johnson, 1999b). In this section the hydrogen adsorption in GNFs is simulated using GCMC. The GNFs are modeled by single graphene sheet stacks shown in Fig. 12. The interlayer distances H changes to simulate the spacing effect on the hydrogen adsorption capacity. The simulation supercell has a size of 19.7 Å in the z direction and 21.3000 Å in x direction. The cell size in the y direction varies as the interlayer distance H changes. Since the x, y, z dimensions of the supercell are larger than those of the smallest system, we can ignore the finite size effect in Sec. 3.2, and there is no finite size effect in the calculations in this section. In this study, the C – H_2 potential change due to the curvature of the CNT is ignored, and thus the same potential model used in the CNT system is used to model the GNF structures.

GNFs with H of 3.414, 4.414, 5.414, 6.414, 7.414, 8.414, 9.414, 12.900, and 15.000 Å are simulated at temperatures of 77 and 293 K. The calculated hydrogen weight percent for GNFs at these temperatures with H larger than 5.414 Å are plotted in Fig. 13. It is found that no hydrogen can be adsorbed if the equilibrium

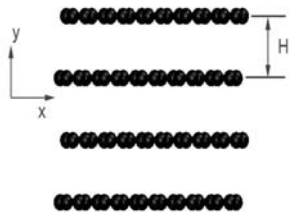

FIG. 12: Simulation supercell of GNF structure

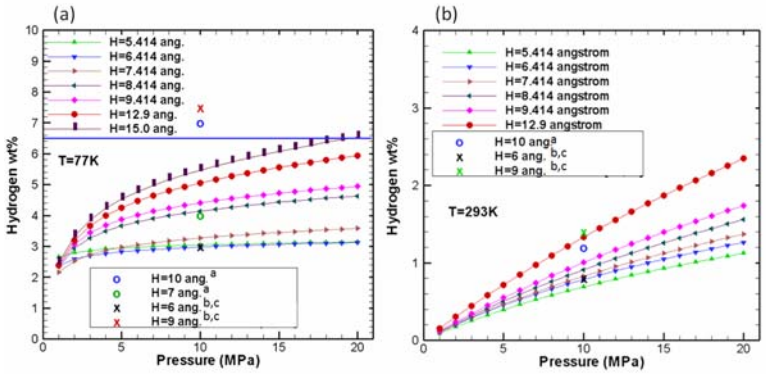

FIG. 13: Interlayer distance effect on hydrogen adsorption weight percent in GNFs. (The horizontal blue line refers to the DOE target of 6.5%.) [Refs: (a) Rzepka et al., 1998; (b) Wang and Johnson, 1999a; (c) Wang and Johnson, 1999b.]

H = 3.414 or 4.414 Å is used, since the interlayer spaces are too small for hydrogen to diffuse into the structure. Sabir et al. (2007) also claimed that molecular hydrogen does not readily intercalate into pure graphite unless the distance between the graphene sheets is artificially enlarged. The calculated weight percent data for a GNF with different interlayer distances from calculations of Wang and Johnson (1999a, 1990b) and Rzepka et al. (1998) are also plotted in Fig. 13. The data from Rzepka et al. (1998) (circles) for GNFs with H = 7 and 10 Å are larger than our predictions for GNFs with H = 7.414 and 9.414 Å, respectively, at 77 K, but at 293 K, Rzepka et al. (1998) predicted hydrogen weight percent for a H = 10 Å GNF that is close to our data for an H = 9.414 Å system. We believe the large discrepancies at low temperatures result because the quantum effect was not considered in Rzepka et al. (1998). Quantum effect greatly reduces the predicted hydrogen weight percent at 77 K, while it does not have much influence at 293 K, as discussed in Sec. 3.1. Compared to the data from Wang et al. (1999a, 1999b) (crosses), our data on a H = 6.414 Å GNF agrees well with their data for a H = 6 Å GNF at both 77 and 293 K, but our predictions for a H = 9.414 Å system are much smaller than Wang's data for a H = 9 Å system at both 77 and 293 K. As discussed at the end of Sec. 3.3.2, Wang et al. (1999a, 1999b) used a different potential model, and that is likely the reason for the differences between their predictions and our data. From our calculation, the GNF with H = 15 Å is needed to reach the 6.5 wt% DOE target, and this can happen only at a low temperature of 77 K and a high pressure of 20 MPa.

The hydrogen equilibrium distributions inside the GNFs are calculated at 77 K for different pressures and are shown in Fig. 14. In the figure only the numbers of hydrogen molecules between two graphene sheets are visualized, and the coordinates in y direction are normalized against the interlayer distances. The normalized interlayer distances are divided into 250 equal intervals, as shown in Fig. 14. For

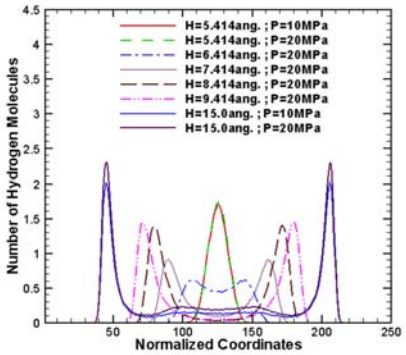

FIG. 14: Hydrogen distribution between two graphene sheets with different interlayer distances

the H = 5.414 Å system, only one layer of molecular hydrogen can be stored in the interlayer space, and it is observed that the pressures of 10 and 20 MPa do not affect the hydrogen weight percent. It is also found that the H = 4.414 Å system will not take any hydrogen at all. As a result, we believe that the interlayer distance threshold for GNFs to adsorb hydrogen is between 4.414 and 5.414 .

It is also found that the distribution profile of the H = 6.414 Å GNF has a concave shape, meaning two layers of hydrogen molecules are being formed, but the two layers still exhibit overlaps. As a result, we believe the single-layer adsorption reaches maximum capacity when H is between 5.414 and 6.414 Å. Patchkovskii et al. (2005) predicted that a monolayer hydrogen with the maximum adsorption capacity of 3.3% can be stored in a H = 6 Å GNF. Our distribution profile suggests the same results, and our weight percent (3%) is also very close to their data. There are two layers of hydrogen molecules between two graphene sheets in GNFs with H = 7.414, 8.414, and 9.414 Å. It can be seen that there are many more hydrogen molecules in each layer in the H = 8.414 Å system than that in the H = 7.414 Å system. This results in a large jump in the weight percent [see Fig. 13(a)]. It is possible that the hydrogen in the H = 7.414 Å system is still in the transition phase from one layer to two layers, meaning there is still overlap between layers. The H = 8.414 Å system has enough space for two complete layers of molecules with no overlap. This transition process can be clearly seen from the distribution profile change from the H = 5.414 Å system to the H = 8.414 Å system. For the H = 15 Å system, two complete layers of hydrogen molecules can be adsorbed, and two other layers are emerging at coordinates of 100 and 200. The hydrogen number density of these two emerging layers increases as the pressure increases from 10 to 20 MPa.

Patchkovskii et al. (2005) also predicted that a H = 9 Å system will accommodate two close-packed monolayers of hydrogen and suggested 6.6 wt%. However, from Fig. 14 the two-layer hydrogen will not reach a maximum weight percent capacity until the interlayer distance H is near 15 Å. Patchkovskii et al. (2005) used

a free energy method with a different treatment of the quantum effect. It is possible that the different treatments of quantum effect result in the difference in the predicted hydrogen weight percent. However, when the GNF system can take two layers of hydrogen with the maximum capacity, the predicted weight percent from our calculation (around 6%) is close to that predicted by Patchkovskii et al. (2005).

3.5 C60 Intercalated Graphite (CIG)

As discussed in the previous section, it is found that GNF will not be able to take hydrogen unless the interlayer distance H is enlarged artificially. It is also found that the larger H is, the more hydrogen that can be adsorbed. To enlarge H, an intercalation method using C60 was found experimentally possible by Gupta et al. (2004). Kuc et al. (2007) used a free energy method and predicted that such a C60 intercalated graphite (CIG) can easily reach the 6.5 wt% target at a temperature of 275 K and a pressure around 15 MPa. In this section, the GCMC is performed on the hydrogen adsorption inside the CIG structures at 77 and 293 K.

The simulation supercell is presented in Fig. 15 and the interlayer distance (H = 12.9 Å) is taken from the experimental values from Gupta et al. (2004). The C60 are placed in a rectangular lattice with a_x = 10.65 Å and a_z = 9.84 Å. (The uneven lattice constants are the results of the uneven supercell dimensions of the graphene sheet in x and z directions.) The size of the supercell is chosen so that no finite size effect could influence the weight percent results. The results are shown in Fig. 16, together with the hydrogen weight percent for a GNF with the same interlayer distance. It can be seen that the CIG has largely reduced weight percent values compared to the GNF. The hydrogen distributions between two graphene sheets in the CIG and GNF at 77 K and 20 MPa are plotted in Fig. 17. It is very interesting to observe that the number of hydrogen molecules between two graphene sheets is not greatly reduced, even though the C60s occupy many interlayer spaces (e.g., 219 molecules are adsorbed in the CIG and 242 molecules are

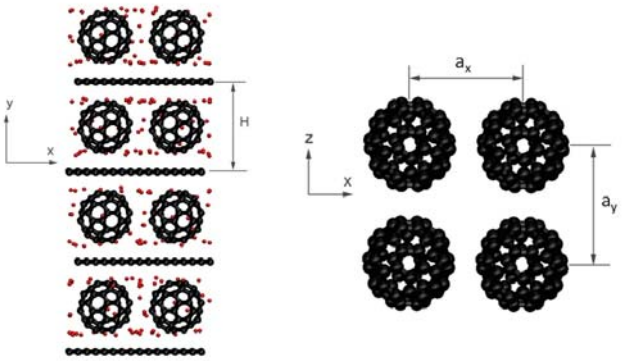

FIG. 15: Simulation supercell of the CIG system: (a) projection on x–y plane and (b) projection on x–z plane without the graphene sheets

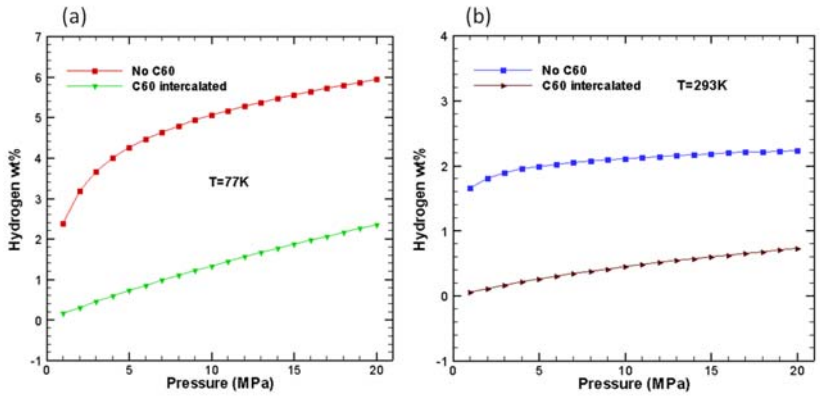

FIG. 16: Comparison of hydrogen weight percent in graphite with C60 intercalation and without C60 intercalation

adsorbed in the GNF at 77 K and 20 MPa). Kuc et al. (2007) suggested that the C60 lowered the interaction free energy between hydrogen and the carbon structure and compensated the effect of reduced effective adsorption space due to C60s. It is the C60s which add the weight of the carbon structure that lead to a much lower hydrogen weight percent in CIG.

The spaces inside the C60 cages do not provide reversible adsorption spaces for hydrogen molecules, however, we did not exclude those spaces in our calculations as was done in the work by Kuc et al. (2007). We found that each C60 cage is capable of containing only one hydrogen molecule. Kuc et al. (2007) used a free energy method together with a real gas equation of state to calculate the hydrogen physisorption weight percent in the CIG and found weight percent values (e.g. 300 K, 20 MPa, 6%) much higher than the results of the present work. We are not

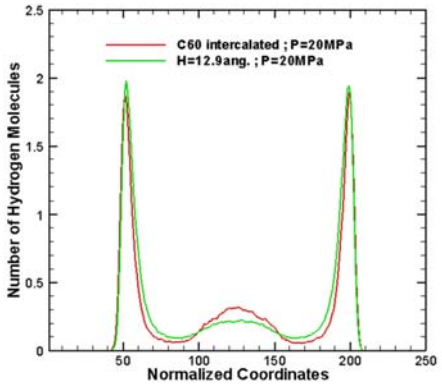

FIG. 17: Hydrogen distribution between two graphene sheets with or without C60 as pillars

aware of the exact gas equation of state used for their calculation. Kuc et al. (2007) also calculated active volumes of hydrogen storage, which was defined as the space of attractive H2-host potential using a LJ potential parameterized on the basis of post-Hartree-Fock *ab-initio* calculation on the interaction of H2 with polyaromatic hydrocarbons. They reported an active volume of 62% for the GNF with interlayer distance of 12.5 Å without C60 pillars. However, using the potential model in our work, the value is only about 45%.

We believe the CIG will not reach the 6.5 wt% target at room temperature and medium pressure, since the upper weight percent limit is the case of the GNF with the same interlayer distance.

4. SUMMARY AND CONCLUSION

In this work, GCMC is used to study hydrogen adsorption in CNT arrays, GNFs, and CIG. Fugacity and quantum effects are studied. It is found that the fugacity correction becomes more pronounced at high temperature (293 K) and high pressure, while the quantum effect is significant at low temperature (77 K). It is also found that temperature has strong influence on the hydrogen weight percent. For CNT arrays with the equilibrium vdW gaps, weight percent increases with CNT diameter increase. Increase of the vdW gap will result in larger hydrogen weight percent due to the increased interstitial spaces among CNTs. Squarely packed CNT arrays will hold more hydrogen than the triangularly packed arrays with the same vdW gaps. We found that GNFs with an equilibrium lattice constant cannot store hydrogen at all unless the interlayer distance is enlarged artificially. The interlayer distance threshold for GNF to store hydrogen is between 4.414 and 5.414 Å. Hydrogen molecules form layers inside the space between graphene layers. The CIG holds comparative numbers of molecules to the GNFs with the same interlayer distance. It is the C60s which increased the structural weight that brings down the hydrogen weight percent.

Our calculated hydrogen weight percent data generally agree well with other calculations at relatively low hydrogen concentration but are lower than other references which either used different potentials or ignored quantum effects. Both treatments of the quantum effect and the different methods used to calculate the weight percent influence the prediction at high hydrogen concentration.

From our study, CNT arrays, GNFs, and CIG are not promising methods by which to attain the 2010 DOE target of 6.5 wt% for hydrogen storage at room temperature and moderate pressure. To reach the target, a low temperature of 77 K is necessary and large internal spaces of carbon structures are required.

ACKNOWLEDGMENTS

The authors thank Dr. N. Priezjev for valuable discussions. The calculations were performed on the high-performance computers of Michigan State University.

REFERENCES

Braga, S.F., Coluci, V.R., Baughman, R.H., and Galvao, D.S., Hydrogen storage in carbon nanoscrolls: An atomistic molecular dynamics study, *Chem. Phys. Lett*., vol. **441**, pp. 78–82, 2007.

Cao, A., Zhu, H., Zhang, X., Li, X., Ruan, D., Xu, C., Wei, B., Liang, J., and Wu, D., Hydrogen storage of dens-aligned carbon nanotubes, *Chem. Phys. Lett*., vol. **342**, pp. 510–514, 2001.

Chambers, A., Park, C., Baker, R.T.K., and Rodriguez, N.M., Hydrogen storage in graphite nanofibers, *J. Phys. Chem. B*, vol. **102**, 4253–4256, 1998.

Chen, P., Wu, X., Lin, J., and Tan, K.L., High H2 uptake by alkali-doped carbon nanotubes under ambient pressure and moderate temperatures, *Science*, vol. **285**, pp. 91–93, 1999.

Cheng, J., Zhang, L., Ding, R., Ding, Z., Wang, X., and Wang, Z., Grand canonical Monte Carlo simulation of hydrogen physisorption in single-walled boron nitride nanotubes, *Int. J. Hydrogen Energy*, vol. **32**, pp. 3402–3405, 2007.

Cheng, J., Zhang, L., Ding, R., Ding, Z., Wang, X., Wang, Z., and Fang, X., Influence of chemical potential on the computer simulation of hydrogen storage in single-walled carbon nanotube array, *Comput. Mater. Sci*., vol. **44**, 601–604, 2008.

Darkrim, F. and Levesque, D., Monte Carlo simulations of hydrogen adsorption in single-walled carbon nanotubes, *J. Chem. Phys.*, vol. **109**, pp. 4981–4984, 1998.

Dillon, A.C., Jones, K.M., Bekkedahl, T.A., Kiang, C.H., Bethune, D.S., and Heben, M.J., Storage of hydrogen in single-walled carbon nanotubes, *Nature,* vol. **386**, pp. 337–338, 1997.

Dimitrakakis, G.K., Tylianakis, E., and Froudakis, G.E., Pillared graphene: A new 3-D network nanostructure for enhanced hydrogen storage, *Nano Lett.*, vol. **8**, pp. 3166–3170, 2008.

Frenkel, D. and Smit, B., *Understanding Molecular Simulation: From Algorithms to Applications*, San Diego, CA: Academic Press, 2nd ed., 2002.

Girifalco, L.A., Hodak, M., and Lee, R.S., Carbon nanotubes, buckyballs, ropes, and a universal graphitic potential, *Phys. Rev. B*, vol. **62**, pp. 13104–13110, 2000.

Gupta, V., Scharff, P., Risch, K., Romanus, H., and Muller, R., Synthesis of C60 intercalated graphite, *Solid State Commun*., vol. **131**, pp. 153–155, 2004.

Knippenberg, M.T., Stuart, S.J., and Cheng, H., Molecular dynamics simulations on hydrogen adsorption in finite single walled carbon nanotube bundles, *J. Mol. Model*, vol. **14**, 343–351, 2008.

Kuc, A., Zhechkov, L., Patchkovskii, S., Seifert, G., and Heine, T., Hydrogen sieving and storage in fullerene intercalated graphite, *Nano Lett.*, vol. **7**, pp. 1–5, 2007.

Lee, S.M. and Lee, Y.H., Hydrogen storage in single-walled carbon nanotubes, *Appl. Phys. Lett*., vol. **76**, pp. 2877–2879, 2000.

Levesque, D., Gicquel, A., Darkrim, F.L., and Kayiran, S.B., Monte Carlo simulations of hydrogen storage in carbon nanotubes, *J. Phys. Condens. Matter,* vol. **14**, pp. 9285–9293, 2002.

Liu, C., Fan, Y.Y., Liu, M., Cong, H.T., Cheng, H.M., and Dresselhaus, M.S., Hydrogen storage in single-walled carbon nanotubes at room temperature, *Science*, vol. **286**, pp. 1127–1129, 1999.

Maruyama, S. and Kimura, T., Molecular dynamics simulation of hydrogen storage in single-walled carbon nanotubes, *ASME Intl. Mechanical Engineering Congress and Exhibit*, Orland, Orlando, FL, November 5–11, 2000.

Meregalli, V. and Parrinello, M., Review of theoretical calculations of hydrogen storage in carbon-based materials, *Appl. Phys. A*, vol. **72**, pp. 143–146, 2001.

Mpourmpakis, G., Tylianakis, E., and Froudakis, G.E., Carbon nanoscrolls: A promising material for hydrogen storage, *Nano Lett*., vol. 7, pp. 1893–1897, 2007.

Patchkovskii, S., Tse, J.S., Yurchenko, S.N., Zhechkov, L., Heine, T., and Seifert, G., Graphene nanostructures as tunable storage media for molecular hydrogen, *PNAS*, vol. **102**, pp. 10439–10444, 2005.

Rzepka, M., Lamp, R., and de la Casa-Lillo, M.A., Physisorption of hydrogen on microporous carbon and carbon nanotubes, *J. Phys. Chem. B*, vol. **102**, pp. 10894–10898, 1998.

Sabir, A.K., Lu, W., Roland, C., and Bernholc, J., Ab initio simulations of H_2 in Li-doped carbon nanotubes systems, *J. Phys. Condens. Matter*, vol. **19**, pp. 086226–086234, 2007.

Shaw, H.R. and Wones, D.R., Fugacity coefficients for hydrogen gas between 0 and 1000 ^{o}C, for pressures to 3000 ATM, *Am. J. Sci.*, vol. **262**, pp. 918–929, 1964.

Wang, Q. and Johnson, J.K., Molecular simulation of hydrogen adsorption in single-walled carbon nanotubes and idealized carbon slit pores, *J. Chem. Phys.*, vol. **110**, pp. 577–586, 1999a.

Wang, Q. and Johnson, J.K., Computer simulations of hydrogen adsorption on graphite nanofibers, *J. Phys. Chem. B*, vol. **103**, no. 2, pp. 277–281, 1999b.

Wang, Q. and Johnson, J.K., Optimization of carbon nanotube arrays for hydrogen adsorption, *J. Phys. Chem. B*, vol. **103**, no. 23, pp. 4809–4813, 1999c.

Wicke, B.G., Olk, C.H., Tibbetts, G.G., Meisner, G.P., Meyer, M.S., and Herbst, J.F., Thermogravimetric measurement of hydrogen absorption in alkali-modified carbon materials, *J. Phys. Chem. B*, vol. **104**, pp. 9460–9467, 2000.

Yang, R.T., Hydrogen storage by alkali-doped carbon nanotubes–revisited, *Carbon*, vol. **38**, pp. 623–626, 2000.

Ye, Y., Ahn, C.C., Witham, C., Fultz, B., Liu, J., Rinzler, A.G., Colbert, D., Smith, K.A., and Smalley, R.E., Hydrogen adsorption and cohesive energy of single-walled carbon nanotubes, *Appl. Phys. Lett.*, vol. **74**, pp. 2307–2309, 1999.

Zheng, H., Wang, S., and Cheng, H., Effect of chemical potential on the computer simulation of hydrogen storage in single walled carbon nanotubes, *Sci. China, Ser. B: Chem.*, vol. **47**, pp. 222–227, 2004.

International Journal of Energy for a Clean Environment 10(1–4), 57–72 (2009)

DESIGN, CONSTRUCTION, AND TESTING OF A CYLINDRICAL SOLAR WATER HEATER

N. V. Ogueke,[*] M. C. Njoku, & E. E. Anyanwu

Mechanical Engineering Department, Federal University of Technology, P.M.B. 1526, Owerri, Nigeria

[*]Address all correspondence to N. V. Ogueke, E-mail: nvogueke@futo.edu.ng

The design, construction, and performance test of a cylindrical solar water heater are presented. It consists of a transparent 900 mm long and 300 mm diameter cylindrical tube made from a 2 mm thick polyvinyl chloride (PVC) material housing a spiral copper tube painted black for improved solar energy harvesting. The copper tube is 15,000 mm long with outer and inner diameters of 12.70 and 11.40 mm, respectively. The transparent PVC material acts as the glazing. Experimental tests on the system were carried out for three different mass flow rates of 10.8, 7.2, and 3.6 kg/h. The results reveal that the maximum efficiency obtained during the test period were 57.09%, 53.99%, and 56.21%, respectively, for mass flow rates of 3.6, 7.2, and 10.8 kg/h. The Hottel–Whillier–Bliss characterization test performed on the solar water heater revealed an intercept on the y axis of 0.30–0.40, while the gradient gave values in the range of –2.94 to –6.91. Overall, the solar water heater has the potential of generating hot water at a very fast rate, with a response time to insolation change that is less than 30 minutes.

KEY WORDS: *solar, water heater, cylindrical solar collector, design, testing*

1. INTRODUCTION

Most countries of the world still depend on conventional energy sources to meet all their energy demands. Conventional energy sources have been identified as being responsible for the increasing ozone layer depletion and the global warming scourge facing the world today. Apart from these environmental concerns, its finite nature and unpredictable cost arising from very high demand and sometimes political supply factors have made it very unattractive as our main source of energy. Consequently, efforts are being intensified worldwide to find a reliable alternative to conventional energy sources. At present, the emphasis is on significantly reducing our dependence on conventional energy sources by utilizing renewable energy sources. Hot water production using solar energy is one major area through which this can be done. Hot water is essential in both industries and homes. It is required for bathing, washing clothes and utensils, and for other domestic purposes in both urban and rural areas. Hot water is also required in large quantities in hotels, hos-

2150-3621/09/$35.00

NOMENCLATURE

A_c	collector area, m^2	q_{ab}	net rate of heat energy absorption by copper tube, W/m^2
c_p	specific heat capacity of water, J/kg·K	q_u	heat transfer rate from copper tube to water, W/m^2
D	diameter of cylinder, m	T_{am}	ambient temperature, K
Gr	Grashof number	T_{mean}	mean temperature of air and transparent cover, K
h_{rc}	radiation coefficient from the transparent cylindrical housing, $W/m^2·K$	T_{wall}	temperature of the copper tube wall, K
h_{rt}	radiation coefficient between copper tube and transparent housing, $W/m^2·K$	U_L	overall heat loss coefficient, $W/m^2·K$
h_{tc}	convection coefficient between copper tube and transparent housing, $W/m^2·K$	v_{wind}	wind velocity, m/s
h_{wind}	heat transfer coefficient due to the wind, $W/m^2·K$	**Greek symbols**	
I_t	total insolation on a horizontal surface, W/m^2	α_p	absorptivity of copper tube
$\dot{m}$	mass flow rate of water, kg/s	η	efficiency of solar water heater
Nu	Nusselt number	ΔT	temperature increase of water between inlet to and exit from the heater, K
Pr	Prandtl number	τ_c	transmissivity of transparent cover

pitals, hostels, and industries such as textile, paper, food processing, dairy, edible oil, etc. (Nahar, 2002).

Several research projects on the use of solar energy to generate hot water have been reported in open literature. They include the passive systems reported by Chun et al. (1999), Kalogirou (2009), Esen and Esen (2005), Shariah and Shalabi (1997), Smyth et al. (2001), Arthur and Norton (1988), Smyth et al. (2005), Tripanagnostopoulos and Souliotis (2006), and Chaurasia and Twidell (2001); and the active system reported by Kumar and Kumar (1997) and Wongsuwan and Kumar (2005). All these works show that water heating using solar energy is technically feasible. However, there is need for continuous research and development to improve on the performance and popularity of the systems. This can be achieved through different methods, ranging from the use of selective surfaces to increase the collector plate heat absorption capacity to employing reversed absorption technology, which reduces heat loss from the water-heating system. Better focusing of the collector plate through optimization of the angle of inclination of the collector is another method of improving solar water-heating performance. These methods, apart from being expensive and in some cases leading to the production of complex systems, can only effectively utilize the direct component of solar radiation.

Thus, their performance during the winter months and other seasons of the year with low insolation levels is not very encouraging. So far, most of the commercially available solar water heating systems are of the flat-plate type. Flat-plate systems have enjoyed this popularity because they are simple in design and inexpensive to own and operate. Unfortunately, they also have high heat loss and poor performance during winter months, when the demand for hot water is generally the greatest.

In this work, the design, construction, and test performance of a cylindrical water-heating system, capable of utilizing both the direct and diffuse components of solar radiation, is presented. The system is tested in Owerri, a tropical southeastern town in Nigeria. It has three major seasons in a year (rainy, dry, and harmattan seasons), with an average daily global solar radiation on a horizontal surface ranging between 13 MJ m^{-2}, during the rainy season, and 16 MJ m^{-2}, during the dry season. Hours of bright sunshine exceeding 8 hours in a day is at about 12% occurrence, and that between 6 and 8 hours a day is at about 25% occurrence, while its mean monthly K_T curve is between 0.36 and 0.42 (Anyanwu and Oteh, 2003). Hence, Owerri has a predominantly overcast atmosphere. It is therefore necessary to also test the performance of such a system in a location with a predominantly overcast atmosphere and for which less than 6 hours of bright sunshine has a greater percentage of occurrence.

2. DESCRIPTION OF THE CYLINDRICAL SOLAR WATER HEATER

The solar water heater consists of a spiral copper tube housed in a cylindrical transparent tube. This is shown in Fig. 1a. The transparent tube, which acts as a housing for the copper tube and also as a glazing material, is made from a transparent polyvinyl chloride (PVC) material 2 mm thick and turned into a cylindrical shape 900 mm long and 300 mm in diameter. The ends of the cylinder were sealed with circular transparent plates made from the same PVC material. Holes were made on the end plates for the spiral copper tubes to pass through. The function of this cylindrical housing is the same as that of transparent covers employed in other types of conventional solar collectors. The choice of transparent plastic as glazing material is informed by the fact that collector cost can be reduced by 20–70%, depending on the degree to which such material is used to replace glass as a glazing material within a collector. Furthermore, plastic materials have excellent toughness, transparency, and thermal stability, and choosing to use them as a glazing material results in a significant reduction of the overall weight of the solar water heater.

The copper tube is painted black and acts as a collector of the incident solar energy on the solar water heating system. It is made from a 15,000 mm long copper tube turned into a spiral. The outer and inner diameters are 12.70 mm and 11.40 mm, respectively. A spiral shape is considered in this work for two reasons: (i) to reduce the length of the entire assemblage, since the length of the cylindrical hous-

(a)

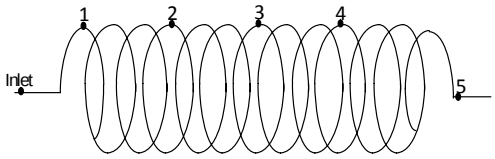

(b)

FIG. 1: (a) Photograph of the cylindrical solar water heater and (b) schematic diagram of the copper tube showing the thermocouple positions, i.e., points 1, 2, 3, 4, and 5. Point 1 is the inlet while point 5 is the outlet

ing is dependent on the tube, and (ii) to generate more exposed tube surface area for better solar energy harvesting. This is possible because there is some space between each spiral to allow part of the radiation to pass through, thus heating the inner portion of the coil as well. Hence, both the upper portion of the spiral and its inner portion can be directly heated by solar radiation.

A tank containing the water to be heated is placed at a height of about 2000 mm above the solar water heater to provide a sufficient gradient for the water to flow at the desired flow rate through the heater. The water tank is connected to the copper tube through a flexible plastic hose. Two valves are employed for water flow control. The first one is used to maintain flow at the desired rate, while the second valve is used to start or stop flow at the beginning or end of the experimentation period. Both the tank and the flexible plastic hose are properly insulated with glass fiber to reduce heat ingress from the ambient air into the water before it enters the solar water heater. That way, water heating is achieved only in the solar water heater. In order to measure the water temperature along the tube, K-type thermocouples are fixed at six different points between the inlet to and exit from the copper tube (Fig. 1b). The first thermocouple measures the water temperature just before it enters the heater, while the remaining ones are distributed at five equidistant points along the tube within the solar collector. The thermocouples are connected to a ten-channel Comark electronic thermometer with an accuracy of $\pm 0.1^{o}$C. Flow rate through the tube is obtained by adjusting the valve at the cold water storage

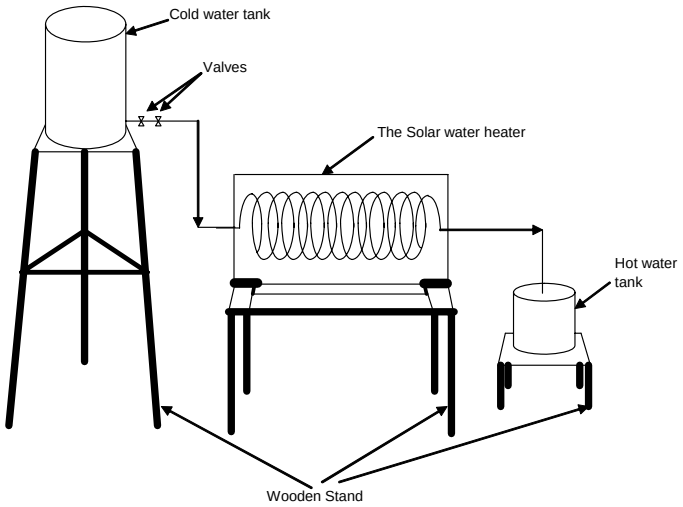

FIG. 2: Schematic diagram of the experimental rig of the cylindrical solar water heater

tank and noting how long it takes to fill a 4 L container. In order to ensure that the flow rate remains reasonably constant throughout the experiment, a cold water tank with a large diameter is selected. This will ensure that a 4 L change in volume will not produce appreciable change in the height of the water column before fresh cold water is added to replace what is lost.

The schematic diagram of the entire experimental rig is shown in Fig. 2. The experiment began each day with an empty hot water tank, while fresh cold water was continuously added to the cold water tank in order to ensure that the tank was always full and thus maintained relatively constant head. Fresh cold water is added each time a volume equivalent to 4 L flows out of the tank. Because of the large diameter of the tank, the 4 L will not produce an appreciable change in water height, and the flow rate remains relatively constant.

3. DESIGN CALCULATIONS

At steady state, the net rate of heat energy absorption by the absorber tube from the incident solar radiation equals the net rate of heat transfer to the water, which in turn produces the useful heating. Hence

$$q_u = q_{ab} \, . \tag{1}$$

The net rate of heat energy absorption per unit area of the tube q_{ab} is given as

$$q_{ab} = I_t R \tau_c \alpha_p - U_L \, (T_{wall} - T_{am}) \, . \tag{2}$$

Because of the cylindrical shape of the solar water heater, it does not require to be inclined to the horizontal at a value that is equal to the location's local latitude. Thus the tilt correction factor, R in Eq. (2) is unity (i.e., R = 1). U_L, the overall heat-transfer coefficient between the copper tube and ambient environment, is obtained from Eq. (3) by assuming that the spiral copper tube approximates to a cylinder which is concentric to the transparent cylindrical housing. Consequently, the resistances to heat flow are those caused by convection and radiation between the copper tube and its cylindrical housing, that due to radiation from the cylindrical housing surface and that due to the wind effect. Losses from the ends of the cylindrical housing are assumed to be negligible due to the poor thermal conductivity of the material of the cylindrical housing.

$$U_L = \left(\frac{1}{h_{tc} + h_{rt}} + \frac{1}{h_{wind} + h_{rc}} \right)^{-1} \tag{3}$$

Contribution to U_L by the wind h_{wind} is obtained from the correlation for flow over horizontal cylinders given in the ASHRAE Handbook (2005).

$$h_{wind} = (4.22 - 0.00257\, T_{mean}) \frac{v_{wind}^{0.633}}{D^{0.367}} \tag{4}$$

The convection heat-transfer coefficient between the copper tube and cylindrical housing h_{tc} is obtained from the correlation given in Holman (2002) as

$$\mathrm{Nu} = 0.550.55\, (\mathrm{Gr} \times \mathrm{Pr})^{0.25} . \tag{5}$$

The water heating rate in the solar water heater is related to the mass flow rate of water and the water temperature increase across the collector by

$$q_u A_c = Q_u = \dot{m} c_p \Delta T . \tag{6}$$

By substituting Eq. (1) into Eq. (2) and then substituting the resulting equation into Eq. (6), the collector tube surface area can be obtained. The solar water heater instantaneous efficiency given as

$$\eta = \frac{Q_u}{A_c I_t} \tag{7}$$

is used to compare the performance of the solar water heater with other similar systems built and tested in similar climatic conditions.

4. RESULTS AND DISCUSSION

Experimental tests of the solar water heater were carried out between October 21 and November 9, 2009, under the meteorological conditions of the Federal University of Technology, Owerri, Nigeria. During the experimentation, the following pa-

rameters were measured: ambient temperature, insolation, total hourly values of sunshine, water temperature along the tube, and water temperature before entering the solar water heater. These readings were taken at intervals of 30 minutes, beginning from 9:00 a.m. to 5:00 p.m. each day. The insolation was measured using a Daystar hand-held digital solar meter which uses a polycrystalline silicon PV cell as a sensor. Its accuracy is ≤3% within the measuring range of 0–1200 W/m^2 with a resolution of 1 W/m^2. The water temperature along the tube was obtained with a K-type thermocouple connected to a 10-channel Comark electronic thermometer with an accuracy of ±0.1^{o}C.

The solar water heater was tested under three different mass flow rates of 0.001, 0.002, and 0.003 kg/s, capable of generating at least a minimum daily hot water demand of 20 L/day (Nieuwoudt and Mathews, 2005). Figure 3 shows the temperature variation of the water as it flows through the tube at a mass flow rate of 0.003 kg/s for 3 days with different insolation patterns. On each of the days, an increase in the water temperature was achieved, with day 2 presenting the highest temperature increase of about 25^{o}C. This corresponds to an exit water temperature of about 57^{o}C. This was followed by day 3, which gave a water temperature increase of about 22^{o}C, corresponding to about 54^{o}C, while day 1 presented a temperature increase of about 18^{o}C, or an exit water temperature of 48^{o}C. Figure 4 shows the variation pattern of the insolation on some of the days tested. Comparing Figs. 3 and 4 reveals that the variation pattern of the water temperature as it

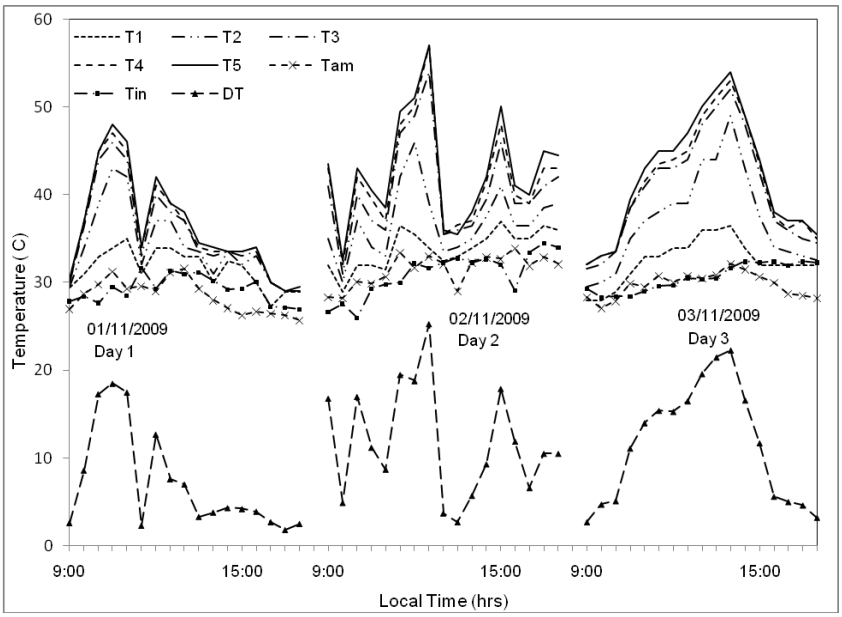

FIG. 3: Water temperature variation through the solar water heater at 0.003 kg/s. T1–T5 are temperature points along the tube, T_{in} is the inlet water tempertaure, and *DT* is the temperature increase achieved equal to T5 minus T_{in}

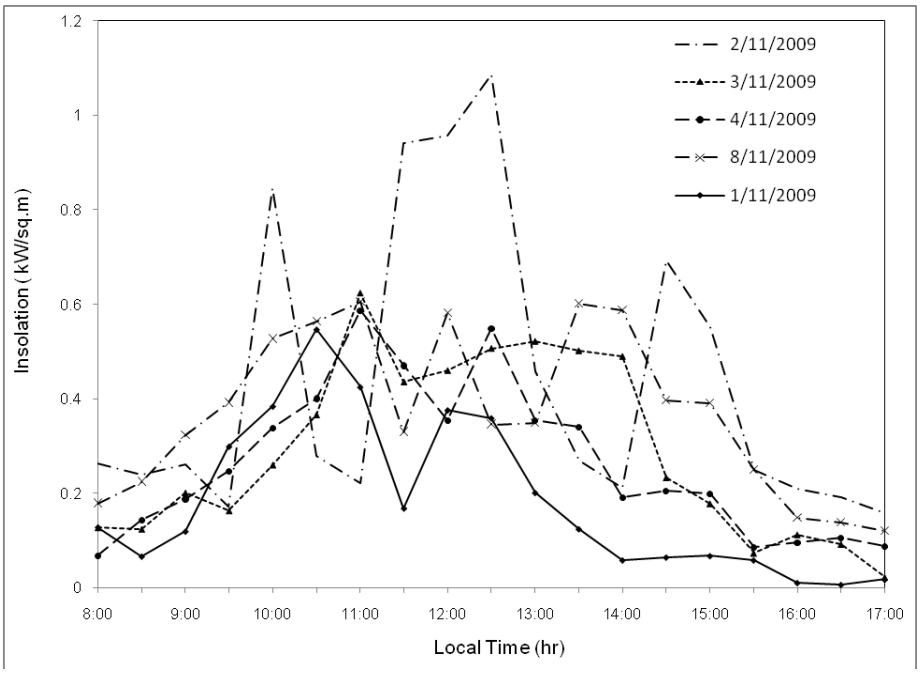

FIG. 4: Insolation pattern for some of the days tested

flows through the water heater is strongly dependent on the insolation, with the maximum temperatures occurring mostly at the times when the insolation was highest. Figures 3 and 4 also show that the solar water heater performs well under very clear and partly overcast days. From Fig. 4 it can be seen that the insolation level for day 1 was generally low, yet a water temperature elevation up to 18^{o}C was recorded. Overall, the temperatures achieved are well within the range of the hot water temperatures required in most domestic applications and in slaughter-houses. In other applications like fowl processing, which requires hot water temperatures between 65–70^{o}C, the solar water heater can serve as a preheater, thereby reducing the amount of electrical or fossil fuel energy required to generate hot water for such purposes.

The temperature profile of water flowing between the inlet and the outlet of the water heater appears to follow the same pattern on all the days for the different mass flow rates, increasing or decreasing in response to the changing weather conditions. This is confirmed by Figs. 5 and 6, which show the water temperature profile as it flows through the solar water heater at mass flow rates of 0.002 and 0.001 kg/s, respectively. The most significant temperature increase occurred between 10:00 a.m. and 3:30 p.m., which corresponds to the period when most of the insolation recorded is about 0.50 kW/m^2 and above, as revealed in Fig. 4. Therefore, when a hot water storage tank is employed, it will be most profitable to

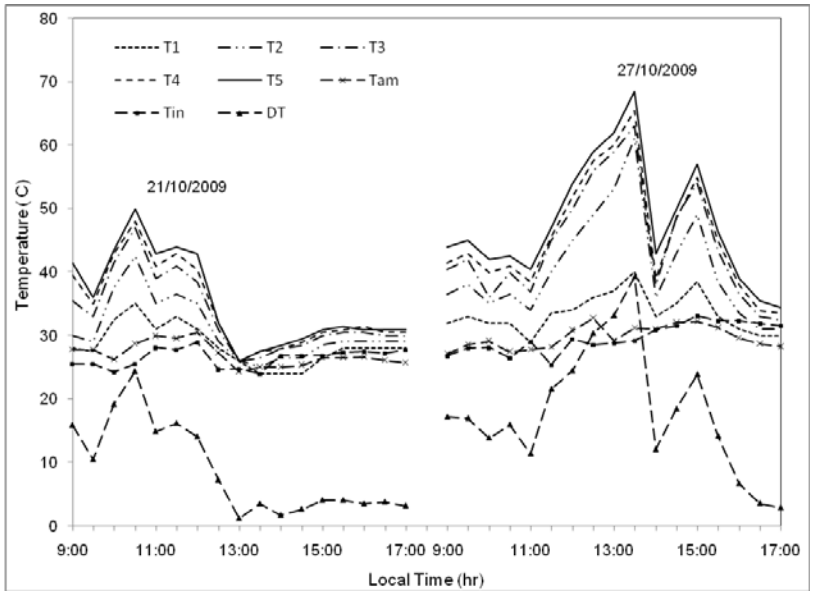

FIG. 5: Water temperature variation through the solar water heater at 0.002 kg/s. T1–T5 are temperature points along the tube, T_{in} is the inlet water tempertaure, and DT is the temperature increase achieved equal to T5 minus T_{in}

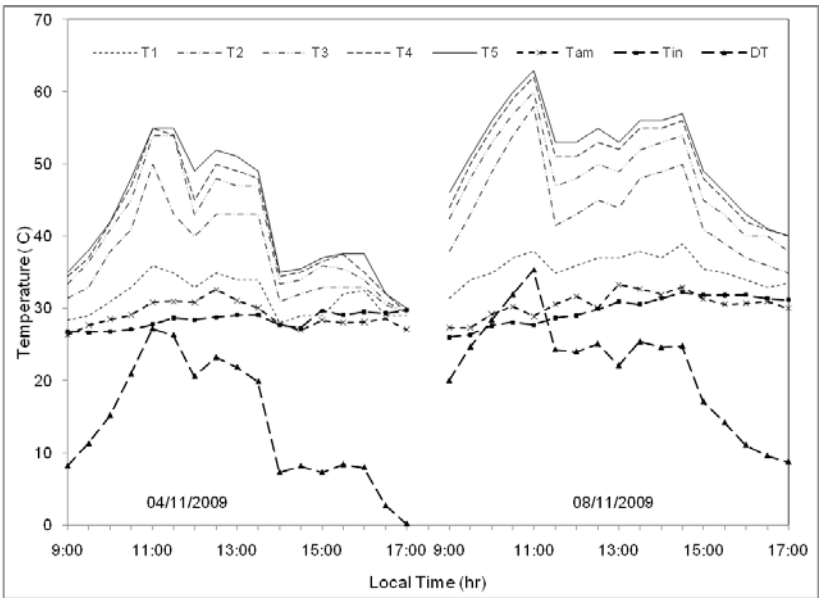

FIG. 6: Water temperature variation through the solar water heater at 0.001 kg/s. T1–T5 are temperature points along the tube, T_{in} is the inlet water tempertaure, and DT is the temperature increase achieved equal to T5 minus T_{in}

operate the solar water heater within this time range so as not to dilute the hot water coming from the solar water heater within the periods of fairly and very good insolation with the colder water coming from other time periods. Because our solar water heater was tested between 9:00 a.m. and 5:00 p.m., which is inclusive of both the periods of predominantly high insolation (i.e., 10:00 a.m.–3:30 p.m.) and the low insolation periods, the storage tank temperature was almost consistently lower than the exit water temperature from the solar water heater, as shown in Fig. 7. It can also be inferred from Figs. 3, 5, and 6 that the highest temperature increases in the water as it flows from the inlet to the exit of the solar water heater occurred between the inlet point and point 3. In fact, for all the days tested, the water was often heated to between 77 and 85% of the exit temperature at point 3, which represents about 50% of the entire tube length.

Figure 8 shows the variation patterns of the instantaneous thermal efficiency of the solar water heater for some of the test days. This reveals that the efficiency of the solar water heater varies throughout the test period, just as the insolation varies, with the range falling between about 16 and 57%. Most of the low efficiency values were recorded during a period of low insolation or on overcast days. In general, the system is capable of functioning at high efficiency, regardless of the mass flow rate used. In fact, the maximum efficiencies obtained for the three mass flow rates considered are 57.09, 53.99, and 56.21% for 0.001, 0.002, and 0.003 kg/s, respectively. These results are in the same order of magnitude with the efficiency values reported by Al-Madani (2006) and Kudish et al. (2003). The common and enhanced flat-plate-type solar water heaters also have efficiency in the same order of magnitude

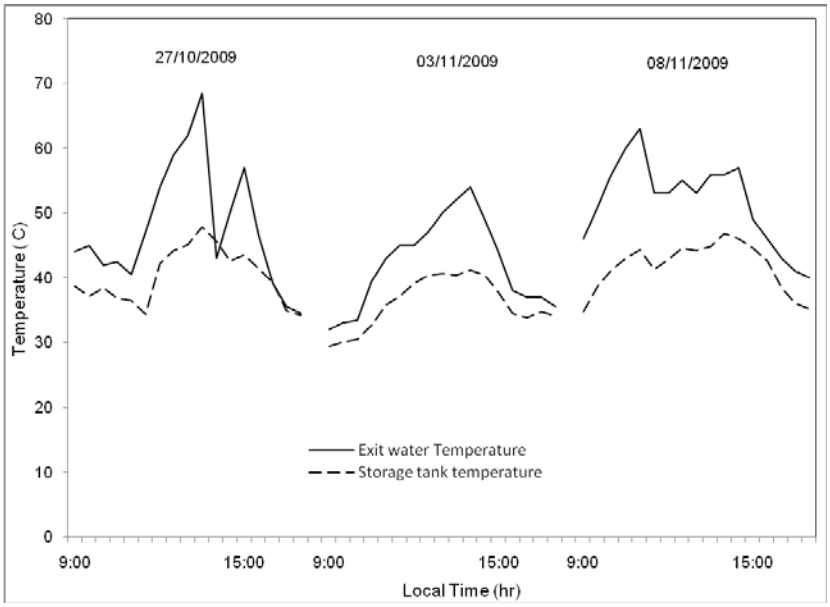

FIG. 7: Variation pattern of the storage tank and exit water temperature

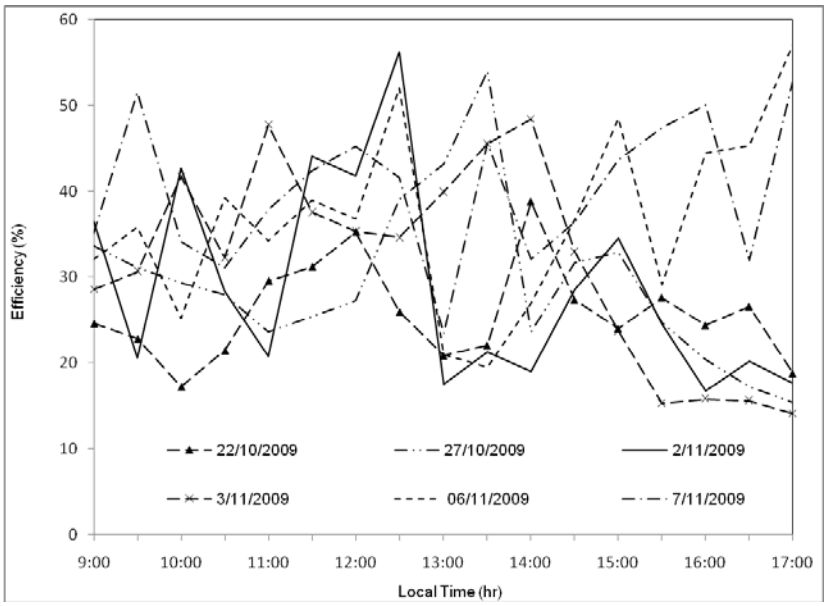

FIG. 8: Variation pattern of the efficiency with time

(Ogueke et al. 2009). However, the cylindrical solar water heater has the advantage of less cost, smaller area, and not requiring focusing on the sun for its best performance. For instance, it costs N23,250.00 ($1.00 = N150.00) to construct our cylindrical solar water heater capable of generating 50 L/day of water at an average temperature of 52°C on a clear day. Equivalent flat-plate-type solar water heaters constructed in the Department of Mechanical Engineering, Federal University of Technology, Owerri, Nigeria, cost between N30,750.00 and N37,500.00, depending on whether they are of the integrated collector storage (ICS) or thermosyphon type. Although efficiency varied throughout each test day, as shown in Fig. 8, its average daily values lie between 25 and 42% for the entire test period, as shown in Fig. 9.

Efficiency may not be the only parameter to properly ascertain the level of performance of any solar water heating system. This is because efficiency depends on collector operating temperature and ambient temperature; therefore, its value changes with time in most collector applications. This probably explains the variation in efficiency values observed earlier in Fig. 8. Therefore, the Hottel–Whillier–Bliss characterization, which is a plot of η versus $(T_{in} - T_{am})/I_t$, is required to more appropriately ascertain the performance level. Figures 10–12 show the plots for our solar water heater when operated at three different mass flow rates. From these figures it can be seen that the solar water heater's capability to absorb energy, as shown by the intercept on the y axis $[F_R(\tau\alpha)]$, is in the range 0.30–0.40, while the energy loss represented by the gradient of the plot (i.e., $F_R U_L$) is in the

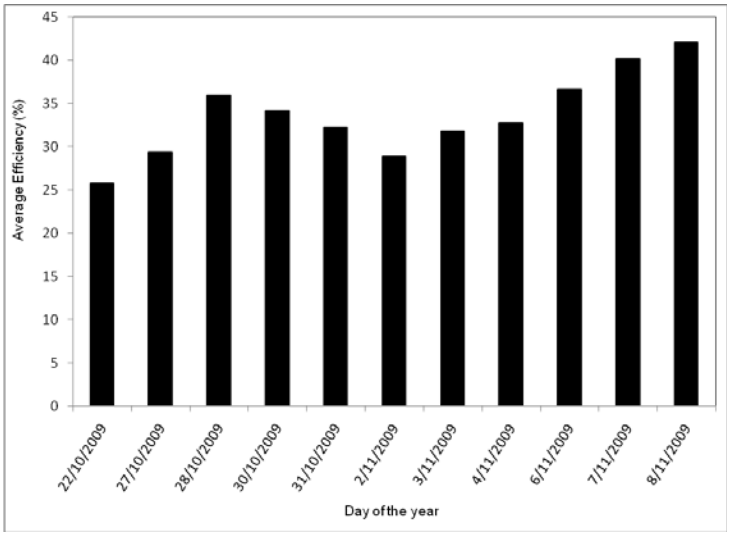

FIG. 9: Average efficiency of the solar water heater for the different days

range –2.94 to –6.91. The fact that $F_R(\tau\alpha)$ is low and $F_R U_L$ is high may be attributed to the inadequacies in the local construction of the solar water heater. For instance, in order to form the cylinder acting as the glazing from the flat PVC material, naked flame was used to heat the PVC to enable it to be transformed to that cylindrical shape. This obviously affected its transmissivity. Also, the sealing

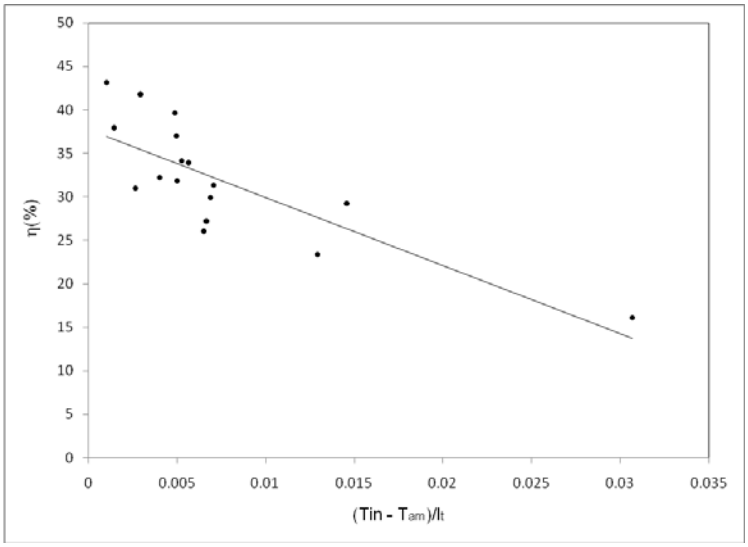

FIG. 10: Plot of η vs $(T_{in} - T_{am})/I_t$ for the solar water heater at a mass flow rate of 0.001 kg/s

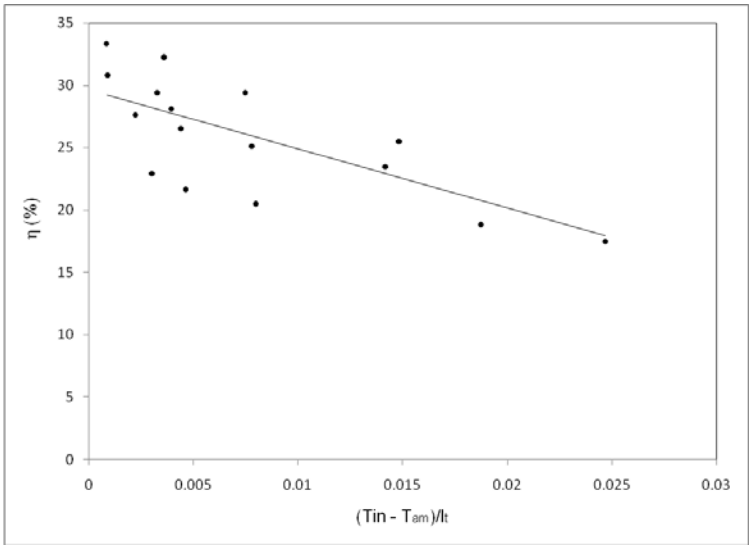

FIG. 11: Plot of η vs $(T_{in} - T_{am})/I_t$ for the solar water heater at a mass flow rate of 0.002 kg/s

of its edges was not very perfect, thereby increasing heat loss by convection from the system. In fact, the effects of these inadequacies in its construction can be seen from how scattered the points on the η versus $(T_{in} - T_{am})/I_t$ plots are, especially in Figs. 10 and 11. Furthermore, some of the assumptions made, like negligible edge heat loss and treating the coiled copper tube as a concentric cylinder with the

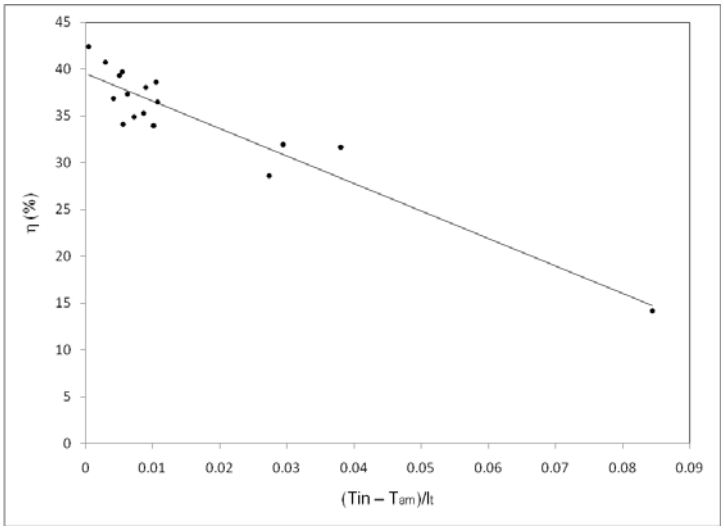

FIG. 12: Plot of η vs $(T_{in} - T_{am})/I_t$ for the solar water heater at a mass flow rate of 0.003 kg/s

transparent PVC housing, may also have contributed to the observed values $F_R(\tau\alpha)$ and F_RU_L. With improved construction, these characteristics of the solar water heater are expected to improve. Considering the obtained values of $F_R(\tau\alpha)$ and F_RU_L, there is the need for improved construction of the system; however, these values are in the same order of magnitude with those obtained from systems constructed and tested elsewhere (see Solar Rating and Certification Corporation). The data obtained from the Solar Rating and Certification Corporation indicate that for tubular solar water heaters, $F_R(\tau\alpha)$ is in the range of 0.28–0.63, with about 50% of these values falling below 0.5. For F_RU_L, values in the range of –1 to –5.7 were reported.

5. CONCLUSIONS

The design and performance evaluation of a cylindrical solar water heater has been undertaken. The system was constructed from locally available materials, making it easy for construction in localities of deployment. From the test results, the following conclusions may be drawn:

1. The cylindrical solar water heater has a fast response time to insolation changes — the value being less than 30 minutes. This reveals good potential for generating hot water at a fast rate.
2. An efficiency of 50% or more is possible. However, the present test gave an average daily maximum efficiency of about 42%.
3. The $F_R(\tau\alpha)$ and F_RU_L are in the range of 0.3 to 0.395 and –2.94 to –6.91, respectively.
4. The solar water heater can generate hot water for most domestic applications, with low insolation in the range of 0.45 W/m^2.
5. There is a time range within which operation of the solar water heater yields the best results. For our system, this time range is between 10:00 a.m. and 3:30 p.m.
6. When compared with the flat-plate collector method, producing the same volume per day of hot water, this system is relatively cheaper, costing about N23,250.00 ($1.00 = N150.00) to generate 50 L/day of hot water at 52^{o}C, compared with about N30,750.00–N37,500.00 for an equivalent flat-plate collector. Furthermore, it does not require focusing the sun at an angle for maximum efficiency.
7. The cylindrical solar water heater in its present state has room for further improvement. For instance, it is possible to evacuate the space enclosed by the transparent plastic cylinder to reduce heat loss by convection.

ACKNOWLEDGMENT

The authors acknowledge with thanks the financial support of the World Bank under its STEP-B research grant for renewable energy research at the Federal University of Technology, Owerri, Nigeria.

REFERENCES

Al-Madani, H., The performance of a cylindrical solar water heater, *Renewable Energy*, vol. **31**, no. 11, pp. 1751–1763, 2006.

Anyanwu, E. E. and Oteh, U. U., Analysis of solar radiation measurements at Owerri, Nigeria, Afr. *J. Sci*., vol. **4**, no. 1, pp. 893–906, 2003.

Arthur, A. C. and Norton, B., Factors affecting the performance of integral passive solar energy water heaters, *Proc. of the Sixth Int'l. Solar Energy Forum*, Berlin, Germany, pp. 189–194, 1988.

ASHRAE Handbook, Fundamental Volume 2005.

Chaurasia, P. B. L. and Twidell, J., Collector cum storage solar water heaters with and without transparent insulation material, *Sol. Energy*, vol. **70**, no. 5, pp. 403–416, 2001.

Chun, W., Kang, Y. H., Kwak, H. Y., and Lee, Y. S., An experimental study of the utilization of heat pipes for solar water heaters, *Appl. Therm. Eng.*, vol. **19**, pp. 807–817, 1999.

Esen, M. and Esen, H., Experimental investigation of a two-phase closed thermosyphon solar water heater, *Sol. Energy*, vol. **79**, pp. 459–468, 2005.

Holman, J. P., *Heat Transfer*, Tata McGraw-Hill ed., Tata McGraw-Hill Pub. Co. Ltd., New Delhi, 2002.

Kalogirou, S., Thermal performance, economic and environmental life cycle analysis of thermosiphon solar water heaters, *Sol. Energy*, vol. **83**, pp. 39–48, 2009.

Kudish, A. I., Evseev, E. G., Walter, G., and Preiebe, T., Coaxial tubular solar collector constructed from polymeric materials: An experimental and transient simulation study, *Energy Convers. Manage.*, vol. **44**, pp. 2549–2566, 2003.

Kumar, S. and Kumar, N., Constant delivery temperature solar water heater — An integrated approach, *Energy Convers. Manage.*, vol. **38**, no. 1, pp. 61–71, 1997.

Nahar, N.M., Capital cost and economic viability of thermosyphonic solar water heaters manufactured from alternate materials in India, *Renewable Energy*, vol. **26**, no. 4, pp. 623–635, 2002.

Nieuwoudt, M. N. and Mathews, E. H., A mobile solar water heater for rural housing in southern Africa, *Build. Environ.*, vol. **40**, pp. 1217–1234, 2005.

Ogueke, N. V., Anyanwu, E. E., and Ekechukwu, V., A review of solar water heating systems, *J. Renewable Sustainable Energy, vol.* **1**, no. 4, pp. 1–21, 2009.

Shariah, A. and Shalabi, B., Optimal design for a thermosyphon solar water heater, *Renewable Energy*, vol. **11**, no. 3, pp. 351–361, 1997.

Smyth, M., Eames, P. C., and Norton, B., Annual performance of heat retaining integrated collector/storage solar water heaters in a northern maritime climate, *Sol. Energy*, vol. **70**, no. 5, pp. 391–401, 2001.

Smyth, M., McGarrigle, P., Eames, P. C., and Norton, B., Experimental comparison of alternative convection suppression arrangements for concentrating integral collector storage solar water heaters, *Sol. Energy*, vol. **78**, no. 2, pp. 223–233, 2005.

Solar Rating and Certification Corporation, Independent certification of solar water and swimming pool heating collectors and systems, http://www.solar-rating.org/ratings/ratings.htm.

Tripanagnostopoulos, Y. and Souliotis, M., ICS solar systems with two water tanks, *Renewable Energy*, vol. **31**, no. 11, pp. 1698–1717, 2006.

Wongsuwan, W. and Kumar, S., Forced circulation solar water heater performance prediction by TRNSYS and ANN, *Int. J. Sustainable Energy*, vol. **24**, no. 2, pp. 69–86, 2005.

International Journal of Energy for a Clean Environment, 10(1–4), 73–101 (2009)

RENEWABLE ENERGY PROSPECTS AND FEASIBILITY FOR ISOLATED COMMUNITIES

Constantine M. Tarawneh,[1*] Horacio Vasquez,[1] Lariza Navarro,[1] Vanessa Reyna,[1] Michael A. Acosta,[1] & Van A. Reidhead[2]

[1]*Department of Mechanical Engineering, The University of Texas-Pan American, Edinburg, Texas 78539-2999, USA*

[2]*College of Social and Behavioral Sciences, The University of Texas-Pan American, Edinburg, Texas 78539-2999, USA*

[*]Address all correspondence to Constantine M. Tarawneh E-mail: tarawneh@utpa.edu.

We are nearing the end of the first decade in the twenty-first century, yet there remain millions of people around the world living in poorly developed areas without electricity. Motivated by their needs, small- to medium-size solar power systems (250–650 W) were set up and utilized to conduct numerous tests to study renewable energy prospects and feasibility for isolated communities outside the power grid. In particular, the experimental efforts focused on modeling the power needs of several rural areas of the Municipality of Ciudad Valles, San Luis Potosi, Mexico, whose mayor approached the authors to design a sustainable working model for the region, which was found to be a good representative of the power needs of many isolated communities. System performance was characterized for a number of parameters including rated power of solar panels, size and number of storage batteries, and electric loads used. The experiments conducted included charging deep-cycle batteries using photovoltaic solar panels and discharging those utilizing different power consumption scenarios. Additional experiments included several week-long tests aimed at determining the real-time operating capability of the devised systems. The experimental results obtained indicate that carefully constructed solar power systems can provide people living in isolated communities with sufficient energy to meet their basic power needs sustainably and without interruption. Achieving this outcome, however, requires not only factoring in standard environmental data but also human factors research to make perfectly clear the end consumer's expectations about what they will power with it, how often, and for how long.

KEY WORDS: *small-scale solar power systems, power for isolated communities, alternative energy solutions, local culture in sustainable energy planning*

1. INTRODUCTION AND BACKGROUND

A solar power system provides a viable option as an alternative energy source to create electricity under environmentally friendly operating conditions. Research and development of solar energy systems has become an important factor in solving the present energy crisis and in preventing the environmental damage caused by the burning of fossil fuels [1]. In spite of the relatively high initial investment cost, a solar power system can provide great benefits, especially in isolated regions that lack a power grid but enjoy abundant sunshine throughout the year. In general, even where power grids exist, demand and thus electric bills become unusually high in the summer, resulting in periodic blackouts that disrupt businesses, cause refrigerated food and medicines to spoil, which shuts down much-needed pumps, fans, air-conditioning, communication, and other systems. Hence there is a need to implement solar and other alternative energy systems, not only in isolated communities, but also in cities and towns throughout much of the world. In fact, to encourage the wide use of renewable energy, some governments currently allow people to use expenses incurred in the installation of renewable energy systems in their homes or businesses as tax deductions and subsidize startup costs for community civic use.

Solar or photovoltaic (PV) cells are made of semiconductor materials such as silicon that convert sunlight into electricity. When sunlight strikes the PV cells, a portion of its energy is absorbed within the semiconductor material and it displaces electrons, creating electric fields capable of generating electric currents to power loads connected to the solar cells. A typical 100 cm^2 silicon solar cell can produce 0.5 V and generate up to 3 A of electrical current [2]. The rated power (in Watts) of a solar cell or solar panel is specified by its characteristic output voltage multiplied by the electric current flowing out of the cell under specific operating conditions. Solar cells have relatively low efficiency (generally between 15 and 20%) because part of the sunlight energy striking the solar cells is required to make the electrons move, leaving holes which are then occupied by other electrons, thus producing electricity. However, new technology has resulted in the creation of solar cells that are about 40% efficient [3], and researchers are continuously trying to make them cheaper and better.

A solar module is an array of solar cells, and a solar panel consists of several solar modules that produce a specific rated output voltage, current, and power. Solar panels usually require fuses to protect the solar cells against overcurrent and have diodes to protect them against reverse-current flow. PV panels produce silent, pollution-free electricity wherever sunlight is available, but their power output depends on numerous factors such as solar irradiance, incidence angle, ambient temperature, and the electric loads being powered, which is determined by people whose lack of knowledge about PV-generated power is likely to cause them to have unrealistic expectations of the system.

In designing power systems for underserved regions, solar and wind are two energy sources that complement each other, allowing the generation of renewable energy under a variety of atmospheric conditions for rural and urban settings [4]. For a static solar panel, energy production has a parabolic shape from 7 a.m. to 7 p.m. (daylight hours), with maximum output occurring at about 1 p.m. [5], whereas wind energy production is generally irregular, peaking at different times depending on geographic location and weather conditions [4]. However, this paper focuses on solar energy as a source of electricity, because we found that wind rows throughout the Ciudad Valles Municipality (county) are insufficient to economically incorporate wind generation into a system that meets their needs.

Optimization and control algorithms can be implemented to maximize renewable energy harvesting, particularly when charging batteries during periods when the state of charge (SOC) of the batteries and solar radiation are both at equal extremes — too high or too low. Unless the energy demand is similar to the electricity being produced, two critical situations frequently occur: (a) the renewable energy is wasted or not collected because batteries have reached their full storage capacity, or (b) not enough energy is produced by the system to fully charge the batteries and satisfy human demand. In such situations, a control algorithm is needed to make decisions about when to turn loads on, or off, in a prioritized way determined by established usage expectations for the system. At present, ongoing research is also focused on developing better ways to store energy in the form of hydrogen for fuel cells [6, 7]. Nonetheless, regardless of how the energy is stored, a smart control system strategy constructed with culturally informed human factors research, resulting in a training program for local system users and managers, is required to manage the renewable energy system, protect the system components, and prevent overuse from unplanned consumption.

Storing electricity is both difficult and expensive, which is one of the main limitations to implementing reliable renewable and sustainable energy systems using solar and wind power sources [8]. Even though lithium-ion batteries have better performance than lead batteries, because they cost more, lithium-ion batteries are used mainly for low-energy-capacity systems, while lead batteries are better suited for higher energy storage applications [8]. Batteries are charged and discharged daily, and the SOC is usually estimated by measuring their voltage and current history [9]. Also, batteries experience self-discharge and therefore must continuously be recharged to prevent low SOC. Extended periods of low SOC reduce battery life, requiring more frequent replacement and higher system cost. Since batteries are one of the major costs of a renewable energy PV system, a battery management system is required to optimize its performance, preventing over- or undercharging operating conditions. Failure to account for this will result in the system falling into disuse, because consumers cannot afford unplanned replacement batteries, thus resulting in customer dissatisfaction. In communities where alternative energy systems are most needed, traditional knowledge systems are generally dominant and knowledge of

electrically driven technology limited. In the face of unexpected system failures and costs, people in such communities will abandon renewable energy systems and revert to traditional systems, which although inadequate to improve quality of life, are at least predictable to them.

Al Kalaani [10] indicated that even though there is great enthusiasm for renewable energy, there is a lack of understanding of the benefits of using renewable energy sources. Hence it is essential that some engineering courses at the university level incorporate sustainable energy concepts and applications to encourage education and implementation of these technologies. To this end, a small-scale solar energy system was implemented in the mechanical engineering department at The University of Texas-Pan American (UTPA). Initial experimental efforts were focused on investigating the charge–discharge performance of batteries while varying load, solar panel power, panel inclination angle, and sun-tracking effect [11]. A series of current and voltage transducers and signal-conditioning components were installed and monitored using a data acquisition system which allowed for the system performance and efficiency to be quantified. Additionally, the data collected were analyzed to determine the peak hours of electric generation. The main objective of the initial study was to identify potential residential and commercial applications of small-scale solar power systems. To lay a foundation for eventually establishing consumption and management expectations, a working relationship was established with Ciudad Valles decision makers through the Mexican Consul of McAllen, TX, coordinated by the Office of the Dean of the College of Social and Behavioral Sciences. UTPA researchers and administrators (lead by the university provost) visited Ciudad Valles, whose decision makers in turn visited UTPA to view and learn about the system in its proof-of-concept stage and to discuss human factors issues with researchers in the College of Social and Behavioral Sciences. The current work presented in this paper is an extension of the earlier study conducted by the authors and is aimed at exploring renewable energy prospects and feasibility for isolated communities and remote areas.

2. PARADIGM APPLICATION DETAILING SYSTEM REQUIREMENTS AND CONSTRAINTS

Ciudad Valles, located in San Luis Potosi, Mexico, is home to more than 150,000 people and is the third largest municipality in the state. At its center is the populated city of Ciudad Valles proper, surrounded by small towns, villages, and isolated homesteads inhabited by people of Huastecan ethnicity, with Huastec the first language and Spanish second. The region is equipped with an electric power grid; however, government planners deemed it unfeasible to extend power lines to the county's outer rural regions, meaning that a substantial percentage of the overall population does not have electricity for basic needs (e.g., light, refrigeration, and emergency equipment). The people living in these remote communities want electricity, understanding that it will give them access to services that do not currently

exist for them. The authors of this paper and Ciudad Valles municipal representatives met on several occasions in order to gain a better understanding of the needs and requirements of the people living in the region's isolated rural areas, establish initial knowledge about design constraints so that a suitable solar power system can be implemented to meet expected electric power needs, establish a baseline for testing and improvement, and produce knowledge to optimize systems as they are implemented throughout the region.

To emphasize the worldwide importance of renewable energy projects, Zahnd et al. [12] explained how in poor villages in Nepal, and in many other countries including developed countries, about 2 billion people endure harsh living conditions in part because of the lack of electricity. For instance, in many villages people prepare meals on open fireplaces that require burning logs inside their houses, generating smoke clouds that create respiratory problems with negative health consequences manifesting in increased morbidity and a shortened lifespan. Deforestation problems are also caused because of the logs needed for the fireplaces and tree resin extraction needed to create candles. As an example of small-scale electricity generation, Zahnd et al. [12] installed a 150 W hydropower generator to provide 30 houses with three 1 W white light-emitting diode (LED) lights which, although a seemingly small contribution, tangibly benefited people of that village. Increasingly, developing countries are realizing the importance of using renewable energy systems to provide distance learning programs to children and parents in rural communities without access to education, as exemplified by the works of Ross et al. [13] and Foster et al. [14], whose projects were funded by the U.S. Department of Energy and the U.S. Agency for International Development (USAID).

Ciudad Valles is situated in a valley characterized by a very warm climate with no substantial amount of wind but an abundance of sunlight; more than 329 days (90%) of each year are sunny, indicating that solar energy is the most viable candidate of all prospective renewable energy sources to generate electricity for the people of Ciudad Valles. With that in mind, the main goal of this project was to identify, implement, and test affordable, low-maintenance, environmentally friendly solar power systems with sufficient energy storage capacity to meet the everyday needs of the people living in rural Ciudad Valles, sustainably, without interruption. Incoming solar radiation, or "Insolation," is defined as the solar radiation received on the earth's surface measured in units of kilowatt hours per square meter per day ($kWh/m^2/day$). Most of the southern states in the United States of America (USA), all of Mexico, Central America, and the northern parts of South America have insolation values between 4.0 and 6.0 ($kWh/m^2/day$) [15]. In Ciudad Valles, the yearly average insolation is 4.7 ($kWh/m^2/day$) [16], and rainfall is approximately 4.88 days per month [17]. Rainfall typically entails cloudy climates, and therefore reduces the amount of sunlight. The relatively high insolation value and low rainfall frequency in the Ciudad Valles region further supports the implementation of a solar power system as opposed to other renewable energy systems.

Based on the latitude of the Ciudad Valles region (~22^o north), solar panels should be installed at an inclination angle of about 22^o facing south in order to maximize energy collection.

As mentioned previously, the basic power needs of people living in the rural communities were determined after several meetings with Ciudad Valles municipality officials. The authors were asked to devise small- to medium-size solar power system configurations capable of powering a mobile clinic, a house, a two-classroom school, and a community center. Detailed information regarding the various electric loads to be powered along with the total power requirement for each of the four different energy consumption scenarios are summarized in Tables 1–4. The mobile clinic (Table 1) is equipped with a small refrigerator (50 W) to store medicines and vaccines, a satellite phone for emergencies, a laptop to keep track of patient medical records, and an 18 W light. The house (Table 2) is intended to model a two-room home, and contains a small refrigerator running continuously, a ceiling fan and one light per room, and a radio. The school (Table 3) is modeled after a modest elementary school with two classrooms and one office, each of which contains a fan and lights, one computer allocated per room with a shared printer, and a radio. Finally, the community center (Table 4), which is planned for the general use of the people living in the community, is made up of two large rooms and a bathroom and is equipped with two fans and five lights (one fan and two lights per large room, and one light in the bathroom), a satellite phone for emergencies, a television for entertainment, education, and information, a laptop computer, and a radio for recreation and information during emergencies. Note that the inverter that appears in all four tables is essential to the operation of the solar power system as it converts the DC voltage of the batteries into the AC voltage supplied by the wall outlets. The inverter is connected to the batteries at all times and it draws a small amount of current to power LED indicators and some other electronic components that dissipate energy. Furthermore, even though Tables 1–4 show the refrigerator operating only 12 h per day, it is in fact running continu-

TABLE 1: Mobile clinic energy consumption requirements (24 h basis)

Mobile clinic					
Item	**Quantity**	**Power per item [W]**	**Total power [W]**	**Period of operation [h/day]**	**Energy consumption [Wh]**
Light	1	18	18	4	72
Satellite phone	1	14	14	3	42
Laptop	1	45	45	4	180
Refrigerator	1	50	50	12	600
Inverter	1	4	4	24	96
Total power requirements for the system					**990**

TABLE 2: House energy consumption requirements (24 h basis)

Mobile clinic					
Item	**Quantity**	**Power per item [W]**	**Total power [W]**	**Period of operation [h/day]**	**Energy consumption [Wh]**
Light	2	18	36	4	144
Fan	1	55	55	4	220
Radio	1	4	4	1	4
Refrigerator	1	50	50	12	600
Inverter	1	4	4	24	96
Total power requirements for the system					**1064**

ously but draws power only when the compressor turns on. It was determined through several battery discharge tests that the refrigerator draws power for 12 h per day as an average. The aforementioned result will be discussed further in a later part of this paper.

The information presented in Tables 1–4 was used to setup three solar power system configurations and establish a test plan aimed at verifying the four different energy consumption schemes. The three system configurations varied in the rated power of the solar panels utilized (250, 450, and 650 W), the energy capacity of the batteries (1243 Wh per pair of small batteries, and 4100 Wh per pair of large batteries), and the number of battery pairs used to store the energy (one or two pairs). In short, the objective of the experiments was to demonstrate that the devised solar power system configurations are capable of providing sufficient energy to power the mobile clinic, house, school, and community center with no interruption (except to conduct maintenance).

TABLE 3: School energy consumption requirements (24 h basis)

School (two classrooms + one office)					
Item	**Quantity**	**Power per item [W]**	**Total power [W]**	**Period of operation [h/day]**	**Energy consumption [Wh]**
Light	5	18	90	4	360
Laptop	3	45	135	2	270
Fan	3	55	165	4	660
Radio	1	4	4	2	8
Printer	1	15	15	2	30
Inverter	1	4	4	24	96
Total power requirements for the system					**1424**

TABLE 4: Community center energy consumption requirements (24 h basis)

Community center (two large rooms + one bathroom)					
Item	**Quantity**	**Power per item [W]**	**Total power [W]**	**Period of operation [h/day]**	**Energy consumption [Wh]**
Light	5	18	90	6	540
Satellite phone	1	14	14	3	42
Laptop	1	45	45	3	135
Fan	2	55	110	6	660
Radio	1	4	4	6	24
Television	2	90	180	3	540
Inverter	2	4	8	24	192
Total power requirements for the system					**2133**

For this paper, only the house energy consumption scenario was validated; however, by verifying the house configuration, the mobile clinic was validated as well, considering that the loads for both scenarios are very similar. Performance predictions for the school and community center system configurations based on the results obtained from the house scheme and the charging tests conducted utilizing the 650 W solar panels are also presented here.

3. EXPERIMENTAL TESTING

Several experiments were carried out in order to examine and quantify the performance of the solar power system set up at UTPA. The various tests were designed to obtain accurate estimates of the time required to charge and discharge deep-cycle batteries under several operating conditions and to perform a feasibility study on the house energy consumption scenario discussed previously. Eight experiments were chosen for inclusion in this paper. A brief description of these eight tests is given in Table 5, with details about each experiment to be provided in the following sections of this paper.

3.1 Experimental setup

The solar power system setup at UTPA is comprised of five PV solar panels (one 150 W panel, two 200 W panels, and two 50 W panels), a battery charge controller, six 12 V rechargeable deep-cycle batteries (four 74 Ah batteries and two 225 Ah batteries), and a 1500 W pure sine-wave inverter. A schematic diagram of the experimental setup is shown in Fig. 1, and a picture of the various components

TABLE 5: A summary of the eight experiments performed to quantify the performance of the solar power system setup at the University of Texas-Pan American (UTPA)

Test no.	Test type	Duration of test [h]	Battery set used	Test description
1	Charge	24	Set 1	Batteries were charged using the 250 W solar panels. [Partly cloudy day]
2	Charge	24	Set 2	Batteries were charged using the 250 W solar panels. [Clear sunny day]
3	Charge	24	Set 3	Batteries were charged using the 650 W solar panels. [Partly cloudy day]
4	Discharge	9.75	Set 1	Fully charged batteries were discharged utilizing a daily continuous power consumption rate of 2688 Wh/day
5	Discharge	10.9	Set 2	Fully charged batteries were discharged utilizing a daily continuous power consumption rate of 2688 Wh/day
6	Discharge	19.5	Set 2	Fully charged batteries were discharged utilizing a daily intermittent power consumption rate of 1884 Wh/day
7	Charge and discharge	24	Sets 1 and 2	Batteries were charged using the 250 W solar panels while being discharged utilizing a daily intermittent power consumption rate of 1884 Wh/day
8	Charge and discharge	192	Sets 1 and 2	Batteries were charged using the 250 W solar panels while being discharged utilizing a daily intermittent power consumption rate of 1064 Wh/day

utilized in the experimental testing along with a detailed description of these components is provided in Fig. 2 and Table 6, respectively.

The PV panels have the advantage of being capable of providing either 12 or 24 V, depending on the type of application sought; the 24 V configuration was utilized here. The solar panels were mounted on the roof of the engineering building at UTPA, facing south at a 26^{o} angle, corresponding to the latitude of Edinburg, TX. Two 175 ft, gauge eight cables were used to connect the solar panels to the charge controller located in the laboratory that housed the remaining components of the solar power system (see Fig. 2). A Morningstar TriStar TS-60 charge controller was connected in the system to regulate the incoming power from the solar panels. Four 12 V deep-cycle batteries rated at 74 Ah and two 225 Ah large batteries were utilized in this study. Note that these batteries were divided into three different sets: set 1 consisted of a pair of used deep-cycle batteries (2 years in service), set 2 was a pair of newly purchased deep-cycle batteries, and finally,

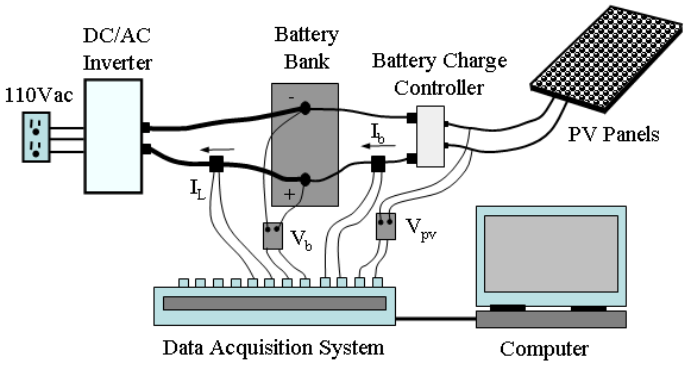

FIG. 1: A schematic diagram of the solar power system and instrumentation setup showing the locations of the current and voltage transducers used to monitor system performance

set 3 represents a pair of large batteries rated at 225 Ah. Each pair of the small batteries (74 Ah) was connected in series, providing 24 V and a maximum energy storage capacity of 1776 Wh; however, to avoid damaging the deep-cycle batteries, only 70% of this energy can be efficiently utilized. Therefore, only 1243 Wh of the energy stored in the batteries is available for usage. The pair of large batteries (225 Ah) was also connected in series to provide 24 V and a maximum energy storage capacity of 5400 Wh. In the case of the large batteries, 76% (4100 Wh) of

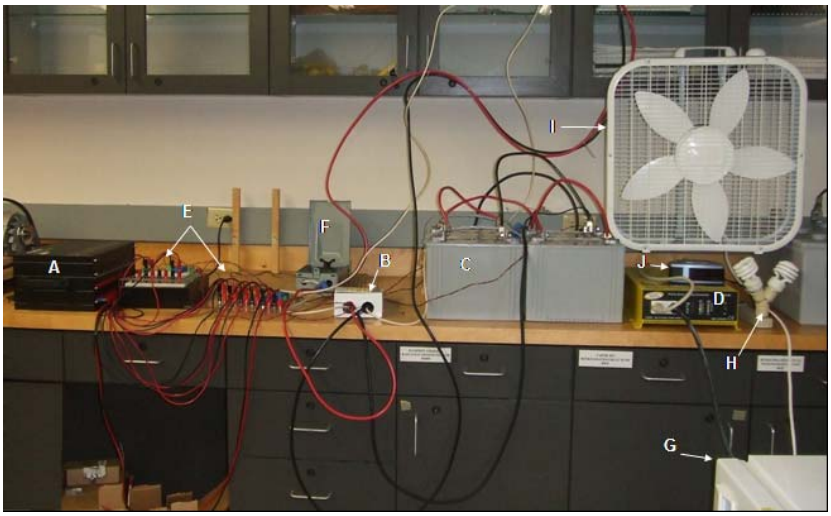

FIG. 2: A picture of the various components utilized in the experimental testing conducted at the University of Texas-Pan American (UTPA). A detailed description of the labeled components can be found in Table 6

TABLE 6: A list and description of the various components used in the experimental testing conducted at the University of Texas-Pan American (see Fig. 2)

Component (label in Fig. 2)	Quantity	Manufacturer/brand	Model no.	Specifications
Data acquisition system (A)	1	Omega Engineering	OMB-ChartScan-1400	Analog inputs ±10 V
Charge controller (B)	1	Morningstar Corporation	TriStar TS-60	12–48 V, 60 A
Deep-cycle batteries (C)	4	MK Powered	M24SLDG	Gel, 12 V, 74 Ah
Inverter DC/AC (D)	1	Go Power!	GP-SW1500-12	24 V, 1500 W
Switch box (F)	1	Cutler-Hammer	DPU222R	240 V, 60 A, one phase, two wires
Refrigerator (G)	1	Sanyo	SR-560W	120 V, 0.8 A, 60 Hz
Light bulbs (H)	2	Greenlite Energy Star	18W/ELS-M	18 W
20″ Box floor fan (I)	2	Galaxy	4733	110 W
Alarm clock radio (J)	1	RCA	RC05	4 W
Deep cycle batteries	2	Deka	8G24	Gel, 12 V, 225 Ah
50 W solar panels	2	GE Energy	GEPV-050-M	17.3 V, 2.9 A, 50 W
150 W solar panels	1	Photowatt	M-PW1650	24 V, 4.56 A, 150 W
200 W solar panels	2	BP Solar	SX3195B	24.4 V, 7.96 A, 195 W

the energy stored was available for usage. In order to convert the battery bank voltage to regular 110 VAC outlet power, the battery terminals were connected to a Go Power 1500 W pure sine-wave inverter.

The performance of the solar power system was quantified by continuously monitoring and recording the voltage and current at key locations (see Fig. 1) using a series of voltage and current transducers and a portable data acquisition system. Two voltage transducers were utilized: one to measure the voltage across the PV panels V_{PV} and another to measure the battery bank voltage V_b. The current in the system was monitored and recorded using two current transducers, one to measure the current flowing between the battery charger and the battery bank I_b and another to measure the current drawn by the electric loads I_L. The transducers along with carefully selected signal conditioning circuits converted the measured

voltages and currents into DC voltages in the 0–5 V range. This conversion was necessary to meet the data acquisition system limits and to eliminate potential electrical hazards.

An Omega Engineering OMB-ChartScan-1400 data acquisition system (DAQ) equipped with a 16-channel analog input card was used to acquire all data. The DAQ system software (ChartView) allows the user to control all aspects of the data acquisition process, as well as display the real-time data on-screen and save it in a spreadsheet for later analysis. In addition, the software was used to set specific conversion factors to every input channel to perform the required calibration. To calibrate the system, a multimeter and a clamp meter were used to verify the readings displayed on the computer, which allowed for the determination of proper conversion factors that were used to display the correct voltages and currents measured from the system.

3.2 Experimental Procedure

Numerous experiments were performed in which the selected battery bank was either charged, discharged, or simultaneously charged and discharged using different configurations of the solar panels and electric loads. The procedure followed for each of the three different types of tests is provided here.

3.2.1 *Charge Procedure*

The charging experiments were geared toward identifying the timeline required for charging the deep-cycle batteries under different daytime conditions, i.e., clear sunny, partly cloudy, and cloudy. The batteries were first inspected to ensure that they were discharged (down to 30% capacity for the 74 Ah batteries, and down to 24% capacity for the 225 Ah batteries) before starting the test. The data acquisition system was then turned on, and the ChartView software was initiated and set to acquire data at a sampling rate of 0.1 Hz. To maximize daylight utilization, all charging experiments were started before sunrise. Charging was complete when the voltage across the deep-cycle batteries reached 28 V, at which point the battery charge controller stopped current from flowing into the batteries to protect the batteries from damage caused by overcharging. Once the batteries were fully charged, the acquisition of data was terminated and a feature in the ChartView software converted the collected data into a suitable spreadsheet for later analysis.

3.2.2 *Discharge Procedure*

The purpose of the discharge experiments was to verify the discharge times under different electrical load conditions. To begin the discharge test, the batteries were first inspected to ensure that they were fully charged. The desired electric load(s) was connected to the inverter with the inverter turned off. The cutoff switch in-

stalled on the input side of the battery charge controller was turned off, eliminating any power input into the batteries from the solar panels. The data acquisition system was then turned on, and the ChartView software was initiated and set to acquire data at a sampling rate of 0.1 Hz. At this point the inverter was turned on, allowing power to flow from the batteries to the electric load(s). The inverter has a built-in safety feature that protects the batteries from excessive discharge. Therefore, data collection continued until the inverter cut off power to the load.

Different combinations of the following devices provided the various electrical loads used in the discharge experiments: a 100 W small refrigerator, four 18 W CFLs (compact fluorescent light bulbs), two 110 W floor fans, and a 4 W alarm clock radio (see Table 6 for a detailed description of these components). Note that some of these loads were used continuously and others intermittently in an attempt to recreate the conditions of a house environment, e.g., the lights were turned on during the night and not during the day, the fans were turned on during the warmest time of the day, and the refrigerator was filled with food and opened frequently to simulate normal operation. Furthermore, since the fans listed in Tables 2–4 are 55 W ceiling fans, the 110 W floor fans were operated for half the time shown in Tables 2–4 in order to achieve the same power consumption.

3.2.3 *Simultaneous Charge and Discharge Procedure*

The charge-discharge experiments represent the feasibility study conducted on the proposed house energy consumption scenario. For these tests, the experimental setup depicted in Figs. 1 and 2 was utilized with the 150 W panel and the two 50 W panels connected in series, providing a 250 W solar power system. Theoretical calculations validated by initial charge and discharge tests indicated that two pairs of 74 Ah batteries should be sufficient for the house energy consumption scenario. Therefore, battery sets 1 and 2 were employed and connected in parallel with the batteries in each set connected in series to provide the required 24 V. The latter step allowed for a larger battery bank capable of supplying up to 2486 Wh of energy. Note that in these tests the battery bank was charged during the day via the solar panels while simultaneously being discharged through a number of electrical loads.

The charge-discharge experiments started with the two sets of batteries fully charged. The data acquisition system was turned on, and the ChartView software was programmed to collect data at a sampling rate of 0.1 Hz. The electrical loads listed in Table 2 for the house scenario were then connected to the inverter and were activated throughout the day at scheduled times to simulate actual operating conditions. The periods of operation listed in Table 2 were followed as closely as possible. All tests were initiated before sunrise in order to maximize daylight utilization. The targeted duration for these tests was 8 days of continuous operation without completely discharging the batteries. Hence, a successful test is one for which the energy stored within the battery bank at the end of the eighth day is

more than sufficient to power the selected electrical loads the following day without fully discharging the batteries.

4. EXPERIMENTAL RESULTS

In this section, selected plots from the tests described in Table 5 are provided along with an explanation of the main features in these figures. In an effort to give the reader an overall synopsis of the results analyzed, the graphs presented here include all three types of tests conducted for this study, namely, charge experiments, discharge experiments, and simultaneous charge-discharge experiments.

4.1 Charge Experiments

As mentioned previously, the main objective of the charge experiments was to quantify the amount of energy that could be accumulated in a day using the available solar panels under different daytime conditions.

The data acquired from the first charge experiment (test 1) listed in Table 5 is plotted in Fig. 3. The plot gives the current flowing to the battery bank (I_b), the voltage across the solar panels (V_{PV}), and the power ($I_b \times V_{PV}$) obtained during charging using the 250 W solar panels. The condition of the day was partly cloudy, and the solar power system was able to collect 954 Wh of energy, which was stored in battery set 1 (the two 74 Ah used batteries). Figure 3 shows that the solar panels start accumulating power a little after 7 a.m., but significant power generation greater than 40 W does not begin until about 9 a.m., with peak power obtained around 1 p.m. Fluctuations in the power collected by the solar panels are caused by variations in the intensity of sunlight throughout the day and scattered clouds blocking the sun sporadically. An example of the latter is the large drop in power generation that occurred between 2 and 3 p.m. as a result of clouds obstructing the sunlight. The 30 minute duration of cloudy conditions at peak sunlight hours accounted for a substantial loss of power, approximately 110 W. Note that several significant power fluctuations ensued that afternoon, each caused by scattered clouds partially blocking the sun's rays.

A second charging experiment (test 2), plotted in Fig. 4, was carried out for a clear sunny day in which the 250 W solar panels were used to charge battery set 2 (the two 74 Ah new batteries). In sunny, clear-sky conditions, the solar power system accumulated approximately 1228 Wh of energy, a 28.7% (274 Wh) increase in energy collection from that of test 1 with partly cloudy day conditions. Figure 4 clearly shows the highest power accumulation occurring between the hours of 12 and 2 p.m., with power peaking at about 1 p.m. Furthermore, the numerous power fluctuations observed in Fig. 3 are nonexistent in Fig. 4, in which the power curve follows a smooth and symmetric bell-shaped profile centered at 1 p.m.

In test 3 the 650 W solar panels were used to charge battery set 3 (the two 225 Ah large batteries) during a day characterized by partly cloudy conditions in the

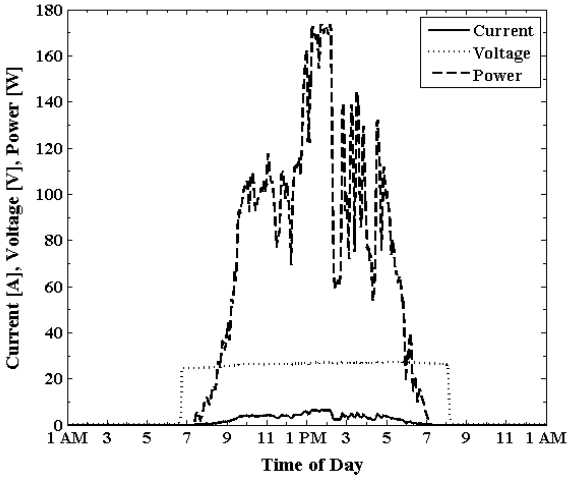

FIG. 3: A plot of the current (I_b), voltage (V_{PV}), and power ($I_b \times V_{PV}$) acquired from a charging experiment during a *partly cloudy* day using the 250 W solar panels. The total energy collected in this day was 954 Wh. The data in this plot is for test 1, listed in Table 5

morning hours and clear-sky conditions in the afternoon hours, as evident by the power profile of Fig. 5. Once again, significant power generation starts at around 9 a.m. and reaches a maximum a little after 1 p.m. Scattered clouds during the morning hours partially blocked the sunlight, which accounted for the lower solar power accumulation between the hours of 11 a.m. and 1 p.m. The total energy col-

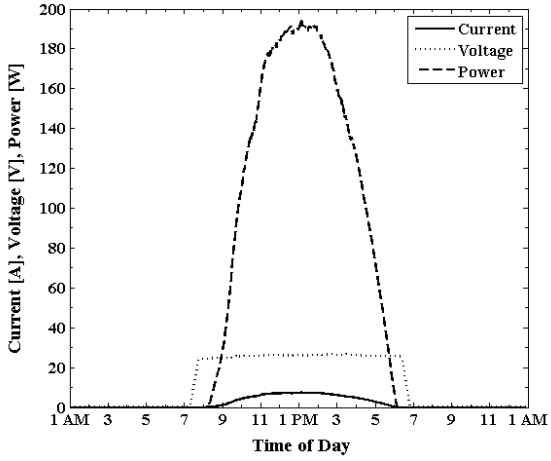

FIG. 4: A plot of the current (I_b), voltage (V_{PV}), and power ($I_b \times V_{PV}$) acquired from a charging experiment during a sunny day using the 250 W solar panels. The total energy collected in this day was 1228 Wh. The data in this plot is for test 2, listed in Table 5

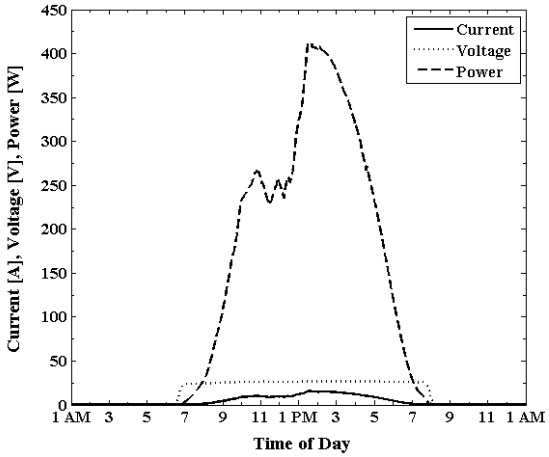

FIG. 5: A plot of the current (I_b), voltage (V_{PV}), and power ($I_b \times V_{PV}$) acquired from a charging experiment during a partly cloudy day using the 650 W solar panels. The total energy collected in this day was 2674 Wh. The data in this plot is from test 3, listed in Table 5.

lected in this day using the 650 W solar panels was 2674 Wh, which is almost half the maximum energy storage capacity of battery set 3 (5400 Wh).

A study of Figs. 3–5 shows that there are, on average, approximately 10 hours of charging time available in a typical day in Edinburg, TX. Furthermore, the 250 W solar panels produced a maximum power of 174 W and collected 954 Wh of total energy in a partly cloudy day, whereas the same solar panels provided a maximum power of 195 W and accumulated 1228 Wh of energy in a sunny day with clear skies. Based on the latter numbers and using an average value of 1091 Wh of energy collection per day, the 250 W solar panels can fully charge a pair of 74 Ah batteries in about 11.4 hours, which translates roughly to 1.2 days. Remember that even though the maximum energy storage capacity of the small battery set is 1776 Wh, only 1243 Wh of the energy stored in these batteries is available for use, which corresponds to the amount of energy that needs to be recharged. The 650 W solar panels produced a maximum power of 413 W and collected 2674 Wh of total energy during a partly cloudy day. The aforementioned implies that the 650 W solar panels can fully charge the large battery set (set 3) in 2 days, or equivalently, can fully charge the two small battery sets (sets 1 and 2) in only 1 day, even if parts of the day are cloudy.

4.2 Discharge Experiments

Before commencing the continuous operation testing of the solar power system, it was imperative to perform discharge experiments to establish a timeline for how long the battery sets can power the various electrical loads. The latter information

was used to estimate the duration of operation for the selected electrical loads for the house energy consumption scenario.

In tests 4 and 5 (see Table 5), the two small battery sets, sets 1 and 2, were discharged separately using a daily continuous power consumption rate of 2688 Wh/day produced by two 110 W floor fans operating for 5 hours, one 4 W clock radio operating for 1 hour, four 18 W lights operating for 4 hours, one 100 W refrigerator operating continuously, and one 4 W inverter operating continuously. Note that the refrigerator draws power only when the compressor is on, which was found to cycle on and off approximately every 32 minutes; hence the refrigerator only consumes power for 12 hours a day. The results of tests 4 and 5 indicate that the two 74 Ah battery sets 1 and 2 lasted 9.75 and 10.9 hours, respectively. The aforementioned implies that battery set 1 supplied 1092 Wh of total energy, while set 2 provided 1221 Wh of energy. Remembering that the pair of small batteries has 1243 Wh of energy available for use, it can be seen that battery set 2 discharged almost all (98%) of its available energy during the test, whereas battery set 1 discharged only 88% of its available energy. The latter can be explained by the fact that battery set 2 consists of two new deep-cycle batteries, while set 1 is a pair of batteries that have been in service for at least 2 years and have been charged and discharged numerous times, which has slightly reduced their efficiency.

Based on the findings of tests 4 and 5, it was decided that the power consumption rate of 2688 Wh/day was too large for the pair of 74 Ah batteries. Therefore, a daily intermittent consumption rate of 1884 Wh/day was utilized in test 6, generated by one 110 W floor fan operating for 4 hours, one 4 W clock radio operating for 1 hour, two 18 W lights operating for 4 hours, one 100 W refrigerator operating continuously, and one 4 W inverter operating continuously. The current supplied to the electric loads I_L and the voltage across the battery bank V_b during the discharge experiment is plotted in Fig. 6.

Figure 6 shows that the voltage across the battery bank starts at about 26 V and decreases as the batteries are being discharged. The ripples seen in the voltage profile correspond to the periods where the refrigerator compressor turns off, effectively decreasing the current drawn by the electric loads. The current curve resembles a periodic waveform caused by the refrigerator compressor that cycles on and off approximately every 32 minutes. The spikes in the current curve are due to the compressor requiring more power initially to reach steady-state operating conditions. During the first 4 hours of the test, the current drawn was high because all of the electric loads were turned on; after that, the refrigerator was the only appliance powered by the batteries. When the desired refrigerator temperature was reached, the compressor would turn off and the current drawn would drop to about 0.15 A, which corresponds to the current needed by the inverter to operate. It took 19.5 hours to fully discharge the batteries (set 2), at which point the voltage across the battery bank was down to 22.5 V and the inverter turned off power to protect the batteries from excessive discharge. Based on the results of test 6, it

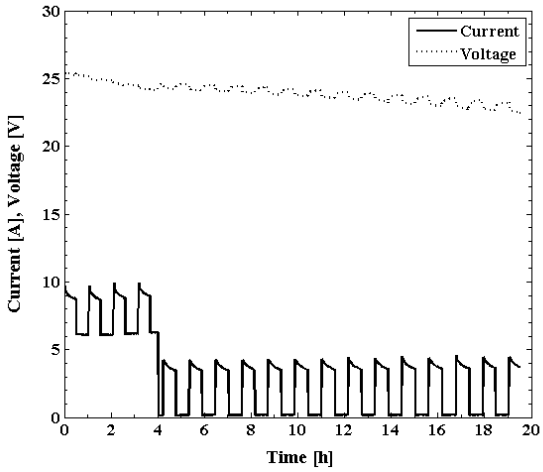

FIG. 6: A graph of the current supplied to the electric loads (I_L) and the voltage across the battery bank (V_b) during the discharge experiment of test 6. A daily intermittent consumption rate of 1884 Wh/day was used in this test.

was concluded that using only one set of small batteries will not be sufficient to maintain the intermittent consumption rate of 1884 Wh/day in the proposed week-long tests. Therefore, it was decided to use both sets of small batteries, sets 1 and 2, in the charge–discharge experiments.

Note that in Fig. 5, the starting voltage across the battery bank was 26 V, yet earlier in this paper it was mentioned that the deep-cycle batteries used in this study are fully charged when the voltage across the battery bank reaches 28 V. The aforementioned is an operational characteristic of these deep-cycle batteries. The voltage tends to drop from 28 to 26 V once the batteries are connected to the inverter. This does not imply any loss of energy, as evidenced by the results of test 5, for which 1221 Wh (98%) of the total available energy was discharged.

4.3 Charging-While-Discharging Experiments

The charging-while-discharging experiments are a proof-of-concept type of test in which the renewable solar power system devised at UTPA was used to run continuous operation experiments (week-long tests) to study the feasibility of using such systems to power small households in remote areas.

4.3.1 *One-Day Test*

The analysis of the data obtained from the separate charge and discharge experiments provided useful information that was used to plan the continuous operation tests. The discharge of battery set 2 in test 6 gave promising results, and it was assumed that adding another small battery set (set 1) to the battery bank would provide a system that can sustain a daily intermittent consumption rate of 1884

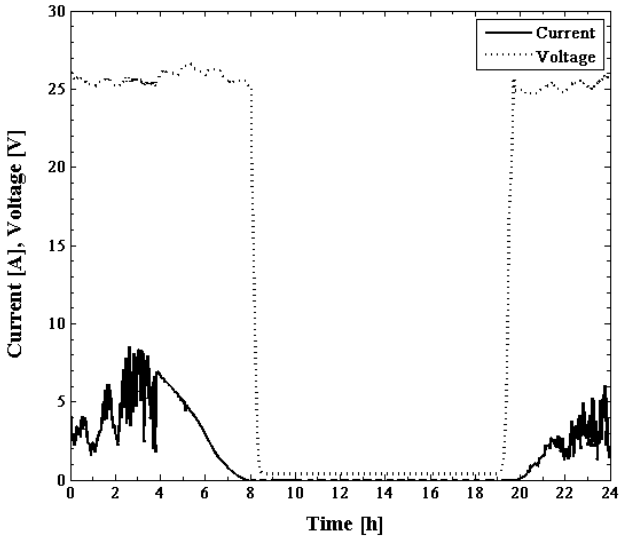

FIG. 7: A plot of the current delivered to the battery bank (I_b) and the voltage supplied by the 250 W solar panels (V_{PV}) during the 1 day charging-while-discharging experiment, test 7 (see Table 5). The total energy collected in this day was 978 Wh. The test was initiated at 12:45 p.m.

Wh/day continuously. However, before committing to a full-week test, it was decided to set up a 1-day charging-while-discharging experiment to ensure that our assumption was correct. With that in mind, test 7 was carried out with the results given in Fig. 7, which represents the current delivered to the battery bank I_b and the voltage supplied by the 250 W solar panels V_{PV} during the 24 hour test, and Fig. 8, which provides the current drawn by the electric loads I_L and the voltage across the battery bank V_b.

The 1-day charging-while-discharging experiment was started at 12:45 p.m. with the two sets of 74 Ah batteries, sets 1 and 2, fully charged. The batteries were simultaneously charged by the 250 W solar panels while being discharged using a daily intermittent consumption rate of 1884 Wh/day, similar to that used in the discharge experiment of test 6.

It can be seen from Fig. 7 in the current curve that the weather conditions were partly cloudy during the test, as evident by the current fluctuations. The current gradually decreased over several hours as the sun started to set, whereas the solar panel voltage dropped sharply over the twilight period and reached about zero at dusk. The current and voltage remained approximately zero over the night hours and started increasing again as the sun rose the next day.

As mentioned earlier, the discharge portion of test 7, plotted in Fig. 8, is very similar to the discharge experiment of test 6, as expected. However, unlike test 6, the batteries did not fully discharge at the end of the 24 hour experiment (test 7),

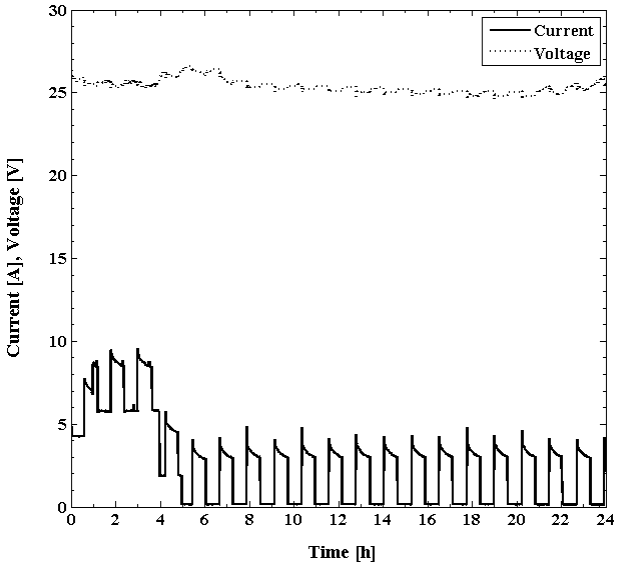

FIG. 8: A plot of the current drawn by the electric loads (I_L) and the voltage across the battery bank (V_b) during test 7. A daily intermittent consumption rate of 1884 Wh/day was utilized in this test. The experiment was started at 12:45 p.m.

as evident by the voltage across the battery bank V_b remaining above 24.8 V throughout the test. The current drawn from the batteries I_L varied based on the loads being powered. At the start of the test, the refrigerator, the radio, and the fan were on. One hour later, the radio was turned off and the lights were turned on, accounting for the rise in current drawn. The fans were turned off 3 hours later, which resulted in a decrease in the current drawn. An hour later the lights were turned off, leaving the refrigerator as the only appliance drawing current for the remainder of the test.

At the conclusion of test 7, the results acquired were analyzed and it was found that the total energy collected during this 24 h test was only 978 Wh, which implies that even with the two sets of 74 Ah batteries utilized, the 250 W solar panels will not be sufficient to provide a continuous operation at a daily intermittent consumption rate of 1884 Wh/day. Hence two solutions were considered: either use the 650 W solar panels with the two sets of small batteries, or reduce the daily intermittent consumption rate. The latter solution was chosen since cost was an important factor, and it was desired to keep the cost of the solar system that powers the mobile clinic and the house as low as possible. With that in mind and based on the results of tests 1 and 2 which indicate that the total energy collected per day in partly cloudy and sunny conditions is 954 and 1228 Wh, respectively, a daily intermittent consumption rate of 1064 Wh/day was selected to carry out the continuous operation experiments.

4.3.2 *Week-Long Test*

The week-long charging-while-discharging experiment was aimed at validating the house consumption scenario summarized in Table 2. The test was run using a daily intermittent consumption rate of 1064 Wh/day, which was produced by one 55 W ceiling fan operating for 4 hours, one 4 W radio operating for 1 hour, two 18 W lights operating for 4 hours, one 50 W refrigerator operating continuously (compressor on for ~12 h/day only), and one inverter running continuously. The week-long experiment (test 8) was started at 8:00 p.m. with both sets of 74 Ah batteries (sets 1 and 2) fully charged. The data acquired from test 8 are plotted in Fig. 9, which gives the current delivered to the battery bank I_b and the voltage supplied by the 250 W solar panels V_{PV} during the 192 hour (8 day) test, and Fig. 10, which provides the current drawn by the electric loads I_L and the voltage across the battery bank V_b.

Figure 9 shows that five out of the 8 days were characterized by unfavorable weather conditions (cloudy conditions), which resulted in low sunlight intensity and thus, low energy input from the solar panels. The latter becomes evident by observing the low current of day 1 and days 4–7, with the fifth and seventh days being the worst. Earlier in this paper it was pointed out that the yearly average rainfall in Ciudad Valles is approximately 4.88 days per month [17]. Hence it was decided to consider the week-long experiment (test 8) a worst-case scenario that simulates a week containing several consecutive cloudy days. To compensate for the days of low charging power, the electric load was reduced in those days to en-

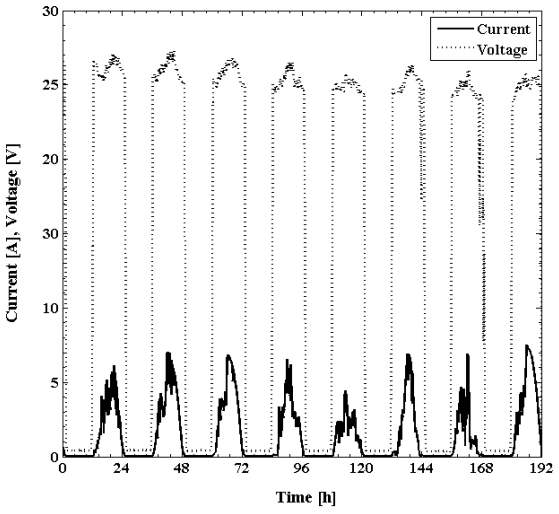

FIG. 9: A plot of the current delivered to the battery bank (I_b) and the voltage supplied by the 250 W solar panels (V_{PV}) during the 8 day charging-while-discharging experiment, test 8 (see Table 5). The test was initiated at 8:00 p.m.

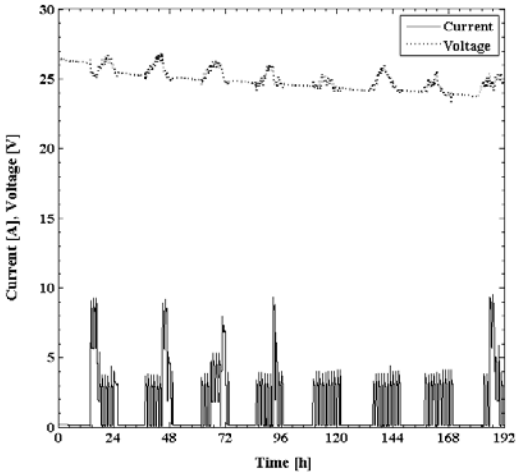

FIG. 10: A plot of the current drawn by the electric loads (I_L) and the voltage across the battery bank (V_b) during test 8. A daily intermittent consumption rate of 1064 Wh/day was used in this test. The experiment was started at 8:00 p.m.

sure that the test would be completed successfully. Therefore, all appliances other than the refrigerator were in operation for half of their proposed time on the fourth day, and on the fifth, sixth, and seventh day, all appliances were turned off except for the refrigerator. On days 1, 2, 3, and 8, the full electric load was used, as can be seen in Fig. 10. The values for the total energy collected in each of the 8 days are given in the following section accompanied with a detailed discussion.

In Fig. 10 it can be observed that the refrigerator ran for only 12 hours each day, even though it was stated earlier that it was in continuous operation. The latter can be explained by the fact that the house energy consumption scenario calls for a 50 W refrigerator running continuously; however, since the only refrigerator readily available was rated at 100 W, it was powered by the inverter from 8:00 a.m. to 8:00 p.m. (the time of highest demand), and switched to regular outlet power from 8:00 p.m. to 8:00 a.m. in order to keep the food from spoiling.

5. DISCUSSION OF RESULTS

The mathematical software MATLAB was used to plot all the graphs provided in this paper and conduct an analysis of the results. Utilizing a toolbox within this software, the area under the power curve can be calculated, which gives the total energy collected by the solar panels at any given day and the total energy consumed by the electric loads connected to the system's inverter. The power delivered by the solar panels was acquired by multiplying the voltage across the solar panels V_{PV} by the current flowing to the battery bank I_b, whereas the power used by the electric loads was obtained by multiplying the voltage across the battery

TABLE 7: A breakdown of the total energy supplied by the 250 W solar panels and the energy consumed by the electric loads for each of the 8 days in test 8

Day	Energy supplied by solar system [Wh]	Actual energy consumed by electric loads [Wh]	Actual energy remaining in batteries [Wh]	Theoretical energy consumed by electric loads [Wh]	Theoretical energy remaining in batteries [Wh]
1	831	934	2383	1064	2253
2	1111	977	2486	1064	2300
3	1102	972	2486	1064	2338
4	758	734	2486	1064	2032
5	527	526	2486	1064	1495
6	761	514	2486	1064	1192
7	505	518	2473	1064	633
8	1147	666	2486	1064	716

bank V_b by the current supplied to the inverter I_L. Table 7 provides a breakdown of the total energy supplied by the 250 W solar panels and the energy consumed by the electric loads for each of the eight days in test 8.

Examining the data shown in Table 7 reveals that 5 out of the 8 days had inadequate (less than the needed 1064 Wh) supply of energy to the battery bank, which is in agreement with Fig. 9. As previously mentioned, Ciudad Valles experiences approximately 5 days of rainfall per month, on average, indicating cloud cover during part or all of those days. Therefore, the week-long experiment (test 8) unintentionally simulated a worst-case-scenario week, incorporating 5 days of limited sunlight. The highest value of energy supplied by the 250 W solar panels in test 8 occurred on the eighth day and was equal to 1147 Wh of energy, which is approximately 76.5% of the maximum attainable theoretical value of 1500 Wh/day based on an insolation value of 4.0 kWh/m^2/day in South Texas, and a solar panel area of 2.5 m^2 performing at an efficiency of 15%. The Ciudad Valles region has a higher insolation value of 4.7 kWh/m^2/day, so the maximum possible energy collection in that area using the same solar panels would be about 1762 Wh/day. Hence, for a day similar to that of day 8 in test 8, where 76.5% of the maximum possible energy collection was attained, the energy collected in Ciudad Valles should measure about 1348 Wh, which is approximately 200 Wh of energy per day more than what was collected in this test. The foregoing discussion implies that the conditions in Ciudad Valles are even more favorable than in South Texas, so validation of the solar power system in South Texas signifies its feasibility in the Ciudad Valles region.

As discussed previously, in test 8 the actual energy consumed by the electric loads was adjusted to compensate for the days with low energy collection, as shown in Table 7 and corroborated in Fig. 10. Note that the actual energy consumed by the electric loads when operated as proposed in Table 2 differs from the theoretical energy consumption rate of 1064 Wh/day for two main reasons: first, the load from the refrigerator varies depending on usage, and second, the power requirements for each of the appliances has been rounded up, meaning that these appliances draw a little less power than what is stated. The actual energy remaining in the battery bank at the end of each day was calculated by subtracting 2486 Wh, which is the total energy available for usage in both battery sets (sets 1 and 2) that start off fully charged, from the actual energy consumed by the electric loads, and adding the energy supplied by the solar panels. For example, on the first day more energy was consumed than supplied; hence the remaining energy in the batteries dropped slightly. On the following day the energy supplied by the solar panels was more than the energy consumed by the electric loads, so the battery bank was fully recharged back to 2486 Wh. Remember that the battery charge controller does not permit any additional charging of the batteries past 100% to prevent damage to the batteries caused by overcharging.

By looking at the fourth column in Table 7, it can be seen that by reducing the amount of energy consumption in the days with low energy collection, the battery bank was allowed to recover and the actual energy stored in the batteries remained very close to fully charged conditions. However, in real application mode, it is not possible to regulate how people will use appliances on a cloudy day; thus, theoretical calculations were performed to ensure that the system would run continuously had the 1064 Wh/day consumption rate been used consistently during the worst-case-scenario week. The latter calculations are shown in columns five and six of Table 7, demonstrating that the solar power system would still be able to run continuously, even after 5 days of inadequate energy collection. Using the average value of the energy collection in days 2, 3, and 8 (which is 1120 Wh of energy) as the basis to calculate the amount of time required for the batteries to fully recover their initial charge of 2486 Wh, it would take about 30 days if the 1064 Wh/day consumption rate were consistently utilized. On the other hand, the energy reserve in the battery bank could be depleted if bad weather persisted, resulting in more days with low energy collection, assuming no efforts were made to reduce the amount of energy consumed per day. The aforementioned underscores the necessity of advance research to assess the expectations of the people that will use a renewable energy system, coupled with training designed to manage expectations when they take control of the system, including follow-up maintenance checks and continuing education to train users to understand, manage, and maintain their power system.

Based on the results of test 8, theoretical predictions for the school and community center energy consumption scenarios were carried out and are presented in Tables 8 and 9, respectively. The energy supplied by the 450 W solar panels was

calculated by multiplying the insolation of Ciudad Valles (4.7 kWh/m^2/day), times the total surface area of the solar panels that form the system (3.38 m^2), times the efficiency of the solar panels (15%), times the percentage of maximum possible energy collection discussed earlier in this section (76.5%), which gives a total energy of 1823 Wh/day. The energy supplied by the 650 W solar panels was obtained in a similar fashion using a total solar panel surface area of 5.31 m^2, which gives an energy collection value of 2864 Wh/day. The latter value seems reasonable considering that the energy collected in a partly cloudy day by the 650 W solar panels at UTPA in test 3 was equal to 2674 Wh. The theoretical energy consumed by the electric loads in Tables 8 and 9 was taken from Tables 3 and 4, respectively. To provide realistic predictions, four consecutive days were modeled as bad days, supplying only half the energy of a good day. The theoretical analysis demonstrates that both systems are capable of sustaining a continuous operation. Furthermore, it can be observed that it takes the system powering the school about 5 days to recover to fully charged battery bank condition, while the system powering the community center recovers in only 4 days.

Finally, a simple cost analysis was conducted to provide a basis of comparison for the three different size solar power systems devised at UTPA. The total cost, including all accessories and wiring, of the system developed for the house and mobile clinic, which consists of 250 W solar panels and two pairs of 74 Ah deep-cycle batteries, comes out to about $3000 per household or mobile clinic. The cost of the system designed for the school, which consists of 450 W solar panels and two pairs of 74 Ah deep-cycle batteries, is approximately $4500, and the cost of

TABLE 8: Theoretical predictions for the school energy consumption scenario utilizing a system consisting of 450 W solar panels and two sets of 74 Ah deep-cycle batteries

Day	Theoretical energy supplied by solar system [Wh]	Theoretical energy consumed by electric loads [Wh]	Theoretical energy remaining in batteries [Wh]
1	1823	1424	2486
2	1823	1424	2486
3	912	1424	1974
4	912	1424	1461
5	912	1424	949
6	912	1424	436
7	1823	1424	835
8	1823	1424	1234
9	1823	1424	1633
10	1823	1424	2032
11	1823	1424	2431

TABLE 9: Theoretical predictions for the community center energy consumption scenario using a system consisting of 650 W solar panels and one set of 225 Ah deep-cycle batteries

Day	Theoretical energy supplied by solar system [Wh]	Theoretical energy consumed by electric loads [Wh]	Theoretical energy remaining in batteries [Wh]
1	2864	2133	4100
2	2864	2133	4100
3	1432	2133	3399
4	1432	2133	2698
5	1432	2133	1997
6	1432	2133	1296
7	2864	2133	2027
8	2864	2133	2758
9	2864	2133	3489
10	2864	2133	4100
11	2864	2133	4100

the system developed for the community center, which consists of 650 W solar panels and one set of 225 Ah deep-cycle batteries, is roughly $8000. The cost estimate information given here along with the experimental results presented can be used to assess the feasibility of implementing these solar power systems in South Texas, in Ciudad Valles, and in any region with comparable weather conditions.

6. CONCLUSIONS AND FUTURE WORK

The main focus of the study presented in this paper was to provide an economical, efficient, and practical (i.e., feasible) design of a renewable energy system for isolated communities without any power grid. The design took into account human factors in culturally and educationally variable developing regions. This project was specifically applied to the outer, rural regions of the Municipality of Ciudad Valles, a 925 square mile county in the state of San Luis Potosi, Mexico.

The project assessed the feasibility of various sources of renewable energy. Ultimately, after an initial study of the region's topography, it was decided that an optimized solar energy system would be most suited to provide electricity for the residents of this developing region that live outside the power grid. Three different size solar systems were proposed to power four different energy consumption scenarios, namely, a mobile clinic, a two-room home, a two-classroom school, and a medium-size community center. A series of tests and experiments were conducted in an effort to evaluate and quantify the performance of the proposed energy systems. Analysis of the results indicates that proof of concept has been established.

The administration of Ciudad Valles plans to implement community support systems providing health care, education, and infrastructure for community meetings in the first phase of development. The plan includes a residence for on-site personnel to provide and coordinate services. A good deal of advance human factors planning went into this project. However, when implemented the proposed energy system will be studied to address unforeseen problems that will arise after local people take control of the system. During planning for the implementation phase, social scientists on the research team will study successful systems with an eye toward Bolivia, where coordination between centralized nongovernmental organizations (NGOs) and indigenous Aymara-speaking people has resulted in widespread adoption of sustainable, renewable energy systems from solar and water sources [18].

There are many alternative models, ranging from wholly commercial to grass roots NGOs, to provide the energy necessary to advance development in health, education, civic engagement and democratization, and economics in developing regions. The Ciudad Valles approach begins with governmental (Ciudad Valles Municipal Administration and Mexican Consulate) and institutional (UTPA) planning and research. The municipal government will lead the way in setting up an initial system for a rural community. However, by establishing an infrastructure to support local community education, training, and decision-making meetings, it is laying a foundation from which the community will eventually be able to take full ownership of its own renewable energy infrastructure, with the know-how to grow it for economic development. Rural Ciudad Valles is plagued with the negative local side of emigration; a large portion of adult males are absent from the local labor market and working in the United States due to lack of local jobs. In the media there is much discussion of the need for Mexico to develop its economy, but in the United States there is little understanding of the challenges this poses for a country with large, isolated indigenous populations that have no experience in their own communities with the energy infrastructure required to participate competitively in more than the impoverished local labor economy. Achieving regional, national, and global knowledge economy development in indigenous regions of Mexico will require multistaged, long-term planning to achieve success. Ciudad Valles and researchers at UTPA are approaching this project with that in mind. Consequently, future work will require building local technical and cultural support, which will include ongoing energy system and human factors data collection for improvement of the plan and its outcomes as it is implemented across the region. In the early stages, this will have to be managed by UTPA researchers and Ciudad Valles administrators, while local communities, educators, and entrepreneurs are identified and assisted in developing the skills needed to profitably sustain and grow the plan.

ACKNOWLEDGMENTS

The authors thank Hon. Romulo Garza, President of the Municipality of Ciudad Valles, Lic. Porfirio Ramos, and the entire municipality development team who

visited our campus several times to discuss plans and share information related to the energy needs of the people living in remote communities. This project was launched largely through the vision and planning of Ambassador Luis Lopez Moreno, former Consul of Mexico to McAllen, TX, and currently Mexico's Ambassador to Belize, and the work of his Deputy Consul, Alejandro Sousa y Brava, currently assigned to the European Union. We appreciate the support of former Provost Paul Sale, UTPA, and a small research grant from UTPA's Integrated Global Knowledge and Understanding Collaboration (IGkNU).

References

1. Lenius, J.M., Klein, S.A., and Beckman, W.A., Utilizing solar energy in mitigating CO_2 emissions, *Annual Meeting SOLAR 2002, American Solar Energy Society*, Reno, NV, June 15–20, 2002.
2. Energy and Engineering Technologies, What is photovoltaic power?, Retrieved Feb. 2009, from http://www.energtech.com/Information/.
3. National Renewable Energy Laboratory, Learning about renewable energy, Retrieved Feb. 2009, from http://www.nrel.gov/learning/re_photovoltaics.html.
4. Salameh, Z.M. and Davis, A.J., Case study of a residential-scale hybrid renewable energy power system in an urban setting, *Proc. of the 2003 IEEE Power Engineering Society Conf., General Meeting*, Vol. 4, pp. 2320–2322, 2003.
5. Mitchell, K., Nagrial, M., and Rizk, J., Simulation and optimization of renewable energy systems, *Int. J. Electr. Power Energy Syst.*, 27(3):177–188, 2005.
6. Ulleberg, O., The importance of control strategies in PV-hydrogen systems, *Solar Energy*, 76(1-3):323–329, 2004.
7. Chaparro, A., Soler, J., Escudero, M., De Ceballos, E., Wittstadt, U., and Daza, L., Data results and operational experience with a solar hydrogen system, *J. Power Sources*, 144(1):165–169, 2005.
8. Ibrahim, H., Ilinca, A., and Perron, J., Comparison and analysis of different energy storage techniques based on their performance index, *IEEE Electrical Power Conf.*, Montreal, Canada, 2007.
9. Duryea, S., Islam, S., and Lawrance, W., A battery management system for stand-alone photovoltaic energy systems, *IEEE Ind. Appl. Mag.*, 7(3):67–72, 2001.
10. Al Kalaani, Y., A solar system project to promote renewable energy education, *Proc. of the ASEE Annual Conf. and Exposition*, pp. 12857–12861, 2005.
11. Tarawneh, C., Vasquez, H., and Acosta, M.A., An experimental study of potential residential and commercial applications of small-scale solar power systems, *Proc. of the Annual ASEE-GSW Regional Conf.*, March 28–30, 2007.
12. Zahnd, A. and Kimber, H., Benefits from a renewable energy village electrification system, *Renewable Energy*, 34(2):362–368, 2009.
13. Ross, M., Hanley, C., Strachan, J., Plata, M.A., Xochipa, F., Ojinaga, L., Rovero, C., Cisneros, G., and Foster, R., Applying solar energy to extend distance education to remote communities in Mexico and Central America, *American Solar Energy Society*, Reno, NV, 2002.
14. Foster, R.E., Estrada, L., Colmenero, J., Ojinaga-Santana, L.M., and Ross, M., Utilizing photovoltaics to support distance education in the state of Chihuahua, Mexico, *American Solar Energy Society*, Paper A196, Austin, Texas, 2003.

15. Advanced Energy Group, Global Solar Power Map no. 3, *Southern North America, Mexico, and Northern South America*, Retrieved Oct. 3, 2007, from http://www.solar4power.com/map3-global-solar-power.html.
16. CONUEE, Irradiación global media en la República Mexicana, Retrieved Oct. 3, 2007, from http://www.conae.gob.mx/wb/CONAE/CONA_1433_irradiacion_en_la_re.
17. World Meteorological Organization, (2000) World Weather Information Service: Climatological Information San Luis Potosi, Retrieved Oct. 3, 2007, from http://www.world-weather.org/179/c01297.htm.
18. Suma-Jayma, Bolivian NGO, (2005) How We Work, Retrieved April 2009, from http://www.su-majayma.org/en/como-trabajamos/.

International Journal of Energy for a Clean Environment 9(1–4), 103–120, 2009

DIESEL EXHAUST EMISSION CONTROL BY SELECTIVE CATALYTIC REDUCTION OF NO_X WITH AMMONIA ON METAL/ZEOLITE CATALYSTS

M. L. M. Oliveira,[1] R. Moreno-Tost,[2] C. M. Silva,[1]*

T. L. Farias,[1] E. Rodríguez-Castellón,[2] & A. Jiménez-López[2]

[1]*IDMEC-Institute of Mechanical Engineering, Instituto Superior Técnico, Technical University of Lisbon, Av. Rovisco Pais, 1049-001, Lisbon, Portugal*

[2]*Universidad de Malaga, Departamento de Química Inorgánica — Campus Teatinos, 29071, Málaga, Spain*

[*]Address all correspondence to M. L. M. Oliveira, E-mail: monalisa@unifor.br

The heavy-duty diesel (HDD) and light-duty diesel (LDD) have been required to meet diesel emission standards that will become mandatory worldwide in the next few years (i.e., Euro 6 for Europe and Tier 2 for USA light-duty vehicles). Currently, selective catalytic reduction (SCR) of NO_x, with urea (commercially known as AdBlue) as a reducing agent, has been employed in the NO_x emission control of HDD. The commercial catalyst used is based on V_2O_5-WO_3-TiO_2, but the V_2O_5 must be replaced because of its toxicity. Catalysts based on metal-exchanged zeolite have been widely studied due to their high catalytic activity and stability for SCR-NO_x. The catalysts, based on the ZSM-5 zeolite (CuZSM5 and FeZSM5) and Cuban natural mordenite (CuMORD), have been prepared by a conventional ion-exchange method and tested in the SCR of NO_x with ammonia in presence of water vapor and SO_2. This paper deals with these experimental results and will exploit a neural network based on the approach to predict the NO conversion efficiency of a commercial catalyst and implement the derived mathematical function into a numerical model for diesel road vehicle simulation. Light-duty and heavy-duty vehicles are going to be simulated in both congested and noncongested roads to analyze the SCR system behavior in such conditions.

KEY WORDS: *diesel, vehicle, SCR-NO_x, NH_3, N_2O, catalysts, zeolites*

1. INTRODUCTION

The nitrogen oxides (NO_x) emitted from the exhaust gases of a diesel engine are usually composed of more than 90% NO. NO_x may cause the formation of ground-level ozone (in the presence of volatile organic compounds and solar light), contributes to the formation of acid rain, and moreover, the N_2O is responsible for

NOMENCLATURE

ANN	artificial neural network	MSE	mean square error
CATCO	commercial catalyst	NO_x	nitrogen oxides
CuMORD	catalyst based in the mordenite natural with copper	S_{BET}	surface area by Brunauer–Emmett–Teller method
CuZSM5	catalyst based in the ZSM5 zeolite with copper	SCR	selective catalytic reduction
FeZSM5	catalyst based in the ZSM5 zeolite with iron	$V_{micropore}$	micropore volume calculated using the Dubinin–Astakhov method
		ZSM5	Zeolite Socony Mobil

global warming and the destruction of stratospheric ozone (RIA, 2000). The selective catalytic reduction (SCR) is the after-treatment technology being adopted by the majority of heavy-duty diesel (HDD) manufacturers for meeting diesel emission standards that will become mandatory worldwide in the next few years (i.e., Euro 6 for Europe and Tier 2 for USA light-duty vehicles) (Colombo et al., 2010; Gabrielsson, 2004).

The concentration of NO_x in the flue gases is reduced by reacting with a reducing agent to convert NO_x into harmless nitrogen and water in the presence of a catalyst. This reaction requires a reducing agent like ammonia, hydrocarbons, CO, etc. For stationary sources, as this reaction takes place in an oxidant environment, ammonia is used as a reducing agent, due to its preferential selectivity for reacting with NO instead of oxygen in the range of temperatures of maximum conversion of NO to N_2. However, for mobile applications, urea is the preferred selective reducing agent due to safety and toxicity reasons. The solution contains 32.5 wt% urea and is named AdBlue® (Fulks et al., 2009). The dosed urea in the exhaust gases suffers the decomposition and hydrolysis to form ammonia (Birkhold et al., 2007). Therefore, in the surface of the catalyst, the main reaction taking place in the presence of oxygen is

$$4NH_3 + 4NO + O2 \rightarrow 4N_2 + 6H_3O. \quad (1)$$

On the other hand, the reaction rate with equimolar amounts of NO and NO_2 is much faster than that of the main reaction [Eq. (1)]. This reaction is catalyzed by catalysts based on vanadium as active phase:

$$NO + NO_2 + 2NH_3 \rightarrow 2N_2 + 3H_3O. \quad (2)$$

It has been clarified that the reaction in Eq. (2) occurs negligibly under the diluted conditions of exhaust gases. It has been concluded that nitrogen monoxide NO is the actual reactant in SCR and that oxygen does participate in the reaction.

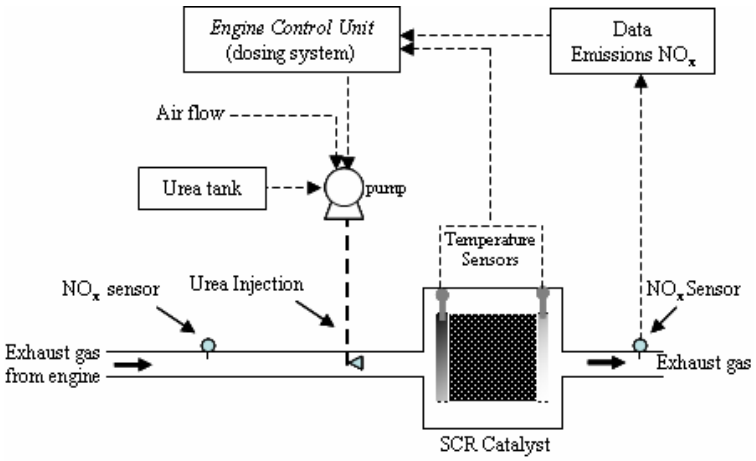

FIG. 1: SCR–NO_x system for diesel vehicles

The amount of NO_x in the exhaust of the engines before the SCR catalyst can be measured in a dynamometer-test bench using NO_x gas analyzers or be estimated by simulation codes. Figure 1 shows the SCR system for diesel vehicles. The most commonly used catalysts are based on the mixed oxides V_2O_5–WO_3–TiO_2 for the SCR of NO with ammonia (Djerad et al., 2006; Nova et al., 2006). These catalysts show a high NO conversion at low temperatures. However, at high temperatures (400°C), this catalyst has a tendency to form nitrous oxides (N_2O), a green house gas (Kobel et al., 2000). One of the possible reactions leading to nitrous oxide is

$$4NH_3 + 4NO + 3O_2 \rightarrow 4N_2O + 6H_2O \ . \tag{3}$$

At higher temperatures, ammonia may also be oxidized to NO, thus limiting the maximum NO_x conversion:

$$4NH_3 + 5O_2 \rightarrow 4NO + 6H_2O \ . \tag{4}$$

This shows that the use of these catalysts in oxidant environments is still an open area of investigation to prevent extra NO formation in diesel exhaust (Gense and Vermeulen, 2002).

Metal-exchanged zeolites are receiving much attention because they can operate in a wider temperature window and they do not contain toxic vanadium (Yahiro and Iwamoto, 2001). The ZSM5 and mordenite (MORD) zeolites are much more active than commercial vanadium catalysts in the SCR reaction. Moreover, the SCR activity was further improved by the presence of H_2O and SO_2 at high temperatures (350°C), which was attributed to an increase in surface activity due to the SO_2 oxidation (Moreno-Tost et al., 2004; Sjovall et al., 2006). The CuMORD

catalyst (synthetic) has not been studied as extensively as CuZSM5 catalysts, although it has also shown a high catalytic activity for NO reduction when hydrocarbons are used as reducing agents (Park et al., 2006). The catalysts based on natural mordenite have shown to be excellent catalysts for the SCR–NO_x using ammonia or methane as reducing agent but may suffer deactivation by water, SO_2, or HCl (Torres-Abreu et al., 1997). The FeZSM5 showed the highest SCR activity, and the selectivity to N_2 was 100% (Melián-Cabrera et al., 2006).

In the present work, two zeolites (natural Cuban mordenite and ZSM5) have been selected for the preparation of metal exchanged with Cu and Fe and tested as catalysts in the SCR of NO with ammonia. The catalyst stability was studied in the presence of H_2O and SO_2. Finally, a neural network based on the approach to predict the NO conversion efficiency of a commercial catalyst was implemented to derive and input a mathematical function into a numerical model for diesel road vehicle simulation. In this way, SCR system behavior was analyzed in different vehicle and roadway conditions.

2. EXPERIMENTAL

2.1 Catalyst Preparation

The catalysts were prepared by the ion-exchange method. The cationic exchange of copper was carried out by adding an aqueous solution of acetate of the corresponding cation (reagent grade 99.9%) to the fresh sample. Table 1 shows general parameters of the catalysts' synthesis. Finally, the catalysts were dried at 60°C and calcined at 550°C for 6 h with a 2°C min^{-1} heating rate. The details of the preparation method are described elsewhere (Qingjun, 2003; Morento-Toste et al., 2004; Oliveira et al., 2009a).

2.2 Catalyst Characterization

The chemical composition of the prepared catalyst was examined by atomic absorption (AA) techniques using a Peking-Elmer 3100 spectrometer. Powder x-ray diffraction (XRD) patterns were obtained with a Siemens D500 diffractometer, equipped with a graphite monochromator, and were using Cu K_α radiation. The XRD spectrum was recorded in the range $5^o < 2\theta < 50^o$ with a scanning speed of

TABLE 1: Synthesis conditions of the catalysts

Zeolite	Source	Si/Al molar ratio	Temperature (°C)/time	Metal (wt%)	Sample name
Natural Cuban mordenite	Palmarito deposit	5.0	Room/24 h	4.0	CuMORD
ZSM5	Zeolyst International Co.	20	Room/24 h	2.0	CuZSM5
		20	60°C/12 h	2.0	FeZSM5

TABLE 2: Textural parameters and metal content (wt%) of pristine zeolites and catalysts

Sample	Metal (wt%)	[a]S_{BET} ($m^2 \cdot g^{-1}$)	[b]$V_{micropore}$ ($cm^3 \cdot g^{-1}$)
ZSM5	–	285.9	0.159
MORD	–	166.6	0.085
Cu-ZSM5	1.98	239.9	0.124
Fe-ZSM5	2.12	240.7	0.120
CuMORD	4.01	178.2	0.089

[a]Specific surface areas from the BET equation ($0.05 \leq P/P^o \leq 0.35$).

[b]Determined by the Dubinin–Astakhov method, applied to microporous solids ($0.01 \leq P/P^o \leq 0.05$).

0.01 min^{-1}. The specific surface areas of the catalysts were determined by nitrogen adsorption at 77 K using a Micromeritics ASAP 2020 apparatus.

Table 2 shows the specific surface areas (S) and metallic loading (wt%) of the pristine zeolites and synthesized catalysts. The FeZSM5 and CuZSM5 catalysts show, as expected, a slight decrease in the specific surface area and in the pore volume in comparison with the ZSM5 zeolite. In contrast, the incorporation of copper into the mordenite hardly modifies the SBET and pore volume of the pristine mordenite, in spite of the higher metal loading.

Figure 2 shows the XRD patterns of the ZSM5 support and the Fe and Cu exchanged zeolite.

The catalysts prepared from ZSM5 zeolite display the typical diffraction patterns of the MFI zeotype. Moreover, we have not detected any diffraction lines of metallic oxides like α-Fe_2O_3 or any other iron oxide. This is also shown for CuZSM5

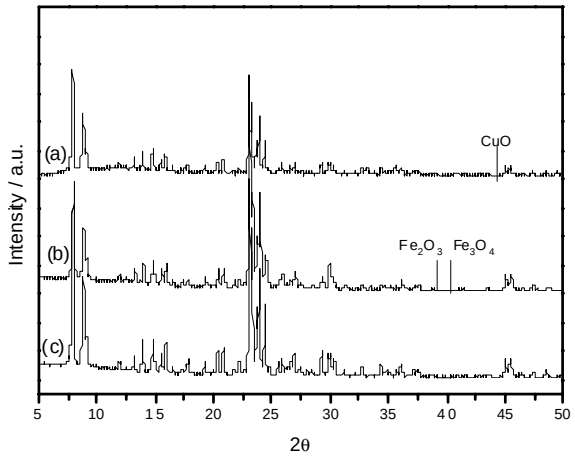

FIG. 2: XRD patterns of the zeolites: (a) CuZSM5, (b) FeZSM5, and (c) ZSM-5

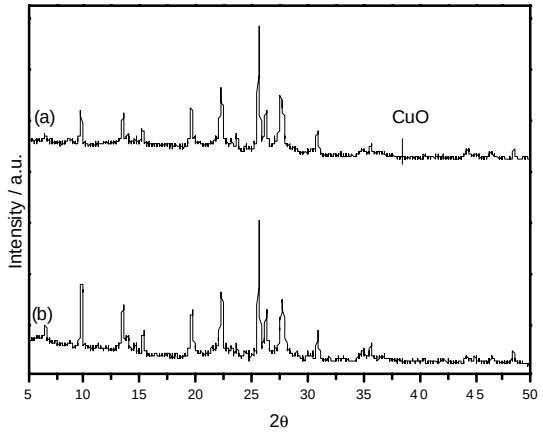

FIG. 3: XRD patterns of the zeolites: (a) CuMORD and (b) natural MORD

(copper oxides at $2\theta = 35.5^{o}$–39^{o}) (Kustova et al., 2006). However, the presence of these metallic oxide particles cannot be ruled out, since they could be present in an amorphous phase, or the particle sizes may not be large enough to be detected by XRD analysis.

Figure 3 shows the XRD pattern of natural mordenite and the copper-exchanged MORD. The incorporation of copper by the ion-exchange method does not provoke the loss of crystallinity of the pristine mordenite. Moreover, as in the case of ZSM5 catalysts, the presence of CuO is not observed.

2.3 Catalytic Activity Measurements

2.3.1 *SCR-NO_X Test Over Prepared Catalyst*

The catalyst activity of the prepared catalysts was tested in a flow microreactor consisting of a Pyrex glass reactor [0.27 in. outside diameter (o.d.)] connected on-line to a quadrupole mass spectrometer (Balzers GSB 300 02), as shown in Fig. 4.

The catalysts were pelletized with a particle size of 0.25–0.40 mm. About 150 mg of pelletized solids were set into a reactor and plugged with glass wool (Oliveira et al., 2009b). The catalysts' activities were compared with a $V_2O_5/WO_3/TiO_2$ commercial catalyst (CATCO). Before the catalytic runs, the catalysts were pretreated at 350^{o}C in situ for 3 h under a helium flow (30 $cm^3 \cdot min^{-1}$). The reaction mixture typically consisted of 1000 ppm NO, 1000 ppm NH_3, and 2.5 vol % O_2 (balance with He). For the water and SO_2 tolerance tests of the catalysts, 10% of H_2O and 50 ppm of SO_2 were employed, respectively, maintaining the composition of the feed and balance with He gas. The water was added by passing helium through a saturator with deionized water. The gas pipes were heated to 120^{o}C in order to prevent condensations in them. The flows were independently controlled by channel mass flow meters (Brooks brand). The system was operated at atmospheric

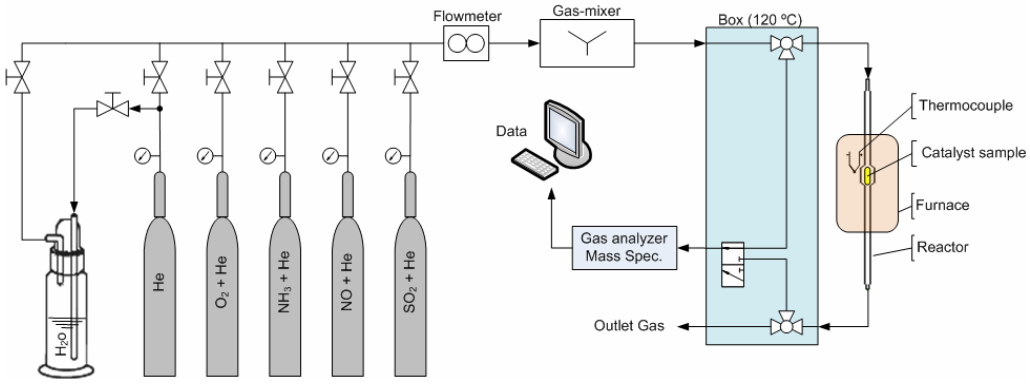

FIG. 4: Apparatus scheme

pressure, with a total flow of 150 $cm^3 \cdot min^{-1}$. The gas hourly space velocity (GHSV) was about 48.000 h^{-1}; under these conditions, both external and internal diffusional limitations were absent. The interval of temperature studied ranged between 100 and 550°C. The analysis of reactants and products (NO, NH_3, O_2, N_2, N_2O, H_2O, and SO_2) was monitored by using the mass spectrometer mentioned above.

2.4 Discussion

2.4.1 *Catalytic Performances*

Figure 5 shows the NO conversion versus temperature for the studied catalysts, including the CATCO catalyst as reference. The CATCO catalyst shows the highest activity, especially at low temperature, attaining the 100% NO conversion at 250°C.

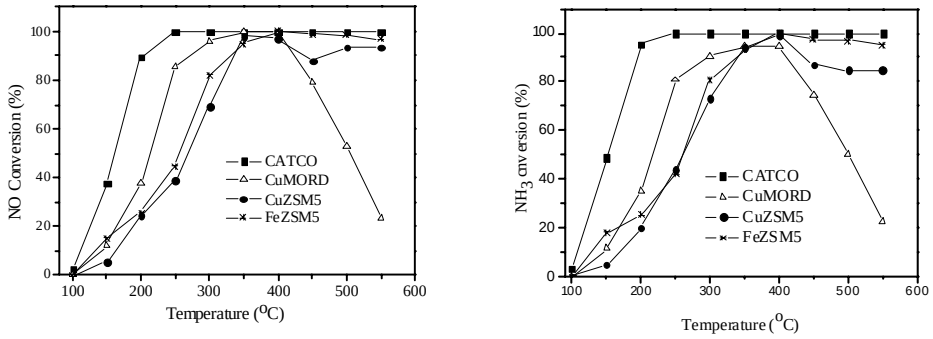

FIG. 5: NO and NH_3 conversion vs temperature of the tested catalysts. Experimental conditions: 1000 ppm NO, 1000 ppm NH_3, and 2.5% O_2 (balanced with He); flow rate 150 $cm^3 \cdot min^{-1}$ and GHSV = 48.000 h^{-1}.

The CuMORD catalyst shows the best catalytic performance at low temperature in the case of the catalysts based on ZSM5 and MORD zeolites, respectively. In any case, these catalysts based on zeolites attained 100% NO conversion at 350°C. The NO and NH_3 plots (see Fig. 5) exhibit a similar behavior with their conversions very close, so all ammonia molecules react with NO according to the reaction in Eq. (1). While the catalysts based on the ZSM5 zeolite maintain the NO conversion at temperatures higher than 350°C, the CuMORD catalyst shows a strong decrease of NO and NH_3 conversion. This different catalytic behavior between catalysts based on ZSM5 and mordenite zeolites may be related to the Si/Al ratio and the zeotype.

Water and SO_2 are present in real diesel exhaust gas; therefore, the effect on catalytic activity must be taken into account. This effect on catalysts was studied at 350°C for 10 hours, adding 10 vol % of H_2O in the feed and 50 ppm of SO_2.

Figures 6 and 7 show the NO conversion at 350°C in the presence of H_2O and SO_2, respectively. The catalytic performance in atmospheres without steam and SO_2 exhibited a 100% NO conversion for the CATCO and CuMORD catalysts, 98.1% for the CuZSM5 catalyst, and 95% for the FeZSM5 catalyst at 350°C.

The CuMORD did not show deactivation in the presence of H_2O and SO_2. The catalysts based on the ZSM5 zeolite show a slight decrease (around 20%) in catalyst activity in the presence of the SO_2. The presence of 10 vol % water vapor in the feed caused the deactivation of the CuZSM5 catalyst and a slight decrease in the selectivity toward nitrogen (Qingjun, 2003; Melián-cabrera et al., 2006). Table 3 shows a summary of the experimental results for the tested catalysts. The studied catalysts show an almost negligible formation of N_2O in the whole range of assayed temperatures. In fact, the CuMORD catalyst does not show any forma-

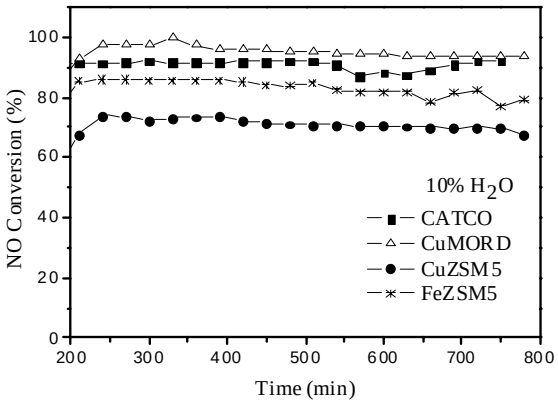

FIG. 6: Water tolerance of tested catalysts at 350°C. Gas composition: 1000 ppm NO, NH_3 1000 ppm, and 2.5% O_2, 10 vol % H_2O (balance with He), flow rate 150 ml·min^{-1}, and SV = 48.000 h^{-1}.

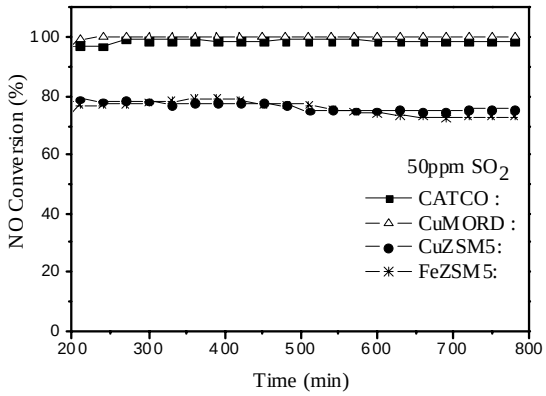

FIG. 7: NO conversion vs time for tested catalysts at 350°C in presence of 50 ppm SO_2. Gas composition: 1000 ppm NO, NH_3 1000 ppm, and 2.5% O_2, 50 ppm SO_2 (balance with He), flow rate 150 ml·min^{-1} and SV = 48.000 h^{-1}.

tion of N_2O. The presence of N_2O could be due to the nonselective reaction of NO with ammonia to yield N_2O [Eq. (3)], since the plots of NO and NH_3 conversion (Fig. 5) follow a similar behavior. The CuMORD catalyst shows the highest N_2 selectivity (100%). Some authors reported that the copper(II) ions seem to be

TABLE 3: Catalytic data[a]

Catalyst		Tb (°C)	NO conversion (%)	NH_3 conversion (%)	N_2O formation (ppm)	N2 selectivity (%)
CATCO	Standard	350	100	100	32.0	97.0
	H_2O	350	91.8	92.4	65.0	93.0
	SO_2	350	99.2	97.6	43.0	91.0
CuMORD	Standard	350	100	94.3	0.00	100
	H_2O	350	99.6	100	0.00	100
	SO_2	350	100	100	0.00	100
CuZSM5	Standard	350	98.1	94.0	47.0	95.1
	H_2O	350	73.8	72.6	41.0	94.6
	SO_2	350	78.9	77.9	0.00	100
FeZSM5	Standard	350	95.0	93.5	64.0	93.5
	H_2O	350	85.9	91.2	21.0	97.6
	SO_2	350	79.2	81.3	0.00	100

[a]Feed conditions general (standard test and stability): 1000 ppm NO, 1000 ppm NH_3, 2.5% v/v O_2 balance with helium; flow rate = 150 ml·min^{-1}, 0.150 g catalyst, and SV = 48.000 h^{-1}
[b]Temperature medium at which the catalysts reach their highest conversion.

present in a structural configuration where the formation of a Cu-H_2O complex on the catalyst surface is difficult; consequently, this catalyst does not suffer deactivation by water (Moreno-Tost et al., 2004; Chung et al., 2000).

3. NEURAL NETWORK APPROACH

The neural network approach has been successfully applied predictively in various fields of chemistry, such as structure-activity relationships. The usual models for catalytic converters are based on the fundamental finite difference 1D [i.e., three-way catalytic converters in Silva et al. (2006b)] or 1D + 1D with fundamental and improved kinetics models for SCR, as in Tronconi et al. (2005). Such models are well suited for replicating test bench analysis. However, these kinds of models are not suitable for integration with an energy and emissions road vehicle simulator, due to the detailed information required on the catalytic device, and because such kinds of energy and emission models usually require a converter efficiency curve as a function of temperature, as in Wipke et al. (1999) and Silva et al. (2006c). In order to build such a curve, the authors adopted an artificial neural network (ANN) model with fast convergence.

The measured results obtained from the experimental apparatus for commercial catalysts described above were used to train an ANN. The main goal is to obtain the bias and weights for each neuron and the activation functions for hidden and output layers with the lowest mean squared error (MSE). Of the data gathered, 15% was not used to train the ANN but was used instead of testing. The best ANN will be used to construct the correlation function between the inputs and outputs and will be integrated in a road vehicle fuel consumption and emission model.

3.1 Model

The relevant inputs considered for the outputs NO_x conversion efficiency, NH_3 conversion efficiency, and N_2O formation were space velocity (SV), exhaust gases temperature (T, ^{o}C), oxygen concentration (O_2), water concentration (H_2O), sulfur dioxide concentration (SO_2), nitrogen oxide concentration (NO), and ammonia concentration (NH_3).

Figure 8 schematically shows an overview of the structural organization of the neural network used for the estimation of the catalytic activity for model SCR of the commercial catalyst.

ANN design is constituted by an input layer with seven neurons, a single hidden layer with three neurons, and one output layer with one neuron, for each output considered. A Stochastic back propagation with the Levenberg–Marquardt (L–M) algorithm (MatLab®) was used to train the network (Durán et al., 2005). The activation functions used are

$$f_0 = \log \text{ sig } (n) = \frac{1}{[1 + \exp(-n)]} . \quad (4)$$

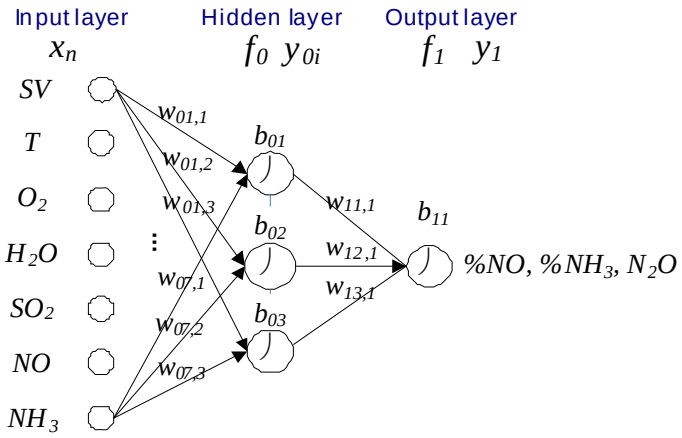

FIG. 8: ANN architecture of SCR model network

For the hidden layer and for the output layer,

$$f_1 = \tan \text{ sig } (n) = \frac{2}{[1 + \exp(-2n)] - 1} . \tag{5}$$

The derived correlation for the ANN is

$$y_{0i} = \log \text{ sig } (w_{0n,i} \times x_n + b_{0i}) , \tag{6}$$

$$y_1 = \tan \text{ sig } (w_{0i,1} \times y_{0i} + b_{11}) , \tag{7}$$

and

$$\%\text{NO},\%\text{NH}_3,\text{N}_2\text{O} = \tan \text{ sig } (w_{0i,1} \times \log \text{ sig } (w_{0n,i} \times x_n + b_{0i}) + b_{11}) . \tag{8}$$

Different weights and biases are generated for each different output (y_1) (Oliveira et al., 2009). For example, the mathematical correlation that describes the NO conversion efficiency for CATCO by using the ANN approach is the following: tan sig [log sig (–0.28SV – 0.02T – 0.05O_2 – 0.74H_2O + 1.44SO_2 – 0.57NO – 0.06NH_3 + 19.66) × (–1.83) + log sig (1.09SV – 0.32T + 5.42O_2 – 0.20H_2O + 0.10SO_2 + 5.34NO + 0.06NH_3 + 2.17) × (21.47) + log sig (0.00SV – 36.27T + 2.99O_2 – 1.56H_2O – 27.05SO_2 – 2.87NO + 1.37NH_3 – 1.91) × (51.75) – 23.61].

This result is between –1 and 1, but it is the converter to NO conversion efficiency values using the correspondence –1 equivalent to 0% and 1 equivalent to 100%. All mathematical correlations derived from the ANN application were used in a road vehicle simulator exhaust after-treatment module. The resulting application was capable of predicting the NO_x conversion efficiency (%), the NO_x out

emissions, the NH_3 emissions, and the N_2O emissions (in ppm, g/s, g/km, or g/kWh) for several driving conditions, including the standard ones.

3.2 Validation of the Artificial Neural Network Solution

A total of 600 sets of measurements were performed, and 85% of that data was used to train and to validate several networks. The networks with a low sum squared error were used to obtain the correlation function between the inputs and outputs. The weights and biases for each network are presented for the CATCO catalyst in Table 4. Of the data points measured (from the database), 15% were used to test the SCR ANN model. Mean absolute errors are given in the same table.

The ANN developed in the present study is constituted of a single hidden layer containing three neurons, which proved to be the best solution for the application of an input layer with seven inputs and one output layer with one neuron. A stochastic back propagation with the L-M algorithm was used to train the network. This algorithm is a trust region-based method with a hyperpherical trust region. This method has proved to be extremely viable in practice and is considered to be the most efficient algorithm in the training of median sized artificial neural networks (Morgan and Scofield, 1991). The ANN's mean and absolute output errors for all catalysts and for all the emissions/species simulated (NO_x emissions, NH_3 slip, and N_2O formation) are also presented in Table 4, and the neural networks used (see Fig. 9) were chosen according to a minimum error values approach. The first column shows the weights for each neuron in the hidden layer. The first seven values are for bias b01, the other seven are for b02, and so forth (see Eqs. 6 and 7). The first column of the output layer shows the weights for the output layer

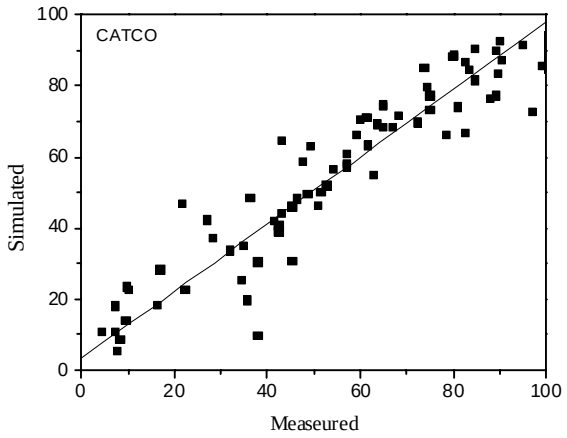

FIG. 9: Simulated and measured data for the test values of NO conversion efficiency for CATCO

TABLE 4: Parameters for the neural network for the CATCO SCR system

Output (min-max)	Hidden layer		Output layer		Mean absolute error (train and validation)	Mean absolute error (test)
	Weights (1–7, for b01, b02, b03)	Biases (b01, b02, b03)	Weights (1–3, for b11)	Biases (b11)		
CATCO						
% conversion NO (0–100)	–0.28, –0.02					
	–0.05, –0.74					
	1.44, –0.57					
	–0.06, 1.09					
	–0.32, 5.42	19.66	–1.83			
	–0.20, 0.10	2.17	21.47	–23.61	10	8
	5.34, 0.06	–1.91	51.75			
	0.00, –36.27					
	2.99, –1.56					
	–27.05, –2.87					
	1.37					
% conversion NH_3 (0–100)	–0.17, –0.30					
	0.20, –2.10					
	4.56, 1.10					
	–1.19, 0.55					
	0.47, –0.16	–2.74	–19.87			
	8.25, 0.13	–32.67	0.97	40.46	10	10
	–0.32, –6.48	2.6	–41.64			
	0.22, 3.85					
	49.68, –3.33					
	–3.90, 34.37					
	3.44					
ppm N_2O (0–100)	0.02, –0.02					
	0.08, –0.10					
	–0.18, –11.01					
	0.01, –0.01					
	2.03, –5.65	–13.19	–157.38			
	6.44, 147.37	14.19	–155.04	155.24	3	3
	–11.58, 12.16	139.02	–110.76			
	220.84, –4.20					
	1.91, 674.46					
	3.20, –0.72					
	–667.48					

neuron — 1 to 3 corresponds with b01 to b03 (see Eq. 8). Figure 9 shows the simulated and measured data for NO conversion efficiency.

4. SCR EQUIPPED DIESEL VEHICLE SIMULATION

The best function that describes the measured results was used to model the SCR system for typical European light-duty (1050 kg, 1.7 liters, 60 kW) and heavy-duty (18,000 kg, 10 liters, 173 kW) road vehicles. This model was integrated with a road vehicle fuel consumption and emissions model (Silva et al., 2006a). The FTP75 (bags 1 and 2, see Fig. 10) (Celik and Arcakliglu, 2005) was used to see the potential of SCR to reduce NO_x levels. The SCR system was fitted to the vehicles, resulting in an SCR with 3 liters for the light-duty vehicle and an SCR with 15 liters for the heavy-duty vehicle (see Fig. 11).

The SCR model simulated a maximum, average, and minimum conversion efficiency of 99, 92, and 36% for NO, and 99, 94, and 60% for NH_3 for the light-duty vehicle, as shown in Figs. 12 and 13.

For the heavy-duty vehicle the same values are, respectively, 99, 83, and 15% for NO, and 99, 84, and 35% for NH_3, as shown in Figs. 12 and 13. N_2O formation can reach 100 ppm. NO conversion and NH_3 slippage are consistent with the literature data for heavy-duty vehicles. Lenaers and Van Poppel (2005) experimented with an SCR mounted in a real bus and measured an average NO_x conversion efficiency of 85% and a maximum 30 ppm NH_3 slippage (average 10 ppm).

In this study, no N_2O was measured (see Fig. 10). Data for N_2O was found for isolated SCR systems that are not mounted on real vehicles. Oak Ridge National Laboratory (Sluder et al., 2004) data and Korea Advanced Institute of Science and Technology (Goo et al., 2007) found N_2O emissions in the commercial catalyst below 100 and 30 ppm, respectively. No results for light-duty vehicles were found in the literature.

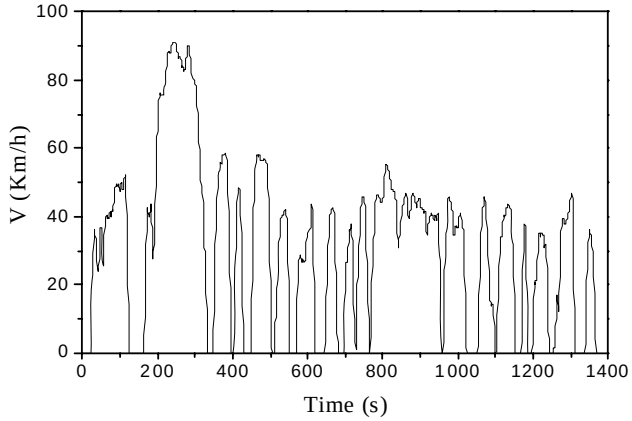

FIG. 10: N_2O formation, for the light-duty (left) and heavy-duty vehicles (right)

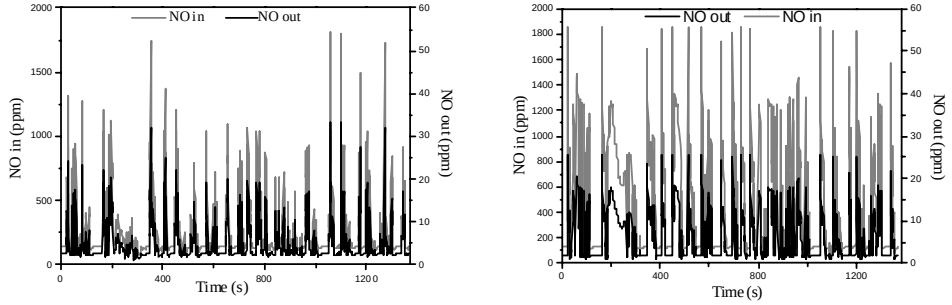

FIG. 11: Drive cycle used for simulations (average speed 32 km/h, distance 12 km)

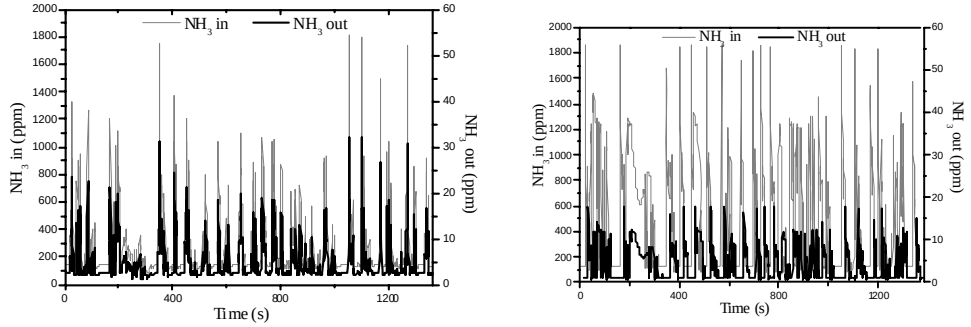

FIG. 12: NO_x emissions before and after the SCR system, for the light-duty (left) and heavy-duty vehicles (right)

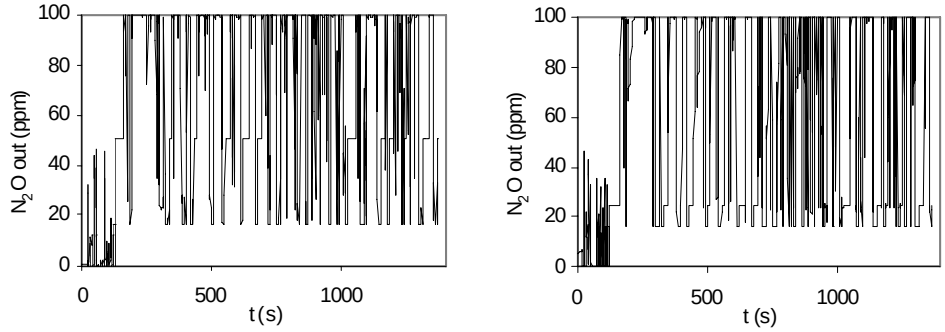

FIG. 13: NH_3 concentration before and after the SCR system, for the light-duty (left) and heavy-duty vehicles (right)

5. CONCLUSIONS

The aim of this paper was to show the viability of using alternatives to toxic-vanadium-based SCR. Taking into account the above results, it can be concluded that metal-exchanged zeolites are efficient catalysts for the SCR of NO by NH_3 in an excess of O_2, since they are very active, displaying conversions of 95%, and do not result in the formation of N_2O. The CuMORD catalyst is water tolerant, maintaining high NO conversion values in the presence of 50 ppm of SO_2. Thus, the CuMORD catalyst could be a competitive catalyst for the current application of SCR-urea technology to light- and heavy-duty diesel vehicles. Additionally, the possibility of using neural network model simulation for improving the performance of SCR systems and the inclusion of energy and emissions diesel vehicle simulators were tested. The results also show that the neural network produces results based on the experimental data which are, on average, consistent with literature and real measurements. In the future, the number of neurons in the hidden layer and the activation functions of hidden and output layers will be changed to analyze some better possible ANN configurations.

ACKNOWLEDGMENTS

The authors acknowledge the National Council for Scientific and Technological Development (CNPq), Brazil, for financial support in the form of a scholarship (GDE/CNPq), and Ministerio de Educación y Ciencia of Spain (project NAN2004-09267-C03-01). The authors acknowledge the National Science and Technology Foundation (FCT) through the national project POCI/ENR/57450/2004. C.M.S. is supported by a postdoctoral grant of the FCT, financed by the programs POCI 2010 and POS_C of the Third Framework Program, and by the national state budget attributed to the Ministry of Science, Technology, and Education.

REFERENCES

Birkhold, F., Meingast, U., Wassermann, P., and Deutschmann, O., Modeling and simulation of the injection of urea-water-solution for automotive SCR DeNO$_x$-systems, *Appl. Catal., B*, vol. 70, pp. 119–127, 2007.

Celik, V. and Arcakliglu, E., Performance maps of diesel energy, *Appl. Energy*, vol. 81, no. 3, pp. 247–259, 2005.

Chung, S.Y., Kim, B.S., Hong, S.B., Nam, I., and Kim, Y.G., Effect of Si/Al ratio of mordenite and ZSM-5 type zeolite catalysts on studies in hydrothermal stability for NO reduction by hydrocarbons, *Stud. Surf. Sci. Catal.*, vol. 130, pp. 1511–1516, 2000.

Colombo, M., Nova, I., and Tronconi, E., A comparative study of the NH_3-SCR reactions over a Cu-zeolite and a Fe-zeolite catalyst, *Catal. Today*, vol. 151, pp. 223–230, 2010.

Djerad, S., Crocoll, M., Kureti, S., Tifouti, L., and Weisweiler, W., Effect of oxygen concentration on the NO_x reduction V_2O_5-WO_3/TiO_2 catalyst with ammonia over V, *Catal. Today*, vol. 113, no. 3–4, pp. 208–214, 2006.

Durán, A., Lapuerta, M., and Rodríguez-Fernández, J., Neural networks estimation of diesel particulate matter composition from transesterified waste oils blends, *Fuel*, vol. 84, no. 16, pp. 2080, 2005.

Fulks, G., Fisher, G.B., Rahmoeller, K., Wu, M.C., D'Herde, E., and Tan, J., Review of solid materials as alternative ammonia sources for lean NO_x reduction with SCR, SAE International, 2009-01-0907, 2009.

Gabrielsson, P.L.T., Urea-SCR in automotive applications, *Top. Catal*., vol. 28, no. 1–4, pp. 177–184, 2004.

Gense, N.J.L. and Vermeulen, R.J., *Report N_2O Formation in Vehicles Catalysts*, Organisatie, Nederlandse, 2002.

Goo, J.H., Irfan, M.F., Kim, S.D., and Hong, S.C., Effects of NO_2 and SO_2 on selective catalytic reduction of nitrogen oxides by ammonia, *Chemosphere*, vol. 67, no. 4, pp 718–723, 2007.

Kustova, M.Yu., Rasmussen, S.B., Kustov, A.L., Christensen, C.H., Direct NO decomposition over conventional and mesoporous Cu-ZSM5 and Cu-ZSM11 catalysts: Improved performance with hierarchical zeólitas, *Appl. Catal., B*, vol. 67, pp. 60–67, 2006.

Lenaers, G. and Van Poppel, M., On-board ammonia measurements for vehicles with recent emission control technology exemplified on a SCR equipped bus, *Proc. of the Eighth Int'l. Conf. on Energy for a Clean Environment — Clean Air*, Lisbon, Portugal, 2005.

Melián-Cabrera, I., Espinosa, S., Groen, J.C., Linden, B.v/d., Kapteijin, F., and Moulijn, J.A., Utilizing full-exchange of zeolite by alkaline leaching: Preparation of FeZSM5 and application in N_2O decomposition, *J. Catal.*, vol. 238, pp. 250–259, 2006.

Moreno-Tost, R., Santamaria-González, J., Rodriguez-Castellón, E., Jiménez-López, A., Autié, M., González, E., and De las Pozas, M., Selective catalytic reduction of nitric oxide by ammonia over Cu-exchanged Cuban natural zeólitas, *Appl. Catal., B*, vol. 50, pp. 279–288, 2004.

Morgan, D. and Scofield, C., *Neural Networks and Speech Processing*, Kluwer, Boston, MA, 1991.

Nova, I., Ciardelli, C., Tronconi, E., Chatterjee, D., and Bandl-Konrad, B., NH_3–NO/NO_2 chemistry over V-based catalysts and its role in the mechanism of the fast SCR reaction, *Catal. Today*, vol. 114, no. 1, pp. 3–12, 2006.

Oliveira, M.L.M., Silva, C.M., Moreno-Tost, R., Farias, T.L., Jiménez-López, A., and Rodriguez-Castellon, E., A study of copper-exchanged mordenite natural and ZSM-5 zeolites as SCR NO_x, *Appl. Catal., B*, vol. 88, no. 3–4, pp. 420–429, 2009a.

Oliveira, M.L.M., Silva, C.M., Moreno-Tost, R., Farias, T.L., Jiménez-López, A., and Rodriguez-Castellon, E., Simulation vehicles equipped with SCR using iron-zeolite catalysts, *Appl. Catal., A*, vol. 366, no. 1, pp. 13–21, 2009b.

Park, J., Park, H.J., Baik, J.H., Nam, I., Shin, C., Lee, J., Cho, B.K., and Oh, S.H., Hydrothermal stability of CuZSM5 catalyst in reducing NO by NH_3 for urea selective catalytic reduction process, *J. Catal*., vol. 240, no. 1, pp. 47–57, 2006.

Qingjun, Z., *Identification of Active Sites for N_2O Activation Over Iron Containing Pentasil Zeolites*, Technische Universiteit Eindhoven, 2003.

Regulatory Impact Analysis (RIA) Report, Control of Emissions of Air Pollution from HHDE, Environmental Protection Agency (EPA), U.S., 2000.

Silva, C.M., Farias, T.L., Costa, M., and Santos, H., Evaluation of SI engine exhaust gas emissions upstream and downstream of the catalytic converter, *Energy Convers. Manage*., vol. 47, no. 18–19, pp. 2811–2828, 2006c.

Silva, C.M., Farias, T.L., Frey, H.C., and Rouphail, N.M., Evaluation of numerical models for simulation of real-world hot-stabilized fuel consumption and emissions of gasoline light-duty vehicles, *Transp. Res. D*, vol. 11, no. 5, pp. 377–385, 2006b.

Silva, C.M., Goncalo, G.A., Farias, T.L., and Mendes-Lopes, J.M., A tank-to-wheel analysis tool for energy and emissions studies in road vehicles, *Sci. Total Environ*., vol. 367, no. 1, pp. 441–447, 2006a.

Sjovall, H., Fridell, E., Blint, R.J., and Olsson, L., Selective catalytic reduction of NO_x with NH_3 over Cu-ZSM-5 — The effect of changing the gas composition, *Appl. Catal., B*, vol. 64, pp. 180–188, 2006.

Sluder, S., Storey, J., Lewis, S., and Lewis, L., Urea decomposition and SCR performance at low temperature, *Proc. of the 10th Annual DEER Workshop*, Coronado, CA (Oak Ridge Laboratory data), 2004.

Torres-Abreu, C., Ribeiro, M.F., Heriques, C., and Ribeiro, F.R., Influence of cocation on catalytic of CuMORD catalysts for NOSCR by propene: Effect of water presence, *Catal. Lett.*, vol. 43, pp. 25–29, 1997.

Tronconi, E., Nova, I., Ciardelli, C., Chatterjee, D., Bandl-Konrad, B., and Burkhardt, T., Modelling of an SCR catalytic converter for diesel exhaust after treatment: Dynamic effects at low temperature, *Catal. Today*, vol. 105, no. 3-4, pp. 529–536, 2005.

Wipke, K., Cuddy, M., and Burch, S., ADVISOR 2.1: A user friendly advanced powertrain simulation using a combined backward/forward approach, *IEEE Trans. Veh. Technol*., vol. 48, no. 6, pp. 1751–1761, 1999.

Yahiro, H. and Iwamoto, M., Copper ion-exchanged zeolite catalysts in deNO_x reaction, *Appl. Catal., A*, vol. 222, no. 1–2, pp. 163–181, 2001.

International Journal of Energy for a Clean Environment, 10(1–4), 121–133, 2009

NO REDUCTION BY SELECTIVE NONCATALYTIC REDUCTION USING AMMONIA-EFFECTS OF ADDITIVES

D. Quang Dao, L. Gasnot, A. El Bakali, & J. F. Pauwels*

Physicochimie des Processus de Combustion et de l'Atmosphère (PC2A), UMR CNRS 8522, Université Lille 1 — Sciences et Technologies, 59655, Villeneuve d'Ascq Cedex, France

*Address all correspondence to L. Gasnot E-mail: laurent.gasnot@univ-lille1.fr

An experimental study of nitric oxide removal by selective noncatalytic reduction (SNCR) using ammonia as reducing agent has been performed in a semi-industrial reactor over the temperature range 973–1200 K. Several chemical compounds, such as CH_4, C_2H_4, C_2H_6, CH_3OH, C_2H_5OH, and CO, which are usually used in the literature as additives for the SNCR process, have been evaluated. As a result, very high efficiencies (up to 82%) have been achieved in our optimal experimental conditions with the classical SNCR process. The additives seem to make the NO reduction process more effective at lower temperatures. These additives induce a downward shift (up to more than 100 K) of the optimal temperature window for the reduction process, and a slight decrease of the maximum NO reduction level depending on the species and on the additive concentration. The additive utilization effectively decreases residual NH_3 emissions.

KEY WORDS: *selective noncatalytic reduction, SNCR, NO_x, removal, additives*

1. INTRODUCTION

Nitric oxides (NO_x), including nitric oxide (NO), nitrous oxide (N_2O), and nitrogen dioxide (NO_2), are one of the most important air pollutants generated from high-temperature combustion processes. NO_x have been drawing wide attention because of their particular environmental hazard and difficulty of reduction. Many technologies have been developed and commonly used to reduce the NO_x emissions. Among them, selective noncatalytic reduction (SNCR) technology is known to be a very promising technological approach because of its low investment cost and an interesting efficiency.

The SNCR process is an effective approach for NO_x reduction by injecting into flue gas specific nitrogenous species containing –NH– or –CN– functions such as ammonia (NH_3), urea [$(NH_2)_2CO$], or cyanuric acid [$(HNCO)_3$]. The NO_x reduction efficiency of the SNCR process is linked to various working parameters, such as the burnt gas temperature, gas residence time, the amount of reducing agent, initial

NO_x concentration, residual oxygen concentration in the flue gas, mixing conditions, and the additives. The SNCR process is characterized by a very narrow temperature window usually located in the 1123–1373 K range [1]. Below the lower limit of temperature (i.e., 1123 K), the initiation reactions are too slow to provide any NO_x reduction. For working temperatures higher than 1373 K, the oxidation phenomenon of reducing agents is dominant and leads to NO_x formation instead of reducing this pollutant. Nevertheless, this narrow and relatively high temperature interval may be widened and also lowered by additive effects. Several additives have been tested and evaluated in the literature, such as CO and H_2 [2], alkanes (CH_4, C_2H_6 and C_4H_{10}) [3], alcohols (CH_3OH, C_2H_5OH and $(CH_2OH)_2$) [4, 5], volatile organic compounds (C_6H_5OH and C_7H_8) [6], sodium compounds (Na_2CO_3, HCOONa, CH_3COONa, and $NaNO_3$) [7], or other additives (C_2H_4, C_2H_4O, CH_3CHO, CH_3NH_2, and pulverized coal) [5–8]. More recently, some works presented the effects of multicomponent gas additives, such as the combination of CO, H_2, and CH_4, on the SNCR process [9]. NO_x reduction efficiencies of up to 95% have been obtained in these studies.

The aim of this study is to evaluate the effects of additives on the SNCR process using ammonia as reducing agent in a semi-industrial reactor. The influence of the operating parameters on the efficiency of the reduction process was also determined.

2. EXPERIMENTAL SETUP

The experiments were performed in a semi-industrial reactor which consists of a 1.1 m long tube with inner diameter of 8 cm, as shown in Fig. 1.

The reactor is equipped with 13 accesses that allow temperature measurements and gas sampling. At the base of the reactor, a McKenna flat flame burner is used to generate the flue gas of known compositions and features. A methane–air flame seeded with known amounts of NO (1500 ppm) is stabilized on the burner at atmospheric pressure with a constant equivalence ratio (ϕ = 1.0). The main working parameters consist of a total gas flow rate of 805 $L{\cdot}h^{-1}$ and a gas residence time of 2.4 s. Five electric heaters are placed along the reactor in order to control the flue gas temperature in the 900–1200 K range. The temperature of the reactor wall is measured by 40 K-type thermocouples. The reducing agent mixture [NH_3/(additives)/N_2] is injected in flue gas by a specific device which consists in four water-cooled perforated tubes. This injection system is located 10 cm above the burner surface.

The amount of NH_3 injected as reducing agent is characterized by a parameter usually called normalized stoichiometric ratio (NSR) of the reducing agent ($[NH_3]/[NO]_0$). The NSR is fixed to a value of 5.0, which is the optimum point in the present experimental conditions. The NSR coefficient for the additive species ($[\text{additives}]/[NO]_0$) varies from 0 to 3 for CH_4, C_2H_4, C_2H_6, CH_3OH, C_2H_5OH, and CO. Gas sampling is performed by using a specific microprobe connected to

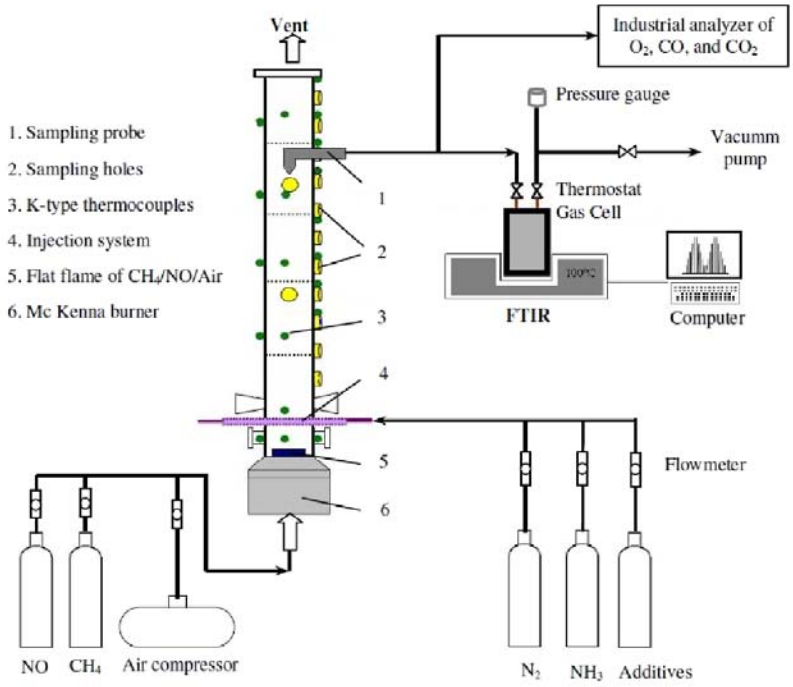

FIG. 1: Schematic diagram of the semi industrial reactor

an experimental setup that allows measurements by Fourier transformed infrared spectroscopy (FTIR). A warmed cell with a 10 m optical path is used to analyze the sampled gas. Chemical species such as NO, CO, CO_2, NH_3, and additives species, which play important roles in the process, have been measured.

The typical experimental configuration of the SNCR process studied in this work is summarized in Table 1.

Some previous experiments were performed to characterize the semi-industrial reactor used in this study. The objective of these experiments was notably to determine the axial flue gas temperature profiles in the reactor. These measurements were investigated by using a specific temperature probe which was constituted of two Pt/Pt-10%Rh thermocouples with different diameters, allowing a radiative loss correction of the measured temperatures.

The axial temperature profiles were measured for different setpoint values and are displayed in Fig. 2. The results showed that the shape of the temperature profiles was very similar for all the temperature setpoints, from 773 to 1173 K. From the height of 36 cm above the burner surface, the reactor can be considered as isothermal. This critical position corresponds to the 4th sampling access, as shown in Fig. 1.

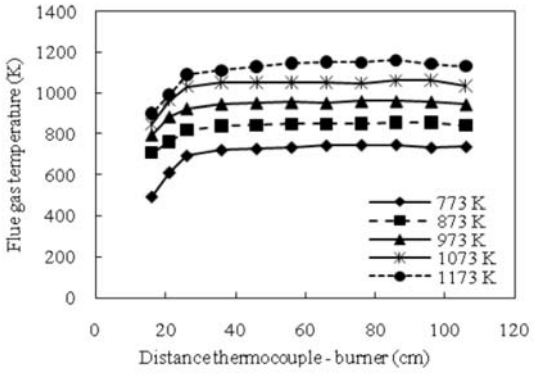

FIG. 2: Axial profiles of the flue gas temperature in the reactor for different setpoint values

TABLE 1: Experimental configuration

Working parameters	
Reducing agent mixture	NH_3/additive/N_2
Flue gas temperature range (K)	900–1200
Burner features	
Total flow rate ($L \cdot h^{-1}$)	745
Inlet air ($L \cdot h^{-1}$)	670
Inlet CH_4 ($L \cdot h^{-1}$)	74
Seeded NO ($L \cdot h^{-1}$)	1.1
Flame stoichiometry	1
Injectors features	
Total flow rate (NH_3 + additive + N_2) ($L \cdot h^{-1}$)	60
Injected NH_3 ($L \cdot h^{-1}$)	5.5
NSR ($[NH_3]/[NO]_0$)	5
NSR ($[additive]/[NO]_0$); (Additive: CH_4, C_2H_4, C_2H_6, CH_3OH, C_2H_5OH, CO)	0–3
Injected N_2 ($L \cdot h^{-1}$)	Balance
Initial NO concentration (ppm)	1370
Gas residence time (s)	2.4

3. RESULTS AND DISCUSSION

3.1 Ammonia Injection Without Additives

A parametric study of the classical SNCR process by using ammonia for the NO reduction has been performed in this work. The influence of several parameters, such as the flue gas temperature in the injection zone, the NSR of ammonia, the initial concentration of NO, and the gas residence time, has been studied.

The effect of the flue gas temperature on the residual NO concentration with various ratio of $[NH_3]/[NO]_0$ is presented in Fig. 3. As a result, a competition between the NO formation from the oxidation of NH_3 and the NO reduction process is observed over the experimental range of temperature from 873 to 1193 K. For a given molar ratio of $[NH_3]/[NO]_0$, the NO concentration increases when increasing the flue gas temperature from 873 to ~1073 K. In this temperature range, the NO evolution is observed by comparing the measured concentration with the initial NO level fixed to 1370 ppm. Further increase of flue gas temperature leads to a significant reduction of the residual NO concentration. As can be seen in Fig. 3, for a $[NH_3]/[NO]_0$ ratio of 5 and by increasing the temperature from 1073 K, the NO concentration decreases to reach a NO reduction efficiency near 80% at 1193 K.

Furthermore, the influence of the NSR of ammonia ($[NH_3]/[NO]_0$) on the NO reduction is also presented in Fig. 3. Three values of NSR (NSR = 1, 3, and 5) were tested. As a result, for each temperature the NO emission is found to decrease with the NSR value. The measurements clearly point out that the effect of the NSR parameter on the efficiency of the NO reduction process is more significant when a high value of NSR is used.

The kinetic mechanism involved in the SNCR process has been discussed in detail elsewhere [9–11]. The outlet NO concentration is dependent on the competition between NO consumption and NO production during the NH_3 oxidation. This competition mainly depends on both the flue gas temperature and the residual oxygen concentration. In a low-temperature range, the NO reduction kinetic scheme predominates and mainly involves the following reaction sequence:

$$NH_3 + OH \rightarrow NH_2 + H_2O \ , \qquad (1)$$

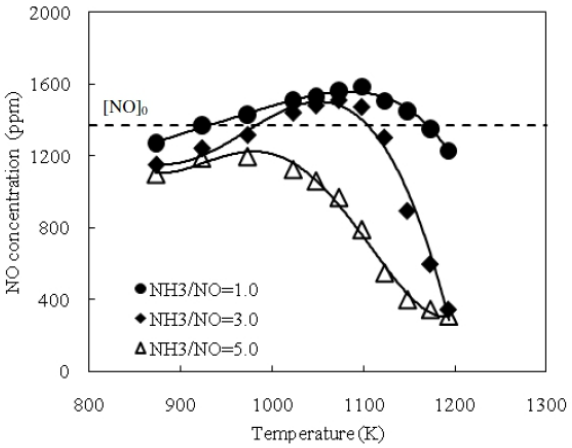

FIG. 3: Effect of the flue gas temperature on the residual NO concentration by using classical SNCR process with different NSR ($[NH_3]/[NO]_0$). (Gas residence time is 2.42 s; initial NO concentration $[NO]_0$ = 1370 ppm.)

$$NH_2 + NO \rightarrow N_2 + H_2O \ , \tag{2}$$

$$NH_2 + NO \rightarrow NNH + OH \ , \tag{3}$$

$$NNH + NH_2 \rightarrow N_2 + NH_3 \ , \tag{4}$$

$$NNH \rightarrow N_2 + H \ , \tag{5}$$

$$H + O_2 \rightarrow O + OH \ , \tag{6}$$

$$O + H_2O \rightarrow OH + OH \ . \tag{7}$$

The NH_2 radical plays an important role in the NO reduction by the SNCR mechanism. Otherwise, the NH_2 radical is principally produced by the reaction of NH_3 with OH via reaction equation (1). For that reason, the presence of OH radical plays a very important role in the SNCR process.

In our temperature conditions, experimental results show that the injected ammonia is very sensitive to the residual oxygen and tends to be oxidized to finally produce NO. The combined influence of both flue gas temperature and oxygen level needs to carefully adjust the working parameters. Consequently, the NO reduction process via the SNCR mechanism will be more efficient since the residual oxygen will be low. As shown in Fig. 3, this dependence on the oxygen concentration can be monitored by the flue gas temperature.

The effect of the initial NO concentration ($[NO]_0$) on the NO reduction efficiency is also evaluated in this study, and it is illustrated in Fig. 4. The performance of the SNCR process was evaluated in a wide range of initial NO concentration, from 400 to 2500 ppm, by maintaining the other working parameters

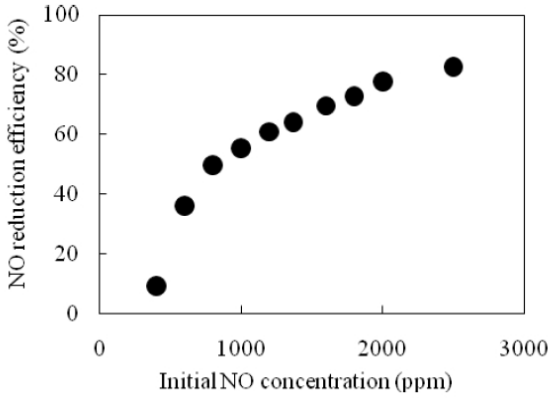

FIG. 4: Influence of the initial NO concentration ($[NO]_0$) on the NO reduction efficiency. (Flue gas temperature is 1123 K, gas residence time is 2.4 s, NSR = 5.0.)

at a constant value. The NSR of ammonia is fixed at 5, which corresponds to the optimal value in our experimental conditions.

As can be seen in Fig. 4, the NO reduction efficiency increases fairly well with the initial NO concentration $[NO]_0$. A very low concentration of NO in the burnt gases does not favor the NO reduction process. This observation is in perfect agreement with the experimental results obtained recently by Lee et al. [1], who studied the NO reduction process using ammonia in the initial NO concentration range from 100 to 500 ppm, with an NSR value of 3 and a wide temperature range, from 923 to 1423 K.

3.2 Effect of Additives on the SNCR Process

One of the disadvantages of the SNCR process consists of a narrow and relatively high reduction temperature range. The addition of some specific additives in the initial reducing agent mixture may solve this problem. As mentioned in the Introduction of this paper, several chemical species have been evaluated in this work as additives of the classical SNCR process. We have chosen some of them to evaluate the effects on the SNCR process in our low-temperature experimental conditions. The main results obtained are presented in the following.

3.2.1 *Alkanes*

The influence of the addition of alkanes (CH_4, C_2H_6) in the initial reducing mixture (NH_3/N_2) on the NO reduction efficiency is displayed in Fig. 5. The case of no additive corresponds to that of the classical SNCR process with a NSR ($[NH_3]/[NO]_0$) value equal to 5, which is the optimal condition in the present experiments.

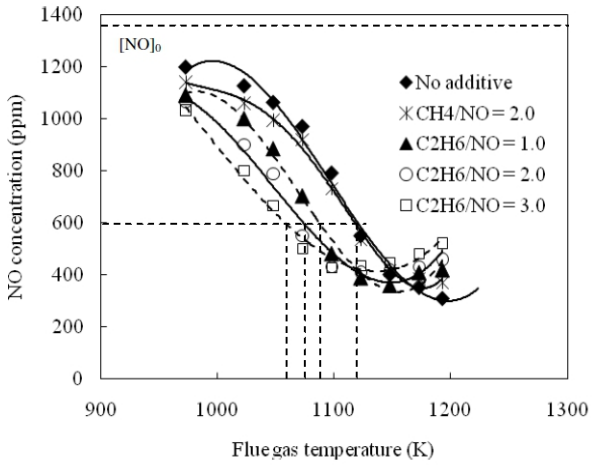

FIG. 5: Effect of alkanes addition on SNCR NO reduction (Gas residence time is 2.4 s; the initial NO concentration is 1370 ppm; NSR($[NH_3]/[NO]_0$) = 5.0.)

As can be seen in Fig. 5, the addition of methane and ethane induces a downward shift of the reduction temperature window and a slight decrease of the maximum NO reduction efficiency, depending on both the alkane and the additive concentration. When CH_4 or C_2H_6 are added to the initial reducing agent mixture, the optimum reduction temperature is found to be lowered. By comparing the addition of these two different additives and by considering the same hydrocarbon content (the CH*i* group with i = 2, 3, or 4), CH_4 is observed to have a lower effect than C_2H_6, first on the shift of the optimal temperature and second on the efficiency of the global NO reduction process. This qualitative observation has been already pointed out and agrees with the results obtained by Duo et al. [5] and Robin et al. [12], who compared the effect of several hydrocarbons such as CH_4, C_2H_6, C_4H_{10}, and C_2H_4 on the SNCR process.

When C_2H_6 is added to the NH_3/N_2 reducing mixture, the NO reduction level increases with the $[C_2H_6]/[NO]_0$ molar ratio. For a NO residual concentration of 500 ppm, when the NSR of ethane ($[C_2H_6]/[NO]_0$) increases to 3, a shift of near 100 K of the reduction temperature window toward the lower points is observed, as seen in Fig. 5. Nevertheless, for temperatures higher than 1150 K for C_2H_6 and 1200 K for CH_4, the addition of these two compounds induces a significant increase of the residual NO concentration in the flue gas. In these higher temperature conditions, the additives participate in chemical mechanisms which contribute to NO formation [Eqs. (8)–(11)]. The NO formation in these operating conditions (temperature near 1200 K and a high level of CH*i* compounds in the flue gas) is mainly due to the prompt NO chemical mechanism [4, 13]:

$$C_xH_y + NO \rightarrow HCN + O \rightarrow HNCO \ , \tag{8}$$

$$HNCO + OH \rightarrow NCO + H_2O \ , \tag{9}$$

$$NCO + NO \rightarrow N_2 + CO_2 \ , \tag{10}$$

$$NCO + O \rightarrow NO + CO \ . \tag{11}$$

Thus, the use of these additives needs to imperatively control the working parameters of the installation in order to avoid NO formation.

3.2.2 *Alkenes*

The effect of C_2H_4 on the NO reduction by the SNCR process has been also evaluated for different $[C_2H_4]/[NO]_0$ molar ratios. The experimental results are displayed in Fig. 6. The addition of C_2H_4 lowers the optimum reduction temperature, and this result is similar to that obtained with the alkanes. Nevertheless, this effect seems to be more significant in the temperature range from 1000 to 1150 K. In this temperature range and for a NO residual concentration of 600 ppm, the increase of the $[C_2H_4]/[NO]_0$ molar ratio to 3 leads to a shift of more than 100 K in the reduction temperature range.

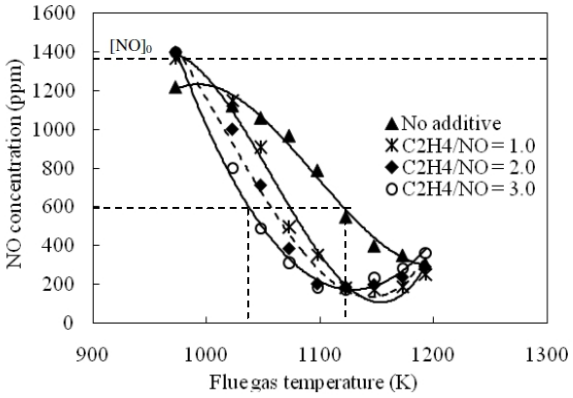

FIG. 6: Effect of ethylene addition on SNCR NO reduction. (Gas residence time is 2.4 s; initial NO concentration 1370 ppm; NSR($[NH_3]/[NO]_0$) = 5.0.)

Below 1000 K, C_2H_4 seems to become an inhibitor of the SNCR process. The quantitative measurement of NO at 973 K does not point out the reduction of this species. Moreover, some cautions have been proposed for flue gas temperature higher than 1130 K. From this limit temperature, the presence of C_2H_4 trends to favor an increase of NO concentration via the prompt NO chemical mechanism. The same observation has been made when alkanes are added to the NH_3/N_2 reducing mixture. Globally, C_2H_4 used as an additive seems to be more effective than CH_4 and C_2H_6 in comparing the decrease of the reduction temperature range for addition of the same amount of carbon.

3.2.3 *Carbon Monoxide*

In the same way, we have studied the effect of the addition of CO to the NH_3/N_2 reducing mixture on the efficiency of the NO reduction process. The experimental observation of the CO effect for different $[CO]/[NO]_0$ molar ratios is shown in Fig. 7. As previously observed, the presence of CO in the flue gas induces a shift of the optimal temperature range to the lower values. For a given temperature, increase of the CO concentration in the reducing mixture induces a more efficient reduction process. Nevertheless, the CO effect is less pronounced than those pointed out with the hydrocarbon additives as C_2H_6 and C_2H_4. Our experimental observations agree qualitatively with the results of Bae et al. [4] and Carton and Siebers [14].

The effect of CO addition on NO reduction by the SNCR process can be explained by the CO oxidation reaction in the presence of water vapor (12), which increases the supplies of OH and O radicals at lower temperatures via Reactions (6) and (7) [4]:

$$OH + CO \rightarrow H + CO_2 \ . \qquad (12)$$

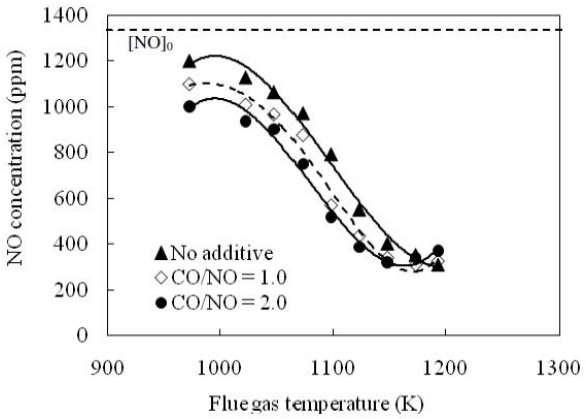

FIG. 7: Effect of CO addition on NO reduction. (Gas residence time 2.4 s; initial NO concentration 1370 ppm; NSR($[NH_3]/[NO]_0$) = 5.0.)

The availability of OH and O radicals shifts the optimum temperature for NO reduction to lower points.

3.2.4 *Alcohols*

A last family of chemical compounds was studied as an additive for the SNCR reduction process. Methanol and ethanol were chosen because of their low boiling points. These compounds were added to the NH_3/N_2 mixture by varying the [alcohol]/$[NO]_0$ molar fraction from 0 to 3. Figure 8 presents the NO concentration as a function of the flue gas temperatures for different [alcohol]/$[NO]_0$ molar fractions.

As shown in Fig. 8, the addition of alcohol additives (CH_3OH and C_2H_5OH) provides a strong positive effect on the SNCR process in comparison with the previous additives. We note that the addition of CH_3OH and C_2H_5OH greatly lowers the reduction temperature range with a shift of more than 100 K, and causes a slight decrease in the maximum degree of NO reduction. The C_2H_5OH seems to be more effective than CH_3OH with regard to decrease of the reduction temperature range. For the same flue gas temperature, the addition of alcohols provides an effective NO reduction at lower temperatures. For example, at 1023 K the addition of C_2H_5OH with a $[C_2H_5OH]/[NO]_0$ molar ratio of 3 can increase the NO reduction efficiency from 17% in the classical SNCR process to 57% (see Fig. 8b). The efficiency of alcohols in the promotion of the SNCR process can be explained by the presence of an OH group in the alcohol molecule. In the SNCR process, the OH radical plays an important role in propagation reactions, and the overall process is promoted by increasing the OH radical concentration [5]. The more significant effect of C_2H_5OH compared to CH_3OH seems to be caused by the presence of the double content of the hydrocarbon group.

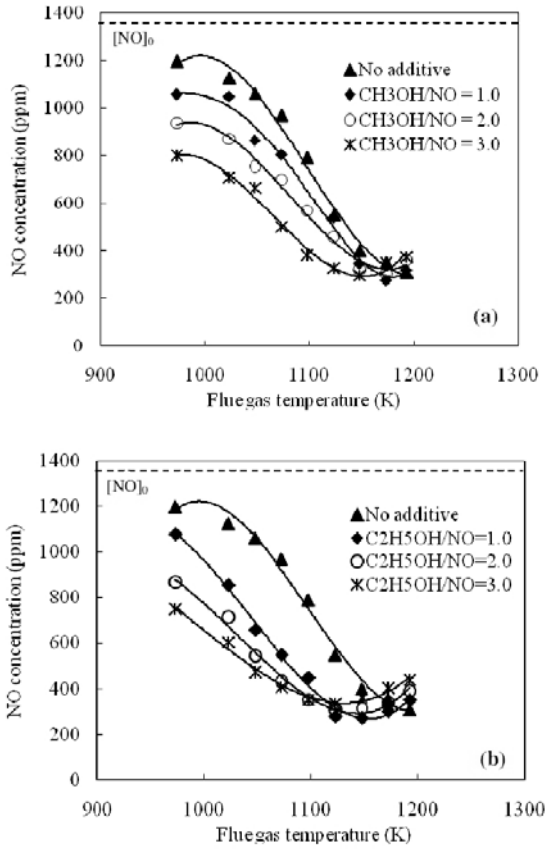

FIG. 8: Effect of (a) CH_3OH addition and (b) C_2H_5OH addition on SNCR NO reduction. (Gas residence time is 2.4 s; initial NO concentration 1370 ppm; NSR($[NH_3]/[NO]_0$) = 5.0.)

The results observed in this study agree qualitatively with the observations of Bae et al. [4], who also evaluated the influence of CH_3OH and C_2H_5OH with a molar ratio of $[NH_3]/[NO]_0$ equal to 2 in a relatively high range of temperature, from 1073 to 1273 K.

3.2.5 *Ammonia slip*

NH_3 slips refer to trace levels of NH_3 in postcombustion products of NO_x reduction processes. One of the disadvantages of the SNCR processes is the risk of the presence of NH_3 in the burnt gases as a byproduct. Naturally, a minimum of unreacted NH_3 from the NO reduction process is desirable for environmental reasons. That is why the ammonia slips are an important factor that needs to be considered with regard to industrial applications of the SNCR processes.

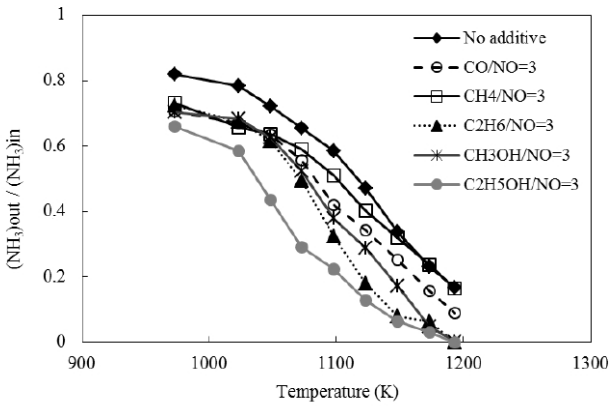

FIG. 9: Effect of additive addition on the ammonia slip of the SNCR process. (Gas residence time is 2.4 s; NSR ($[NH_3]/[NO]_0$) = 5.0.)

Measurements of NH_3 slips in the reactor were also performed in this study. Figure 9 displays the NH_3 slips as a function of flue gas temperature and additive utilization. The case "no additive" corresponds to the classical SNCR process with NSR ($[NH_3]/[NO]_0$) equal to 5.

Generally, the NH_3 slip decreases rapidly with the flue gas temperature. For all temperatures, the use of additive tends to reduce the residual NH_3 in the flue gases. This phenomenon is more significant with temperatures higher than 1050 K. For lower temperatures, the additive induces only a slight decrease of ammonia slips. In the optimal temperature condition (1200 K), the addition of some additives, such as C_2H_6, CH_3OH, and C_2H_5OH, leads to a negligible NH_3 residual emission.

Thus, in our operating conditions the additive we tested sensitively promotes NO reduction by the SNCR process but also efficiently reduces the residual NH3 emissions in the flue gases.

4. CONCLUSIONS

NO reduction by selective noncatalytic reduction (SNCR) using ammonia has been performed in a semi-industrial reactor at a temperature range of 873–1173 K. A maximum NO reduction efficiency of about 80% was achieved with a classical SNCR configuration. Several representative chemical species, such as CH_4, C_2H_6, C_2H_4, CO, CH_3OH, and C_2H_5OH, were tested as additives for the SNCR process. The addition of these compounds shifts the reduction temperature range up to more than 100 K to the lower points, and slightly decreases the maximum level of NO reduction. In our experimental conditions, CH_3OH and C_2H_5OH are the more efficient additives for shifting the reduction temperature range and reducing NO levels at lower temperatures. The additives have also a significant effect on the ammonia

slips. The residual NH_3 emissions are decreased by using additives in the initial reducing mixture (NH_3/N_2).

ACKNOWLEDGMENTS

This work was supported by the CNRS and by the Air Quality Program of IRENI (Institut de Recherche en Environnement Industriel) of France. The authors thank the Nord-Pas-de-Calais region and the European Funds for Regional Economic Development for their financial support.

REFERENCES

1. Lee, G.W., Shon, B.H., Yoo, J.G., Jung, J.H., and Oh, K.J., The influence of mixing between NH_3 and NO for a De-NO_x reaction in the SNCR process, *J. Ind. Eng. Chem.*, 14:457–467, 2008.
2. Javed, M.T., Nimmo, W., and Gibbs, B.M., Experimental and modeling study of the effect of CO and H_2 on the urea DeNO_x process in a 150 kW laboratory reactor, *Chemosphere*, 70:1059–1067, 2008.
3. Leckner, B., Karlsson, M., Dam-Johansen, K., Wenell, C.E., Kilpinen, P., and Hupa, M., Influence of additives on selective non-catalytic reduction of NO with NH_3 in circulating fluidized bed boilers, *Ind. Eng. Chem. Res.*, 30:2396–2404, 1991.
4. Bae, S.W., Roh, S.A., and Kim, S.D., NO removal by reducing agents and additives in the selective non-catalytic reduction (SNCR) process, *Chemosphere*, 65:170–175, 2006.
5. Duo, W., Dam-Jonhansen, K., and Ostergaard, K., Widening the temperature range of the thermal DeNO_x process: An experimental investigation, *Twenty-third Symp. (Intl.) on Combustion/The Combustion Institute*, pp. 297–303, 1990.
6. Noda, S., Harano, A., Hashimoto, M., and Sadakata, M., Development of selective non-catalytic reduction by ammonia in the presence of phenol, *Combust. Flame*, 122:439–450, 2000.
7. Zamansky, V.M., Lissianski, V.V., Maly, P.M., Ho, L., Rusli, D., and Gardiner, W.C., Reactions of sodium species in the promoted SNCR process, *Combust. Flame*, 117:821–831, 1999.
8. Zhang, Y., Cai, N., Yang, J., and Xu, B., Experimental and modeling study of the effect of CH_4 and pulverized coal on selective non-catalytic reduction process, *Chemosphere*, 73:650–656, 2008.
9. Cao, Q.X., Wu, S.H., Lui, H., Liu, D., and Qiu, P., Experimental and modeling study of the effects of multicomponent gas additives on selective non-catalytic reduction process, *Chemosphere*, 76:1199–1205, 2009.
10. Miller, J.A. and Bowman, C.T., Mechanism and modelling of nitrogen chemistry in combustion, *Prog. Energy Combust. Sci.*, 15:287–338, 1989.
11. Coda Zabetta, E. and Hupa, M., A detailed kinetic mechanism including methanol and nitrogen pollutants relevant to the gas-phase combustion and pyrolysis of biomass-derived fuels, *Combust. Flame*, 152:14–27, 2008.
12. Robin, M.A.I., Price, H.J., and Squires R.T. Tailoring NH_3 based SNCR for installation on power plants boilers, *Joint EPA/EPRI Symp. on Stationary Combustion NO_x Control*, Springfield, VA, Sec. 5A, pp. 99–118, 1991.
13. Lodder, P. and Lefers, J.B., Effect of natural gas, C_2H_6 and CO on the homogeneous gas phase reduction of NO_x by NH_3, *Chem. Eng. J.*, 30:61–167, 1985.
14. Carton, J.A. and Siebers, D.L., Comparison of nitric oxide removal by cyanuric acid and by ammonia, *Combust., Sci. Technol.*, 65:277–293, 1989.

International Journal of Energy for a Clean Environment, 10(1–4), 135–146 (2009)

INVESTIGATION OF DESIGN PARAMETERS INFLUENCING THE PERFORMANCE OF PREMIXED SURFACE BURNERS

A. Zbogar-Rasic,[1] M. Altendorfner,[1] M. Steven,[1] F. Issendorff,[1] & D. Trimis[2]*

[1]*Institute of Fluid Mechanics, University of Erlangen-Nuremberg, 91058 Erlangen, Germany*

[2]*Institute of Gas and Heat Technology, Technical University Bergakademie Freiberg, 09599 Freiberg, Germany*

[*]Address all correspondence to A. Zbogar-Rasic
E-mail: azbogar@lstm.uni-erlangen.de

Compared to diffusion and partially premixed burners, fully premixed burners have the advantage of low NO_x emissions. On the other hand, fully premixed combustion is sensitive toward flame instabilities, i.e., flashback, blow-off, and acoustical emissions. These instabilities limit the power modulation of a burner, thus decreasing its application range on the market. The scope of this investigation is the performance of fully premixed gas burners with a perforated surface pattern (i.e., a slits and/or holes pattern), focusing on the influences of burner surface pattern design and burner shape on burner operation. Experiments showed that the surface pattern design strongly influences the burner power modulation range and the emission of pollutants. Visualization and numerical simulation of the cold flow through a perforated surface pattern indicate that the dimensions of the flow recirculation zone in the vicinity of the slits/holes outlet are responsible for flame stabilization. Redesign of the burner surface pattern could lead to a better flow distribution through the burner and an improved power modulation range.

KEY WORDS: *emissions, flame stability, flame pattern, modulation*

1. INTRODUCTION

The combustion process, in the case of surface burners, is stabilized at the burner surface. They can be categorized based on the surface material: porous ceramic burners, metal fibre burners, etc. This investigation is focused on burners whose surfaces are made of a metallic sheet on which a pattern (usually consisting of slits and/or holes) is punched.

Flame type and its characteristics depend on the degree of mixing of the oxidizer (usually air) and fuel prior to the combustion zone: (1) diffusion flame, i.e., oxidizer and fuel are not mixed prior to the combustion zone, (2) partially premixed flame, i.e., amount of air which is premixed with fuel is not enough for a complete combustion, and (3) fully premixed flame, when the amount of air which is premixed with fuel is enough for a complete combustion, i.e., overstoichiometric air/fuel mixture. In partially premixed flames, the combustion reaction takes place at stoichiometric conditions, i.e., at the maximum flame temperature, which results in high emission of thermal NO_x (Recknagel et al., 2000). Due to a homogeneous overstoichiometric air/gas mixture, high-temperature peaks in fully premixed flames are avoided, which leads to a significantly lower NO_x emission.

One of the main demands for modern burners is low emission of pollutant gases, especially NO_x. In order to meet this demand, modern burners increasingly use lean, overstoichiometric fuel/air mixtures. This results in a complete combustion (leading to low CO emissions) at a relatively low flame temperature (leading to low NO_x emissions).

Due to safety considerations, burners for small-scale combustion equipment are often manufactured to operate as partially premixed (Jones, 1990). Diffusion and partially premixed flames are more stable compared to fully premixed flames. The limiting factor for the burn rate in a diffusion flame is the availability of oxidant, i.e., diffusion and mixing of oxygen from the surrounding air. The burn rate of a fully premixed flame is determined by chemical reaction kinetics with much smaller time scales compared to time scales of the diffusion and mixing process (Mallens, 1996). Fully premixed flames, which have higher burn rates compared to partially premixed flames, exhibit a higher sensitivity toward flame instabilities.

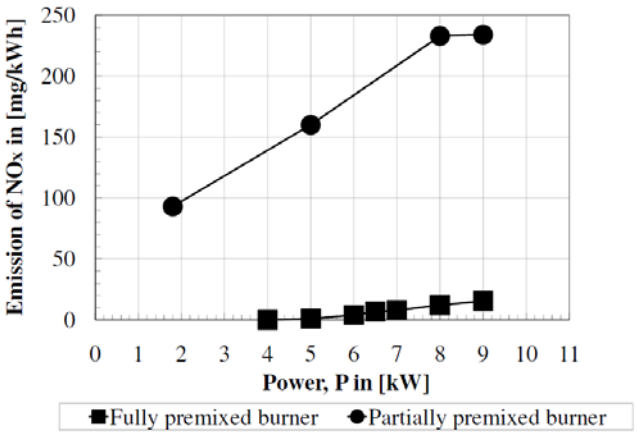

FIG. 1: Comparison of NO_x emissions of a partially and a fully premixed atmospheric burner (fuel: methane)

These instabilities limit the power modulation range of a burner, thus decreasing its application range and potentials on the gas appliances market.

In order to compare NO_x emissions during combustion of methane for the two above-mentioned burner types, a commercially available, partially premixed atmospheric burner (with the range of primary excess air ratio λ_{prim} = 0.5–0.7 for the power range P = 1.8–9 kW) and one fully premixed atmospheric burner (λ_{prim} = 1.4–1.5 for P = 4–9 kW) were tested. Figure 1 shows that the NO_x emission of the partially premixed atmospheric burner is up to 10 times higher than that of the fully premixed atmospheric burner, for which NO_x emissions are below 25 mg/kWh over the whole operational range. On the other hand, the modulation range (i.e., the ratio between the minimum and the maximum burner power) of the partially premixed atmospheric burner is 1:5 due to a better flame stability, while the modulation range of the fully premixed atmospheric burner is 1:2.5.

1.1 Multiport Burners

One of the typical surface designs of metallic surface burners is a multiport design with many different port configurations (Harris and South, 1978). Increased flame stability toward blow-off in multiport burners, compared with a single-port burner, is achieved through interaction between the flames formed over the adjacent ports. A flame's tendency toward blow-off depends on port size (influencing air/fuel mixture velocity), port shape (influencing the fluid flow pattern), and the interport spacing (influencing the interaction between the flames).

The transition from a stable flame to a complete flame blow-off for practical multiport burners is a gradual process, dependent largely on the way in which the ports are arranged. Flame lift tends to occur first from the ports at the edges of the burner surface pattern, where the interaction between the neighboring flames is reduced (Harris and South, 1978).

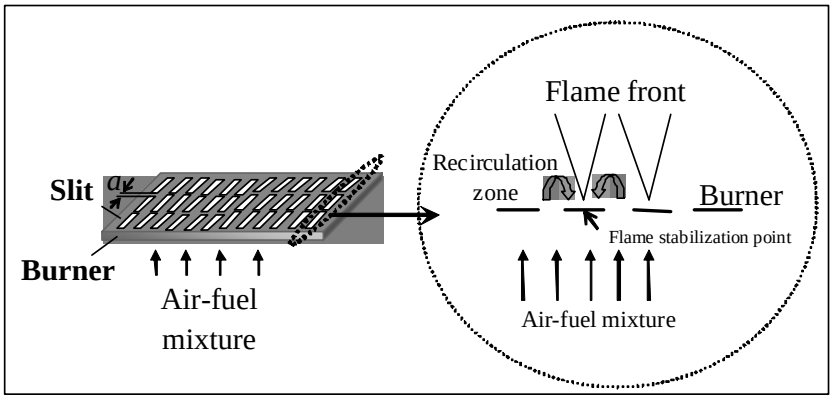

FIG. 2: Sketch of a triple-slit burner pattern and a flame formed over one row of slits (where a is the distance between the rows of slits)

Figure 2 shows one triple-slit pattern (left) and a flame shape formed over it (right) at high power loads. Flame formed over a triple-slit burner pattern consists of two adjacent V-flames. Among other parameters, the flame stabilization is influenced by flow recirculation originating from the air/fuel jets that emerge from the burner ports (Cerbe et al., 2004; Jones, 1990). Recirculation of hot gases heats the burner and the incoming air/fuel mixture, thus increasing the burning velocity and the stability of a flame toward blow-off (Harris and South, 1978).

1.2 Parameters

The aim of this study is to determine the influence of different design parameters on the performance of slits-and-holes burners in terms of emissions, flame stability, and consequently, on power modulation range. As was already mentioned, flame blow-off in multiport burners is influenced by flame interaction, i.e., confinement of a flame between adjacent flames.

Recirculation of hot combustion gases in the vicinity of the flame base further stabilizes the flame. Flame interaction and flow recirculation can be optimized by adjusting the distance between the neighboring flame ports, the port's shape, and the burner's shape. Aside from the surface pattern design, other parameters that influence the flame blow-off are the fuel, heat input, and the temperature of the burner.

It should be kept in mind that if something increases blow-off stability, it may tend to promote flashback. Thus, an optimum design for high port loadings might promote unsatisfactory performance at low port loadings (Harris and South, 1978).

2. EXPERIMENTAL STUDY

In order to determine the influence of the burner pattern design (through flame interaction and recirculation of hot combustion gases) on the burner operation, i.e., flame stabilization and emissions of CO and NO_x, two design parameters were in-

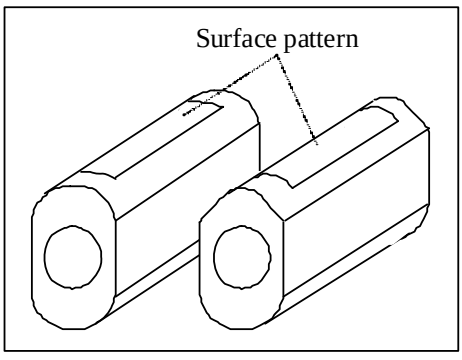

FIG. 3: Experimentally tested burner shapes: (a) cylindrical burner and (b) triangular burner

vestigated under combustion conditions: (1) the distance between the rows of slits (distance a in Fig. 2) was varied: a = 2, 2.75, and 4 mm; and (2) the shape of the burner surface pattern. These parameters were tested on burners with the surface pattern length l = 430 mm. The surface pattern consisted of rows of rectangular slits with smoothed corners (to avoid uncontrolled flow patterns), of dimensions 6 × 0.8 mm. Figure 3 shows the cylindrical and triangular burner shapes tested.

Along with tests under combustion conditions, the influence of the burner surface pattern was investigated by visualization of the cold flow through the pattern. The aim of visualization was to investigate the characteristic structures in the cold flow through the burner surface pattern and the influence of different layouts of slits and holes. In this case, experiments were done on the flat burner surface on which a pattern was placed.

2.1 Experimental Setup

Experimental characterization of the burner surface patterns under combustion conditions included measuring the emissions of pollutant gases (CO, NO_x), determining the burner's modulation range, and determining the flame blow-off limit. Two types of combustion tests were conducted: (1) when the burners were placed inside a commercial room heater with an excess of secondary air, and (2) when burners were placed in the open environment. Flow rates of methane, which was used as fuel, and air were independently controlled by mass flow controllers.

Experiments were done for the burner power range P = 4–10 kW, with the primary excess air ratio set to λ = 1.4, which corresponds to a normal burner operation. Experimental setup and a detailed scheme of the commercial room heater are shown in Figs. 4a and 4b, respectively.

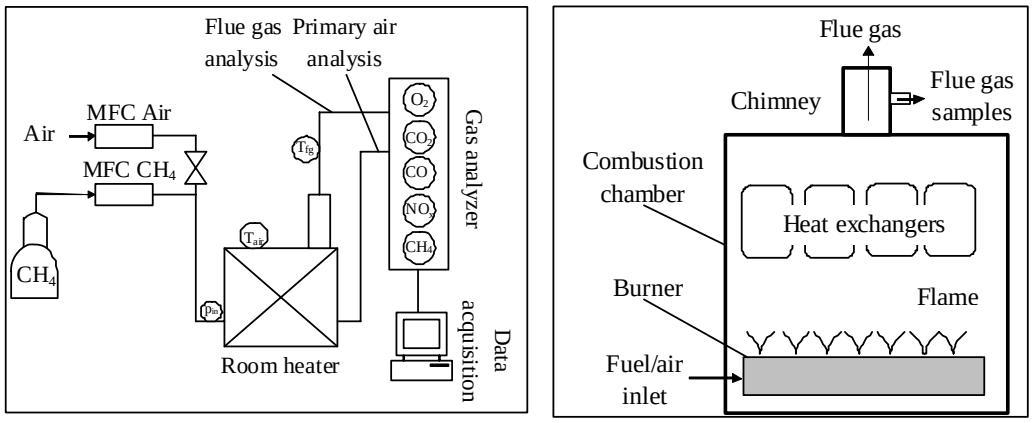

(a) (b)

FIG. 4: (a) Experimental setup for investigation under combustion conditions and (b) scheme of the room heater

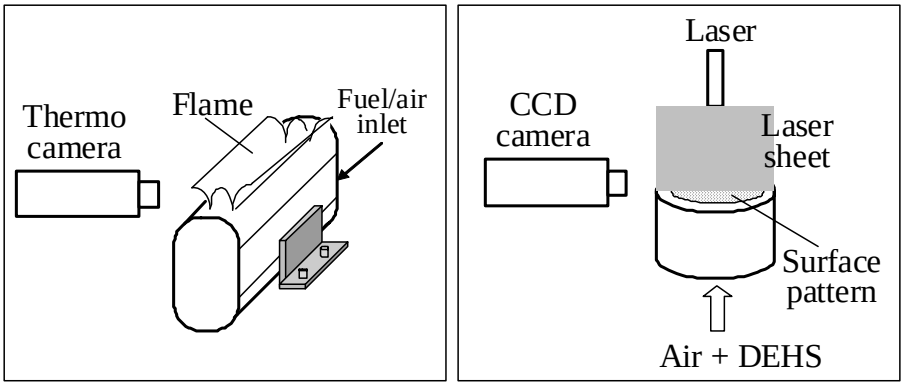

FIG. 5: Experimental setup for (a) flame visualization and (b) cold flow visualization

Visualization of the flame shape (obtained during the combustion of methane) for different burner surface patterns was done with a thermocamera Thermosensorik PtSi 256 (wave band 3–5 μm). The experimental setup for flame visualization is shown in Fig. 5a.

Cold flow visualization was performed with a mixture of air and di-ethyl-hexyl-sebacat (DEHS) using an experimental setup shown in Fig. 5b. DEHS was atomized into droplets of d_p = 4–5 μm using a jet atomizer. The model of the flat burner surface pattern was made of Plexiglas. In the model pattern, the dimensions of the original burner pattern were up-scaled with a factor 5. The Reynolds number, which can be defined for the burner fuel/air inlet, was kept as in the original commercial burner, i.e., Re = 2600 for mixture flow rate corresponding to power P = 10 kW and the primary excess air ratio λ = 1.3. The selected plane within a flow field was visualized using a laser sheet. The cold flow visualization was recorded with a charge-coupled device (CCD) camera.

2.2 Combustion Experiments

The influence of the surface pattern design and the burner shape on the emissions of CO and NO_x was investigated inside a commercial room heater appliance. Gas samples were taken from the chimney for further analysis. Results for three cylindrical burners, with distances between the rows of slits a = 2, 2.75, and 4 mm, and for a triangular burner with a = 2.75 mm, are presented in Fig. 6.

Results show that as the distance between the rows of slits increases, CO emission increases and NO_x emission decreases. The grounds for this behavior should be looked for in the interaction between the flames from the adjacent slits. As the distance between the slits is increased, the flame interaction in terms of heat is decreased, while the flame front, i.e., interaction with the environment, is increased. The flames that overlap less emit more heat to the environment, which leads to decreased specific power and decreased flame temperatures. Finally, decreased flame

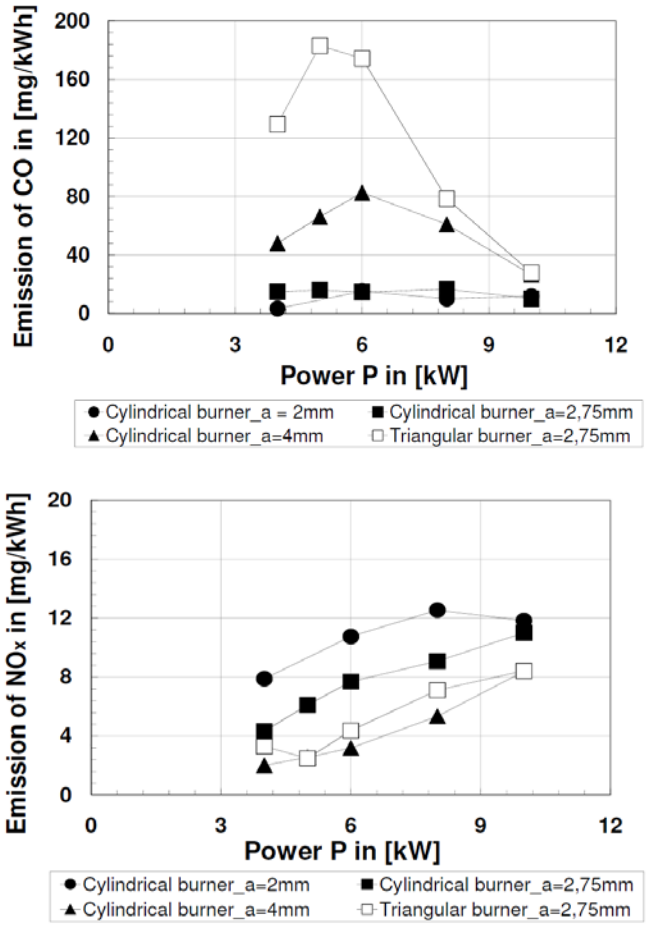

FIG. 6: Comparison of CO (a) and NO_x emissions (b) of three tested surface patterns and two burner shapes (fuel: methane; primary excess air ratio $\lambda = 1.4$)

temperatures cause the change in combustion kinetics, leading to an increase in CO emission and a decrease in NO_x emission.

Figure 6 also shows the influence of the burner shape on emissions of CO and NO_x. Results show that the triangular burner has higher emissions of CO but lower emissions of NO_x compared to the corresponding cylindrical burner. One possible reason for this is that the flame interaction between the adjacent flames for the triangularly shaped burner is decreased, i.e., the flames are less overlapped, thus having bigger flame front, and emit more heat to the environment compared to the cylindrical burner.

Visualization of flames formed over the cylindrical (a = 2.75 and 4 mm) and triangular (a = 2.75 mm) burners are shown in Fig. 7. Flames were visualized during the combustion of methane at P = 8 and 10 kW and for the primary excess air

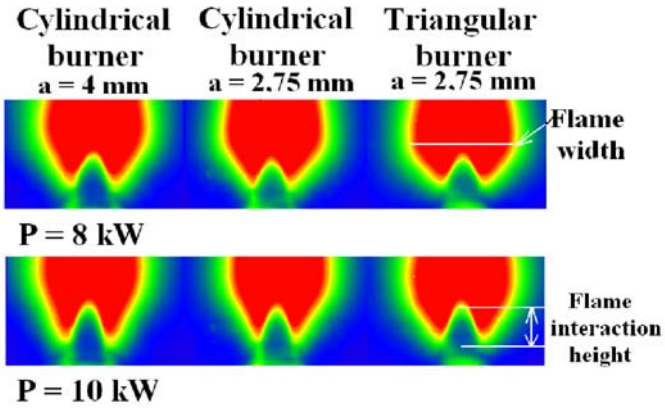

FIG. 7: Flame visualization on tested circular and triangular burners (fuel: methane; primary excess air ratio $\lambda = 1.4$)

ratio $\lambda = 1.4$. Comparison of the flames formed over the three burners at the same power load shows (1) the visible flame interaction on the cylindrical burner with a = 4 mm starts at a higher position than for the cylindrical burner with $a = 2.75$ mm; (2) the flame interaction of the cylindrical burner with $a = 4$ mm and the triangular burner with $a = 2.75$ mm starts approximately at the same position; and (3) flames formed over triangular burners are wider, indicating decreased flame interaction.

The influence of the surface pattern design on flame stabilization was determined through determining a flame blow-off limit. According to Harris and South (1978), the flame blow-off on multiport burners is not an instantaneous process. Thus, it can be considered as the point at which 50% of the flames remain attached to the burner. For the purpose of determining the blow-off limit, the tested burners were placed outside the appliance (in the open environment) in order to visually follow the blow-off process.

Figure 8 shows measured primary excess air ratios in the blow-off point for two cylindrical and two corresponding triangular burners ($a = 2$ and 4 mm) at powers $P = 6$ and 8 kW. As the distance between the rows of slits was increased, the primary excess air ratio at blow-off was slightly increased as well. This indicates the positive influence of the limited increase of recirculation zone in the vicinity of the flame base on flame stabilization.

Although the results indicate that the triangular burners have a higher blow-off point, the difference in blow-off characteristics of the two burners should be taken into account. As was schematically shown in Fig. 8, the flame blow-off on cylindrical burners starts from one side of the surface pattern, while for triangular burners, flame blow-off occurs on both sides of the pattern. So, although the flame is still attached to 50% of the burner, the blow-off behavior is not the same. Since

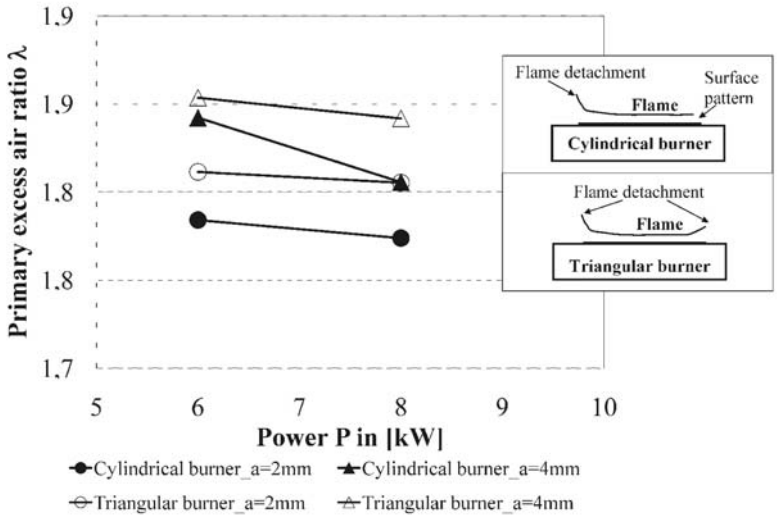

FIG. 8: Blow-off limit for tested burners of different shapes (cylindrical and triangular) and patterns

the inside construction of the two burners is identical, a possible reason for the increased excess air ratio at blow-off conditions is that the flame interaction is decreased, but the flame stabilization due to the recirculation of hot gases in the vicinity of the flame base is increased. Further experimental and numerical work is needed in order to support this hypothesis.

2.3 Cold Flow Visualization

Cold flow visualization was done for two flat surface patterns consisting of slits and holes, shown in Figs. 9b and 9d. The major difference between the two patterns is the distribution between slits and holes. On the pattern shown in Fig. 9b, the zone of slits and the zone of holes are separated, but on the pattern shown in Fig. 9d, slits and holes are combined over the characteristic area section. Also, the distance between a slit and an adjacent hole in the second surface pattern is two times smaller than the corresponding distance in the first surface pattern. Figures 9a and 9c show the visualization of the cold flow having Re = 2600 (inlet gas velocity v = 0.05 m/s). This Re number corresponds to the Re number at the original burner setup for the power of 10 kW (when methane is used as fuel) and the primary excess air ratio of λ = 1.3. This power load corresponds to the blue-flame mode, i.e., the mode of burner operation in which no significant radiation is emitted (Scheffler and Colombo, 2005).

Figure 9b shows the recirculation zones formed in the region between the row of slits and the rows of holes. For the pattern shown in Fig. 9d, only occasional re-

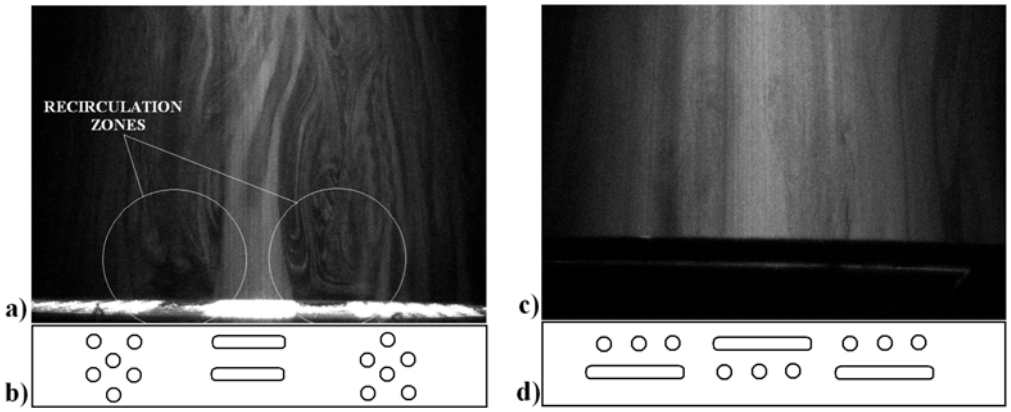

FIG. 9: Visualization of cold flow visualization (a, c) on two tested slits-and-holes patterns (b, d)

circulation could be noticed without a fixed recirculation zone. Based on the cold flow visualization, it can be concluded that a transient behavior of the flow field originates from the jets which emerge from the slits.

Based on the presented results, two pattern design details were identified as important for the formation of flow recirculation zones — the rows of slits and the distance between the ports. Figure 9c indicates that slits alone would not produce permanent recirculation. On the other hand, if the distance between the ports (holes in the pattern shown in Fig. 9b, and slits and holes in the pattern shown in Fig. 9d) is too small, the recirculation zone cannot be formed.

We can expect that under combustion conditions, the recirculation zones would lead to a better flame stabilization. Recirculation of hot combustion gases would heat the burner surface, which consequently would heat the incoming air/fuel mixture. This finally leads to an increase in the burning velocity and increased flame susceptibility toward blow-off. This finding is in agreement with Harris and South (1978), who claim that the influence of the recirculation currents at the base of the flames in a series of long slits increases the flame stabilization, while for circular ports, such currents are oriented in different directions and cannot stabilize the flame to the same extent.

3. NUMERICAL SIMULATION

The cold flow field through the slits-and-holes pattern, corresponding to the one shown in Fig. 9b, was simulated. The burner geometry was set according to the visualization setup, in order to validate the simulation results with the experiments.

A commercial software ANSYS CFX was used for numerical simulation. The mesh consisted of 900,000 hexahedral cells. Inlet was defined as the mass flow

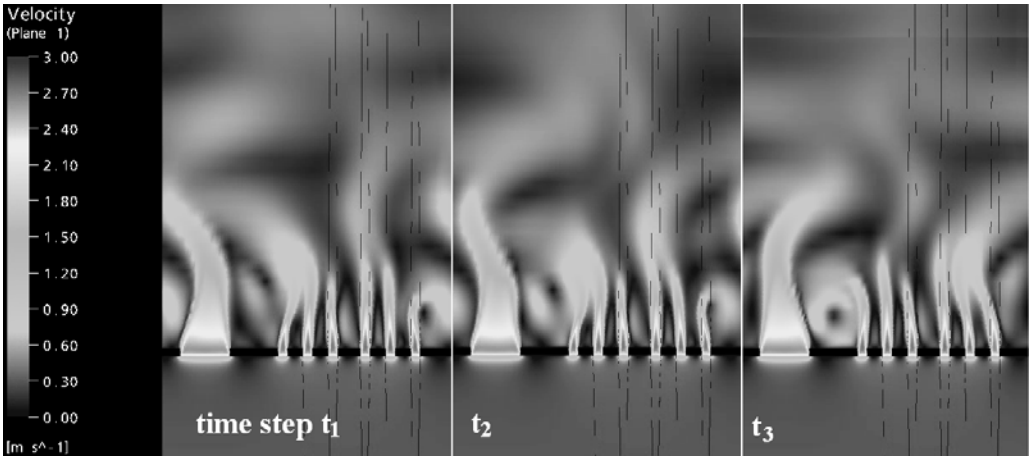

FIG. 10: Simulation of the cold flow through a slits-and-holes pattern

rate of the mixture of air and methane, keeping the same Re number as in the cold flow visualization, i.e., Re = 2600 (inlet gas velocity v = 0.25 m/s). An outlet boundary condition was used on the downstream side. Since the characteristic area section of the pattern is periodic in x and y direction, the periodic boundary conditions perpendicular to the main flow direction were used.

For the turbulence modelling, the shear stress transport model (SST) with scalable wall function was used. This model combines several desirable elements of existing two-equation models, i.e., it uses k–ε model near solid walls and k–ω model near boundary layer edges and in free shear layers (Cebeci, 2004). The advantage of this model is that due to an improved near wall formulation, a reduced near wall grid resolution is required (Menter et al., 2003).

Figure 10 shows the numerical simulation of the cold flow through the slits-and-holes pattern. The qualitative outcome of the numerical results (i.e., the existence of the recirculation zone) leading to the transient behavior of the fluid flow is in agreement with the visualization findings. It could be observed that the gas jet, emerging from the slit, periodically moves, which depends on the creation and movement of swirls that appear between the slit and the neighboring holes.

4. CONCLUSIONS

The question of flame stability, and consequently of the power modulation for small-scale burners, came to focus with the increased use of fully premixed combustion as a way to decrease the emission of NO_x. The aim of this experimental and numerical study was to determine the influence of different design parameters of multiport, metallic, fully premixed burners on their operation performance, i.e., emissions of CO and NO_x, and the power modulation range. The following design

parameters were considered: (1) the distance between the burner ports, (2) the shape of the burner, and (3) the distribution of slits and holes over the burner surface pattern.

Experimental investigation showed that as the distance between the neighboring ports is increased, flame interaction is decreased, which leads to increased CO and decreased NO_x emissions. As the distance between the slits is increased, the primary excess air ratio at the blow-off is slightly increased. This leads to the conclusion that the flow recirculation of hot combustion gases increases the flame stability through the heating-up of the burner and the incoming air/fuel mixture, which consequently increases the burning velocity. Based on this, it can be assumed that an optimum distance between the rows of adjacent ports exists, which would lead to the optimum flow recirculation zone dimensions. If the distance between the adjacent ports were too great, the flame interaction would eventually vanish and each flame would behave as separate, leading to a sudden decrease in stability.

The investigation of the influence of the burner shape on flame stabilization gave the advantage to the triangularly shaped burner, but in order to draw more certain conclusions, further experimental and numerical work is necessary.

Visualization and numerical simulation of the cold flow through the slits-and-holes pattern showed intensive flow recirculation in the region between the zone of slits and the zone of holes. Cold flow visualization showed that the flow recirculation depends on the distribution of the slits and holes over the pattern.

Finally, it can be concluded that more stable combustion in fully premixed surface burners can be achieved by optimizing the flow distribution through the burner surface pattern.

REFERENCES

Cebeci, T., *Turbulence Models and Their Application: Efficient Numerical Methods with Computer Programs*, Springer, Berlin, 2004.

Cerbe, G., Dehli, M., and Kaetelhoen, J.E., *Grundlagen der Gastechnik*, Fachbuchverlag, Leipzig, 2004.

Harris, J.A. and South, R., Flame stability — principles and practice, *Gas Eng. Manage.*, vol. 18, no. 5, pp. 153–173, 1978.

Jones, H.R.N., *The Application of Combustion Principles to Domestic Gas Burner Design*, Spon Press, London, 1990.

Mallens, R.M.M., *Stabilization of Laminar Premixed Methane/Air Flames*, PhD Thesis, Eindhoven University of Technology, 1996.

Menter, F.R., Kuntz, M., and Langtry, R., Ten years of industrial experience with the SST turbulence model, *Proc. of the 4th Intl. Symp. on Turbulence, Heat, and Mass Transfer*, pp. 625–632, 2003.

Recknagel, H., Sprenger, E., and Schramek, E., *Taschenbuch fuer Heizung und Klimatechnik*, Oldenbourg Verlag, München, 2000.

Scheffler, M. and Colombo, P., *Cellular Ceramics: Structure, Manufacturing, Properties and Applications*, Wiley-VCH, Weinheim, 2005.

International Journal of Energy for a Clean Environment, 10(1–4), 147–166 (2009)

SCANNING ELECTRON MICROSCOPY AND ENERGY-DISPERSIVE X-RAY SPECTROSCOPY OF LOW-SULFUR COAL FLY ASH

Bruno Valentim,[1,] James C. Hower,[2] Alexandra Guedes,[1] & Deolinda Flores[1]*

[1]*Centro de Geologia e Departamento de Geociências, Ambiente e Ordenamento do Território da Faculdade de Ciências, Universidade do Porto, Portugal*

[2]*University of Kentucky Center for Applied Energy Research, Lexington, Kentucky, USA*

[*]Address all correspondence to Bruno Valentim, E-mail: bwalent@fc.up.pt

Fly ash is a heterogeneous material produced during the burning of pulverized coal in thermoelectric power stations, and its phase and mineral composition includes (i) an inorganic constituent, amorphous and crystalline; (ii) an organic constituent composed of char materials (slightly changed, semicoked and coked particles) and organic minerals; and (iii) fluid constituent. Hence the characterization of fly ash is usually made using several methods. However, scanning electron microscopy (SEM) is the best method and is, along with X-ray diffraction, one of the most widely used techniques for the identification and characterization of phases in fly ash, especially with an SEM equipped with an energy-dispersive X-ray spectrometer (EDS). In this study SEM/EDS was carried out to analyze two high-volatility low-sulfur coals and the fly ash resulting from the combustion of a 50:50 ratio blend of these coals.

KEY WORDS: *scanning electron microscopy, char, cenosphere, plerosphere, dermasphere, ferrosphere*

1. INTRODUCTION

Fly ash (FA) contains a variety of homogeneous and heterogeneous phases, amorphous, crystalline, and fluids, composed of several types of particles (Gieré et al., 2003; Vassilev and Vassileva, 1996). Investigations at microscopy level revealed subcomponents such as char (Lightman and Street, 1968; Nandi et al., 1977), minerals (Ramsden and Shibaoka, 1982), and glassy spheres (Fischer et al., 1978). Detailed microscopic studies identified specific morphotypes, such as the following:

1. *Cenosphere*, from the Greek *kenos* (hollow) and *sphaira* (sphere), is a term used since 1924 (Newall and Sinnatt, 1924; Lightman and Street, 1968) to characterize pulverized fuel particles. In petrographic studies, the term is used for hollow char spheres resulting from melting and volatile matter crack of coal particles (Lightman and Street, 1968) or hollow glass spheres (Fisher et al., 1978).

   Glassy cenospheres have sizes from several tens of micrometers to 500 μm and are formed from rapid cooling of ultra-acidic melts of high viscosity which are poorly crystallized and vitrified at cooling (Anshits et al., 2001), coalescing to spherical shape due to expansion of trapped volatile matter, surface tension, and cooling rate (Matsunaga et al., 2002). Physically, they are composed of a glass matrix embedding a skeleton of quartz, chunky mullite, or acicular mullite (Hulett and Weinberger, 1980), calcite, cristobalite, plagioclase, feldspar, ferriferous spinel (magnetite–magnesioferrite type), and other crystalline phases (Sokol et al., 2000; Anshits et al., 2001; Vassilev et al., 2004).

2. *Plerospheres*, larger spheres contained within other cenospheres, that are themselves cenospheres packed with smaller spheres (1 μm in diameter or less) and/or microcrystals, were described and denominated plerospheres (plero-, from the Greek *plérés*, full) by Fischer et al. (1975). Goodarzi and Sanei (2009) divided plerospheres in two classes: (i) primary plerosphere, i.e., a sphere encapsulating indigenous microspheres formed inside; and (ii) secondary plerosphere, formed due to capture of microspheres by a cenosphere during combustion.

3. *Dermaspheres* was a term proposed by Lauf (1982) to describe particles "with a layered structure suggestive of the deposition of a glassy "skin" onto a crystalline core." However, when large cenospheres have microcrystals on the surface, for example, tertiary minerals resulting from handling and storage, leading to extensive crystal growth on the surface of the spheres after storage for several months (Fischer et al., 1975), are also classified as dermaspheres (Vassilev and Vassileva, 1996).

   In the strict sense, outer and inner surfaces of the cenospheres may be covered with 30- to 50-nm-thick nanofilms enriched in nanosized crystalline phases (such as feldspars, ferrispinels, and pyroxenes) (Anshits et al., 2001, 2005), or some elements such as Si and Al may be layered (Anshits et al., 2005; Gieré et al., 2003).

4. *Ferrospheres*, also termed magnetic microspheres or magnetite globules (Sokol et al., 2000), was a term proposed by Lauf et al. (1982) to describe iron-rich spheres with little or no melting or dimensional change. These morphotypes are formed during the process of coal combustion from melts corresponding to the eutectic (T = 1070°C) of wüstite–fayalite ($FeO–Fe_2SiO_4$), with a total content of up to 80 wt% FeO (Sokol et al., 2000).

A large percentage of ferrospheres are commonly 5–50 μm in size and have a mineralogical composition that includes quartz, mullite, magnetite, hematite, anhydrite, and amorphous materials, are mainly composed of Fe, Si, S, Al, and Ca, and exhibit different surface microstructure characteristics: smooth, polygonal, dendritic, granular, and molten drop (Xue and Lu, 2008). Depending on the type of iron (Fe^{2+} or Fe^{3+}), ferrospheres are also divided in two types: (i) ferrospheres, essentially composed of magnetite (ferrous-ferric oxide), and (ii) ferrispheres, essentially composed of hematite and limonite (Vassilev and Vassileva, 1996).

Different morphologic types of magnetic iron-rich microspheres were identified: (i) massive globules (CaO + MgO)-rich and (ii) porous globules (SiO_2 + Al_2O_3)-rich (Anshits et al., 2001). Massive globules usually present coarse crystalline spinel structure, while fine crystalline dendrite spinel formations are more common in porous globules (Anshits et al., 2001).

According to their microstructure, Zhao et al. (2006) classified the ferrospheres into seven groups, namely, sheet ferrospheres, dendritic ferrospheres, granular ferrospheres, smooth ferrospheres, ferroplerospheres, porous ferrospheres, and molten drop ferrospheres.

5. *Agglomerates* are typical of fly ash derived from coal combustion and were described as being composed of spherical particles embedded in an amorphous matrix (Fischer et al., 1975). These agglomerates are essentially composed of silicate and aluminosilicate minerals, that once molten, generally have higher viscosities and surface tensions than other molten inorganic phases. However, the physical characteristics are altered when the silicates or aluminosilicates incorporate alkalis, alkaline earth elements, or iron; and the mixed-silicate phase is likely to act as a cement, bridging or coalescing with other mineral particles (Miller and Schobert, 1993, 1994). A very common agglomeration of fly ash may also result from bonding due to electrostatic charges, but these agglomerations are easily dispersed in water by light stirring (Jones et al., 2006).
6. *Minerals in FA* originate several types of morphotypes, such as grains and particles, crystals, and aggregates (Vassilev and Vassileva, 1996).
7. *Particulate matter* (PM) is particularly important, since $PM_{2.5}$ to $PM_{0.1}$ particles may be the cause of respiratory and cardiovascular diseases. Scanning electron microscopy (SEM) studies divided PM into two distinct classes: (i) particulate organic matter with small size (micrometer >1–10 μm; submicrometer 0.1–1 μm; and ultrafine <0.1 μm), variable shape (irregular or spherical), and different surface texture (porous or solid, and smooth) (Griffin and Goldberg 1975, 1979, 1981; Stoffyn-Egli et al., 1997; Chen et al., 2005a), and (ii) particulate inorganic particles composed of submicrometer particles approximately spherical in shape with no fragmented minerals composed of sulfur, silicon, sodium, and phosphorus (Buhre et al., 2005).

Another PM classification based on computer energy-dispersive spectroscopy (EDS) spectral analysis (Shah et al., 1995; Chen et al., 2004, 2005a,b) divides PM into four categories: (i) single-element particles (one element is dominant, ≥80–90%); (ii) two-element particles (>80% of any two elements with no third element >6%); (iii) three-element particles (three elements >80%, with none of the three <6%, and no fourth >6%); and (iv) "other," all particles not meeting any of these criteria.

However, FAs from certain types of coal may not contain all the above-mentioned morphotypes and categories, or may present specific characteristics related with coal. Additionally, FAs do not have the same composition from one location to another inside a thermal power plant (TPP). Since SEM is the best method and one of both the most widely used techniques (in equal position with XRD) for the identification and characterization of inorganic phases in fly ash (Vassilev and Vassileva, 2005), extensive SEM/EDS analysis, representing 170 images and 90 EDS spectra, was conducted on low-sulfur coal FA using two SEM detection modes, as received and on epoxy-bound polished block, collected in four different locations inside the TPP and in the stack.

2. MATERIALS AND METHODS

Two low-sulfur coals (El Cerrejon from Colombia and Kangra from South Africa; Table 1), burned on a 50:50 ratio base, and their FA (Table 2) were collected on

TABLE 1. Coal characterization

Coal	Moisture (a.r., wt%)	Ash (d.b., wt%)	VM (d.b., wt%)	Elemental analysis (d.b., wt%)			
				C	H	N	S
Kangra	8.5	13.8	25.0	72.4	4.1	2.0	0.9
El Cerrejon	5.4	12.0	26.6	70.1	5.5	4.3	0.9
	Calorific value	Vitrinite reflectance		Maceral composition (vol.%)			
	(MJ/kg)	(%) R_r	Standard dev.	V	L	I	MM
Kangra	28.55	0.7	0.06	24	6	64	7
El Cerrejon	29.01	0.6	0.06	74	3	15	8
High temperature (850°C) coal ash major oxides (wt%, dry basis; values normalized to 100%)							
	SiO_2	Al_2O_3	K_2O_3	Ti_2O	P_2O_5	CaO	MgO
Kangra	42.87	23.72	0.53	1.21	0.64	9.45	2.15
El Cerrejon	61.08	20.62	1.96	0.89	0.18	2.21	1.78
	Na_2O	MnO	Fe_2O_3	SO_3			
Kangra	0.19	0.06	9.40	9.77			
El Cerrejon	0.67	0.06	7.31	3.26			

TABLE 2: Chemical characterization of the fly ash

Sample location:	Economizer	Air-heater	ESP-h12	ESP-h42
Moisture (a.r., wt%)	0.4	0.5	1.3	0.7
Ash (a.r., wt%)	90.8	98.3	89.8	89.4
Ash (d.b., wt%)	91.2	98.8	91.0	90.0
[1]Total sulfur (%)	0.12	0.11	0.20	0.62
[1]Total carbon (%)	9.24	1.46	8.67	9.27
[1]Organic carbon (%)	7.73	1.19	7.28	7.63
[1]Graphitic carbon (%)	1.23	0.15	1.04	1.48
[2]Inorganic carbon (CO_2; %)	1.02	0.44	1.26	0.60
[1]LOI (%)	10.5	1.6	9.8	11.1
Major oxides and LOI (normalized to 100%), wt%				
SiO_2	49.08	56.96	45.91	41.99
Al_2O_3	19.20	16.48	23.50	23.15
K_2O	0.77	0.67	0.79	0.90
Ti_2O	0.94	0.93	1.11	1.32
P_2O_5	0.35	0.31	0.51	1.30
Na_2O	0.27	0.24	0.34	0.34
CaO	8.52	6.95	8.09	8.69
MgO	1.98	1.80	1.98	2.67
MnO	0.06	0.07	0.05	0.07
Fe_2O_3	10.42	13.69	8.09	7.89
SO_3	0.25	0.26	0.57	1.89
LOI	8.16	1.65	9.04	9.81
Total	100.02	100.00	9.99	100.01

[1]Total carbon and total sulphur (Leco method), carbon species, inorganic carbon (CO_2) and LOI (1000^oC) were conducted at ACME Analytical Laboratories, LTD.

four locations [economizer, air heater, and electrostatic precipitator system (ESP) hoppers 12 and 42] inside a TPP burning pulverized coal. Afterward, as-received FA and epoxy-polished block-mounted FA was carbon coated for SEM/EDS analysis.

As-received FA was analyzed on a JEOL JSM-35C microscope equipped with an EDS X-ray spectrometer analyzer EDS Noran-Voyager with a thin window detector (which detects elements with atomic number lower than Na), while FA mounted for polished-block analysis was carried out on a high-resolution (Schottky) environmental scanning electron microscope equipped with EDS, FEI Quanta 400FEG ESEM/EDAX Genesis X4M.

The utilization of the secondary electron (SE) mode was alternated with backscattered electron (BSE) mode to obtain three-dimensional (3D) micrographs

or composition micrographs based on the element atomic number. SE mode was particularly useful for morphology characterization and dark spot location, and BSE mode for phase discrimination. Both modes and magnification change were conducted for micrograph overviews, up to micrometer-particle observation. EDS was used to obtain the elemental data spectra of a particle or specific areas of one particle. As a guideline for classification and characterization, the EDS spectra were compared with spectra of common-rock-forming minerals (Severin, 2004). Since SEM/EDS is an expensive, time-consuming analysis, first a global image of each sample was obtained and analyzed, after the most common morphotypes were characterized using the BSE detector and EDS, and the following morphotypes were expected to be characterized: (i) glassy spheres composed mostly of aluminosilicate glass, mullite, quartz, calcite, Fe-bearing species, Ca silicates, and Ca sulfates, with size varying between 5 and 250 μm; (ii) char particles and fragments; (iii) primary minerals, such as quartz and others, occurring as discrete particles or bounded to char particles, and newly formed secondary minerals and phases, crystallized mainly on glass and char matrices or as discrete particles; and (iv) tertiary minerals as surface enrichment and incrustation on coarser phases or as materials and discrete particles.

Another method for FA characterization was used following the classifications, based on BSE mode brightness, proposed by Mukhopadhyay et al. (1996) and Gieré et al. (2003).

3. RESULTS AND DISCUSSION

3.1 Coal

Characterization of the mineral matter of the coals using SEM/EDS was particularly useful to identify the addition and characterization of fines in El Cerrejon coal, the identification of the most frequently observed minerals, and the observation of trace minerals.

El Cerrejon coal particles are surrounded by fines which are composed of finer coal particles mixed with illite, quartz, and smaller amounts of other minerals such as barite, pyrite, etc. (Fig. 1a). However, the most frequently observed mineral is illite (Fig. 1b). Other minerals present are pyrite framboids, detritic quartz, and traces of titanium oxides.

Fines are the result of upgrading coal to reduce impurities. The operations of processing fine coal by particle-size enlargement is responsible for the addition of substances used in bridging flocculation or agglomeration of the fines (Laskowski, 2001), generating unusual features in coal and chars (Valentim et al., 2006). In the present case it seems that agglomeration operations were conducted using clay (Fig. 1a).

Kangra coal has a more complex mineralogy than El Cerrejon coal, composed mostly of kaolinite (Fig. 1c), calcite, dolomite (Fig. 1d), ankerite, and detritic

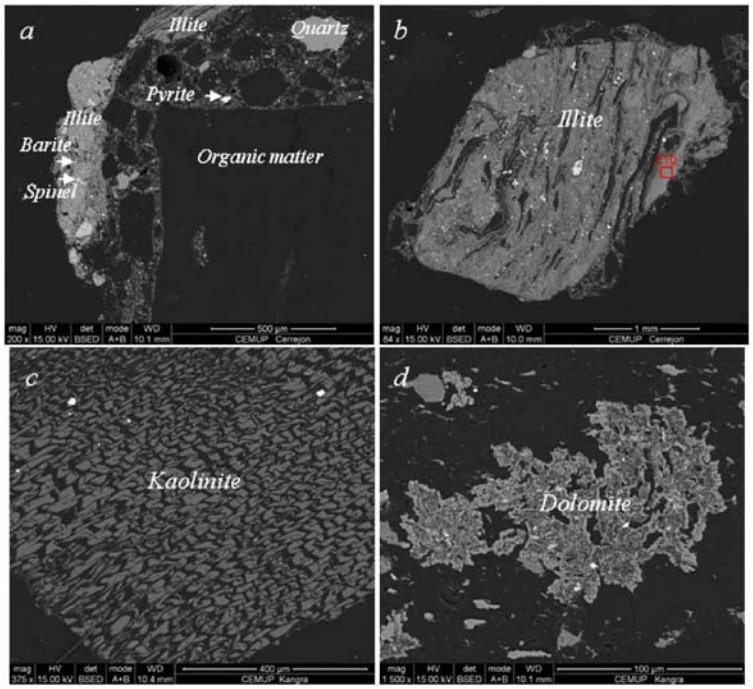

FIG. 1: Polished blocks, BSE detector. El Cerrejon coal: (a) fines (×200) and (b) illite mass (×100). Kangra coal: (c) kaolinite filling lumen cells (×375) and (d) dolomite nodules

quartz. To a lesser extent detritic feldspar, pyrite, and chalcopyrite, and trace amounts of monazite and Sr-bearing minerals.

3.2 Fly Ash

3.2.1 *Overview*

Visual characterization of the size distribution and morphotypes present in the FA samples (Fig. 2) shows that (i) the economizer is composed essentially of large-size particles such as char, glassy spheres, agglomerates, and quartz; (ii) the air heater sampling point is char poor and essentially composed of larger size particles, such as agglomerates and quartz; and (iii) the ESP hoppers 12 (ESP-h12) and 42 (ESP-h42) have a high number of small glassy particles.

This size decrease is due to the upstream end of the ESP collecting the most (about 80%) and coarsest ash. At the downstream end the smallest and least-conductive particles are captured (Hower et al., 2001; Mardon and Hower, 2004). Two dominant types of glass were found, derived from melting and recrystallization of residues from thermal decomposition of the minerals and nonmineral inorganics in the feed coal at the high temperatures of the combustion chamber

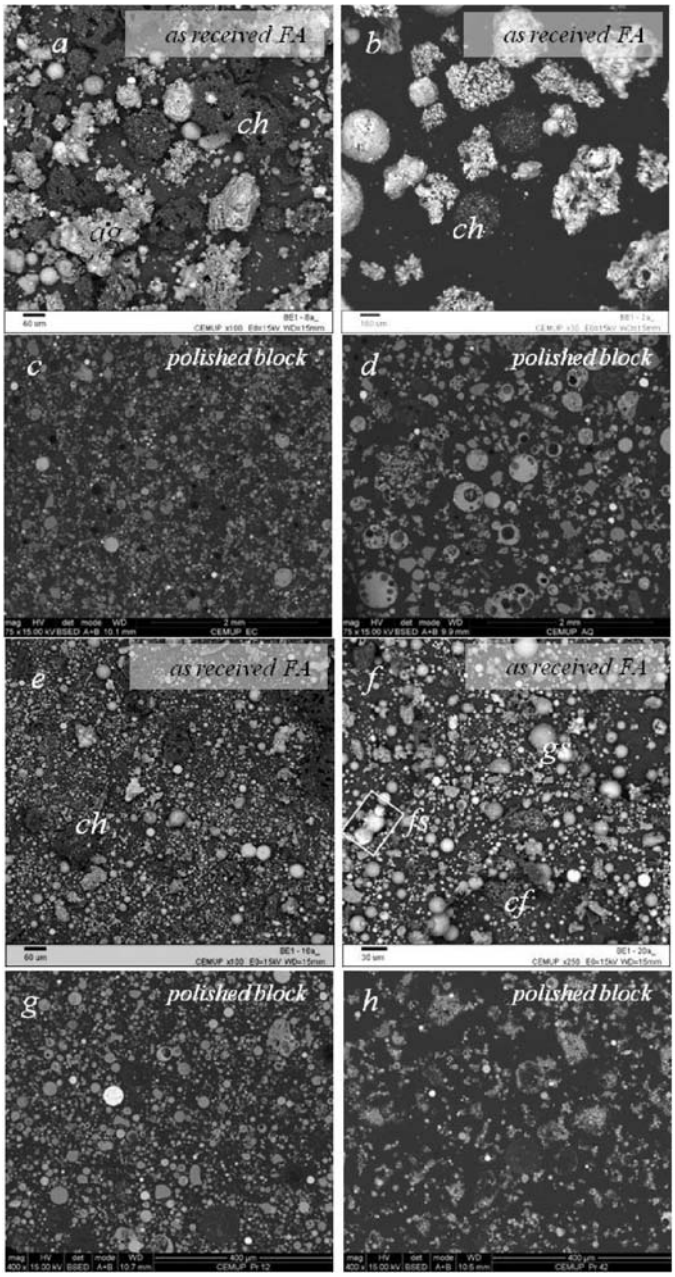

FIG. 2: Sampling locations overview: (a, c) economizer: large char particles (ch) and glassy agglomerations (ag); (b, d) air heater: most particles are large and irregular, and char is a minor component; (e–g) ESP-h12: large char particles, small glass spheres, iron spheres, and a background of microglassy spheres; (f–h) ESP h42: char fragments (cf), glassy spheres (gs), and ferrospheres (fs) in a background of microglassy spheres

(Matjie et al., 2008): (i) Si–Al glass, resulting from kaolinite, and (ii) Si–Al–K–Mg glass from illite (Figs. 6a and 6b), reflecting the feed composition, and melts of different composition (Anshits et al., 2001).

Finding ferro- and ferrispheres using the BSE detector was a fast and easy process due to the high atomic number of iron. Only few small sizes (>45 μm) of these morphotypes were found in the samples studied. This was expected, since the feeds are low-sulfur coals with low amounts of pyrite and other-iron bearing minerals.

3.2.2 *Morphotypes*

Char morphotypes.

Since carbon has low atomic number, SEM BSE mode is the best method to find char in "as-received" FA samples, the char being darker than glass and minerals in FAs. Only after SEM should the SE mode be used.

In the samples the diversity of char morphotypes is low (Fig. 3), mostly rounded and porous, with secondary vacuoles on their walls (Fig. 3a), probably originating

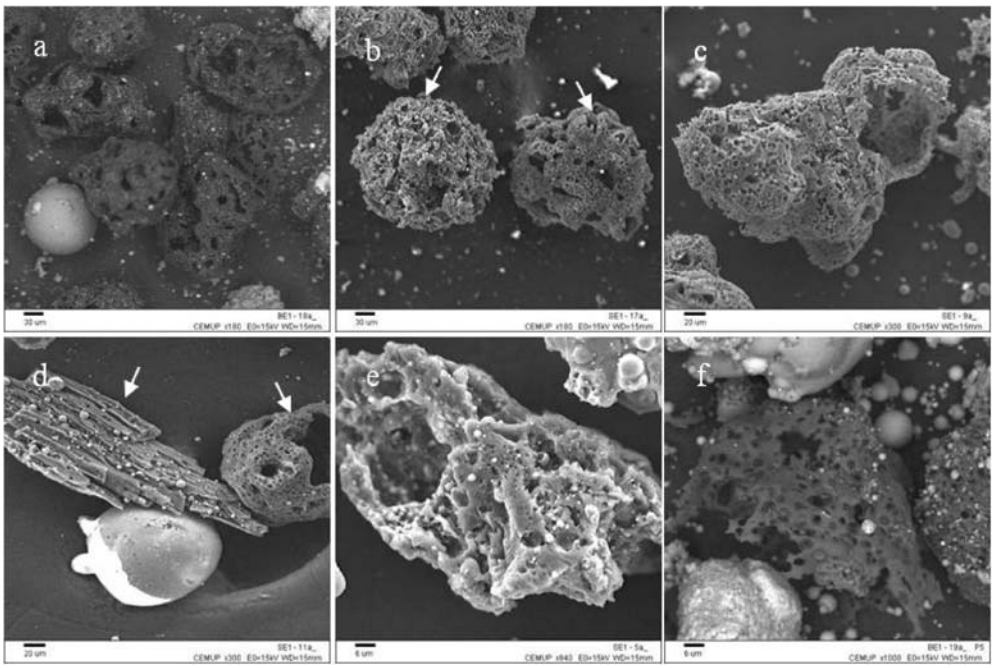

FIG. 3: Char morphotypes: (a) the most common char morphotypes observed (ESP-h12, ×30, BSE); (b) left, rounded particle with rough surface (ESP-h12, ×180, SE) and right, rounded particle with large pores on its surface connected to major vacuolization chambers (see also d); (c) thin-walled cenosphere (economizer, ×300, SE); (d) left, massive inertinitic (economizer, ×300, SE) and right, thin-walled cenosphere; (e) mixed char [large chamber (left) and dense (right)] (air heater, ×940, SE); and (f) thin-walled fragment showing secondary devolatization (ESP-h12, ×1000, BSE)

from vitrinite and semifusinite macerals (Bailey et al., 1990; Milenkova et al., 2003). These are divided into subtypes according to internal porosity, wall texture, and open pores: (i) rough surface, without large open pores (Fig. 3b-left), probably originating from semifusinite, and (ii) smooth surface, secondary devolatilization, open pores and large devolatilizaton chambers (Figs. 3b-right, 3c, and 3d-right), probably originating from vitrinite.

These subtypes occur most probably because the feed is composed of two different coals with 0.1% difference in vitrinite reflectance, very different maceral composition, and maceral associations.

Other morphotypes found are inertinitic dense char (Fig. 3d-left), mixed char (Fig. 3e), and cenosphere fragments (Fig. 3f). These result from the less reactive high reflectance inertinite macerals (Bailey et al., 1990; Rosenberg et al., 1996).

Glassy spheres.

In the samples two types of aluminosilicate glassy spheres prevail: (i) thick-walled cenospheres and (ii) dense spheres. These occur either as discrete particles or forming agglomerates, reflecting that a basic melt most probably proceeded from clay with Fe_2O_3 and alkaline oxides MnO, MgO, and CaO (Fig. 2; Fig. 4-left).

Thin-walled glassy spheres (Fig. 4-right) were also observed in lesser amounts, most probably resulting from an acid melt (Sokol et al., 2000), with mullite composition (Hulett and Weinberger, 1980).

Plerospheres.

In the samples studied, plerospheres are not a typical morphotype, most probably because the majority of the glass spheres are closed, thick-walled, or dense. How-

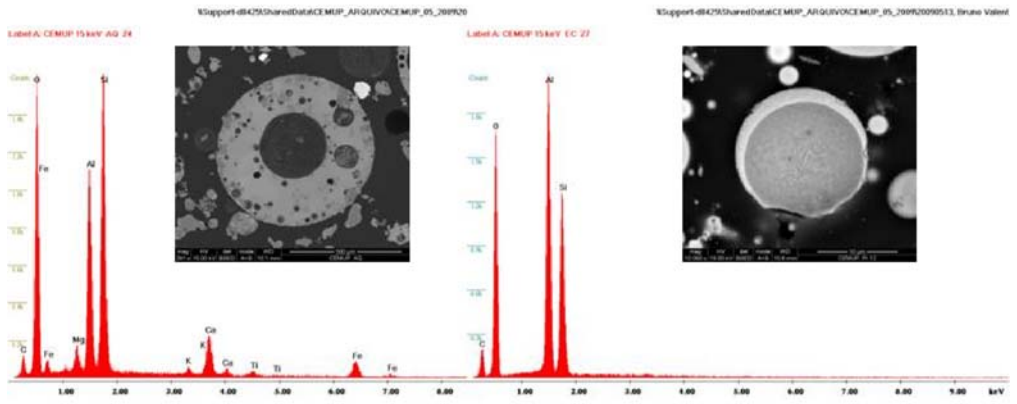

FIG. 4: SEM/EDS of glassy cenospheres (BSE, polished blocks): (left) thick-walled Si–Al–Mg–Ca–K–Fe–Ti cenosphere (air heater) and (right) thin-walled Si–Al cenosphere with mullite (economizer)

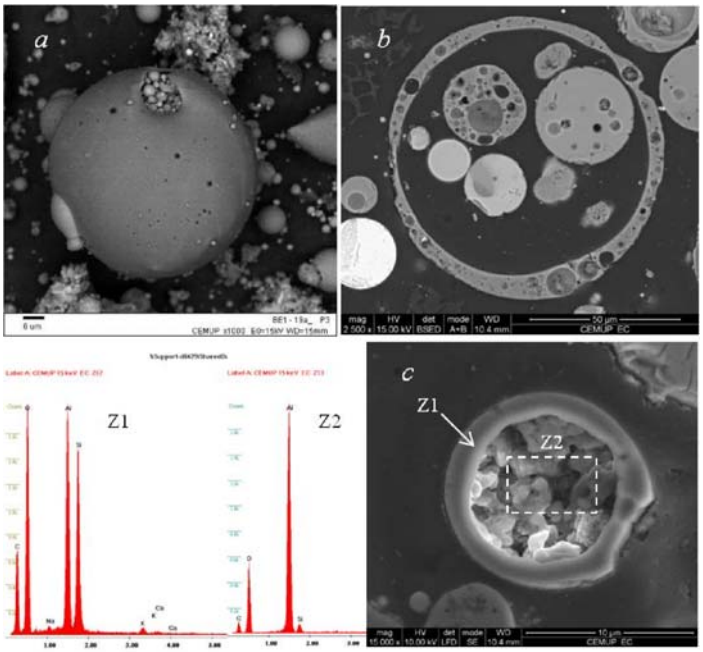

FIG. 5: Plerospheres (BSE; polished blocks): (a) as-received FA (ESP-h12, ×1000, BSE); (b) cross-section secondary plerosphere (economizer, ×2500, BSE); and (c) primary plerosphere (economizer, ×15,000, SE, cross section)

ever, some secondary or primary plerospheres were observed encapsulating microspheres (Figs. 5a and 5b), and almost pure Al (Fig. 5c) was also found in a primary plerosphere.

Dermaspheres.

Layered glassy spheres, as defined by Lauf (1982), are not abundant in the samples studied; otherwise cross sections of FA in polished blocks would reveal it. However, some particles present a thin layer of spinel microcrystals on a Si-Al glass surface (Fig. 6a). Most probably, some ferrospheres of "as-received FA" samples are dermaspheres with a similar phase distribution.

The BSE detector also revealed bright variations, intra- and intersphere related, with the EDS Al and Si peaks high. Usually, differences in brightness are related with Ca, Fe, Mg, Ti, and other elements.

For darker glassy spheres, dark zones, and near hole edges the Si–Al association seems to be the main factor for brightness differentiation, since in the EDS spectra the Al peak was higher than the Si peak (Figs. 6b and 6c).These peaks are not directly related with amounts but with electron emission and detection; however, darker areas and dark spots (best seen with SE detector) most probably result from

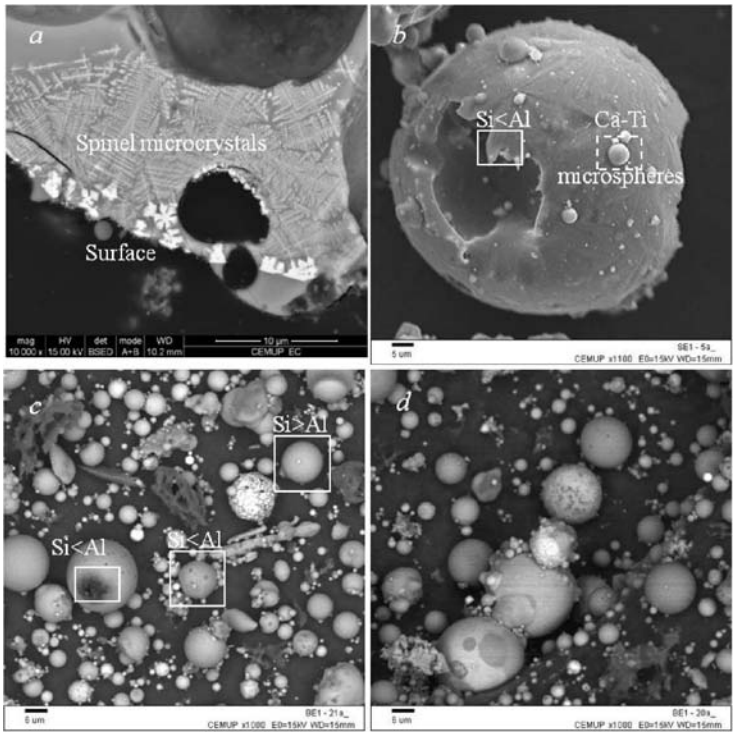

FIG. 6: Intra- and intervariability of glassy spheres (BSE; polished blocks): (a) dermasphere with a layer of spinel crystals; (b, c) brightness relation with Si–Al EDS peaks; and (d) economizer glassy sphere diversity

element partitioning, such as Fe, Cr, As, Ca, Ti, Al, Si, and O originating variations in size, wall thickness, density, and inner porous structure on the glass phase (Anshits et al., 2001, 2005; Booher et al., 1994; Gieré et al., 2003; Kutchko and Kim, 2006; Matsunaga et al., 2002; Mukhopadhyay et al., 1996; Spears, 2000).

SEM-BSE observations and respective EDS analysis also revealed that the same feed, combustion conditions, and sampling location may produce glassy sphere heterogeneity related with Si–Al proportions, partitioning of other elements such as Fe, Mg, and Ca, and immiscibility of melts (Fig. 6d).

Agglomerates.

Around a dozen EDS analyses performed on agglomerates showed that these are composed of fused micrometer glassy spheres with different compositions, having in common being aluminosilicates (Si > Al; similar to individual brighter glass cenospheres) with Ca and Fe. Likely, Ca–Fe low-viscosity melts enhanced coalescence and agglomeration of small particles.

Agglomerates are mentioned in several works (e.g., Fisher et al., 1975; Kutchko and Kim, 2006), but it seems that they were not considered important components. However, in the samples studied large (>75 μm) agglomerates are major components in the economizer and in the air heater. The technological implications of the agglomerates is not documented, but the size, irregular shape, and heterogeneity must have some impact.

Agglomerates may be divided into three types of particle clustering:

1. Interrupted coalescence clustering — two or more particles are bonded together during the melting phase of the places where they are to be bonded. Eventually, coalesced liquid will solidify in the contact zones, but at the end of this process the joined particles did not have become one continuous solid (Figs. 7a and 7b).
2. Weld pool clustering — a filler material from a pool of molten material (the weld pool) that cools to become a strong joint for individual particles, i.e., a coalescing molten filler aluminosilicate glass and flux interacts with a thin layer of the solidified particles, cooling to form a strong, sealed joint (Fig. 7c).

   The observation of weld pool clustering can only be accurately made by SEM backscattered electron mode using cross sections in polished blocks.

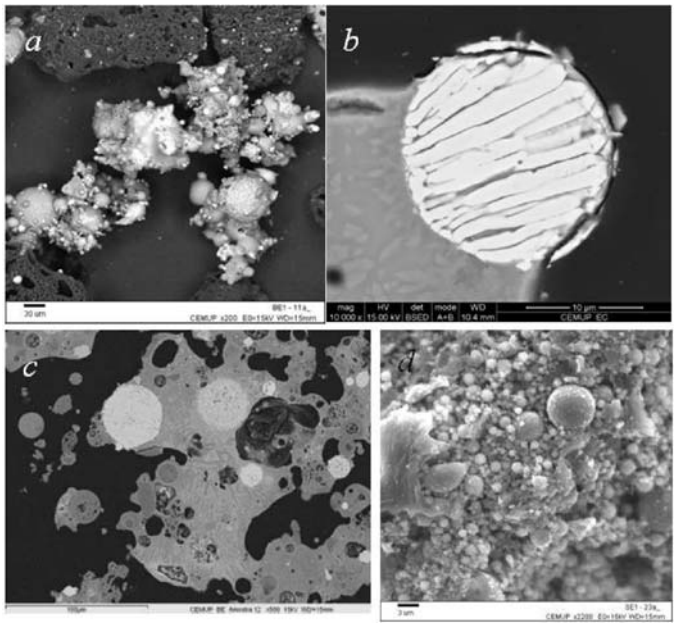

FIG. 7: Agglomerates. Interrupted coalescence clustering (economizer FA): (a) large agglomerate (as-received; BSE mode; ×200); (b) agglomerate composed of Si–Al sphere ferrosphere (polished block; BSE; ×440); (c) weld pool clustering (economizer; BSE; ×10000); and (d) Si–Al spheres pseudoclustering at char surface (ESP-h42; SE; ×2200)

3. Pseudoclustering — agglomeration of small particles on larger particles surface due to weak surface forces, whereby the individual particles do not lose their identity and may be easily dispersed by agitation or water suspension (Fig. 7d).

The basicity of the melts [(CaO + MgO)/(SiO_2 + Al_2O_3)], related to the original feed composition, leads to variations in the viscosity and gas retention explains in part the morphologies found in FA glass (Anshits et al., 2001). In the present study, coals are rich in basic element minerals, so massive microspheres prevail as discrete particles or agglomerates (Valentim et al., 2009).

Ferrospheres, ferrispheres, and other spheres.

The ferro- and ferrispheres found in this study are small (>75 μm) and are composed of hematite, magnetite, and other spinels. These morphotypes may be composed of submicrometer iron mineral top-layering dermaspheres, micrometer dendritic spinel crystals embedded in a Si–Al glass matrix, or monomineral (hematite) spheres (Figs. 8a–8c, respectively).

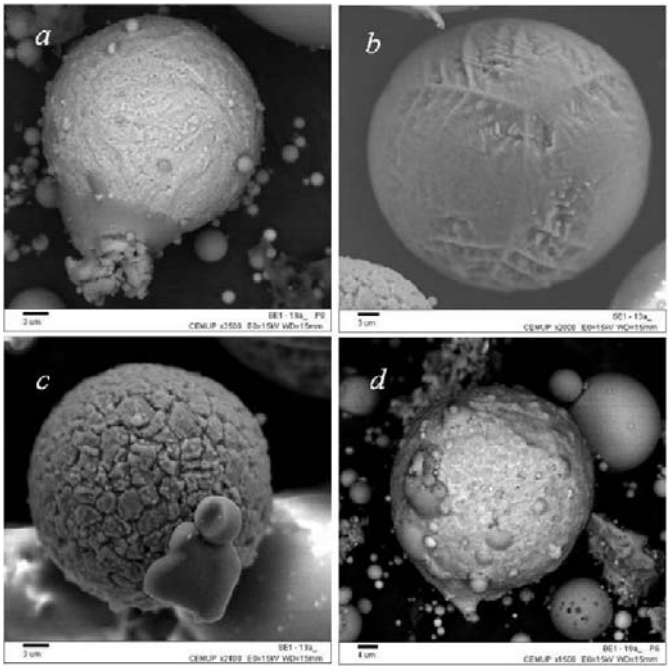

FIG. 8: Fe-rich spheres: (a) iron-rich dermaplerosphere (ESP-h12; ×2500; BSE); (b) ferrosphere: dendritic crystals of Ca–Fe spinel embedded in Si–Al glass (economizer; ×2000; SE); (c) ferrisphere: hematite composition (economizer; ×2000; SE); and (d) Ca-rich sphere (ESP-h12; ×1500; BSE)

Other BSE bright FA morphotypes (generally 5m), which may be mistaken by iron-rich spheres, were identified by EDS as being Ca–Ti bearing aluminosilicate glasses with no iron. These Ca-rich spheres were first reported by Mukhopadhyay et al. (1996) and could be denominated calcispheres (Fig. 8d).

Minerals.

In the samples studied, primary quartz was easily identified at the locations closest to the furnace (economizer and air heater ashes) or inside small glassy fly ash spheres. In many cases, quartz, probably of detrital origin, preserved its angular shape (Fig. 9a), which seems to be related to combustion conditions, since quartz minerals do not melt at combustion temperatures of 1300–1350°C (Goodarzi, 2006). In cross-sectioned polished blocks using a BSE detector, it was found that a high amount of quartz was embedded inside the glass matrix (Fig. 9b).

Other primary minerals could only be found using a BSE detector in cross sections of FA, since they are of submicrometer size and embedded inside the glass matrix, such as monazite.

Newly formed minerals include cristobalite at the quartz surface, iron-bearing minerals (hematite, magnetite, and other spinels; Fig. 8), and mullite microcrystals (Fig. 4).

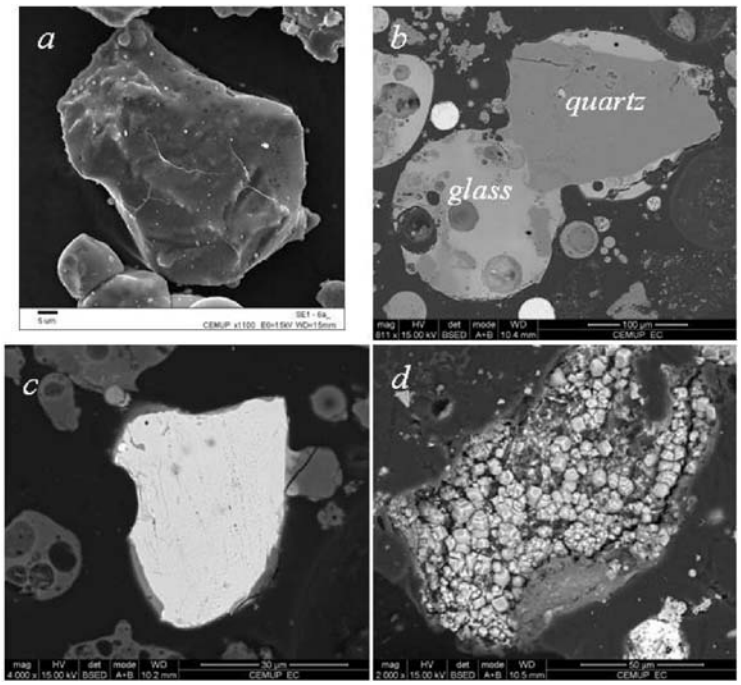

FIG. 9: Minerals: (a) primary quartz (air heater; ×1100; SE); (b) primary quartz embedded in Si–Al glass (economizer; ×811; BSE); (c) monazite (economizer; ×4000; BSE); and (d) calcite (economizer; ×4000; BSE)

Tertiary minerals, resulting from reactions after FA capture inside the hoppers (Bauer and Natusch, 1981), storing, and handling, resume to calcite minerals.

Particulate matter.

The sample to study particulate matter was collected at the stack, and it was found that it is essentially composed of glassy micrometer and submicrometer (1–10 μm and <1 μm) spheres with different compositions, particles (0.1–1 μm) attached to the surface of the larger spheres, and char particles.

No holes or pores are visible at the glassy spheres, and their small size indicates that most probably they are dense, as shown by Goodarzi (2006) in the $PM_{2.5}$ fraction of Canadian FA. The EDS spectrum of these particles (except char) revealed a complex composition made of three and more dominant elements composing the particle matrix. However, Ca, P, and S in these particles most probably resulted from condensation at the particle surface (Fig. 10).

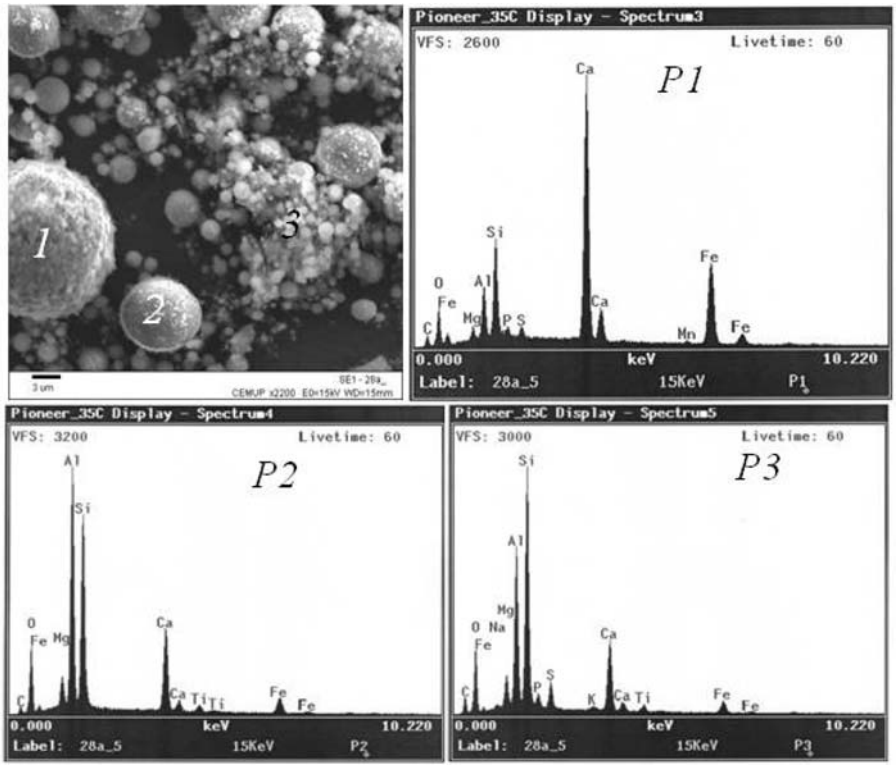

FIG. 10: Particulate matter (from stack). Micrograph of micrometer and submicrometer FA (×2200; SE) and EDS spectra

4. CONCLUSIONS

The SEM overview of the fly ash showed that the coarsest, most irregular, and residual minerals are collected near the furnace. From the upstream end to the downstream end of the ESPs, particles are smoother, spherical, and smaller, meaning that inside the ESPs variations in particle capture also occur. Most probably density and aerodynamics of the particles in the gas flow influence the particle capture at first, while the electrostatic properties of the particles are crucial for collection in the ESPs. So the most inert and small particles are captured only at the output end of the precipitator.

According to their inner structure, brightness, and Si–Al peaks it was found that in the same TPP several different types of glassy cenospheres are produced, including also glassy agglomerates that are very large and irregular.

Ferro- and ferrispheres were observed to be small and not abundant, which is due to the low availability of pyritic iron in the coals. In general, that is a solution to decrease sulfur dioxide emissions but may contribute to reduce particles capture in the ESPs.

Using the BSE mode and the high resolution of the SEM, it was possible to see that the particulate matter from the stack includes char, complex aluminosilicate glass, and condensed elements such as Ca, P, and S.

These observations have implications on particulate capture, economy, technology, and environment, e.g., too large and irregular particles of glass agglomerates and large char are captured near the furnace together with many other particles, making them not saleable for concrete production and requiring disposal on landfills or ponds; low iron availability in the coals could be responsible for higher amounts of inert particles in the output end of the precipitator and an increase in particulate matter emissions; and too much heterogeneity of fly ash morphotypes decrease its quality.

ACKNOWLEDGMENTS

The authors thank the Fundação para a Ciência e a Tecnologia (Portugal) and FEDER (UE) for financing the project (contract POCTI/CTA/38997/01).

REFERENCES

Anshits, A.G., Kondratenko, E.V., Fomenko, E.V., Kovalev, A.M., Anshits, N.N., Bajukov, O.A., Sokol, E.V., and Salanov, A.N., Novel glass crystal catalysts for the processes of methane oxidation, *Catal. Today*, vol. 64, pp. 59–67, 2001.

Anshits, N.N., Vereshchagina, T.A., Bajukov, O.A., Salanov, A.N., and Anshits, A.G., The nature of nanoparticles of crystalline phases in cenospheres and morphology of their shells, *Glass Phys. Chem.*, vol. 31, pp. 306–315, 2005.

Bailey, J.G., Tate, A., Diessel, C.F.K., and Wall, T.F., A char morphology system with applications to coal combustion, *Fuel*, vol. 69, pp. 225–239, 1990.

Bauer, C.F. and Natusch, D.F.S., Identification and quantitation of carbonate compounds in coal fly ash, *Environ. Sci. Technol*., vol. 15, pp. 783–88, 1981.

Booher, H.B., Martello, D.V., Tamilia, J.P., and Irdi, G.A., Microscopic study of spherical particulates in fly ash, *Fuel*, vol. 73, pp. 205–213, 1994.

Buhre, B.J.P., Hinkleya, J.T., Gupta, R.P, Walla, T.F., and Nelson, P.F., Submicron ash formation from coal combustion, *Fuel*, vol. 84, pp. 1206–1214, 2005.

Chen, Y., Shah, N., Huggins, F.E., Huffman, G.P., Linak, W.P., and Miller, C.A., Investigation of primary fine particulate matter from coal combustion by computer-controlled scanning electron microscopy, *Fuel Process. Technol*., vol. 85, pp. 743–761, 2004.

Chen, Y., Shah, N., Braun, A., Huggins, F.E., and Huffman, G.P., Electron microscopy investigation of carbonaceous particulate matter generated by combustion of fossil fuels, *Energy Fuels*, vol. 19, pp. 1644–1651, 2005a.

Chen, Y., Shah, N., Braun, A., Huggins, F.E., and Huffman, G.P., Transmission electron microscopy investigation of ultrafine coal fly ash particles, *Environ. Sci. Technol*., vol. 39, pp. 1144–1151, 2005b.

Fischer, G.L., Chang, D.P.Y., and Brummer, M., Fly ash collected from electrostatic precipitators: Microcrystalline structures and the mystery of the spheres, *Sci. Magazine*, vol. 7, pp. 553–555, 1975.

Fisher, G.L., Prentice, B.A., Silberman, D., Ondov, J.M., Biermann, A.H., Ragaini, R.C., and McFarland, A.R., Physical and morphological studies of size-classified coal fly ash, *Environ. Sci. Technol.*, vol. 12, pp. 447–51, 1978.

Hulett, L.D. and Weinberger, A.J., Some etching studies of the microstructure and composition of large aluminosilicate particles in fly ash from coal-burning power plants, *Environ. Sci. Technol.*, vol. 14, pp. 965–970, 1980.

Gieré, R., Carleton, L.E., and Lumpkin, G.R., Micro- and nanochemistry of fly ash from a coal-fired power plant, *Am. Mineral*., vol. 88, pp. 1853–1865, 2003.

Goodarzi, F., Morphology and chemistry of fine particles emitted from a Canadian coal-fired power plant, *Fuel*, vol. 85, pp. 273–280, 2006.

Goodarzi, F. and Sanei, H., Plerosphere and its role in reduction of emitted fine fly ash particles from pulverized coal-fired power plants, *Fuel*, vol. 88, pp. 382–386, 2009.

Griffin, J.J. and Goldberg, E.D., The flux of elemental carbon in coastal marine sediments, *Limnol. Oceanogr*., vol. 20, pp. 456–463, 1975.

Griffin, J.J. and Goldberg, E.D., Morphologies and origin of elemental carbon in the environment, *Science*, vol. 206, no. 2, pp. 563–565, 1979.

Griffin, J.J. and Goldberg, E.D., Sphericity as a characteristic of solids from fossil fuel burning in a Lake Michigan sediment, *Geochim. Cosmochim. Acta*, vol. 45, pp. 763–769, 1981.

Hower, J.C., Trimble, A.S., and Eble, C.F., Temporal and spatial variations in fly ash quality, *Fuel Process. Technol.*, vol. 73, pp. 37–58, 2001.

Jones, M.R., McCarthy, A., and Booth, A.P., Characteristics of the ultrafine component of fly ash, *Fuel*, vol. 85, pp. 2250–2259, 2006.

Kutchko, B.G. and Kim, A.G., Fly ash characterization by SEM–EDS, *Fuel*, vol. 85, pp. 2537–2544, 2006.

Laskowski, J.S., Coal flotation and fine coal utilization, *Developments in Mineral Processing*, vol. 14, D.W. Fuerstenau (Adv. Ed.), Elsevier, p. 368, 2001.

Lauf, R.J., Microstructures of coal fly ash particles, *Am. Ceram. Soc. Bull*., vol. 61, pp. 487–490, 1982.

Lauf, R.J., Harris, L.A., and Rawlston, S.S., Pyrite framboids as the source of magnetite spheres in fly ash, *Environ. Sci. Technol*., vol. 16, pp. 218–220, 1982.

Lightman, P. and Street, P.J., Microscopical examination of heat treated pulverized coal particles, *Fuel*, vol. 47, pp. 7–28, 1968.

Mardon, S.M. and Hower, J.C., Impact of coal properties on coal combustion by-product quality: Examples from a Kentucky power plant, *Int. J. Coal Geol*., vol. 59, pp. 153–169, 2004.

Matjie, R.H., Li, Z., Ward, C.R., and French, D., Chemical composition of glass and crystalline phases in coarse coal gasification ash, *Fuel*, vol. 87, pp. 857–869, 2008.

Matsunaga, T., Kim, J.K., Hardcastle, S., and Rohatgi, P.K., Crystallinity and selected properties of fly ash particles, *Mater. Sci. Eng*., vol. A325, pp. 333–343, 2002.

Milenkova, K.S., Borrego, A.G., Alvarez, D., Xiberta, J., and Menéndez, R., Tracing the origin of unburned carbon in fly ashes from coal blends, *Energy Fuels*, vol. 17, pp. 1222–1232, 2003.

Miller, S.F. and Schobert, H.H., Effect of fuel particle and droplet size distribution on particle size distribution of char and ash during pilot-scale combustion of pulverized coal and coal–water slurry fuels, *Energy Fuels*, vol. 7, pp. 520–531, 1993.

Miller, S.F. and Schobert, H.H., Effect of the occurrence and composition of silicate and aluminosilicate compounds on ash formation in pilot-scale combustion of pulverized coal and coal–water slurry fuels, *Energy Fuels*, vol. 8, pp. 1197–1207, 1994.

Mukhopadhyay, P.K., Lajeunesse, G., and Crandlemire, A.L., Mineralogical speciation of elements in an eastern Canadian feed coal and their combustion residues from a Canadian power plant, *Int. J. Coal Geol*., vol. 32, pp. 279–312, 1996.

Nandi, B.N., Brown, T.D., and Lee, G.K., Inert coal macerals in combustion, *Fuel*, vol. 56, pp. 125–130, 1977.

Ramsden, A.R. and Shibaoka, M., Characterization and analysis of individual fly-ash particles from coal-fired power stations by a combination of optical microscopy, electron microscopy and quantitative electron microprobe analysis, *Atmos. Environ*., vol. 16, pp. 2191–2206, 1982.

Rosenberg, P., Petersen, H.I., and Thomsen, E., Combustion char morphology related to combustion temperature and coal petrography, *Fuel*, vol. 75, pp. 1071–1082, 1996.

Severin, K.P., *Energy Dispersive Spectrometry of Common Rock Forming Minerals*, Kluwer Academic Publishers, Dordrecht, Boston, London, p. 225, 2004.

Shah, A.D., Huffman, G.P., Huggins, F.E., Shah, N., and Helble, J.J., Behavior of carboxyl-bound potassium during combustion of an ion-exchanged lignite, *Fuel Process. Technol*., vol. 44, pp. 105–120, 1995.

Sokol, E.V., Maksimova, E.V., Volkova, N.I., Nigmatulina, E.N., and Frenkel, A.E., Hollow silicate microspheres from fly ashes of the chelyabinsk brown coals (the South Urals, Russia), *Fuel Process. Technol*., vol. 67, pp. 35–52, 2000.

Spears, D.A., Role of clay minerals in UK coal combustion, *Appl. Clay Sci.*, vol. 16, pp. 87–95, 2000.

Stoffyn-Egli, P., Potter, T.M., Leonardby, J.D., and Pocklington, R., The identification of black carbon particles with the analytical scanning electron microscope: methods and initial results, *Sci. Total Environ.*, vol. 198, pp. 211–223, 1997.

Valentim, B., Guedes, A., Flores, D., Ward, C.R., and Hower, J.C., Variations in fly ash composition with sampling location: Case study from a Portuguese power plant, *Coal Combust. Gasification Products*, vol. 1, pp. 14–24, 2009.

Valentim, B., Lemos de Sousa, M.J., Abelha, P., Boavida, D., and Gulyurtlu, I., The identification of unusual microscopic features in coal and their derived chars: Influence on coal fluidised bed combustion, *Int. J. Coal Geol*., vol. 67, pp. 202–211, 2006.

Vassilev, S.V., Menendez, R., Diaz-Somoano, M., and Marinez-Tarazona, M.R., Phase-mineral and chemical composition of coal fly ashes as a basis for their multicomponent utilization. 2. Characterization of ceramic cenosphere and salt concentrates, *Fuel*, vol. 83, pp. 585–603, 2004.

Vassilev, S.V. and Vassileva, C.G., Mineralogy of combustion wastes from coal-fired power stations, *Fuel Process. Technol*., vol. 47, pp. 261–280, 1996.

Vassilev, S.V. and Vassileva, C.G., Methods for characterization of composition of fly ashes from coal-fired power stations: A critical overview, *Energy Fuels*, vol. 19, pp. 1084–1098, 2005.

Vassilev, S. and Vassileva, C., A new approach for the classification of coal fly ashes based on their origin, composition, properties, and behaviour, *Fuel*, vol. 86, pp. 1490–1512, 2007.

Xue, Q. and Lu, S., Microstructure of ferrospheres in fly ashes: SEM, EDX and ESEM analysis, *J. Zhejiang Univ., Sci*., vol. A9, pp. 1595–1600, 2008.

Zhao, Y., Zhang, J., Sun, J., Bai, X., and Zheng, C., Mineralogy, chemical composition, and microstructure of ferrospheres in fly ashes from coal combustion, *Energy Fuels*, vol. 20, pp. 1490–1497, 2006.

International Journal of Energy for a Clean Environment, 10(1–4), 167–179 (2009)

FORMULATION OF COMMERCIALLY FEASIBLE MARINE MICROALGAE CULTIVATION MEDIA FOR BIOFUEL PRODUCTION

Beena Patel, Bharat Gami, & Hiral Bhimani*

Abellon Cleanenergy, Ltd., Research and Development, Sydney House, Premchand Nagar Road, Bodakdev, Ahmedabad-380054, India

*Address all correspondence to Beena Patel,
E-mail: beena.patel@abelloncleanenergy.com
web address: www.abelloncleanenergy.com.

Algae was initially examined as a potential replacement fuel source for fossil fuels in the 1970s, but prohibitive production costs and limitations discouraged the commercial development of algae-based fuel production. Subsequent studies, continued through the 1980s and heightened in the last 15 years, illustrate that research developments are enabling the commercial potential of microalgae to shift from aquaculture, fine chemicals, and health food to fuel production for large-scale production. Cultivation models practiced so far are through open raceway ponds and photobioreactors. The feasibility of the process depends on the cultivation medium coating, which gives high productivity, a desirable end product, and the components of the medium are easily available. Abellon Cleanenergy is a company focusing on developing feasible process parameters for biofuel production. The present study is on algae cultivation for viable commercial propositions through low-cost cultivation mediums with enhanced growth. It is the first of its kind from India reporting experimental results for Dunaliella tertiolecta (marine microalgae) in a fertilizer-based medium (AG 11), showing high oil yield at a low ingredient cost compared to other synthetic media.

KEY WORDS: *Dunaliella tertiolecta, biodiesel, photobioreactor, fertilizer, biofuel*

1. INTRODUCTION

It has been discovered that certain strains of microalgae contain 50% dry weight lipid (oil) content. As a result, interest is being generated for research and development of algae farms for the cultivation of microalgae which could then be harvested and/or processed into a number of new energy sources and byproducts. During the aquatic species program in 1970 (USA), algae was explored for its high lipid yield, which can be used as a new source of renewable energy for transportation fuel. Although there is a concerted effort to produce a strategic plan for the development of an algal biofuels industry (McGraw, 2009), there is still no commercial production facility for algal biofuels.

Microalgae possess vast potential in different industrial applications such as pharmaceutical, health food, carotenoids, dyes, fine chemicals, biofuels, and many more (Faulker, 1986; Markov et al., 1997; Borowitzka, 1999). Microalgae convert solar energy into chemical energy through photosynthesis and store this energy in the form of lipids, carbohydrates, and proteins. These cellular constituents can be used to derive lots of energy products including biodiesel, gasoline, and ethanol. These transportation fuels are of interest as they help in energy security by reducing dependency on import of foreign oil. Second, being less environmentally detrimental than the fossil fuels currently in use, these biofuels have potential to reduce greenhouse gas (GHG) emissions. In addition to these fuels, other energy products such as methane, biohydrogen, and other hydrocarbons can be elicited and produced from algae (Chisti, 2007; Aden, 2007).

Microalgae cultivation is not a new subject. The first microalgae (*Chlorella vaulgaris*) culture was achieved by Beijierinck (1890). Commercial large-scale cultivation of some microalgae commenced in the early 1960s in Japan (Tsukada et al., 1977). At the same time, two other microalgae, *Spirulina* and *D. salina*, were also explored for commercial cultivation (Borowitzka, 1999). For the last two decades these miniature organisms have been targeted for biofuel production. The value gained from algae cultivation for medicine, nutraceuticals, and for food/feed will be very high as compared to an energy product derived from algae. Thus reduction in cultivation cost is one of the most crucial steps for cultivation of microalgae at a commercial scale in the energy sector. Development of a low-cost medium is one such parameter which can help in reducing cultivation costs. Along with cost reduction as a primary concern, one needs to ensure that the required nutrients are present in an appropriate form and at noninhibitory concentration (Greasham and Herber, 1997).

However, to be able to make the best use of these miniature organisms, they need to be cultivated in large quantities. Algae are a very undemanding life form — they need only water, carbon dioxide, nutrients, and sunlight. Except for the nutrients, everything is available freely and abundantly in nature. The amounts and types of nutrients play an important and vital role to minimize the cost of production in large-scale cultivation. Our efforts in this direction led to this first-of-its-kind study from India reporting on a low-cost cultivation medium for *Dunaliella tertiolecta.*

2. MATERIALS AND METHODS

Algae strain procurement: A pure culture of *Dunaliella tertiolecta* Butcher (CCMP1320) strain was procured from the Culture Collection of Marine Phytoplankton (CCMP, USA).

Inoculum development: Pure culture was maintained in sterile (at 121^{o}C for 15 min) artificial sea water, medium full strength (100%), as mentioned in Table 1 at 25^{o}C under 4500 lux fluorescent light. A 10-day-old *D. tertiolecta* culture was used as inoculum for experiments.

TABLE 1: Ingredient of medium used in cultivation of *D. tertiolecta*

Ingredient	Medium					
	Full concentration (100%)			Half concentration (50%)		
	ASW (g/L)	f2-Si (g/L)	AG 11 (g/L)	ASW (g/L)	f2-Si (g/L)	AG 11 (g/L)
NaCl	23.926	23.926	23.926	11.96	11.96	11.96
Na_2SO_4	4.088	4.088	0.0	2.044	2.044	0.0
KCl	0.677	0.677	0.677	0.338	0.338	0.338
$NaHCO_3$	0.196	0.196	0.196	0.098	0.098	0.098
KBr	0.098	0.098	0.0	0.049	0.049	0.0
H_3BO_3	0.026	0.026	0.0	0.013	0.013	0.0
NaF	0.003	0.003	0.0	0.0015	0.0015	0.0
$SrCl_2$–$6H_2O$	0.002	0.002	0.0	0.001	0.001	0.0
$MgCl_2$–$6H_2O$	0.053	0.053	0.0	0.026	0.026	0.0
$CaCl_2$–$2H_2O$	1.518	1.518	0.0	0.759	0.759	0.0
$NaNO_3$	0.0	0.075	0.0	0.0	0.0375	0.0
NaH_2PO_4–$2H_2O$	0.0	0.0056	0.0	0.0	0.0028	0.0
Mosaic — potassium magnesium sulfate fertilizer	0.0	0.0	0.083	0.0	0.0	0.0415
Soda ($NaHCO_3$)	0.0	0.0	0.5	0.0	0.0	0.25

Algae cultivation: Three media, f2-Si, artificial sea water (ASW), and AG 11 were prepared in distilled water containing ingredient mention in Table 1. All three media used at two different concentrations [full concentration (100%) and half concentration (50%)] in a 1 L erlenmeyer flask containing 245 mL of respective medium were inoculated under aseptic condition with 15% inoculum of *D. tertiolecta* culture. All inoculated flasks were maintained at 25°C under 4500 lux fluorescent light for a 16 h light and 8 h dark period. Table 2 shows composition of the fertilizer used in all three media.

Algae cultivation monitoring: Cultivation of *D. tertiolecta* was monitored by a pH, gravimetric method (dry cell mass measurement) and turbidimetric method [optical density (OD) measure at 670 nm] as described by Payer (1971) every day after inoculation. Total chlorophyll was also measured along with a parameter to understand the pigment behavior of *D. tertiolecta*. Total chlorophyll was extracted from a 4 mL sample from each culture medium after mixing thoroughly. Cells were spun at 3000 g for 5 min and the pelleted biomass mixed with 4 mL of acetone/water (80:20 v/v). The mixtures were vortexed for 1–2 min to ensure com-

TABLE 2: Composition of the fertilizer used in *D. tertiolecta* cultivation

Composition	APS	DAP	Mosaic
Moisture by wt% max.	1.0	1.5	1.0
Total nitrogen by wt% min.	20.0	18.0	0.0
Ammonical nitrogen from by wt% min.	18.0	15.5	0.0
Total N_2 in form of urea, by wt% max.	2.0	2.5	0.0
Neutral ammonium citrate soluble phosphates as (P_2O_5) by wt% min.	20.0	46.0	0.0
Water-soluble phosphate (as P_2O_5), by wt% min.	17.0	41.0	0.0
Sulfur by wt% min.	13.0	0.0	0.0
Potassium	0.0	0.0	22
Magnesium	0.0	0.0	18
Water-soluble sulfate	0.0	0.0	20

plete extraction. Tubes were centrifuged again for 5 min at 3000 g, and the colorless biomass was discarded (Jin et al., 2003). The amount of extracted pigments in the solvent phase was quantified by a spectrophotometric method described by Lichtenthaler (1987).

Oil extraction: After 20 days of cultivation, algae cells were harvested by centrifugation at 3000 g for 15 min, washed twice with distilled water, and a dried biomass obtained by keeping it in an oven at 45^{o}C. Lipid was extracted from the dried biomass by a method reported by Takagi et al. (2000). Dried biomass (30 mg) was mixed with a methanol/chloroform solution (2:1, v/v) and sonicated for 1 h. After precipitation of the mixture with methanol/chloroform solution, chloroform and 1% NaCl solution were then added to give a ratio of methanol, chloroform, and water of 2:2:1. The mixture was centrifuged at 1000 g for 10 min and the chloroform phase was recovered in a clean paperweight tube. Finally, chloroform was evaporated by vacuum in a rotary evaporator and the remainder was weighed as lipid.

Ingredient costing: All laboratory-grade ingredients (except SSP, ASP, mosaic), as mentioned in Table 1, were purchased from Ranbaxy Fine Chemicals, Ltd. Fertilizers such as DAP (di-ammonium phosphate) and APS (ammonium phosphate fertilizer) were bought from an authorized distributor, Gujarat State Fertilizers & Chemicals, Ltd. Mosaic, potassium magnesium sulfate fertilizer was obtained from the Anand Agricultural University, Anand. The final cost for ingredients was derived from the required chemical amount in respective media.

Statistical analysis: Data were statistically analyzed using the SPSS statistical software (version 15.0; SPSS, Inc., Chicago, IL). A student's paired "t" test was performed to compare OD, dry biomass, and chlorophyll content during the growth

period between all three media at full-strength and half-strength concentration. The correlation between OD, dry biomass, and chlorophyll content was performed by all three media at full- and half-strength concentration using Person and Spearman correlation analysis. Statistical significance was considered when "p" values were less than 0.05.

3. RESULTS

3.1 Algae Growth and pH Change

Results obtained for pH change during cultivation of *D. tertiolecta* are shown in Fig. 1. In all three media at both concentrations, pH was set at 7.5 at the time of the inoculation of *D. tertiolect*a, but at the end of the experiment (after 20 days) the pH value was toward basic. Except AG 11 half strength, in almost all media pH was from 8.5 to 9.5 at the time of termination. In all media, the pH value gradually moved toward basic. In AG 11 medium at both concentrations (half and full), the pH behavior during cultivation was similar to the pH behavior of f2-Si and ASW media. In all media during cultivation, the l pH value moved toward basic as the culture became older.

3.2 Algae Growth Monitoring

Growth of *D. tertiolecta* was measured by the turbidimetric method (optical density). Gradually an increase in OD was observed in all three media at both concentrations (Fig. 2). Chronologically, in all six media OD increased from 0.2 to 0.66 OD. After 20 days cultivation of *D. tertiolecta*, the highest OD value was reported in half-strength ASW medium while the lowest value was reported in AG 11 full-

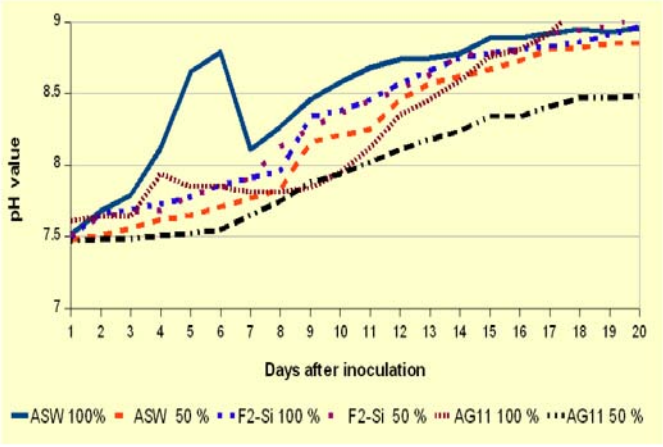

FIG. 1: pH of the culture medium

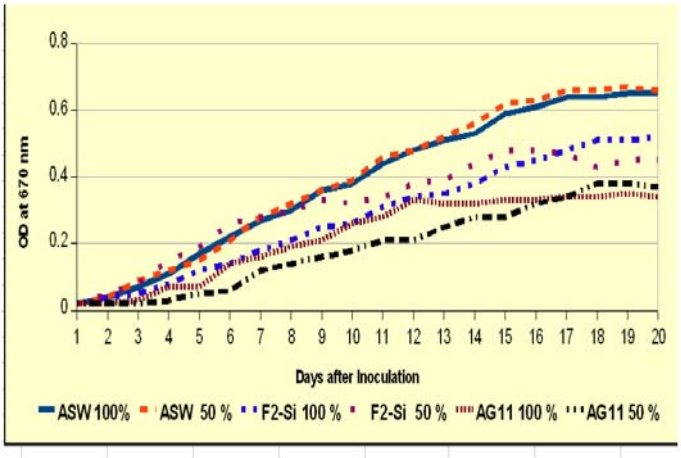

FIG. 2: Optical density of the culture medium measured at 670 nm

strength medium. A twofold increase in OD was observed in ASW medium as compared to AG 11 medium, and the same result was observed for dry biomass as well.

3.3 Algae Dry Biomass and Growth Monitoring

The gravimetric method (cell dry weight determination) was used for growth monitoring (Fig. 3). Among all applied concentrations, nominal differences were observed for a total yield of biomass, between half-strength and full-strength concentration, respectively. At the time of inoculation, 0.08–0.09 g/L dry weight

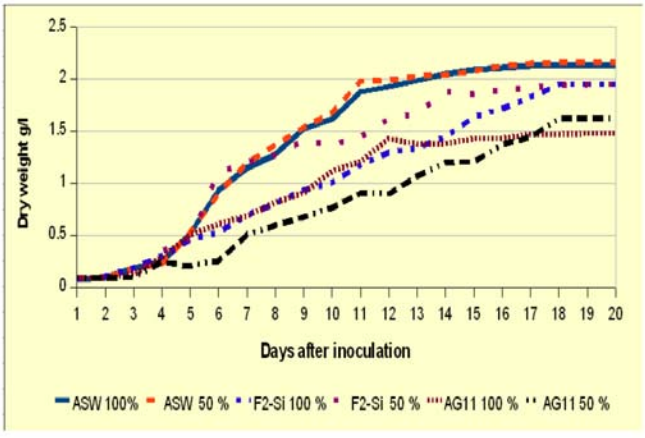

FIG. 3: Yield of biomass

was reported, but after 20 days of cultivation the highest dry weight (2.16 g/L) was observed in half-strength ASW medium, while in full strength of ASW medium the dry weight was 2.16 g/L. In the case of f2-Si medium, both at full strength and half strength, the same amount of dry weight (1.95 g/L) was recorded. Like the ASW medium, in Ag 11 medium the high amount (1.62 g/L) of dry weight was observed in half-strength medium as compared to a full-strength medium (1.48 g/L).

3.4 Growth of Algae and Chlorophyll Content

The chlorophyll content of algae cells directly represents the growth status of algae cells in respective medium during cultivation periods (Table 3). Total chlorophyll

TABLE 3: Total chlorophyll content of algae biomass during cultivation

Days	Total chlorophyll (mg/l)					
	ASW medium		f2-Si medium		AG11 medium	
	100.00%	50.00%	100%	50%	100%	50%
1	0.01	0.01	0.013	0.018	0.019	0.018
2	0.04	0.01	0.044	0.046	0.022	0.018
3	0.07	0.03	0.055	0.073	0.031	0.021
4	0.013	0.08	0.086	0.137	0.078	0.027
5	0.2	0.13	0.130	0.173	0.078	0.034
6	0.31	0.31	0.154	0.237	0.157	0.076
7	0.32	0.33	0.192	0.255	0.179	0.094
8	0.38	0.38	0.228	0.273	0.212	0.152
9	0.4	0.4	0.275	0.301	0.226	0.190
10	0.42	0.42	0.285	0.292	0.276	0.217
11	0.48	0.48	0.342	0.310	0.291	0.285
12	0.5	0.49	0.378	0.364	0.331	0.287
13	0.55	0.54	0.385	0.355	0.367	0.329
14	0.53	0.54	0.420	0.401	0.351	0.382
15	0.54	0.56	0.476	0.437	0.369	0.381
16	0.53	0.54	0.459	0.437	0.369	0.425
17	0.42	0.51	0.437	0.428	0.380	0.425
18	0.42	0.49	0.436	0.392	0.380	0.410
19	0.41	0.48	0.426	0.387	0.391	0.410
20	0.41	0.46	0.418	0.381	0.380	0.410

content was gradually increased as the culture became older. At full strength and half strength in ASW and f2-Si medium, chlorophyll content increased from 0.012 to 0.528 mg/L, 0.011 to 0.555 mg/L, 0.013 to 0.476 mg/L, and 0.018 to 0.437 mg/L, respectively, and over the period of time chlorophyll content decreased. In the case of AG 11 at full-strength medium, the highest amount of chlorophyll content (0.391 mg/L) was observed the day before termination of the experiment. Algae cultivated at half strength of AG 11 medium showed the maximum chlorophyll content (0.425 mg/L) on day 16 of the cultivation. Chlorophyll content was significantly greater in SW as compared to the other two media, as well as in f2-Si as compared to AG 11.

3.5 Comparison of Growth Parameters

Results of OD, dry biomass and chlorophyll content were compared using a student paired "t" test during growth time between ASW, f2-Si, and AG 11 media at full- and half-strength concentration (Table 4). OD, dry biomass, and chlorophyll content were compared between all three media at both concentrations. All three parameters were significantly higher at decreasing order in ASW, f2-Si, and AG 11, respectively, at full-strength as well as half-strength concentrations. Dry weight results were in accordance with OD-based results, highest in ASW, followed by f2-Si and AG 11. It is statistically confirmed that OD, dry biomass, and chlorophyll content were significantly higher in ASW than the other two media, as

TABLE 4: Comparison of OD, dry biomass, and chlorophyll content using paired student "t" test between ASW, f2-Si, and AG 11 media at full- and half-strength concentration

Full-strength (100%) medium	**ASW vs f2-Si**	**ASW vs AG 11**	**f2-Si vs AG 11**
OD	t = 8.327	t = 7.042	t = 4.269
	p = 0.0001	p = 0.0001	p = 0.0001
Dry biomass	t = 5.954	t = 7.193	t = 2.248
	p = 0.0001	p = 0.0001	p = 0.0001
Total chlorophyll	t = 4.754	t = 6.976	t = 5.621
	p = 0.0001	p = 0.0001	p = 0.001
Half-strength (50%) medium	**ASW vs f2-Si**	**ASW vs AG 11**	**f2-Si vs AG 11**
OD	t = 3.910	t = 8.824	t = 9.791
	p = 0.001	p = 0.0001	p = 0.0001
Dry biomass	t = 3.980	t = 7.670	t = 7.569
	p = 0.001	p = 0.0001	p = 0.0001
Total chlorophyll	t = 4.659	t = 6.890	t = 4.053
	p = 0.0001	p = 0.0001	p = 0.001

well as in f2-Si than AG 11 medium (Table 4), but in AG 11 and ASW the half-strength medium showed a slight increase in weight.

3.6 Correlation Between Growth Parameters

There was a positive and significant correlation found between OD and biomass, biomass and chlorophyll content, as well as OD and chlorophyll in all three media at both concentrations. Table 5 shows Pearson and Spearman correlation between the three growth parameters in ASW, f2-Si, and AG 11 media at full- and half-strength concentration. OD is positively and significantly correlated with dry biomass. The f2-Si medium contains $NaNO_3$ and $NaH_2PO_4{\cdot}2H_2O$, and the remaining ingredients were similar to the ASW medium, although the OD of *D. tertiolecta* in f2-Si medium was lower than ASW.

3.7 Cost of Cultivation and Oil Recovery

The cost of ingredients to extract 1 g of oil from three media at full and half strength is shown in Table 6. There was not much significant difference observed for average oil content in AG 11 medium (37.12%) as compared to ASW (37.625%) and f2-Si medium (37.195%). More specifically, among all three media, ASW and f2-Si at half-strength medium reduction in oil content was noticed,

TABLE 5: Pearson and Spearman correlation for ASW, f2-Si, and AG 11 media at full- and half-strength concentration

Full-strength (100%) medium	**ASW**		**f2-Si**		**AG 11**	
	Pearson	**Spearman**	**Pearson**	**Spearman**	**Pearson**	**Spearman**
OD vs dry biomass	$r = 0.977$	$r = 0.997$	$r = 1.000$	$r = 0.999$	$r = 0.996$	$r = 0.997$
	$p = 0.0001$	$p = 0.0001$	$p = 0.0001$	$p = 0.0001$	$p = 0.0001$	$p = 0.0001$
OD vs total chlorophyll	$r = 0.874$	$r = 0.998$	$r = 0.97$	$r = 0.939$	$r = 0.997$	$r = 0.991$
	$p = 0.0001$	$p = 0.0001$	$p = 0.0001$	$p = 0.0001$	$p = 0.0001$	$p = 0.0001$
Dry biomass vs total chlorophyll	$r = 0.946$	$r = 0.75$	$r = 0.971$	$r = 0.944$	$r = 0.994$	$r = 0.988$
	$p = 0.0001$	$p = 0.0001$	$p = 0.0001$	$p = 0.0001$	$p = 0.0001$	$p = 0.0001$
Half-strength (50%) medium	**ASW**		**f2-Si**		**AG 11**	
OD vs dry biomass	$r = 0.971$	$r = 0.997$	$r = 0.949$	$r = 0.941$	$r = 0.944$	$r = 0.995$
	$p = 0.0001$	$p = 0.0001$	$p = 0.0001$	$p = 0.0001$	$p = 0.0001$	$p = 0.0001$
OD vs total chlorophyll	$r = 0.929$	$r = 0.842$	$r = 0.937$	$r = 0.986$	$r = 0.967$	$r = 0.974$
	$p = 0.0001$	$p = 0.0001$	$p = 0.0001$	$p = 0.0001$	$p = 0.0001$	$p = 0.0001$
Dry biomass vs total chlorophyll	$r = 0.981$	$r = 0.839$	$r = 0.984$	$r = 0.921$	$r = 0.980$	$r = 1.000$
	$p = 0.0001$	$p = 0.0001$	$p = 0.0001$	$p = 0.0001$	$p = 0.0001$	$p = 0.0001$

TABLE 6: Cost of ingredient to extract 1 g of oil from three media at full- and half-strength

Sr. #	Medium	Medium con-centration	Total ingredient cost/L INR	Biomass yield (dry weight of g/L, after 20 days)	Oil content (g) in 100 g dry biomass	Culture medium (L) require for 100 g dry biomass	Ingredient cost (INR) for 100 g dry biomass production	Ingredient cost (INR) for 1 g oil
			A	B	C	D = 100/B	E = D*A	F = E/C
1	ASW	100%	2.851	2.13	37.65	46.94	133.82	3.55
2		50%	1.425	2.16	37.60	46.29	65.96	1.75
3	F2-Si	100%	2.876	1.96	37.50	51.02	146.73	3.91
4		50%	1.438	1.95	36.89	51.28	73.74	2.00
5	AG 11	100%	0.751	1.48	37.12	67.56	50.73	1.37
6		50%	0.375	1.62	37.12	61.72	23.14	0.62

though it was very significant. AG 11 medium showed high oil yield at low ingredient cost, that is, the unit cost of oil extraction is lowest in AG 11 medium (Table 6). The cost of the medium ingredient for ASW and f2-Si was more than double as compared to AG 11, while the oil yield per 100 g dry weight of ASW and f2-Si was comparable to AG 11.

4. DISCUSSION

Alternative, non-food-based biomass fuel feedstock development is vital for our national security, economy, and the environment. Microalgae are among the most promising of these alternatives. Microalgal cell growth rates and metabolic products are affected by a combination of environmental parameters. A key technical challenge for large-scale production of algae includes the highest growth rates and oil content with adequate media composition. Therefore, emphasis was given to medium compositions where a maximum algae growth is achieved with a minimum cultivation cost and high oil yield. Three compositions of media at full and half strength were analyzed to consider optimization of growth parameters with respect to oil yield. Microalgae cells are able to metabolite inorganic carbon in the form of CO_2 in the cultivation medium where an equilibrium trend for the pH is to increase during the algae growth phase. Increase in pH is a common phenomenon recorded in other microalgae cultivation (Rocha et al., 2003; Vonshak, 1986). We have observed a similar pattern of alkaline pH of all three media at both strengths as the algae grows and the culture ages. For continuous growth of algae at constant pH one can purge CO_2 as a carbon source, which serves a dual purpose: use as a carbon source and to deplete pH of the medium. Thus, the CO_2 input cost plays a vital role in the economy of biodiesel production. In order to optimize mi-

croalgal growth, CO_2 needs to be provided at much higher concentration and this concentration can be attained under natural conditions (Pulz, 2007).

Algae cell growth was monitored with cell absorbency, chlorophyll content, and cell mass at various time intervals. The f2-Si medium contains $NaNO_3$ and $NaH_2PO_4{\cdot}2H_2O$. Such matters affected absorbency of the medium through the amount of matter, size and shape of suspended particles, opacity, wavelength of incident light, etc. To avoid absorbency-related complexities in OD determination, the gravimetric method, i.e., cell dry weight determination, was also used for growth monitoring in the current study.

The linearity of the relationship between the optical density at 680 nm (OD680) and dry biomass has been established for *Dunaliella tertiolecta* by Massart and Hantson (2010).

The f2-Si medium contains $NaNO_3$ and $NaH_2PO_4{\cdot}2H_2O$, and the remaining other ingredients were similar to the ASW medium, although the OD of *D. tertiolecta* in f2-Si medium was lower than ASW.

Agrochemicals (fertilizers) like DAP, APS, and mosaic contain nutrients which are favorable for *D. tertiolecta* growth. In addition, these fertilizers did not affect the oil content of the algae cell.

While working with marine microalgae it is possible that weight can be affected by the amount of salts absorbed on the cell surface and intracellular water (Zhu et al., 1997). In the present experiment this fact was kept in mind; therefore, proper washing with water to remove salt was performed before the dry weight was measured. At the end of cultivation, dry biomass yield in medium at half strength was found higher/similar when compared with the full-strength medium, indicating that ingredient concentration of the half-strength concentration favored growth of *D. tertiolecta.*

Considering the growth parameters (OD, dry biomass, and chlorophyll content), ASW is better than f2-Si and then AG 11. However, ingredient selection in development of medium is as important as other critical factors. In artificial cultivation of *D. tertiolecta*, the goal is to favor high growth rate as much as possible or to push the metabolic route to follow oil production. In the present experiment, *D. tertiolecta* cultivated in AG 11 produced oil content which was similar to *D. tertiolecta* cultivated in ASW and f2-Si medium.

At laboratory scale the amount of ingredients used for cultivation may not affect cost, but at a commercial scale it will play a crucial role and be a decision-making factor in overall production cost. The cost to oil content ratio calculated in the current study suggest that the cost of 1 g of oil extracted from AG 11 media is lowest, suggesting that the cost of oil production at the lowest ingredient cost is possible using AG 11 medium. Massart and Hantson (2010) reported two-phase *D. tertiolecta* cultivation, wherein they reported the first phase of high and rapid growth in a medium poor in sodium chloride and a second phase of lipid storage after increasing the salinity of the medium.

5. CONCLUSION

It was found that *D. tertiolecta* grew better with an average of 37% oil content at half concentration of synthetic medium. Maintenance of *D. tertiolecta* in half-strength medium is advisable at a laboratory level. The cost of 1 g of oil extraction is lowest in AG 11 as compared to other media. *D. tertiolecta* showed comparable growth parameters at both concentrations of AG 11. Therefore, use of AG 11 at half concentration would be strongly recommended for commercial cultivation of *D. tertiolecta*.

However, there are many more untapped areas where large-scale economical and feasible cultivation of algae can be explored. Among them, sequestration of CO_2 from flue gas of industrial and thermal power plants, selecting and screening of highly CO_2-tolerant algal strains before adoption for commercial cultivation, is one of the best strategies to improve the practical feasibility of the process from an economic point of view. Microalgal cells gain their essential nutrition from the water in which they grow. Water usually occurs in treated or untreated livestock wastewater, and they can be reprocessed to conserve resources as well as to reduce the culture medium cost. Conclusively, algae need not compete with other users for fresh water, and cultivating algal mass by utilizing wastewater can be considered a biological remediation phenomenon under wastewater management.

REFERENCES

Aden, A., Biomass and biofuels: Technology and economic overview, National Renewable Energy Laboratory (NREL), 2007.

Beijierinck, M.W., Kulturversuche mit Zoochloren, Lichenenggonidien und anderen Algen, *Bot. Ztg*., vol. 48, pp. 725–785, 1890.

Borowitzka, M.A., Commercial production of microalgae: Pond, tanks, tubes and fermenter, *J. Biotechnol.*, vol. 70, pp. 313–321, 1999.

Chisti, Y., Biodiesel from microalgae, *Biotechnol. Adv*., vol. 25, pp. 294–306, 2007.

Faulker, D.J., Marine natural products, *Nature Prod. Rep*., vol. 3, pp. 1–13, 1986.

Greasham, R.L. and Herber, W.K., Design and optimisation of growth media, In P.M. Rhodes and P.F. Stanbury, Eds., *Applied Microbial Physiology, A Practical Approach*, Oxford University Press: Oxford, pp. 53–74, 1997.

Jin, E.S., Feth, B., and Melis, A., Biodiesel: A mutant of the green algae Dunaliella salina constitutively accumulates zeaxanthin under all growth conditions, *Biotechnol. Bioeng*., vol. 81, pp. 115–124, 2003.

Lichtenthaler, H.K., Chlorophylls and carotenoids: Pigments of photosynthetic biomembranes, *Methods Enzymol*., vol. 148, pp. 350–382, 1987.

Markov, S.A., Weaver, P.F., and Seibert, M., Spiral tubular bioreactors for hydrogen production by photosynthetic microorganisms: Design and operation, *Appl. Biochem. Biotechnol*., vols. 63–65, pp. 577–584, 1997.

Massart, A. and Hantson, A.L., Optimization of the medium composition of the microalgae "Dunaliella tertiolecta Butcher" in order to combine high cell density and accumulation of lipid for

bio diesel production, *Proc. Venice 2010, Third Intl. Symp. on Energy from Biomass and Waste*, Venice, Italy, 8–11 Nov. 2010, http://www.iiasa.ac.at/Research/FOR/downloads/Kraxner/CD%20Venice%20Symposion%202010_Proceedings/data/data/files/060.pdf.

McGraw, L., The ethics of adoption and development of algae as a biofuel feedstock, Prepared under the outline framework of WG9 in the Ethics of Energy Technologies in Asia and the Pacific (EETAP) Project, RUSHSAP, UNESCO, Bangkok, 2009.

Payer, H.D., First report upon the organization and experimental work of the Thailand German project on the production and utilization of single cell green algae as a protein source for human nutrition, *Instant Food Resource*, Product Development Kasetsar Univ., Bangkok, Thailand, 1971.

Pulz, O., Evaluation of green fuel's 3D matrix algal growth engineering scale unit: APS Red Hawk Unit AZ, IGV Institute fur Getreidevararbeitung GmbH, June–July, www.greenfuelonline.com, 2007.

Rocha, J.M.S., Garcia, J.E.C., and Henriques, M.H.F., Growth aspects of the marine microalgae, Nannochloropsis gaditana, *Biomol. Eng*., vol. 20, pp. 237–242, 2003.

Takagi, M., Watanabe, K., Yamaberi, K., and Yoshida, T., Limited feeding of potassium nitrate for intracellular lipid and triglyceride accumulation of Nannochloris sp UTEX LB1999, *Appl. Microbiol. Biotechnol.*, vol. 54, pp. 112–117, 2000.

Tsukada, O., Kawahara, T., and Miyachi, S., Mass culture of chlorerlla in Asian countries, In: Mitsui, A., Miyachi, S., Pitro, A., and Tamura, S., Eds., *Biological Solar Energy Conversion*, pp. 363–365, Academic Press, New York, 1977.

Vonshak, A., Laboratory techniques for the cultivation of microalgae, In: A. Richmond, Ed., *Handbook of Microalgal Mass Cultures*, CRC Press, Boca Raton, FL, pp. 117–199, 1986.

Zhu, C.J., Lee, Y.K., and Chao, T.M., Effects of temperature and growth phase on lipid and biochemical composition of Isochrysis galbana TK1, *J. Appl. Phycol*., vol. 9, pp. 451–457, 1997.

International Journal of Energy for a Clean Environment, 10(1–4), 181–192 (2009)

A MODEL FOR ABATEMENT OF CO_2 EMISSIONS BY DE-ABSORPTION WITH MONOETHANOLAMINE

Timothy Greer,[1] Almat Bedelbayev,[1] José Igreja,[2] João Gomes,[2,3,] & Bernt Lie[1]*

[1]*Telemark University College, Faculty of Technology, Porsgrunn, Norway*

[2]*Instituto Superior de Engenharia de Lisboa (ISEL), Departamento Engenharia Química, Lisboa, Portugal*

[3]*Instituto Superior Técnico, CEBQ, Lisboa, Portugal*

[*]Address all correspondence to João Gomes, ISEL, R. Conselheiro Emídio Navarro, 1949-001 Lisboa, Portugal; E-mail: jgomes@deq.isel.ipl.pt.

Due to the adverse effect of CO_2 from fossil fuel combustion on the earth's ecosystems, finding the most cost-effective method for CO_2 capture is an important area of research. The predominant process for CO_2 capture currently employed by industries is chemical absorption in amine solutions. A dynamic model for the de-absorption process was developed with monoethanolamine (MEA) solution. Henry's law was used for modeling the vapor phase equilibrium of the CO_2, and fugacity ratios calculated by the Peng Robinson equation of state (EOS) were used for H_2O, MEA, N_2, and O_2. Chemical reactions between CO_2 and MEA were included in the model, along with the enhancement factor for chemical absorption. Liquid and vapor energy balances were developed to calculate the liquid and vapor temperature, respectively. The model results compare favorably with other published results.

KEY WORDS: *CO_2 de-absorption, dynamic model, amine*

1. INTRODUCTION

The effect of carbon dioxide on the enhanced greenhouse effect is an important worldwide issue, and there has been increasing emphasis placed on researching the most cost-effective method to capture CO_2 emissions from fossil fuel combustion. Approximately 60% of CO_2 produced is from point sources, with CO_2 fractions up to 14% for coal-fired power stations and 8% for natural gas-fired power stations [1].

The separation of the CO_2 into a pure stream (>95%) can be achieved by a variety of techniques, including membrane separation, low temperature distillation,

2150-3621/09/$35.00

adsorption, and absorption [1]. The absorption of CO_2 into monoethanolamine (MEA) by chemical absorption is presently the most favored method for the capture of carbon dioxide from fossil fuel combustion. A benefit of chemical absorption into amine solution is that at higher temperatures the chemical reaction can be reversed and the MEA recycled.

The majority of previous work on amine CO_2 capture is related to absorption models or small-scale experimental de-absorption. Hansen [2] developed a dynamic model for the absorption of CO_2 in MEA, while Hoff [3] developed an absorption model with MEA and MDEA in a membrane contactor. Jamal et al. [4] published work on absorption and desorption for small-scale laboratory experiments, and Liu et al. [5] developed a full-scale absorption and desorption model utilizing Aspen HYSYS. Bedelbayev [6] developed an absorption model implemented in Matlab for studying controllability issues, and Greer [7] developed a full-scale model which was also implemented in Matlab.

This paper presents the development of a dynamic model for the simulation of the de-absorption process. The first part of the paper describes the full-scale process and the associated components. The dynamic model is developed in Sec. 3 from the principles of diffusion from vapor to liquid, taking into account the chemical reactions between the MEA and CO_2. The model validation and full-scale simulation are included in Sec. 4, and discussion and conclusions are in Sec. 5.

2. PROCESS DESCRIPTION

Amine compounds react with CO_2 to form stable ionic compounds, with the reaction reversing at higher temperatures. A typical schematic of the de-absorption process is shown in Fig. 1 where the main item of equipment is a stripping tower

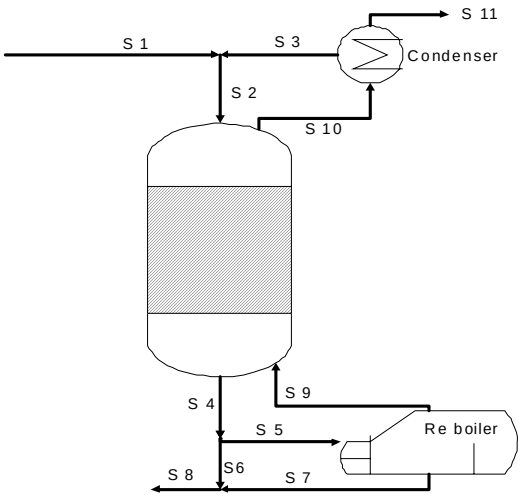

FIG. 1: Process flow diagram of de-absorption tower

filled with packing material with a high surface-to-volume ratio (typically 200 m^2/m^3). For the de-absorption process, a rich stream (S1) of MEA and CO_2 from an absorption tower is pumped to the top of the stripping tower where it flows down over the packing within the de-absorption tower. Stripping steam from the reboiler (S9) enters the tower at the bottom and flows up the tower in a counter-current flow arrangement. As the rich liquid flows down the tower, the chemical reactions act in the reverse reaction and release the bound CO_2 from ionic form into the aqueous solution, which then diffuses into the gas phase. The lean MEA solution exits at the bottom of the de-absorption tower and is returned to the absorption process (S8). A percentage of the lean mixture is directed to the reboiler to provide the stripping steam for the process (S5). The condenser cools the outgoing gas and thus reduces the H_2O content and up-concentrates the amount of CO_2. Typically, the captured CO_2 requires more postprocessing such as dehydration and compression; this postprocessing is not discussed further here.

3. MODEL DEVELOPMENT

The mass-transfer flux of each species is a function of the driving force between the concentration in the bulk vapor and liquid phases as shown in Fig. 2.

The general form of the transfer flux equation is shown in Eq. (1):

$$\dot{n}_d = k_{la} a_w \left(C_i^* - C_i^B\right). \tag{1}$$

Here, $\dot{n}_d$ is the molar diffusion rate, k_{la} is the transfer coefficient, a_w is the interphase surface area, C_i^* is the interphase molar concentration of specie i in vapor liquid equilibrium, and C_i^B is the bulk concentration of species i.

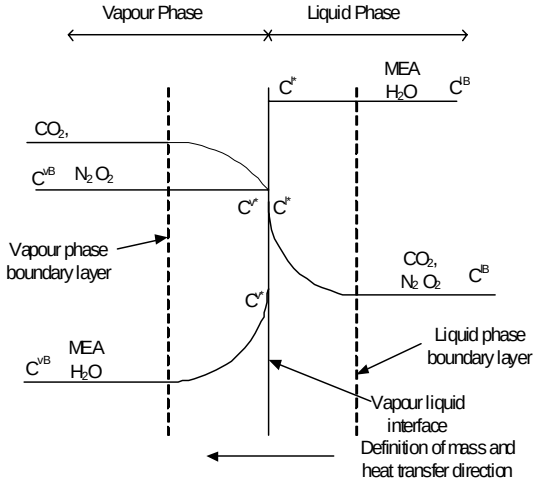

FIG. 2: Interphase concentration profile

It is assumed for the H_2O and MEA that the concentration at the liquid side of the vapor–liquid interface is the same as the bulk liquid concentration. For the N_2 and the O_2 it is assumed that the concentration at the vapor side of the vapor–liquid interface is the same as the bulk vapor phase concentration. The fugacities of the species at the vapor–liquid boundary were calculated and used to evaluate the concentration at the interface. At the interface it is assumed that there is phase equilibrium; therefore the fugacities of the liquid and vapor of each species are equal. Equation (2) relates the mol fraction in the vapor phase to that in the liquid phase by the ratio of the species fugacity

$$y_i = Kx_i = \frac{\hat{\varphi}_i^l}{\hat{\varphi}_i^v} \tag{2}$$

Being stated, we know the liquid bulk phase concentration for the MEA and H_2O and the vapor bulk phase concentration for the N_2 and O_2. The mole fractions at the interface can be found by iteration, and then the interface concentrations can be calculated. Equation (1) has the concentration difference as the driving force and an equivalent transfer area, which is related to the surface area of the packing. The mass-transfer coefficient is taken from an empirical formula derived by Billet [8], which is a function of the packing properties. The surface area available for transfer is a function of the specific surface area of the packing used and the wetted area of the packing. The formula for the wetted surface area is taken from Billet [9].

Henry's law is applied to relate the concentration of CO_2 in the bulk liquid phase to the bulk vapor phase concentration. By applying Henry's law, the interface concentration can be eliminated and a relationship between the bulk vapor and liquids applied. The resistance to mass transfer in the liquid and vapor phases is provided by the same formulas from Billet [8] as used for the other species, and it is assumed there is resistance to mass transfer in the liquid and vapor phases. Henry's law is shown in Eq. (3):

$$\dot{n}_d = \frac{1}{\dfrac{H_{CO_2}}{Ek_{la}^l a_w} + \dfrac{RT^v Z}{k_{la}^v a_w}} {}^v\left(P_{CO_2}^v - H_{CO_2} C_{CO_2}^l\right) . \tag{3}$$

The enhancement factor accounts for the continual removal of the CO_2 from the liquid–film boundary layer by the chemical reaction of CO_2 with MEA.

The main reaction for the system is

$$CO_2 + MEA << MEACOO^- + MEAH^+ . \tag{R1}$$

The forward reaction has a rate as in Eq. (4), and the reverse reaction has a rate as in Eq. (5).

$$r_f = k_f \, [MEA] \, [CO_2] \quad \frac{mol}{s \, m^3} ,$$

where

$$k_f = 3.95 \times 10^{10} \exp\left(-\frac{6864}{T^l}\right) \quad \frac{\text{m}^3}{\text{mol s}} , \tag{4}$$

$$r_k = k_r \, [\text{MEAH}^+] \, [\text{MEACOO}^-] \quad \frac{\text{m}^3}{\text{mol s}}$$

where

$$k_r = \frac{K_e}{k_f} . \tag{5}$$

The e equilibrium constants are taken from Liu et al. [5]. The enhancement factor is shown in Eq. (6) and is the ratio of the mass transfer for a reacting and unreacting system, i.e., what the mass transfer would be if the CO_2 did not react with the MEA in the film boundary layer. The enhancement factor is the Hatta number for this system and is taken from Perry [10]

$$E = \frac{\sqrt{D_{\text{CO}_2} k_f C^l_{\text{MEA}}}}{k^l_{la}} \tag{6}$$

The energy balance is developed to provide the temperature model for the liquid and vapor phases. In the liquid phase the de-absorption reaction is endothermic and thus requires heat to proceed. The heat of reaction is the heat required for one mol of CO_2 to react with two moles of MEA and is 65,000 J/mol CO_2 (ΔH_{RE}) [1]. There are also terms in the temperature equation for the spatial movement of the fluid, sensible heat transfer, and diffusion heat transfer. It is assumed that the diffusion heat transfer is for MEA and H_2O only, and that the liquid changes into a vapor within a control volume at the VLE interface. The sensible heat transfer is modeled by Newton's law of cooling as shown in Eq. (7), where the heat-transfer coefficient is found using the Chilton–Colburn analogy relating the mass-transfer coefficient to the heat-transfer coefficient

$$Q_s = U_T (T^l - T^v) \tag{7}$$

For the diffusion mass transfer, it is assumed that the vaporization of the liquid takes place in the liquid phase; hence it is already a vapor when it enters the vapor phase. Therefore the only terms in the temperature balance for the vapor phase are the spatial movement term and the sensible heat transfer, which is equal but opposite of the sensible heat term from the liquid phase.

The de-absorption column is modeled as a plug flow reactor with partial differential equations (PDEs) describing the species concentrations and the temperature in each phase. A schematic of the stripping tower is shown in Fig. 3, and a summary of the equations is shown below and in Table 1.

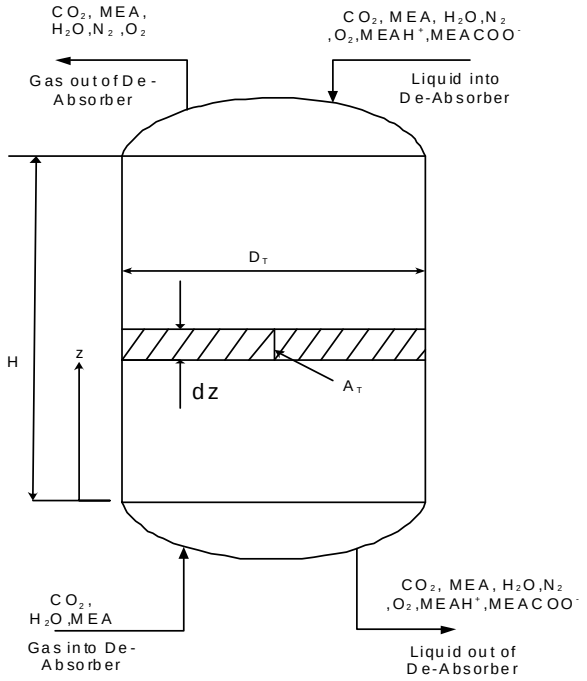

FIG. 3: PDE development of column

$$\frac{\partial c_i^l}{\partial t} = u\frac{\partial c_i^l}{\partial z} - \dot{n}_d + \dot{n}_g ,$$

$$\frac{\partial c_i^v}{\partial t} = -u\frac{\partial c_i^v}{\partial z} + \dot{n}_d ,$$

$$\frac{\partial T^l}{\partial t} = -u\frac{\partial T^l}{\partial z} - \frac{\dot{n}_d^T \Delta\tilde{H}^{vl}}{\left(C^l\right)^T \tilde{C}_p^l} - \frac{\dot{n}_{d,CO_2}\Delta H_{RE}}{\left(C^l\right)^T \tilde{C}_p^l} - \frac{U_T\left(T^l - T^v\right)}{\left(C^l\right)^T \tilde{C}_p^l},$$

$$\frac{\partial T^v}{\partial t} = -u\frac{\partial T^v}{\partial z} + \frac{U_T\left(T^l - T^v\right)}{\left(C^v\right)^T \tilde{C}_p^v}.$$

At the bottom of the de-absorption tower, some of the liquid is transferred to a reboiler where the liquid is vaporized into stripping steam. The reboiler is modeled as a flash calculation with the inputs of flash pressure, temperature, and the percentage of the liquid flow fed into the reboiler. The reboiler consumes the largest amount of energy, as heat is required to vaporize the liquid and provides the en-

TABLE 1: Species modeled by PDE

Species	Gas phase	Liquid phase	Generation term	Diffusion term
CO_2	Yes	Yes	Yes	Yes
MEA	Yes	Yes	Yes	Yes
H_2O	Yes	Yes	No	Yes
N_2	Yes	Yes	No	Yes
O_2	Yes	Yes	No	Yes
$MEAH^+$	No	Yes	Yes	No
$MEACO^-$	No	Yes	Yes	No

ergy to reverse the chemical reactions. Typically the reboiler is heated by steam and has a maximum temperature of approximately 120°C, as this is the temperature at which the MEA will start to degrade.

The reactions in the de-absorption tower are reversed with increasing temperature; the higher the temperature, the larger the amount of CO_2 released. A typical operating regime has an MEA concentration of up to 30% by weight. The greater the percentage of MEA, the less energy is consumed, because if the MEA is 30% and the water is 70%, then energy is required to heat up the 70% water for no benefit. Therefore it is advantageous to increase the MEA concentration and minimize the water concentration, but this has a trade-off, as above 30% MEA is highly corrosive and requires corrosion inhibitors and specialized equipment [5]. At the top of the de-absorption tower is a condenser which cools the vapor phase exiting the de-absorption column. The vapor is cooled to a designated temperature, and a proportion of the vapor condenses into the liquid phase and is returned back to the de-absorption column. The temperature of the cooled liquid and the percentage refluxed back into the column are input variables in the model.

4. SIMULATION

4.1 Model Validation

Model validation is performed by carrying out a simulation of the partial pressure of CO_2 versus CO_2 loading. CO_2 loading is the ratio of the CO_2 in free and ionic form (CO_2 aq. and $MEACOO^-$) and the total MEA of the mixture. A plot of the simulation at a temperature of 400 K is shown in Fig. 4. Various references include other reactions than that of Reaction (R1) in the process, most notably the formation of bicarbonate (HCO_3^-) and the reversion of the $MEACOO^-$ [5, 3]. A plot of the chemical species with the extra reactions is shown in Fig. 4. The operating range of the de-absorption process is an input loading of 0.45 of solution into the top of the tower, where the CO_2 is subsequently stripped, and an output loading of 0.20. The dominant reaction for the typical loading is (R1), where one mol

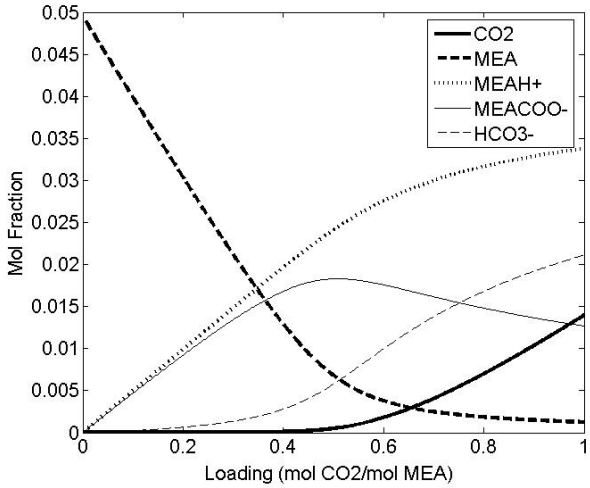

FIG. 4: Chemical species as a function of CO_2 loading at 400 K

of CO_2 reacts with 2 mols of MEA. At this loading the reversion of $MEACOO^-$ into MEA and HCO_3^- is not as significant as at higher CO_2 loadings, as indicated in Fig. 4. CO_2 reacts with H_2O to form bicarbonate, but this reaction is typically slow and can typically be ignored for the de-absorption process [12]. Since the $MEAH^+$ and $MEACOO^-$ lines are so close in the operating range, as shown in Fig. 4, it is justified to run the simulation with only one dominant reaction.

4.2 Full Simulation

The simulation is performed in Matlab from the MathWorks using the method of lines and ordinary differential equations (ODE) solver ODE15s to solve the PDE. In total, 14 PDE equations were solved simultaneously (liquid and gas phase for CO_2, MEA, H_2O, N_2, and O_2; liquid phase for $MEAH^+$ and $MEACOO^-$; and the temperature in the gas and liquid phase).

The inlet values are for a typical 400 MW natural gas power station producing 1 million tons of CO_2 per annum. The input values used in the model are displayed in Table 2.

Plots of the CO_2 concentration in the gas phase, the MEA concentration in the liquid phase, and liquid temperature are shown in Figs. 5, 6, and 7, respectively.

5. DISCUSSION AND CONCLUSIONS

The modeling of the de-absorption process is a complex process because the system is a stiff system, the reactions have a time scale of milliseconds, there is a slower process of diffusion and temperature change, and the spatial movement of the fluids within the tower (which has a retention time in the order of hours) is

TABLE 2: Input values for model simulation

Input	Value	Unit
Stripper height	15	m
Liquid flow rate	0.5	m^3/s
Liquid inlet temperature	383	K
Reboiler temperature	400	K
Reboiler flow (Stream S5)	3.5	%
Packing surface area	200	m^2/m^3
Tower pressure	2	bar
$MEACOO^-$ (Liq)	2300	mol/m^3
$MEAH^+$ (Liq)	2300	mol/m^3
MEA (Liq)	400	mol/m^3
O_2 (Liq)	10^{-3}	mol/m^3
N_2 (Liq)	10^{-3}	mol/m^3
CO_2 (Liq)	10^{-1}	mol/m^3
H_2O (Liq)	38,000	mol/m^3

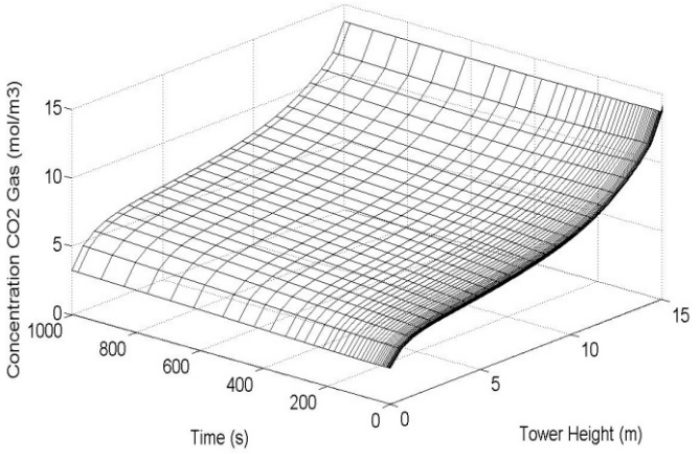

FIG. 5: Concentration of CO_2 in the gas phase

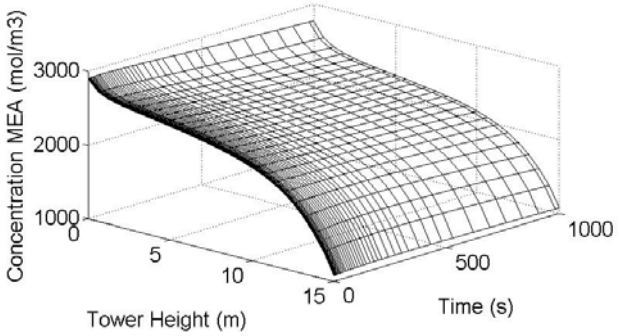

FIG. 6: Concentration of MEA in the liquid phase

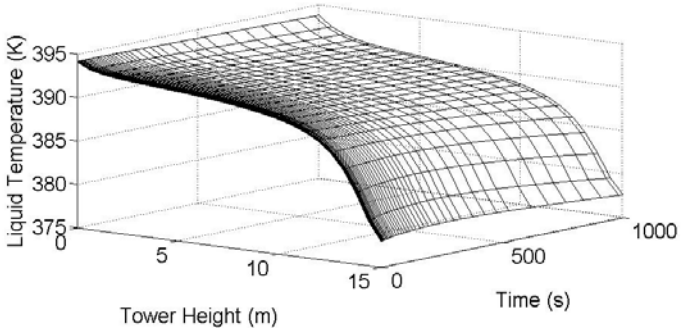

FIG. 7: Liquid temperature (K)

even slower. Furthermore, the reaction rates, as well as diffusion and fluid properties, are all strong functions of the temperature. Effort has been made to provide all variables as a function of temperature including density, diffusivity, viscosity, heat capacity, thermal conductivity, Henry's constants, chemical reaction rates, and equilibrium constants. The dominant reaction is the reaction of one mol of CO_2 with two mols of MEA, forming $MEACOO^-$ and $MEAH^+$, which is reversed at elevated temperature.

The mass transfer of CO_2 is strongly dependent on the equilibrium constant for the chemical reaction. The equilibrium value dictates the ratio of the free aqueous CO_2 to the bound CO_2 in $MEACOO^-$. As the temperature increases, the ratio of free CO_2 increases in the liquid phase. The solubility of CO_2 in the liquid is also a function of temperature and decreases with elevated temperature; therefore the CO_2 diffuses faster into the gas phase. The ratio of the CO_2 in the liquid to vapor phase is given by Henry's constant. Henry's constant is a function of the tempera-

ture and the ionic strength of the mixture. A larger value for Henry's constant equates to a larger concentration of CO_2 in the vapor phase.

For the simulation, an inlet loading of 0.46 was used, where the majority of the MEA was in the form of $MEAH^+$ and $MEACOO^-$. An outlet loading of 0.27 was achieved with a reboiler reflux of 30% and a reboiler temperature of 400 K. This required an energy consumption of 4.25 MJ per kg of CO_2 removed, which is in line with other literature sources [5, 13]. Figure 6 displays how the MEA concentration increases down the column as the reaction is reversed, releasing the bound MEA and CO_2. The reboiler's temperature of 400 K enters the stripper at the bottom and decreases to 377 K over the length of the de-absorption tower as the heat from the steam is transferred to heating up the liquid solution and reversing the chemical reaction. This is displayed in Fig. 7.

The species H_2O, MEA, N_2, and O_2 were modeled using the fugacity ratio between the liquid and vapor phase. The Peng Robinson EOS was used, but the results were dependent on the interaction parameters and mixing rule used in solving the EOS. The accuracy of the liquid phase fugacity from the Peng Robinson EOS is unknown, but the overall results are similar to other estimates. The presence of O_2 and N_2 in the stripping process is low, as the solubility of the N_2 and O_2 in the solution is low; therefore the inlet concentration in the liquid is minimal, and the composition of the captured CO_2 is predominantly CO_2 and H_2O.

The overall control philosophy for the de-absorption process is linked to the absorption process [13]. The removal of CO_2 at minimal cost is the primary objective of the process, and this is achieved by maximizing the loading into the stripper and minimizing the loading-out. The loading-out is reduced by adding stripping energy in the form of steam from the reboiler. The control of the stripping steam is achieved by manipulating the reboiler temperature and the amount of liquid refluxed to the reboiler.

The simulation input does not represent the optimal solution, but it provides a workable solution. For more robust optimization, the absorption process and capital expenditure costs should be considered.

It is intended to further develop this model to study the effect of substituting MEA by other amines, which are potentially more effective in the absorption of CO_2. In fact, the absorption capacity of the most current amines must be improved in order to obtain a more profitable operation. It has been shown previously that relationships exist between the amine structure and the activity/capacity for CO_2 absorption [14]. The introduction of amine substituents at the α-carbon creates a carbamate instability, which causes the hydrolysis to go faster, thus increasing the amount of bicarbonate and allowing for higher CO_2 loadings. Therefore the absorption capacity is enhanced when secondary and tertiary amines are used instead of primary amines, and this effect is also enhanced by the addition of piperazine. Another aspect that should be considered in further studies is the degradation of

the amines, which occurs due to other substances present in combustion flue gases, namely sulfur dioxide and nitrogen dioxide [15].

REFERENCES

1. Wallace, D., Capture and storage of CO_2: What needs to be done?, IEA, 2000, Available at http://www.iea.org/textbase/papers/2000/capstor.pdf, Accessed Apr. 23, 2008.
2. Hansen, D.K., *Dynamic Modeling of an Absorption Tower for the Removal of Carbon Dioxide from Exhaust Gas by Means of Monoethanolamine*, MSc Thesis, Telemark University College, 2004.
3. Hoff, K.A., *Modelling and Experimental Study of Carbon Dioxide Absorption in a Membrane Contactor*, PhD Thesis, NTN University, 2003.
4. Jamal, A., Meisen, A., and Jim Lim, C., Kinetics of carbon dioxide absorption and desorption in aqueous alkanolamine solutions using a novel hemispherical contactor — II: Experimental results and parameter estimation, *Chem. Eng. Sci*., vol. 61, pp. 6590–6603, 2006.
5. Liu, Y., Zhang, L., and Watanasiri, S., Representing vapour-liquid equilibrium for an aqueous MEA–CO_2 system using the electrolyte non-random-two-liquid model, *Indust. Eng. Chem. Res*., vol. 38, pp 2080–2090, 1999.
6. Bedelbayev, A., *Model Based Control of Absorption Column for CO_2 Capturing*, MSc Thesis, Telemark University College, 2008.
7. Greer, T., *Modeling and Simulation of Post Combustion CO_2 Capturing*, MSc Thesis, Telemark University College, 2008.
8. Billet, R.H., *Packed Towers in Processing and Environmental Technology*, Weinheim: VCH Verlagsgesellschaft, 1995.
9. Billet, R. and Schultes, M., Prediction of mass transfer columns with dumped and arranged packings: Updated summary of the calculation method of Billet and Schultes, *Trans. IChemE, Part C*, vol. 77, 1999.
10. Perry, R.H. and Green, D.W., *Chemical Engineers Handbook*, McGraw-Hill: New York, 1999.
11. Draxler, J., Stevens, G., and Kentish, S., Criteria for the selection of reagents for CO_2 absorption, Co-operative Research Centre for Greenhouse Gas Technologies, 2007, Available at https://extra.co2crc.com.au/modules/pts2/download.php?file_ id=847&rec_id=215, Accessed Apr 23, 2008.
12. Maceiras, R., Alvarez, E., and Cancela, M.A., Effect of temperature on carbon dioxide on absorption in Monoethanolamine solutions, *Chem. Eng. J.*, vol. 56, pp. 987, 2007.
13. Oi, L.E., Aspen HYSYS simulation of CO_2 removal by amine absorption from a gas based power plant, *Proc. of the 48th Scandinavian Conf. on Simulation and Modeling*, Goteborg, Sweden, 2007.
14. Singh, P., Niederer, J., and Werstreg, G., Structure and activity relationships for amine base CO2 absorbent, *Int. J. Greenhouse Gas Control*, vol. 1, pp. 5–10, 2007.
15. Rao, A. and Rubin, E., A technical, economic and environmental assessment of amine-based CO_2 capture technology for power plant greenhouse gas control, *Env. Sci. Technol.*, vol. 36, pp. 4467–4475, 2002.

International Journal of Energy for a Clean Environment, 10(1–4), 193–201 (2009)

THE MITIGATION OF METHANE EMISSIONS FROM INDUSTRIALIZED COUNTRIES CAN EXPLAIN THE ATMOSPHERIC CONCENTRATION LEVEL-OFF

I. Savolainen,[1,] S. Monni,[2] & S. Syri[3]*

[1]*Technical Research Centre of Finland, P.O. Box 1000, FIN-02044 VTT, Finland*

[2]*Benviroc, Ltd., Finland*

[3]*Aalto University, Finland*

[*]Address all correspondence to I. Savolainen, E-mail: ilkka.savolainen@vtt.fi

Methane (CH_4) is the second-most important anthropogenic greenhouse gas after carbon dioxide. Recently, CH_4 concentration increase in the atmosphere has been observed to level-off. We analyze the emission trends based on statistics from the United Nations Framework Convention on Climate Change (UNFCCC) and show, using a single box model, that the decrease in the reported emissions from industrialized countries contribute to the reduced increase in CH_4 concentration. The total reduction in CH_4 emissions from industrial countries was 25 Tg yr^{-1} between 1990 and 2003. The reductions consisted of landfill gas recovery and other waste management policies, CH_4 collection in coal mines, the repairing of gas networks, and structural changes in economy. Our study implies that the reduction of CH_4 emissions can effectively mitigate climate change on a short time scale, and that the first results of mitigation measures are already observable in the atmosphere. However, there is an evident risk that the methane concentration will start to rise again due to increasing emissions from developing countries.

KEY WORDS: *methane, climate change, emissions reduction, industrial countries*

1. INTRODUCTION

Increased methane (CH_4) concentration in the atmosphere contributes greatly to the anthropogenic perturbation of the radiative balance of the Earth and to climate change. CH_4 is emitted by anthropogenic and annually varying natural sources. CH_4 concentration has more than doubled since preindustrial times from around 700 ppb to over 1700 ppb. Its direct contribution to the radiative forcing is about one-third that of carbon dioxide (NOAA, 2005). The growth rate of CH_4 concen-

tration in the atmosphere has decreased particularly since 1992 (NOAA, 2005; Dlugokencky et al., 1998, 2003; Hansen and Sato, 2001). Emissions reduction measures in industrialized countries have not been suggested as a reason for the reduced concentration growth rate (Dlugokencky et al., 1998, 2003; Simpson et al., 2002) and halting of the concentration increase. Only the impact of the collapse of the former Soviet Union (FSU) on methane emissions has been recognized (Dlugokencky et al., 1998, 2003; Wang et al., 2004). Recently, deforestation in tropical areas has been suggested as one possible contributor (Keppler et al., 2006). However, the annual emissions reported from industrial countries (Annex I Parties of the UNFCCC) have also decreased from 1990 to 1995 by 13 Tg yr^{-1} and to 2000 by 25 Tg yr^{-1} (UNFCCC, 2005).

The objective of this paper is to show, using a single box atmospheric concentration model, that the significant emissions reduction measures in Annex I countries, together with structural changes leading to emissions reduction, could be important contributors in the observed slowdown and level-off of methane concentration increase in the atmosphere.

2. EMISSIONS ESTIMATES AND ASSOCIATED UNCERTAINTY

Current estimates of anthropogenic methane sources emphasize the role of agriculture (43%), energy (35%), and waste (18%) sectors in total emissions (IEA, 2005). The enteric fermentation of ruminants and rice cultivation are the prominent agricultural sources, which are important particularly in developing countries. The mitigation of these emissions is difficult due to increasing human population and the nature of the processes.

In the energy sector, the most important emission sources are coal and gas production, transmission, and distribution. Natural gas consists mainly of CH_4, and leakages from transmission and distribution networks are important sources of CH_4. Biomass burning is also considered to be a significant source of CH_4 emissions globally (Wuebbles and Hayhoe, 2002; Mikaloff Fletcher et al., 2004a; IPCC, 2001); however, there are large uncertainties in the estimates. In the waste sector, the main contributor is the anaerobic degradation of waste in landfills. These emissions can be mitigated by, e.g., the recovery and combustion of methane.

Estimates of global methane emissions vary notably and contain significant uncertainties (Wang et al., 2004; Wuebbles and Hayhoe, 2002; Mikaloff Fletcher et al., 2004a,b; IPCC, 2001). The current best estimates of total global emissions vary from 500 Tg yr^{-1} up to more than 600 Tg yr^{-1}. It is estimated that around 30–40% of global emissions come from natural sources, of which wetlands and termites are the most important. Keppler et al. (2006) suggest that living plants may contribute as much as 62–236 Tg yr^{-1} to the global methane budget. Uncertainties in the estimates of natural emissions are even larger than those of anthropogenic emissions due to the spatial variability of emissions and the complex

emission generating phenomena. In addition, year-to-year variation causes uncertainty in the estimates of emissions for an individual year.

The total atmospheric burden of methane can be measured rather accurately, but there are large uncertainties in the estimates of emissions from different source categories (IPCC, 2001). Uncertainties in inventories of anthropogenic methane sources in industrial countries are estimated to vary between 20 and 50% (Rypdal and Winiwarter, 2001; Monni et al., 2004; Monni et al., 2006). These uncertainties are mainly due to the nature of CH_4 sources, which makes an accurate estimation of emissions difficult. Methane formation, e.g., in the digestion systems of ruminants or in anaerobic degradation in landfills, is a complex phenomenon, and the estimation of emissions by calculation models contains uncertainties. Additional uncertainty is associated with activity data and calculation parameters. However, the estimates of changes in emissions are less uncertain in the case of CH_4 recovery in landfills and coal mining; even though the absolute amount of methane from these sources remains unknown, emissions reduction can be estimated at an accuracy of a few per cent when the methane is collected and, e.g., combusted (Rypdal and Winiwarter, 2001).

The total reduction in CH_4 emissions from Annex I parties of the Kyoto Protocol was 25 Tg yr^{-1} between 1990 and 2003 (Table 1) (UNFCCC, 2005). In industrial countries, 60–70% of the emission reductions can be considered to have occurred due to structural change (UNFCCC, 2005; EEA, 2005). About half of emissions reduction from industrial countries is due to the collapse of the FSU and the resulting decrease in economic activity, leading to reduced energy consumption and fugitive emissions from fossil fuel production, transmission, and distribution. In addition, the number of cattle in the Russian Federation has more than halved from 1990 to 2000, leading to a corresponding decline in methane emissions from enteric fermentation (UNFCCC, 2004). Coal mining has decreased in many parts of

TABLE 1: Total annual CH_4 emissions from Annex I parties and the main contributors to the emission decreases between 1990 and 2003 (UNFCCC, 2005). Gap filling has been performed for some parties due to a lack of a complete time series

Annex I party	Emissions (Tg CH_4 yr^{-1})				
	1990	1995	2000	2003	Difference
Russia	26	19	14	14	–12
US	29	29	26	26	–2.9
Germany	6.3	5.0	3.9	3.6	–2.7
UK	3.7	3.1	2.4	1.9	–1.8
.....					
All Annex I parties	107	94	83	83	–25

the world, particularly in Germany, the UK, and the FSU. In addition, there is a trend toward more surface mines than underground mines, which also reduces methane emissions (IEA, 2005).

In many Annex I countries of the Kyoto Protocol, important mitigation measures of methane emissions have been committed in the 1990s and the 2000s. These include landfill gas recovery, CH_4 collection in coal mines, repairing of natural gas networks, and policy measures to reduce the amount of waste landfilled. About 30% of CH_4 emissions reduction from industrial countries can be explained by reductions in Germany, the US, and the UK. In the US, landfills are the largest anthropogenic source of methane. Even though the amount of municipal solid waste landfilled has increased, emissions have decreased by 24% (2.0 Tg yr^{-1}) from 1990 to 2003 due to increased landfill gas collection and combustion by landfill operators. In the US, coal mining is another significant source of methane, where emissions have decreased notably due to mitigation measures. CH_4 emissions decreased by 34% (1.3 Tg yr^{-1}) since 1990 due to the mining of less-gassy coal from underground mines and the increased use of methane collected from degasification systems (EPA, 2005).

In Germany, CH_4 emissions have decreased by 43% (2.7 Tg yr^{-1}) since 1990. About 1.0 Tg yr^{-1} of this decrease is due to a reduced amount of waste landfilled, as policy measures have led to increased recycling and energy recovery from waste. Fugitive CH_4 emissions from fossil fuels have decreased by 0.9 Tg yr^{-1} since 1990 due to decreased coal mining activity and to the repair and modernization of gas distribution networks (Umweltbundesamt, 2005).

In the UK, the largest reduction in CH_4 emissions (0.9 Tg yr^{-1} since 1990) has occurred in fugitive emissions from fuels. The largest contributor is coal mining, where coal production has decreased to one-third. Since 1990, CH_4 emissions from landfills have decreased by nearly 70% (0.7 Tg yr^{-1}) as methane recovery systems at landfills have been implemented (Baggott et al., 2005). Table 1 summarizes the main observed changes in methane emissions from Annex I countries.

The anthropogenic methane emissions from the Annex I parties reported to the United Nations Framework Convention on Climate Change (UNFCCC) can be compared with the emissions recently published by the International Energy Agency (IEA) (2005). The latter emissions estimates are based on the Emission Database for Global Atmospheric Research (EDGAR) database developed by TNO (the Netherlands Organization for Applied Scientific Research) and MNP (the Netherland Environmental Assessment Agency) (Olivier et al., 1999; 2005). The EDGAR system provides estimates of global anthropogenic emissions of greenhouse gases and other air pollutants on a 1×1 degree grid. EDGAR applies bottom-up methodology in emissions estimates, with activity data and emission factors mostly from international publications.

The emissions decrease in industrialized countries between the year 1990 and 2000 is 25 Tg yr^{-1} according to UNFCCC and 16 Tg yr^{-1} according to EDGAR. The difference may be an indication of the uncertainty of the emissions reductions.

Estimates of CH_4 emissions from developing countries are very uncertain, and most developing countries have reported emissions for only one or two years (typically 1990 or 1994) to the UNFCCC. It is generally assumed that emissions from developing countries are increasing along with the population and activity increase (IEA, 2005). The IEA estimates that total global anthropogenic CH_4 emissions have increased by 3% from 1990 to 2000, indicating that the emissions increase from developing countries would be slightly more than the decrease of emissions from industrial countries. The majority of CH_4 emissions from developing countries stems from agriculture, where the main contributors are enteric fermentation and rice cultivation.

In developing countries, the number of cattle has increased by around 15% from 1990 to 2003 (FAOSTAT, 2005). If we use the Intergovernmental Panel on Climate Change (IPCC) Tier 1 method to calculate the emissions (IPCC, 1997), this means an emission increase of 4–7 Tg CH_4 yr^{-1}. The rice production area has not increased notably (only 2%) from 1990 to 2003 according to statistics from the Food and Agriculture Organization (FAO), and therefore it does not have a major effect on CH_4 emission trends, even though differences between different cultivation methods cause uncertainty in this conclusion. The share of the energy sector in CH_4 emissions from developing countries is around 25%, but its share of emissions increase is larger. CH_4 emissions from the energy sector in developing countries have been estimated to have increased by 12 Tg yr^{-1} from 1990 to 2000 (IEA, 2005). The emissions derive mainly from coal mining and biomass combustion.

3. DEVELOPMENT OF ATMOSPHERIC CONCENTRATION

The atmospheric CH_4 burden increased between 1984 and 1991 by about 11 ppb yr^{-1} on average (about 30 Tg yr^{-1}) and between 1992 and 1998 by about 6 ppb yr^{-1} (16 Tg yr^{-1}) (Dlugokencky et al., 2003). Between 1999 and 2004, the increase of the CH_4 burden was close to zero (NOAA, 2005). The time behavior of the globally averaged concentration of CH_4 is often described with a single box model (Dlugokencky et al., 2003; IPCC, 2001):

$$dC(t)/dt = -C(t)/\tau + S(t) \ , \tag{1}$$

where C is the atmospheric CH_4 concentration, τ is the lifetime of CH_4 in the atmosphere, and S is the CH_4 source. The concentration can be assessed on the basis of measurements with quite good accuracy; however, the source and lifetime bear greater uncertainty and variation. Using the single box model with a constant lifetime of 8.9 years, global CH_4 emissions have been estimated to be practically constant from 1984 to 2002 (Dlugokencky et al., 2003).

Because Eq. (1) is linear, any source and its contribution to the total concentration can be considered separately. We estimated the impact of the emissions reductions in industrial countries since 1990 on the concentration using the single box

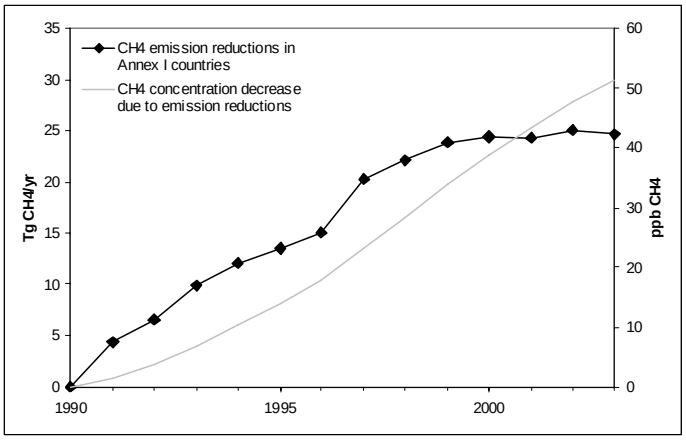

FIG. 1: Potential impact of the emissions reductions in Annex I countries (Table 1) on the atmospheric methane concentrations. The potential impact on the CH_4 concentration has been estimated with a single box model [Eq. (1)]. If the emissions reduction data were based on IEA (2005), the impact of emissions reductions would be about a third smaller.

model [Eq. (1)] with the lifetime of 8.9 years. The source term S in this calculation was the emission reductions described in Table 1. The impact of the emissions reduction on the concentration is about 50 ppb by 2003 (Fig. 1); hence, without the emissions reductions in the Annex 1 countries, the atmospheric concentration of methane would be 50 ppb higher.

This result is sensitive to the strength of the emission reduction. If the emission reductions calculated from the IEA (2005) report are used as S, the impact on the concentration is about a third smaller. However, this result is not sensitive to the assumption of the lifetime τ. A change of 0.5 years in the lifetime caused only a 2% change in the reduced concentration in 2003. Close to the equilibrium concentration, the overall concentration is sensitive to the lifetime τ, but when we consider a growing (but negative) concentration component alone, the term S of Eq. (1) is greater than the term $-C(t)/\tau$, and the impact of the variation of τ is small.

If the impact of the methane emissions reductions on the atmospheric methane concentration (Fig. 1) is added to the measured methane concentration, the total hypothetical concentration seems to increase almost with the same rate as before the year 1990 (Fig. 2).

Thus the decreasing emissions from the Annex 1 countries lead to a decreasing concentration component. At the same time, natural emissions and emissions from non-Annex I countries cause other concentration components. The overall methane concentration in the atmosphere, the sum of all concentration components, is roughly constant after about the year 2000, but it will start to increase if the emissions from developing countries increase.

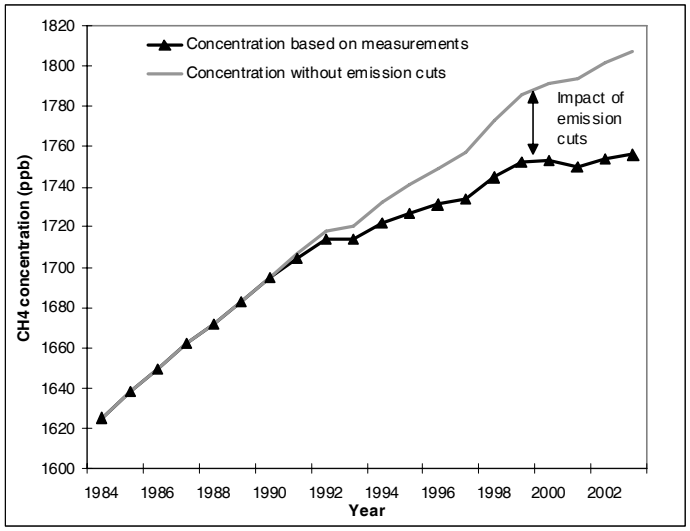

FIG. 2: CH_4 concentration based on observations (NOAA, 2005; Dlugokencky et al., 2003), reflecting the potential impact of the emissions reductions reported by the Annex 1 countries (UNFCCC, 2005; Table 1) and a hypothetical CH_4 concentration, where emissions from the Annex 1 countries would have remained at the 1990 level from 1990–2003.

4. DISCUSSION AND CONCLUSIONS

We demonstrated that significant emissions reduction measures, together with structural changes leading to methane emissions reduction of up to about 25 Tg CH_4 yr^{-1} in the industrialized countries, can be important contributors to the observed decrease and level-off of methane concentration increase in the atmosphere. Our conclusion is in agreement with that of Wang et al. (2004), who estimated CH4 emissions based on geographic and seasonal distribution of CH_4 sources between 1988 and 1997 and pointed out the emissions decline in the FSU as a probable cause. However, we showed that the concentration increase would not have levelled-off without intentional and unintentional emission reductions from industrial countries, unless we assume that the effective lifetime of methane has changed.

The lifetime of CH_4 in the atmosphere is relatively short and, therefore, atmospheric CH_4 concentration responds quite rapidly to changes in the emissions if compared, e.g., to carbon dioxide, the effective lifetime of which is in the order of a hundred years (IPCC, 2001). The effects of mitigation measures of some other well-mixed gases have already been observed by atmospheric measurements. For example, the atmospheric concentrations of CFC-11 and CFC-113 have declined in recent years due to emission reductions under the Montreal Protocol signed at the end of the 1980s (Blake, 2005).

Hansen et al. (2000) have proposed that the control of CH_4 emissions is a rapid way to limit the rate of climate change. Our study suggests, on the basis of emissions statistics and model calculations, that the reduction of methane emissions can effectively mitigate climate change on a short time scale, and that the first results of mitigation measures in industrialized countries may already be observable in the atmosphere. This implies that further methane mitigation measures, e.g., in coal mines, gas fields, biomass burning, and waste management could provide efficient potential for the further limitation of atmospheric methane concentrations. Unless this is done, there is an evident risk that methane concentrations will start to rise again.

REFERENCES

Baggott, S., Brown, L., Milne, R., Murrells, T., Passant, N., Thistlethwaite, G., and Watterson, J., UK greenhouse gas inventory 1990 to 2003, Annual Report for submission under the Framework Convention on Climate Change, Global Atmosphere Research Programme of the Department for Environment, Food, and Rural Affairs, UK, 2005.

Blake, D., Methane, nonmethane hydrocarbons, alkyl nitrates, and chlorinated carbon compounds including 3 chlorofluorocarbons (CFC-11, CFC-12, and CFC-113) in whole-air samples, *Trends: A Compendium of Data on Global Change*, Carbon Dioxide Information Analysis Center, Oak Ridge National Laboratory, US Department of Energy, Oak Ridge, TN, 2005.

Dlugokencky, E.J., Masarie, K.A., Lang, P.M., and Tans, P.P., Continuing decline in the growth rate of atmospheric methane burden, *Nature*, vol. 393, pp. 447–450, 1998.

Dlugokencky, E., Masarie, K.A., Lang, P.M., Miller, J.B., and Tans, P.P., Atmospheric methane levels off: Temporary pause or a new steady-state?, *Geophys. Res. Lett*., vol. 30, pp. 5-1–5-4, 2003.

EEA, Annual European Community greenhouse gas inventory 1990–2003 and inventory report 2005, Submission to the UNFCCC Secretariat, EEA, Copenhagen, Denmark, 2005.

EPA, Inventory of U.S. greenhouse gas emissions and sinks 1990–2003, US Environmental Protection Agency, Washington, DC, 2005.

FAOSTAT, Faostat data 2005, http://faostat.fao.org, 2005.

Hansen, J., Sato, M., Ruedy, R., Lacis, A., and Oinas, V., Global warming in the twenty-first century: An alternative scenario, *Proc. Natl. Acad. Sci. USA*, vol. 97, pp. 8975–9880, 2000.

Hansen, J. and Sato, M., Trends of measured climate forcing agents, *Proc. Natl. Acad. Sci. USA*, vol. 98, no. 26, pp. 14778–14783, 2001.

IEA, CO_2 emissions from fuel combustion 1971–2003, IEA, Paris, France, 2005.

IPCC, *Revised 1996 IPCC Guidelines for National Greenhouse Gas Inventories*, Reference manual, http://www.ipcc-nggip.iges.or.jp/public/gl/invs6.htm, 1997.

IPCC, *Climate Change 2001: The Scientific Basis. Contribution of Working Group I to the Third Assessment Report of the Intergovernmental Panel on Climate Change (IPCC)*, Eds Houghton, J. et al., Cambridge University Press, Cambridge, 2001.

Keppler, F., Hamilton, J., Bras, M., and Röckmann, T., Methane emissions from terrestrial plants under aerobic conditions, *Nature*, vol. 439, pp. 187–191, 2006.

Mikaloff Fletcher, S., Tans, P., Bruhwiler, L., Miller, J., and Heimann, M., CH_4 sources estimated from atmospheric observations of CH_4 and its 13C/12C isotopic ratios: 1. Inverse modeling of

source processes, *Global Biogeochem. Cycles*, vol. 18, GB4004, doi:10.1029/2004GB002223, 2004a.

Mikaloff Fletcher, S., Tans, P., Bruhwiler, L., Miller, J., and Heimann, M., CH_4 sources estimated from atmospheric observations of CH4 and its 13C/12C isotopic ratios: 2. Inverse modeling of CH_4 fluxes from geographical regions, *Global Biogeochem. Cycles*, vol. 18, GB4005, doi:10.1029/2004GB002224, 2004b.

Monni, S., Syri, S., and Savolainen, I., Uncertainties in the Finnish greenhouse gas emission inventory, *Environ. Sci. Policy*, vol. 7, pp. 87–98, 2004.

Monni, S., Syri, S., Pipatti, R., and Savolainen, I., Extension of EU emission trading scheme to other sectors and gases: consequences for uncertainty of total tradable amount, *Water, Air, Soil Pollut.*, vol. 7, no. 4–5, pp. 529–538, 2006.

NOAA, Radiative climate forcing by long-lived greenhouse gases: the NOAA annual greenhouse gas index (aggi), NOAA Earth System Research Laboratory, R/GMD, Boulder, CO, http://www.cmdl.noaa.gov/aggi/, 2005.

Olivier, J.G.J., Bouwman, A.F., Berdowski, J.J.M., Veldt, C., Bloos, J.P.J., Visschedijk, A.J.H., Van der Maas, C.W.M., and Zandveld, P.Y.J., Sectoral emission inventories of greenhouse gases for 1990 on a per country basis as well as on $1^{o} \times 1^{o}$, *Environ. Sci. Policy*, vol. 2, pp. 241–264, 1999.

Olivier, J.G.J, Van Aardenne, J.A., Dentener, F., Ganzeveld, L., and Peters, J.A.H.V., Recent trends in global greenhouse gas emissions: Regional trends and spatial distribution of key sources, A. van Amstel (coord.) Non-CO_2 greenhouse gases (NCGG-4), Rotterdam: Millpress, 2005.

Rypdal, K. and Winiwarter, W., Uncertainties in greenhouse gas emission inventories — evaluation, comparability and implications, *Environ. Sci. Policy*, vol. 4, pp. 107–116, 2001.

Simpson, I., Blake, D., Rowland, F., and Chen, T.-Y., Implications of the recent fluctuations in the growth rate of tropospheric methane, *Geophys. Res. Lett.*, vol. 29, pp. 117-1–117-4, 2002.

Umweltbundesamt, German Greenhouse Gas Inventory 1990–2003, National Inventory Report 2005, Submission under the United Nations Framework Convention on Climate Change, Federal Environmental Agency (Umweltbundesamt), Berlin, Germany, 2005.

UNFCCC, Russian Federation, Report on the in-depth review of the third national communication of the Russian Federation, FCCC/IDR.3/RUS, UNFCCC Secretariat, Bonn, Germany, 2004.

UNFCCC, Key GHG Data, Greenhouse Gas Emissions Data for 1990–2003 Submitted to the United Nations Framework Convention on Climate Change, UNFCCC Secretariat, Bonn, Germany, 2005.

Wang, J., Logan J., McElroy, M., Duncan, B., Megretskaia, I., and Yantosa, R., A 3-D model analysis of the slowdown and interannual variability in the methane growth rate from 1988 to 1997, Global Biogeochem. Cycles, vol. 18, GB3011, doi:10.1029/3003GB002180, 2004.

Wuebbles, D. and Hayhoe, K., Atmospheric methane and global change, *Earth-Sci. Rev.*, vol. 57, pp. 177–210, 2002.

International Journal of Energy for a Clean Environment, 10(1–4), 203–215 (2009)

CONSIDERATIONS ON EXPERIMENTAL STUDIES OF VEGETABLE CHAR COMBUSTION IN FLUIDIZED BED

N. Rangel and C. Pinho[*]

Centro de Estudos de Fenómenos de Transporte (CEFT),
Departamento de Engenharia Mecânica (DEMec),
Faculdade de Engenharia, Universidade do Porto,
Rua Dr. Roberto Frias s/n, 4200-465 Porto, Portugal

[*]Address all correspondence to C. Pinho, E-mail: ctp@fe.up.pt

This paper reports some experimental aspects of the combustion of batches of vegetable chars in a fluidized-bed laboratory reactor at temperatures of 600, 700, and 750^{0}C. Data on the volumic concentrations of carbon oxides and volatile organic compounds along the combustion process are presented and discussed. Tests show that the carbon conversion rate is not only due to combustion, but there are pyrolysis phenomena that accompany it and contribute to the global conversion rate of the carbon. The burned-out and consumed mass fractions of carbon were determined, and it was observed that these two quantities differ, particularly for lower bed temperatures. Vegetable chars when suffering combustion in low-temperature fluidized beds release tars in the form of vapors that escape from the bed without burning.

KEYWORDS: *carbon conversion, fluidized bed, vegetable char combustion*

1. INTRODUCTION

Vegetable char production from wood was one of the first energy-conversion techniques developed by mankind. Its industrial use goes back to prehistoric dates of the Metal Age, where it was used as fuel in the iron industry. Since then it has been used for several centuries, but its most intensive use happened in the 18th and 19th centuries. It was impossible, however, to support the huge energy consumption that the Industrial Revolution demanded, and vegetable chars were slowly replaced by mineral coal and its coke, and afterward by crude oil and natural gas in the second half of 20th century. But taking into account the new challenges raised by global climate changes and the subsequent evolution that seems to impose the future abandon of fossil fuel sources of energy, biomass can be a renewable source of energy that must be taken into account, although it is expected that its importance in a future energy mix will be minor.

The sustainable use of biomass as an energy source may impose the use of some technological approaches. One such approach is carbonization, a kind of densification technique used for biomass-derived fuels (Strezov et al., 2006). The vegetable char has a heating value similar to that of high-ranking mineral coal, but its production is a demanding technological process (Antal and Várhegyi, 1995). The quality of the char depends upon several parameters such as heating rate, controlled atmosphere, final pyrolysis temperature, and pyrolysis time (Strezov et al., 2007). Through the combination of these factors a unique type of vegetable char is obtained, so in the absence of a standardized production method regulating these factors, a great variability in the wood chars properties is expected, particularly with regard to the content of residual tars.

In this work commercially available nut pine and cork oak chars, usually found in Portugal and for which no reliable kinetic data are available, were used in order to show some characteristic aspects connected to the fluidized-bed combustion of biomass. Then the commercial chars were recarbonized under controlled laboratory conditions, and the influence of this second treatment upon properties and combustion performance of the new chars was again evaluated.

The vegetable chars when going through a combustion process release residual tars that ultimately will affect the carbon recovery ratio of the combustion process (Ahrenfeldt et al., 2005; Fjellerup et al., 2005; Chen et al., 2009). Carbon recovery ratio is defined as the quotient between the mass of carbon leaving the bed in the exhaust combustion gases, detected through the time integration of the CO_2 and CO concentration curves, and the mass of carbon initially introduced into the bed through the batch of char particles. So for commercial nut pine char the carbon recovery ratio was previously determined considering the combustion process itself. The extra carbon consumption ratio was also determined due to the release of tars, high-molecular-weight hydrocarbons that left the bed without being burned because of a parallel pyrolysis that takes place simultaneously with combustion of the commercial char. The true carbon consumption ratio is the addition of these two terms.

2. EXPERIMENTAL

Experimental study of the combustion of batches of vegetable chars was done in the setup shown in Fig. 1. The char feeding was done through a stainless steel pipe whose entrance in the bed was 250 mm above the distributor. In this way, because the bed height was 100 mm, the char feeding point was 150 mm above bed-free surface. The distributor was a stainless steel plate 3 mm thick with 177 holes with 0.6 mm diameter, placed in square pitch 4 mm apart. The stainless steel bed riser pipe had 54.5 mm of internal diameter and 2.5 m height. In the bubbling bed region there was an electrical resistance around it with 0.250 m height and it was thermally isolated with a ceramic blanket; the riser was also thermally isolated. Type-K thermocouples were used for bed temperature measurement and control through a proportional integral derivative (PID) controller. The

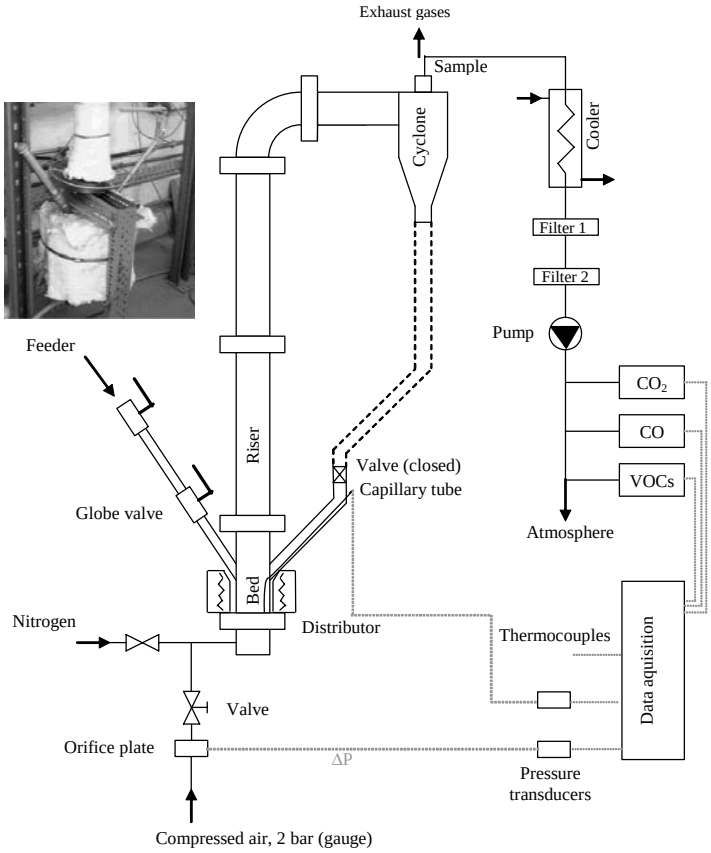

FIG. 1: Experimental setup

static pressure at the bottom of the bed was measured using a capillary tube connected to a pressure transducer. The bed was composed with silica sand particles in a size range of 200–250 μm and a density of 3000 kg/m^3. The particle sizes tested were of 3.6, 2.8, 2.2, and 1.8 mm, which correspond to the average diameters obtained by the Deutsches Institute für Normung (DIN) standard sieves.

Measurements of emissions in exhaust gases were done by infrared gas analyzers for CO_2 and CO, and by a hydrocarbon analyzer with flame ionization detection for the volatile organic compounds. Typical relative uncertainty values for the measurements of gaseous concentrations at the bed exit went from 2 to 4%, depending on the operating range.

2.1 Experimental Procedure

Batches of 5 g of char particles were burned in a bubbling bed of sand fluidized with air, and the evolution of the volumic concentration of CO_2 in the exhaust

gases was monitored at the cyclone exit installed on the top of the riser of the fluidized-bed reactor. In the combustion experiments, commercial and recarbonized chars of nut pine (*Pinus pinea*) and cork oak (*Quercus suber*) were burned at bed temperatures of 600, 700, and 750°C for superficial velocities of 9 and 12 times the minimum fluidizing velocity. The static bed height was in all cases 100 mm.

Particle recarbonization in the laboratory was carried out by immersion of particle batches of commercial char in a sand bed fluidized with nitrogen at 850°C for 5 min.

In another set of experiments, the combustion process was interrupted to carry out measurements of bed carbon content at the instant of combustion stoppage. In this way a simple comparison between carbon consumption due to combustion and the overall carbon consumption of the batch could be obtained. The difference between these two values was the carbon being carried away in tars released through a pyrolysis phenomenon taking place at the same time as the combustion process. This situation happens in reactors where inside conditions are adequate for the occurrence of incomplete combustion (Ross et al., 2002; Nussbaumer, 2003; Conde et al., 2005; Demirbas, 2008), as occurs in the present work, where relatively low-temperature combustion experiments were carried out.

In this new set of experiments, particles with an initial average diameter of 3.6 mm were studied for bed temperatures of 600, 700, and 750°C, and for a superficial velocity of $9U_{mf}$. The combustion was stopped at 30, 60, 120, 180, and 240 s after introduction of the particles inside the bed. At the instant of stoppage, the fluidizing air was replaced by nitrogen and the bed cooled down; the bed was removed afterward and char particles were separated from the inert bed particles through a sieving process. The char particles were then weighed and it was possible to know, at these stoppage instants, the mass of carbon remaining in the bed.

3. DISCUSSION OF RESULTS

3.1 Evolution of Volumic CO_2 Concentration in the Combustion Gases

Typical curves of the evolution of the volumic concentration of CO_2 in a dry basis are shown in Fig. 2 for a commercial nut pine char, two bed temperatures, initial particle diameters of 1.8 and 3.6 mm, and for $9U_{mf}$. Through the analysis of this figure it is found that, as expected, the burnout time increases with the increase of the initial particle diameter. Also, the CO_2 concentration peaks are more intense for smaller particles, and these peaks rise for higher bed temperatures. There is, however, a contradictory fact. For a given initial particle diameter, it is found that the burnout times are approximately the same for different bed temperatures. The expected behavior would be that for the same initial particle diameter but at different bed temperatures, different combustion times would be detected. In fact, although an increase on the combustion rate with temperature is detected, through

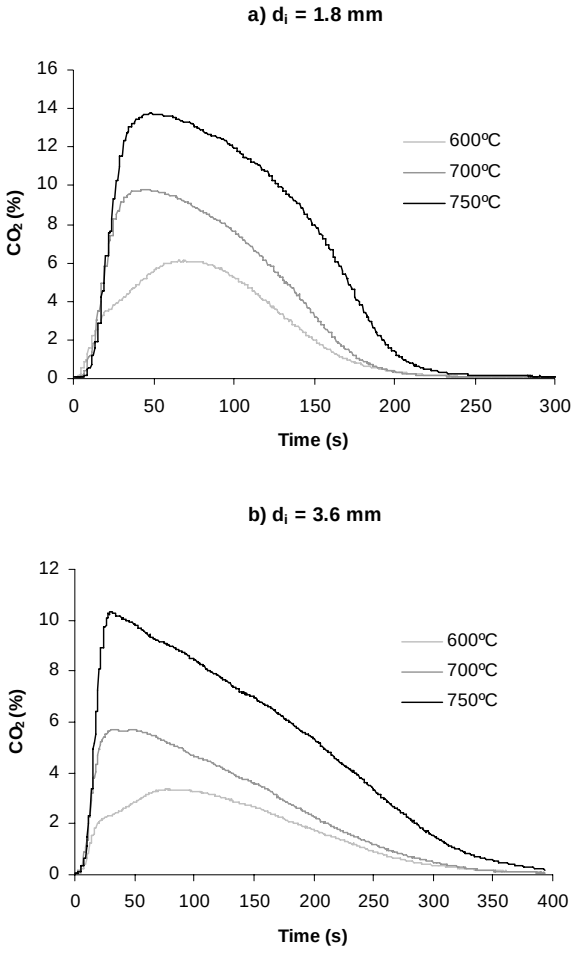

FIG. 2: Evolution of the dry basis volumic concentration of CO_2 for commercial nut pine char particles with initial diameters of (a) 1.8 and (b) 3.6 mm. Bed temperatures of 600, 700, and 750°C, superficial velocity of $9U_{mf}$, and static bed height of 100 mm

the analysis of the derivative of the evolution of the CO_2, which increases as bed temperature rises, combustion times remain the same. This is connected to the fact that carbon of the char particles is also being consumed through pyrolysis, which develops in parallel with the combustion process, and the lifetime of a batch of char particles is a function of these two phenomena. The importance of these pyrolysis phenomena is quantified later in this paper.

Figure 3 shows the influence of the fluidization velocity on the CO_2 concentration curves for commercial nut pine char, $9U_{mf}$ and $12U_{mf}$, and initial particle sizes of 1.8 and 3.6 mm. The air fluidizing velocity has no significant impact

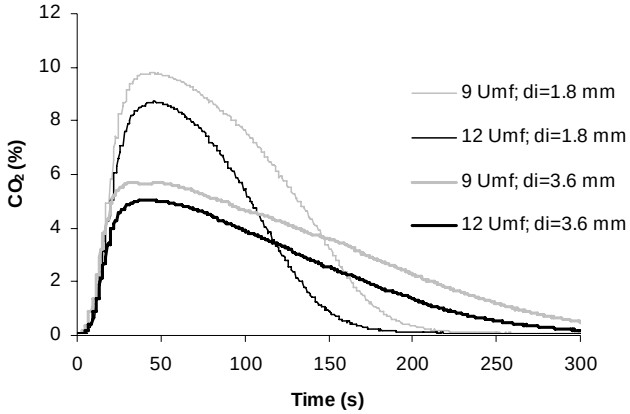

FIG. 3: Influence of the fluidization velocity on the CO_2 curves. Fluidization velocities of 9 and $12U_{mf}$ and initial particle sizes of 1.8 and 3.6 mm

upon the CO_2 concentration curves, but it is detected that higher superficial velocities lead to lower CO_2 concentrations because of dilution effects. For the sake of simplicity, results for only two of the tested sizes, 1.8 and 3.6 mm, are shown, but for all tested sizes the trends are equal. The shape of the CO_2 concentration curves also shows that there is primary fragmentation and absence of secondary fragmentation, phenomena which are discussed elsewhere (Rangel and Pinho, 2010).

3.2 Evolution of the Volumic Concentration of CO in the Exhaust Gases

In Fig. 4 a typical curve for the dry basis volumic concentration of CO in the exhaust gases is presented. There is a short peak of 3.5% (v/v) CO at the beginning of the combustion process, just immediately after the batch of char particles is introduced into the bed. For the remaining of the combustion process, CO concentrations are residual or even nil.

The amount of CO in the combustion gases is irrelevant as far as the calculation of the mass of carbon consumed during combustion is concerned. The amount of carbon obtained through the integration of the CO curve, as for the CO_2 curve, leads to carbon recovery ratios below 2%.

3.3 Evolution of the Concentration of Organic Volatile Compounds

The emission of volatile organic compounds (VOCs) in the exhaust gases is shown in Fig. 5, and a single peak of 1800 ppm (v/v) is observed only at the beginning of the combustion process. The released products of the pyrolysis that is occurring simultaneously with the combustion process leave the bed as high-molecular-mass

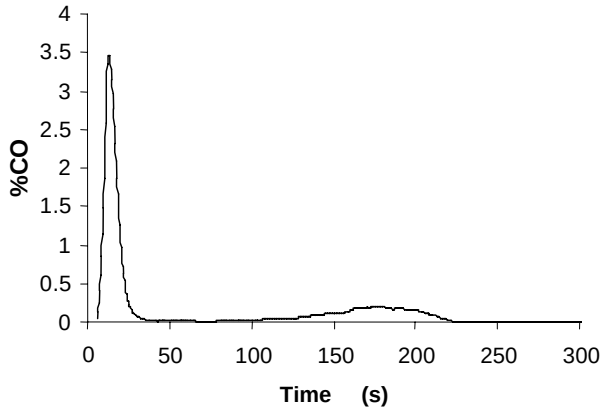

FIG. 4: Typical evolution of the dry basis volumic concentration of CO. Burning 5 g of nut pine commercial char particles with 1.8 mm diameter, at bed temperature of 750°C, for a $9U_{mf}$ superficial velocity, and a 300 mm static bed height

vapors which cannot be detected with the available VOC analyzer; more sophisticated equipment is needed (Branca et al., 2003; Demirbas, 2007; Chen et al., 2009).

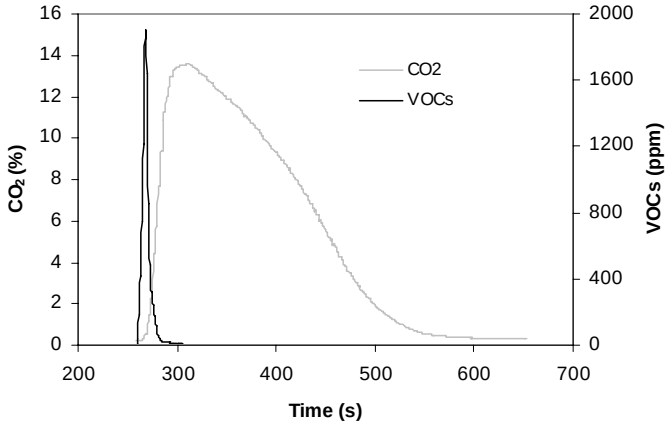

FIG. 5: Evolution of VOCs and CO_2 volumic concentrations for a combustion experiment of a batch of 5 g of commercial nut pine char particles with a diameter of 2.8 mm burning in a bed with temperature of 750°C, 100 mm static height, and $U/U_{mf} = 9$

3.4 Carbon Recovery Ratio and Properties of the Fuel Particles

In theory, if carbon is fully consumed in the combustion reaction, the carbon recovery ratio should be one, because it should be burned to CO_2 according to the sequence of reactions $C + \frac{1}{2}O_2 \rightarrow CO$ and $CO + \frac{1}{2}O_2 \rightarrow CO_2$ (Hayhurst and Parmar, 1998; Basu, 1999). However, it was found that the carbon recovery ratios, determined as referred above, were always below the 100% theoretical value. Table 1 presents average values for carbon recovery ratios for all the experiments done.

The carbon recovery ratio increases with the rise of bed operating temperature; this means that in such a situation the combustion reaction predominates relative to the pyrolysis phenomena and the subsequent exhaust of unburned tars typical of low-temperature reactors (Ross et al. 2002; Nussbaumer, 2003; Conde et al., 2005; Demirbas, 2008). At higher bed temperatures the tars released by the pyrolysis process also burn inside the bed, leading to an increase of the CO_2 concentration at the exit. This leads to higher carbon recovery ratios through the integration of the CO_2 curve. At lower bed temperatures, heavy hydrocarbons, commonly designated by tars, leave the bed unburned and are not detected with the VOC analyzer used in the experiments, and accordingly the carbon recovery ratios are smaller. Another conclusion from Table 1 is that for recarbonized chars the carbon recovery ratios are always higher than those of the corresponding commercial chars. This means that a second pyrolysis, carried out in a situation similar to the combustion situation, reduces the pyrolysis phenomena that take place simultaneously with the combustion process.

This result is a demonstration that while combustion takes place for commercial chars produced at relatively low temperatures and heating rates, pyrolysis happens at the same time. For recarbonized chars the parallel pyrolysis process is less important. The influence of this parallel pyrolysis is important only for low bed combustion temperatures (Table 1). At normal bed temperatures used in fluidized-bed furnaces (850–950^{o}C), this phenomenon has minor impact. However, lower bed temperature experiments are recommended to determine kinetic data (Fennel et al., 2007), and under these conditions the phenomenon should be considered.

There is a strong disparity among carbon recovery ratios for commercial and recarbonized chars (Fig. 6). The plotted values were obtained for superficial velocities of 9 and $12U_{mf}$. For all temperatures there is an increase in the carbon recovery ratio for both chars, but the strongest increase was found for nut pine chars tested at 600^{o}C, when the increase of this ratio was 97%.

Elutriation is out of the question as an explanation for the low carbon recovery rate, as the fragmentation phenomenon occurring with this type of char does not lead to elutriable particle sizes (Rangel and Pinho, 2010).

Table 1 also shows densities and proximate analysis for the studied particles. Comparing the recarbonized nut pine char with the corresponding commercial char,

TABLE 1: Average values for the carbon recovery ratio. Proximate analysis and particle densities of the chars

Parent wood	**Pinus pinea**				**Quercus suber**			
Char	**Commercial**		**Recarbonized**		**Commercial**		**Recarbonized**	
U/U_{mf}	9	12	9	12	9	12	9	12
	Carbon recovery ratio (%)							
Bed temperature (^{o}C)								
600	32	31	63	61	64	60	67	72
700	43	60	78	72	76	66	81	70
750	65	61	90	76	85	67	86	70
Particle density (kg/m^3)	770		740		630		680	
Proximate analysis (% w/w, as received)								
Moisture	7.7		8.3		5.3		3.1	
Ash	0.7		1.4		5.8		8.0	
Volatile matter	17.7		7.3		28.4		8.2	
Fixed carbon	73.9		83.0		60.5		80.7	

(1)Density obtained with a mercury intrusion porosimeter, Quantachrome PoreMaster.

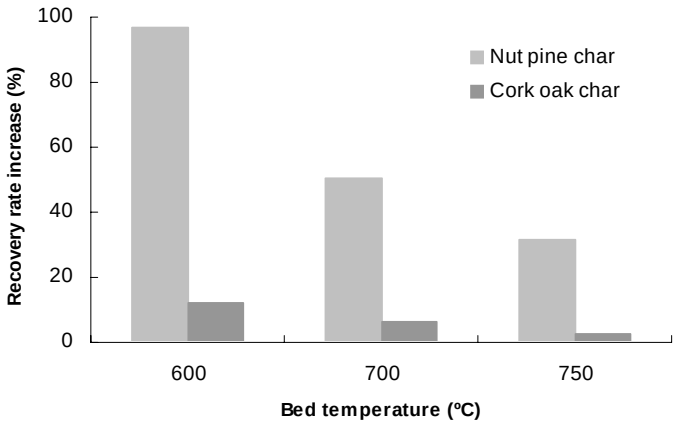

FIG. 6: Percentage of increase of the carbon recovery rate

a 4% reduction of the char density is detected and a 12% increase of the fixed carbon mass fraction. The increase of this parameter is the result of a decrease of the volatile matter. Comparing the properties of both cork oak chars, there is now a slight increase of the recarbonized char density, but the increase of the mass fraction of fixed carbon suffered a remarkable augmentation, once again at the expense of a decrease of volatile matter fraction.

3.5 Burned Fraction and Consumed Fraction

The mass burned fraction for a given time instant corresponds to the carbon recovery ratio at that time through integration of the CO_2 curve. The mass consumed fraction is obtained through interrupted combustion experiments. This consumed mass fraction represents all the carbon that was consumed either through combustion or through the pyrolysis by the tars dragged away from the bubbling bed. This distinction, as it was previously explained, is necessary because for several experiments, mainly at low bed temperature and for commercial chars, the carbon recovery ratio through combustion is rather low (Table 1).

Through the interrupted combustion experiments it was possible to quantify the importance of this phenomenon. The conclusion is that when burning commercial chars at low-temperature conditions, because of the original pyrolyzing process being used, a secondary pyrolysis process takes place at the same time as the combustion process and this leads to high unburned carbon losses. Recarbonizing the chars at higher heating ratios and temperatures, like those found in a bubbling fluidized bed, diminishes the importance of this secondary pyrolysis. It must be stressed, however, that the lower temperature combustion experiments were carried out in order to get kinetic data and that in normal burning conditions the bubbling bed and the bed-free surface regions are hotter and the tars burn as well, and the carbon recovery ratio, obtained through integration of the CO_2 curve, reaches acceptable values, in the 90% range.

Figure 7 shows, for bed temperatures of 600, 700, and 750°C, burned and consumed carbon fractions for several combustion stoppage instants along the reaction. The consumed carbon fractions for a reaction time of 240 s are always around 90%. Although the burned mass fraction is only of the order of 60% at a bed temperature of 750°C, it is lower than 40% for 700°C and around 30% for 600°C. So the carbon losses through heavy hydrocarbons from pyrolytic phenomena may be dominant for low-temperature combustion experiments. This indicates the importance of volatile combustion of this type of commercial vegetable char and provides a warning regarding the caution necessary when collecting kinetic data at relatively low-temperature experiments.

Figure 7 also shows that the discrepancy between the burned mass fraction and the consumed mass fraction increases with combustion time, which means that the pyrolysis process is continuous and occurs along with combustion. This differential diminishes with the increase of bed temperature due to the increase of the combustion rate.

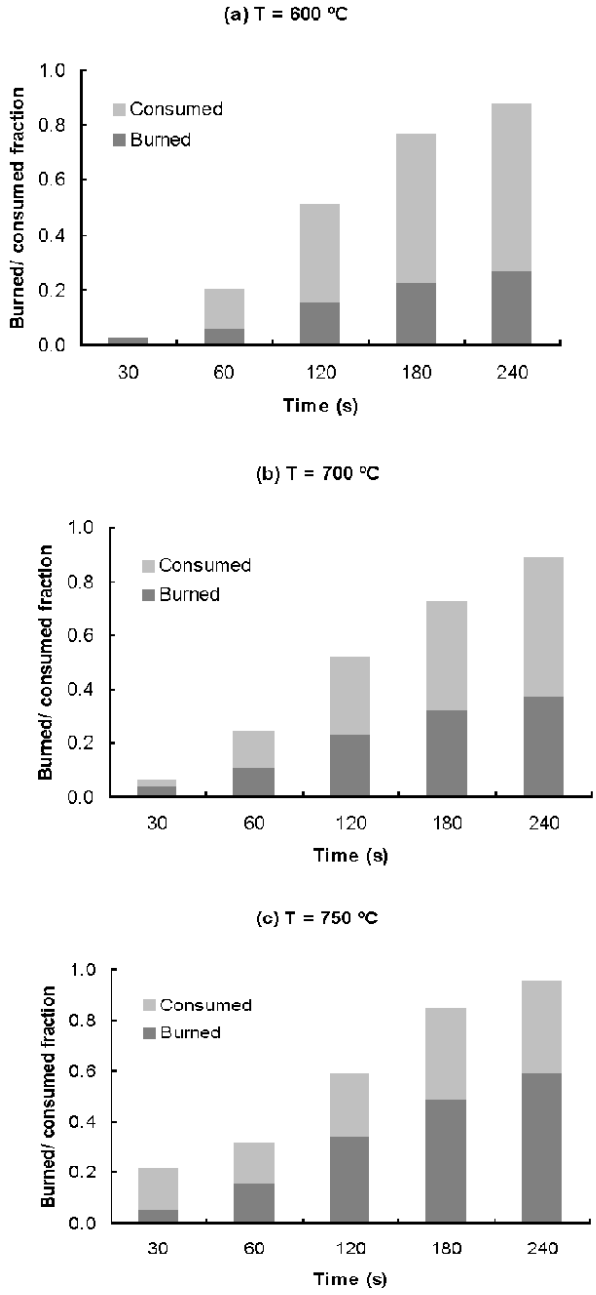

FIG. 7: Evolution of carbon burned and consumed mass fractions over the burning time for bed temperatures of (a) 600, (b) 700, and (c) 750^{o}C. Superficial fluidizing velocity of $9U_{mf}$, 3.6 mm particles, and static bed height of 100 mm

4. CONCLUSIONS

Production of commercial vegetable chars still follows traditional methods and consequently the quality and homogeneity of the resulting char is very limited. Such vegetable chars when suffering rapid heating in fluidized-bed combustion experiments simultaneously undergo a pyrolysis process, releasing tars in the form of vapors that escape from the reaction zone without burning and are undetected by the simpler analyzers for VOCs.

As the calculation of the carbon recovery ratio in combustion experiments is done through integration of the concentration curves of CO_2 in the exhaust gases, while doing low-temperature combustion experiments (600–750^{o}C) for the determination of kinetic data, care must be taken to account for the influence of the carbon extracted in the pyrolysis products flowing in the exhaust gases. Otherwise evaluation of the evolution of the char particle size during combustion will be disregarded and the resulting kinetic and diffusive data will suffer from such failure. Although the evaluation of CO emissions and low-molecular-weight VOCs was not very thorough, the conclusion is that their values were negligible.

Using a recarbonization of the chars in a bed fluidized with nitrogen at 850^{o}C has a dwindling effect upon the parallel pyrolysis but does not remove it. This may be due to the short resident time at 850^{o}C used in the recarbonization process, which was 5 min.

As far as commercial fluidized-bed operation is concerned, adequate kinetic and diffusive data are necessary for the correct design of the burners. Since the kinetic data should be obtained at low bed temperature, a careful approach must be adopted when analyzing the significance of such low-temperature combustion.

REFERENCES

Ahrenfeldt, J., Henriksen, U., Gøbel, B., and Fjellerup, J., *Experimental Characterisation of Residual-Tar in Wood Char* (April 2005), Ret. Nov. 11, 2008, from http://www.dtu.dk/English/Service/Phonebook.aspx?lg=showcommon&id=185351.

Antal, M.J. and Várhegyi, G., Cellulose pyrolysis kinetics: The current state of knowledge, *Ind. Eng. Chem. Res*., vol. 34, pp. 703–717, 1995.

Basu, P., Combustion of coal in circulating fluidized-bed boilers: A review, *Chem. Eng. Sci*., vol. 54, pp. 5547–5557, 1999.

Branca, C., Giudicianni, P., and Di Blasi, C., GC/MS characterization of liquids generated from low-temperature pyrolysis of wood, *Ind. Eng. Chem. Res.*, vol. 42, no. 14, pp. 3190–3202, 2003.

Chen, Y., Luo, Y., Wu, W., and Su, Y., Experimental investigation on tar formation and destruction in a lab-scale two-stage reactor, *Energy Fuels*, vol. 23, no. 9, pp. 4659–4667, 2009.

Conde, F.J., Ayala, J.H., Afonso, A.M., and González, V., Emissions of polycyclic aromatic hydrocarbons from combustion of agricultural and sylvicultural debris, *Atmos. Environ*., vol. 39, pp. 6654–6663, 2005.

Demirbas, A., The influence of temperature on the yields of compounds existing in bio-oils obtained from biomass samples via pyrolysis, *Fuel Process. Technol*., vol. 88, pp. 591–597, 2007.

Demirbas, A., Hazardous emissions from combustion of biomass, *Energy Sources, Part A*, vol. 30, pp. 170–178, 2008.

Fennel, P.S., Kadchha, S., Lee, H.-Y., Dennis, J.S., and Hayhurst, A.N., The measurement of the rate of burning of different coal chars in an electrically heated fluidized bed of sand, *Chem. Eng. Sci.*, vol. 62, pp. 608–618, 2007.

Fjellerup, J., Ahrenfeldt, J., and Henriksen, U., Pyrolysis of pine wood, Experiments and theory, *Proc. of the 14th European Conf. and Exhibition: Biomass for Energy, Industry and Climate Protection*, Paper v2aVI-16, 2005.

Hayhurst, A.N. and Parmar, M.S., Does solid carbon burn in oxygen to give the gaseous intermediate CO or produce CO_2 directly? Some experiments in a hot bed of sand fluidized by air, *Chem. Eng. Sci.*, vol. 53, pp. 427–438, 1998.

Nussbaumer, T., Combustion and co-combustion of biomass: Fundamentals, technologies, and primary measures for emission reduction, *Energy Fuels*, vol. 17, pp. 1510–1521, 2003.

Rangel, N. and Pinho, C., Fragmentation effect on batches of pine wood char burning in a fluidized bed, *Energy Fuels*, vol. 24, pp. 318–323, 2010.

Ross, A.B., Jones, J.M., Chaiklangmuang, S., Pourkashanian, M., Williams, A., Kubica, K., Andersson, J.T., Kerst, M., Danihelka, P., and Barle, K.D., Measurements and prediction of the emission of pollutants from the combustion of coal and biomass in a fixed bed furnace, *Fuel*, vol. 81, pp. 571–582, 2002.

Strezov, V., Evans, T.J., and Nelson, P.F., Carbonization of biomass fuels, in: M.D. Brenes (Ed.), *Biomass and Bioenergy: New Research*, New York: Nova Science Publishers, pp. 91–123, 2006.

Strezov, V., Patterson, M., Zymlab, V., Fisher, K., Evans, T.J., and Nelson, P.F., Fundamental aspects of biomass carbonisation, *J. Anal. Appl. Pyrolysis*, vol. 79, pp. 91–100, 2007.